UNIVERSITY OF ROCHESTER
LABORATORY FOR LASER ENERGETICS

Volume 130
January–March 2012
DOE/NA/28302-1058

LLE Review

Quarterly Report

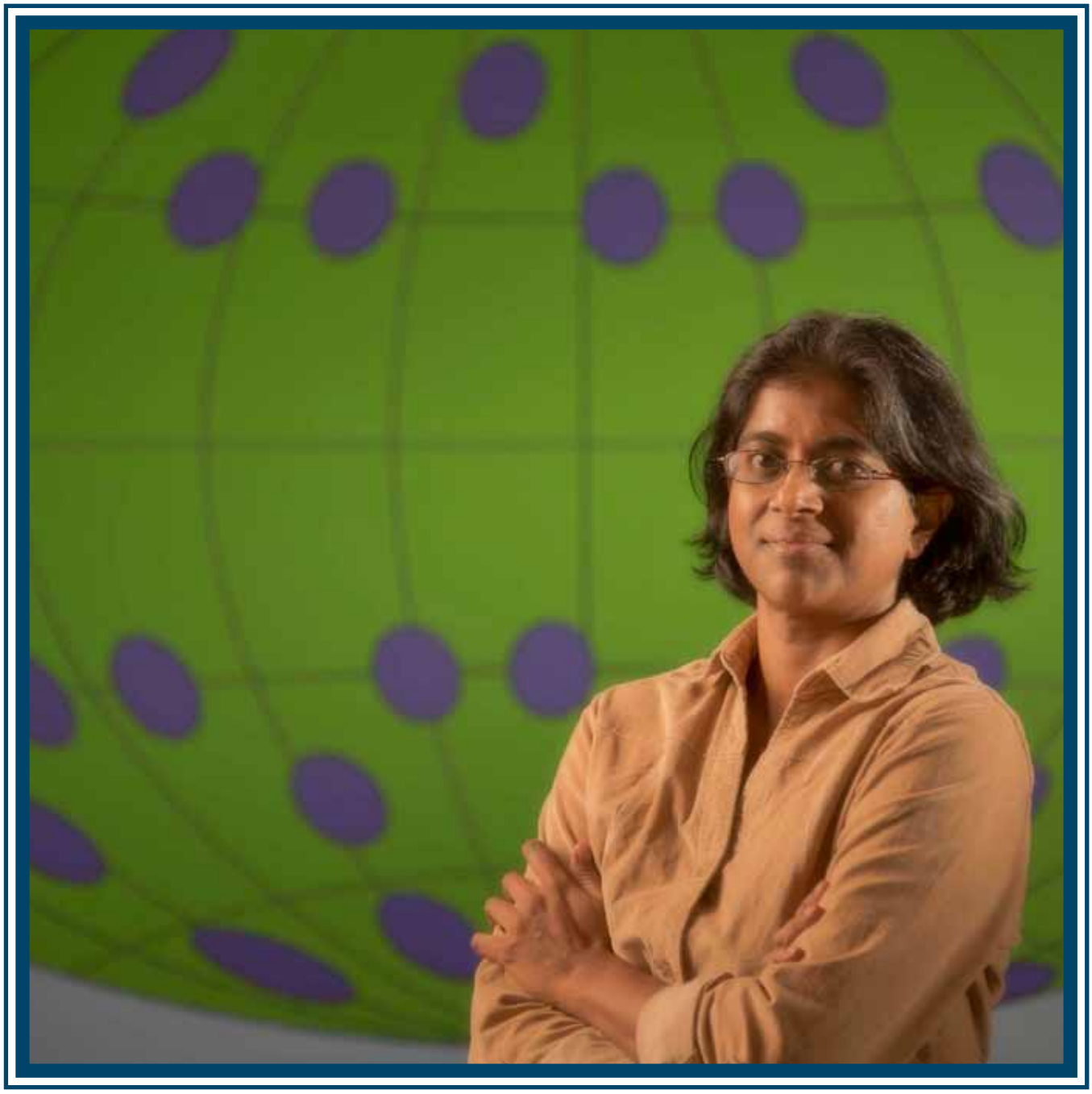

About the Cover:

The cover photo highlights scientist Dr. Radha Bahukutumbi presenting new OMEGA polar-drive target designs. In the background is a schematic that illustrates the 40 OMEGA beams that emulate the NIF x-ray-drive beam geometry. Being an indirect-drive implosion facility, NIF has no laser beams at the equator, which requires modification of the traditional, symmetric direct drive to achieve adequate symmetry. The concept of using the NIF laser with its beams repointed toward the equator is called polar drive and enables one to conduct direct-drive experiments to be carried out on the NIF while it is in its standard x-ray-drive configuration. To emulate polar drive on OMEGA, 20 equatorial beams are dropped and the remaining 40 beams are repointed toward the target's equator. The OMEGA experiments yield valuable data to develop and validate models of laser-energy deposition, heat conduction, nonuniformity growth, and fuel assembly in polar-drive geometry.

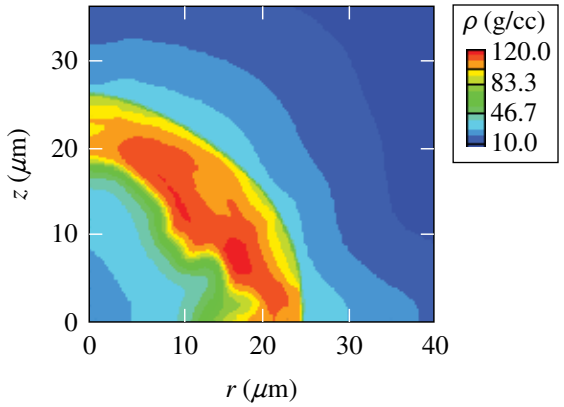

The figure on the left shows a plot of the isodensity contours of a stagnated shell at peak compression obtained from a two-dimensional simulation using the radiation–hydrodynamics code *DRACO*. This OMEGA polar-drive implosion uses a 600-μm-outer-diameter cryogenic-DT fuel target driven with 12.8 kJ of laser energy at a NIF-relevant 7×10^{14}-W/cm^2 intensity and attains a peak fuel areal density of ~240 g/cm^2. An optimized combination of beam pointings, energies, and profiles results in a nearly symmetrical stagnated core. Experiments using these high-intensity implosion designs will commence when new smaller-beam-diameter OMEGA phase plates are obtained.

The work described in this volume includes current research at the Laboratory for Laser Energetics, which is supported by New York State Energy Research and Development Authority, the University of Rochester, the U.S. Department of Energy Office of Inertial Confinement Fusion under Cooperative Agreement No. DE-FC52-08NA28302, and other agencies.

Printed in the United States of America
Available from
National Technical Information Services
U.S. Department of Commerce
5285 Port Royal Road
Springfield, VA 22161
www.ntis.gov

For questions or comments, contact Alex Shvydky, Editor, Laboratory for Laser Energetics, 250 East River Road, Rochester, NY 14623-1299, (585) 275-9539.

Worldwide-Web Home Page: http://www.lle.rochester.edu/

UNIVERSITY OF ROCHESTER
LABORATORY FOR LASER ENERGETICS

Volume 130
January–March 2012
DOE/NA/28302-1058

LLE Review

Quarterly Report

UR LLE

Contents

In Brief

This volume of the LLE Review, covering January–March 2012, features "OMEGA Polar-Drive Target Designs," by P. B. Radha, J. A. Marozas, F. J. Marshall, A. Shvydky, T. J. B. Collins, V. N. Goncharov, R. L. McCrory, P. W. McKenty, D. D. Meyerhofer, T. C. Sangster, and S. Skupsky. This article (p. 57) describes low-adiabat, cryogenic-deuterium–tritium, and warm-plastic-shell polar-drive (PD)–implosion designs for the OMEGA laser. The designs are at two different on-target laser intensities, each at a different in-flight aspect ratio (IFAR). The first design permits one to study implosion energetics and target performance closer to ignition-relevant intensities (7×10^{14} W/cm^2 at the quarter-critical surface), where nonlocal heat conduction and laser–plasma interactions can play an important role, but at lower values of IFAR (~22). The second design permits one to study implosion energetics and target performance at a lower intensity (3×10^{14} W/cm^2) but at higher IFAR (~32), where the shell instability can play an important role. The higher IFAR designs are accessible on the existing OMEGA Laser System only at lower intensities. Implosions at ignition-relevant intensities can be obtained only by reducing target radius, although only at smaller values of IFAR. Polar-drive geometry requires repointing the laser beams to improve shell symmetry. The higher-intensity designs optimize target performance by repointing beams to a lesser extent and compensate for the reduced equatorial drive by increasing beam energies for the repointed beams and using custom beam profiles that improve equatorial illumination at the expense of irradiation at higher latitudes. These designs will be studied when new phase plates for the OMEGA Laser System, corresponding to the smaller target radii and custom beam profiles, are obtained. Implosion results from the combined set of high-intensity and high-IFAR implosions should yield valuable data to validate models of laser-energy deposition, heat conduction, nonuniformity growth, and fuel assembly in PD geometry.

Additional highlights of research presented in this issue include the following:

- V. N. Goncharov presents a comprehensive review of the cryogenic-deuterium and deuterium–tritium implosions that have been performed on the Omega Laser System over the last decade (p. 72). The success of ignition target designs in inertial confinement fusion (ICF) experiments critically depends on the ability to maintain the main fuel entropy at a low level while accelerating the shell to ignition-relevant velocities of $V_{\text{imp}} > 3 \times 10^7$ cm/s. The fuel entropy is inferred from the experiments by measuring fuel areal density near peak compression. Measured areal densities up to $\langle \rho R \rangle_{\text{n}} = 300$ mg/cm^2 (larger than 85% of predicted values) have been demonstrated in the cryogenic implosion with V_{imp} approaching 3×10^7 cm/s and peak laser intensities of 8×10^{14} W/cm^2. Scaled to the laser energies available at the National Ignition Facility, implosions hydrodynamically equivalent to these OMEGA designs are predicted to achieve $\langle \rho R \rangle_{\text{n}} = 1.2$ g/cm^2, sufficient for ignition demonstration in direct-drive ICF experiments.

- G. Fiksel, S. X. Hu, V. N. Goncharov, T. C. Sangster, B. Yaakobi, M. J. Bonino, and R. Jungquist (LLE); D. D. Meyerhofer (LLE and Departments of Mechanical Engineering and Physics, University of Rochester); and V. A. Smalyuk (LLNL) present their study of the effect of medium-Z doping of plastic ablators on laser imprinting and Rayleigh–Taylor instability growth using direct-drive implosions on the OMEGA Laser System (p. 103). The targets were spherical plastic (CH) shells that were volume doped with a varied concentration of Si (4.3% and 7.4%) and Ge (3.9%). The targets were

imploded by 48 beams with a low-adiabat, triple-picket laser shape pulse with a peak intensity of 4×10^{14} W/cm^2 and x-ray radiographed through a 400-μm opening in the side of the target. The results show that volumetric impurity doping strongly reduces the shell's density modulation and instability growth rate. Simulations using the two-dimensional, radiation–hydrodynamics code *DRACO* show good agreement with the measurements.

- D. T. Michel, C. Sorce, R. Epstein, N. Whiting, I. V. Igumenshchev, R. Jungquist, and D. H. Froula present a technique to measure a shell's trajectory in direct-drive inertial confinement fusion implosions (p. 109). The x-ray self-emission of the target was measured with an x-ray framing camera. Optimized filtering limited the x-ray emission from the corona plasma, isolating a sharp intensity gradient to the ablation surface. This technique enables one to measure the radius of the imploding shell with an accuracy of better than 1 μm and determine a 200-ps average velocity to better than 2%.

- W. Theobald, K. S. Anderson, J. A. Delettrez, V. Yu. Glebov, O. V. Gotchev, M. Hohenberger, S. X. Hu, F. J. Marshall, T. C. Sangster, W. Seka, C. Stoeckl, and B. Yaakobi (LLE and Fusion Science Center); R. Nora, R. Betti, D. D. Meyerhofer, (LLE, Fusion Science Center, and Departments of Mechanical Engineering and Physics, University of Rochester); M. Lafon, X. Ribeyre, and G. Schurtz, [University of Bordeaux, CEA, CNRS, CELIA (Centre Lasers Intenses et Applications)]; A. Casner (CEA, DAM, DIF); J. A. Frenje (MIT); and V. A. Smalyuk (LLE, Fusion Science Center, and LLNL) discuss OMEGA shock-ignition experiments that use a novel beam configuration with separate low-intensity compression beams and high-intensity spike beams (p. 113). Significant improvements in the performance of plastic-shell, D_2 implosions were observed with repointed beams. The analysis of the coupling of the high-intensity spike beam's energy into the imploding capsule indicates that absorbed hot-electron energy contributes to the coupling. The backscattering of the laser energy was measured to reach 36% at single-beam intensities of $\sim 8 \times 10^{15}$ W/cm^2. Hard x-ray measurements revealed a relatively low hot-electron temperature of ~30 keV independent of intensity and timing. At the highest intensity, stimulated Brillouin scattering occurs near and above the quarter-critical density and the two-plasmon-decay instability is suppressed.

- W. R. Donaldson, C. Zhao, and R. G. Roides (LLE); K. Miller (National Security Technology); and B. Beeman (LLNL) demonstrate a single-shot, electro-optic data-acquisition system with a 600:1 dynamic range for the NIF Dante instrument (p. 129). The prototype system uses multiple optical wavelengths to allow for the multiplexing of up to eight signals onto one photodetector and provides optical isolation and a bandwidth of 6 GHz.

Alex Shvydky
Editor

OMEGA Polar-Drive Target Designs

Introduction

With the use of polar drive (PD),[1] direct-drive experiments can be conducted at laser facilities such as the National Ignition Facility (NIF),[2] while they are configured for x-ray drive. In this approach to inertial confinement fusion, laser beams directly irradiate a capsule, causing the outer material to ablate and drive the rest of the shell like a rocket. Since the x-ray drive configuration has no beams at the equator, several modifications of traditional symmetric direct drive[3] are employed to achieve adequate symmetry. An important modification repoints beams from higher latitudes toward the equator, resulting in oblique irradiation on target. Laser-energy absorption of the expanding corona is dominated by collisional absorption, where maximum laser energy is deposited at the turning point of the laser rays. The electron density at the turning point of a laser ray scales as $\cos^2\theta$, where θ is the angle subtended by the laser rays. As a result, laser absorption occurs at lower coronal densities for larger values of θ, which correspond to the oblique beams.[1] This results in reduced shell velocity (or the hydrodynamic efficiency, defined as the ratio of the maximum shell kinetic energy to the incident laser energy), relative to when the beams are at normal incidence. Pulse-shape variations among the beams and tailored individual spatial-beam profiles are necessary to recover the shell velocity while achieving adequate shell symmetry. These variations are critical to the polar-drive–ignition design.[4] In the symmetric-drive configuration, the laser irradiation is incident from a range of latitudes including the equator. This results in more-normal incident laser irradiation and for a given ablator material, the maximum-possible energy deposited leading to maximum shell velocity.

Similar to symmetric drive, ignition in PD geometry relies on the formation of a hot spot with a minimum areal density of 300 mg/cm^2 and an electron temperature of ~5 keV. Assuming spherical symmetry, the adiabat and shell implosion velocity are the critical parameters that determine target performance. The minimum laser energy required for ignition, $E_{\min}$, has been shown to depend on α_{inn}, the adiabat on the inside of the compressing shell, defined as the ratio of the pressure to the Fermi-degenerate pressure, the velocity of the shell at maximum kinetic energy or the implosion velocity V_{imp}, and the pressure P on the outside of the fuel when it reaches the implosion velocity:[5]

$$E_{\min}(\text{kJ}) = 50.8\,\alpha_{\text{inn}}^{1.88} \times \left(\frac{V_{\text{imp}}}{3\times 10^7\ \text{cm/s}}\right)^{-5.89}\left(\frac{P}{100\ \text{Mbar}}\right)^{-0.77}. \quad (1)$$

Equation (1) indicates that a lower adiabat on the inside of the shell, a high implosion velocity, and retaining the driving pressure on the outside of the shell until the onset of deceleration are extremely important to lowering the minimum energy required for ignition. The implosion velocity can be written as

$$V_{\text{imp}} \sim \sqrt{\langle\alpha\rangle^{0.6} \times \text{IFAR} \times 1^{0.27}}, \quad \text{(Ref. 6)} \quad (2)$$

where $\langle\alpha\rangle$ is the density-averaged adiabat in the shell, IFAR = R/Δ_{if} is defined as the ratio of the shell radius R to the shell thickness (Δ_{if} is defined as the distance between the 1/e radii of peak density) when the shell has traveled a distance that is 2/3 that of the average of the initial inner and outer target radii, and I is the on-target intensity. A higher implosion velocity can be obtained by increasing $\langle\alpha\rangle$, IFAR, or intensity.

The leverage in $\langle\alpha\rangle$ to increase V_{imp} is limited since it is challenging to increase $\langle\alpha\rangle$ and retain a low value of α_{inn}. Based on multidimensional considerations, IFAR has an upper limit because of nonuniformities seeded by the laser beams and target imperfections that can compromise implosion performance. Short-wavelength nonuniformities ($\ell \geq 10$, where ℓ is the Legendre mode number describing the nonuniformity) grow primarily by the Rayleigh–Taylor (RT) instability[7] and can significantly distort the in-flight shell, thereby increasing α_{inn} (Ref. 8). The number of linear growth factors for $\ell \geq 10$ for RT growth (defined as $N_e = \gamma t$, where γ is the RT growth rate and t is the time over which the shell accelerates) of the most dangerous mode (defined as the mode with wave number k, such that $k\Delta_{\text{if}} \sim 1$) scales approximately as $\sqrt{\text{IFAR}}$ (Ref. 9).

Too high an intensity can compromise target performance by seeding laser–plasma instabilities (LPI's) that reduce the energy coupled to the target (for example, through cross-beam transfer)[10] and/or preheating the shell and raising α_{inn} [via energetic electrons produced by two-plasmon-decay (TPD) instability].[11] As a result, the peak intensity, defined at the initial target radius, is typically restricted to $8 \times 10^{14} \lesssim I \lesssim 1 \times 10^{15}$ W/cm^2. At these intensities the effects of LPI are not completely understood.[12] Nonlocal heat transport by coronal electrons from the tail of the distribution function[13] also plays an important role in establishing the ablation pressure. It is necessary for OMEGA PD implosions to span this range of on-target intensities to permit studies relating to the heat conduction and LPI.

A second aspect of PD designs is the symmetry of the hot spot. Hot-spot symmetry is determined by longer wavelength perturbations ($\ell \leq 10$) that reduce the clean volume and decrease the hot-spot temperature, lowering the neutron yield.[14] In symmetric direct drive, hot-spot distortions are seeded by ice roughness, energy imbalance, beam-pointing variations, and beam-timing variations between the various beams incident on the target. The beam port configuration or beam geometry can cause additional hot-spot distortions to occur in PD.

Target performance, including the extension to multidimensional effects, has been quantified in a recent work by Haan *et al*. in terms of the ignition threshold factor (ITF).[15] A higher value of ITF indicates a greater probability of ignition; a value of 1 for this quantity indicates a 50% probability of ignition. ITF scales as

$$\text{ITF} \sim V_{\text{imp}}^{8} \alpha^{-4} (1 - 1.2\,\sigma) \left(\frac{M_{\text{clean}}}{M_{\text{DT}}} \right), \tag{3}$$

where σ is a measure of the hot-spot distortion given by the root-mean-square distortion of the hot spot, where longer wavelengths are weighted less than the shorter wavelengths, and $M_{\text{clean}} / M_{\text{DT}}$ is the ratio of the clean mass of the hot spot, i.e., the deuterium–tritium (DT) mass that is not contaminated by high-mode mixing of the ablator material, to the total target mass. High-mode mix caused by short-wavelength RT growth and the presence of isolated defects on the target surface is not considered in this article. The effect of this mix on target performance can be studied empirically through implosions by varying the IFAR, similar to what has been done in symmetric drive.[8] Engineering efforts to decrease the number of defects on the capsule surface are ongoing and have already resulted in improved implosion performance.[16] Modifications to the target design through techniques such as radiation preheat[17] and the use of lower-density ablators such as foam[1] can be considered to limit the effect of short-wavelength RT growth. The emphasis in this article is on minimizing hot-spot distortion related to beam geometry on the OMEGA Laser System[18] and to establish the basis for ignition-relevant platforms that can be used to study LPI and heat conduction in PD geometry. In particular, this implies the identification of beam profiles that minimize hot-spot distortion in OMEGA PD designs with ignition-relevant parameters.

In symmetric drive, implosions are primarily designed in one dimension (assuming spherical symmetry) and then simulated in multiple dimensions to verify target performance. Since beam-port geometry has a very small effect on target performance in symmetric drive,[19] it can be ignored in the primary design. Beam profiles for OMEGA beams have been designed for symmetric drive by minimizing the nonuniformity related to the beam geometry when projected on a sphere.[20] This assumes that the laser deposition and hydrodynamic efficiency are uniform in polar angle around the target, valid for symmetric drive where the beams are nearly normally incident on the target. For polar drive, it is critical to account for the nonuniformities imposed by the beam-port geometry and to correct for them using techniques such as an optimal choice of beam profiles, beam pulse shapes, and beam repointing. The PD approach therefore requires iterative multidimensional simulations to design implosions.

Beam profiles are implemented on OMEGA using distributed phase plates (DPP's).[21] The intensity profile across the OMEGA beam, $I_{\text{b}}(x,y)$, is described by a super-Gaussian,

$$I_{\text{b}}(x,y) = I_0 e^{-\left(\frac{\sqrt{x^2+y^2}}{\delta} \right)^n}, \tag{4}$$

where n is the desired super-Gaussian order (approximately 3.7 for the existing phase plates on OMEGA[22]). The $1/e$ radius of the phase plates, δ, is determined by the relationship between the laser energy and target radius and the required scaling between NIF (1.5 MJ) and OMEGA (30 kJ) to conduct ignition-relevant symmetric drive studies on OMEGA ($\delta = 380\ \mu$m for the existing OMEGA Laser System[21]). For PD implosions, a smaller value of n is required to achieve greater irradiation control over localized regions of the target. This can effectively compensate for the reduced equatorial irradiation.

In OMEGA PD experiments, 40 of the 60 beams emulate the NIF x-ray–drive beam-port configuration. A subset of the

20 omitted drive beams at the equator irradiate a Ti/Fe foil to backlight the compressing shell to obtain information about its symmetry. The primary goal of OMEGA experiments is to validate models used to predict ignition. This implies that for low-adiabat implosions with relevant implosion velocities and on-target intensities, necessary models must be developed and simulations validated to reproduce experimental observables. Adiabat-related observables are primarily shock velocity,[23] areal density,[24] and bremsstrahlung radiation from energetic electrons produced from TPD that can potentially preheat the shell.[25] The implosion velocity is related to observations of neutron-production time[26] and scattered light[27] and is primarily determined by laser-energy coupling and heat conduction. Symmetry is inferred experimentally from backlit x-ray images of the converging shell[28] and is determined by adiabat, implosion velocity, and nonuniformity growth. An additional useful metric of PD target performance is the comparison of PD and symmetric-drive implosions at the same laser energy and adiabat.

Current OMEGA warm PD implosions[29] are irradiated with approximately 13 kJ on target at a relatively low intensity at the initial target radius ($\sim 3.5 \times 10^{14}$ W/cm^2). The low-intensity values are driven primarily by the available energy for PD. Since 40 of the 60 beams are used, only 2/3 of the available energy is used to drive the capsule, resulting in low on-target intensity. In this article, we first present cryogenic designs for the existing system that predict implosion velocities of 3.6×10^7 cm/s at low on-target laser intensity. We then present higher-intensity PD designs that use smaller targets ($R_{\text{target}} = 300$ μm) driven with smaller custom laser-beam profiles (with a 1/e radius of ~183 μm or a radius at 5% of peak intensity of 300 μm), with lower values of the super-Gaussian order ($n = 2.2$) and elliptical beam profiles for the equatorial beams. This results in a higher on-target intensity, at the initial target radius, of $\sim 9 \times 10^{14}$ W/cm^2, allowing for LPI and heat-conduction studies.

In the next section, cryogenic-DT polar-drive–implosion designs are presented for the current OMEGA system. It is predicted that the PD implosions will result in reduced implosion velocity relative to symmetric drive implosions at the same energy by ~10%. Observations from warm (CH) implosion related to a similar loss of implosion velocity in PD relative to symmetric drive are also presented in the next section. In the following sections, a PD cryogenic deuterium–tritium (DT) design is presented at ignition-relevant intensities with smaller targets. The sensitivity of these designs to beam profiles is also studied. In addition, a warm plastic (CH) design with ignition-relevant intensities is presented. Observations related to an additional loss of ~10% in PD implosion velocity relative to simulations that include only collisional absorption are discussed and the conclusions are presented.

Low-Intensity Designs for the Current OMEGA Laser System

OMEGA cryogenic-DT implosion designs using laser beams with a super-Gaussian profile of $n = 3.7$ are presented here. The NIF beam configuration [Fig. 130.1(a)] is emulated by using 40 of the 60 OMEGA beams arranged in three rings [Fig. 130.1(b)]. Beams from the higher latitudes are repointed toward the equator in the PD configuration to achieve adequate symmetry [Fig. 130.1(c)]. This is equivalent to each beam in an

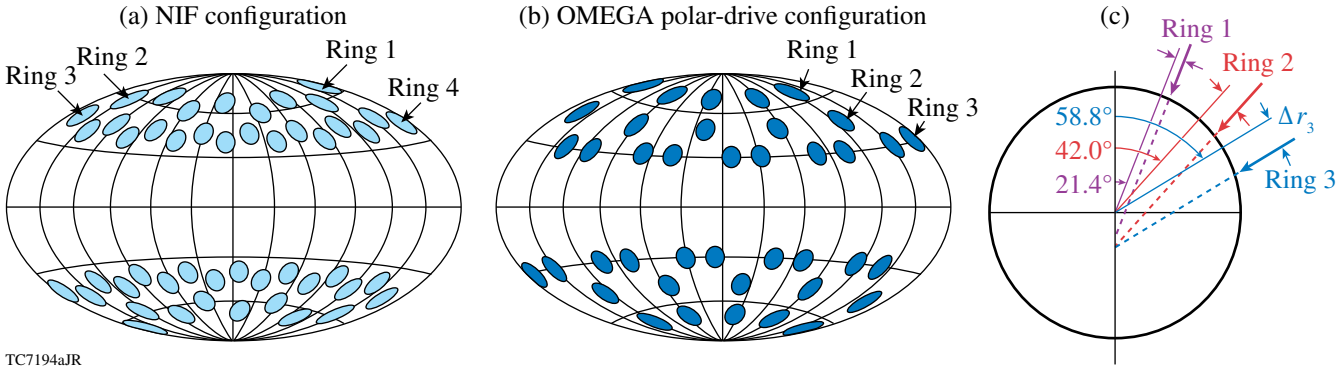

Figure 130.1
(a) NIF beam configuration. (b) Forty of the 60 OMEGA beams, arranged in three rings, emulate the NIF beam configuration. (c) Each ring is repointed by a distance (Δr_3 is shown as an example for Ring 3) toward the equator to improve symmetry. Solid lines—original beam pointing; dashed lines—repointed beams.

OMEGA ring being displaced by a distance Δr perpendicular to the beam axis. Each PD configuration is described by three distances (Δr_1, Δr_2, Δr_3) or equivalently by three angles:

$$\left[\sin^{-1}\left(\Delta r_1 / R_{\text{target}}\right), \sin^{-1}\left(\Delta r_2 / R_{\text{target}}\right), \sin^{-1}\left(\Delta r_3 / R_{\text{target}}\right)\right].$$

The latter description is advantageous because it is independent of the target radius and allows for comparison of OMEGA- and NIF-scale designs. To allow one to make a comparison with previous OMEGA PD work,[28,29] both descriptions are retained here. Implosions are simulated with the two-dimensional (2-D) axisymmetric radiation hydrodynamic code *DRACO* using multigroup diffusive radiation transport and flux-limited heat conduction.[19] A full three-dimensional (3-D) ray trace that uses collisional absorption to deposit the laser energy[30] is employed to accurately model laser ray trajectories of the oblique beams.

The design of a PD implosion begins with a symmetric design that is then iteratively optimized using *DRACO*. Parameters of the 60-beam symmetric design (design A), simulated with collisional absorption and a flux-limited ($f = 0.06$) heat-conduction model, using the spherically symmetric code *LILAC*,[31] are shown in Table 130.I. The laser pulse shape has three pickets followed by a main pulse. This pulse shape has been used to demonstrate a high areal density of nearly 300 mg/cm^2 in previous cryogenic implosions.[32] The PD ignition design[4] also uses a pulse shape of this type. The maximum-possible OMEGA laser energy in the PD configuration is used in this design. This design has an ignition-relevant adiabat implosion velocity and an IFAR comparable to an ignition design value of 36 (Ref. 4). The convergence ratio at bang time is 20, comparable to the ignition design value of 23. The overlapped-beam intensity at the initial target radius is 4.2×10^{14} W/cm^2. While the intensity defined at the initial target radius provides a useful rule of thumb in defining the relevant range for target designs, the physically more-relevant quantity is the intensity at the quarter-critical surface. The quarter-critical intensity $I_{n/4}$ is somewhat less than the intensity at the initial target radius because of absorption in the lower-density corona. For this design, this value is 3×10^{14} W/cm^2, which is significantly lower than the values in the ignition design ($\sim 8 \times 10^{14}$ W/cm^2). Consequently, the TPD threshold parameter, defined as

$$\eta = I_{n/4}\left(10^{14}\ \text{W/cm}^2\right) L_{n/4}(\mu\text{m}) \Big/ 233\, T^{\text{e}}_{n/4}\,(\text{keV}) \text{ (Ref. 11)},$$

where $L_{n/4}$ and $T^{\text{e}}_{n/4}$ are the density scale length and the electron temperature at the quarter-critical surface, respectively, is less than 1, indicating a marginal effect of TPD on electron generation and capsule preheat.[33]

A 40-beam PD implosion with the same energy, based on this design, is optimized using *DRACO* (Fig. 130.2). In the PD case, the single-beam energies are increased by 3/2 to ensure

Table 130.I: Parameters of 60-beam, symmetric-drive OMEGA cryogenic-DT designs simulated with collisional absorption and flux-limited heat conduction. Polar-drive optimization using the 2-D axisymmetric hydrodynamics code *DRACO*[19] is based on these designs (see text).

	Design A	Design B	Design C
R_{outer} (μm)	430	300	300
Ice thickness (μm)	35	35	65
CH ablator (μm)	9	9	9
Peak power (TW)	10	10	10
E (kJ)	15.5	11.5	12.8
V_{imp} (cm/s)	3.6×10^7	3.4×10^7	2.5×10^7
IFAR	32	22	12
DT yield	1.2×10^{14}	2.7×10^{13}	5.0×10^{12}
ρR_{max} (mg/cm^2)	243	240	236
R_{hs} (μm)	20	15	15
CR	20	17	15
$L_{n/4}$ (μm)	150	110	110
$I_{n/4}$ (W/cm^2)	3×10^{14}	7×10^{14}	7×10^{14}
$T^{\text{e}}_{n/4}$ (keV)	2.1	2.8	2.8
$\eta_{\text{TPD}} = I_{n/4}\left(10^{14}\ \text{W/cm}^2\right) L_{n/4}(\mu\text{m}) \Big/ 233\, T^{\text{e}}_{n/4}\,(\text{keV})$	0.9	1.3	1.3

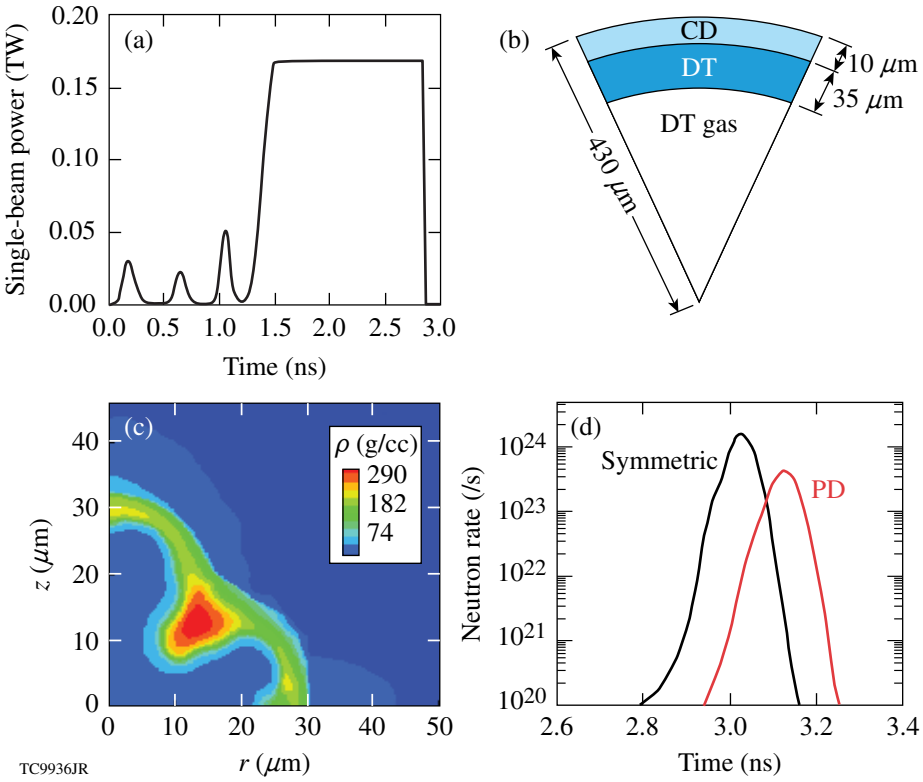

Figure 130.2
(a) Pulse shape and (b) target for cryogenic DT polar-drive (PD) design on the existing OMEGA Laser System with n = 3.7 phase plates. (c) Mass-density profiles at peak neutron production. (d) Neutron-rate histories—symmetric drive (black) and PD (red).

that the target is irradiated with the same total picket energies and total energy [Fig. 130.2(a)]. This PD configuration corresponds to beam ring displacements of 90 μm, 150 μm, and 150 μm. As the density contours at peak neutron production [Fig. 130.2(b)] indicate, the core has a small $\ell = 2$ and a large $\ell = 4$. The implosion velocity for the PD design is approximately 10% less than that of the symmetric design. Bang time, defined as the time of the onset of the neutron yield above the experimental noise threshold, is an important observable to quantify the implosion velocity. For the typical temperatures in these implosions, neutron rate Y_{1n} scales with mass density ρ and the fusion reaction rate as ion temperature T_i of the fuel as $Y_{1n} \sim \rho^2 \langle \sigma v \rangle d^3 r$, where $\langle \sigma v \rangle \sim T_i^4$. Using $T_i \sim \alpha^{-0.15} V_{imp}^{1.3}$ (Ref. 9), the neutron rate can be written in terms of implosion velocity as $Y_{1n} \sim \rho^2 \alpha^{-0.6} V_{imp}^{5.2}$. The measured rate can deviate from this one-dimensional (1-D) formulation because the growth of nonuniformity can reduce both T_i and the neutron-producing volume (or "clean volume"). Simulations indicate that nonuniformity does not significantly influence the rate in these implosions early during the deceleration phase. Therefore comparing the bang time provides a measure of the implosion velocity. This reduced velocity is shown as the delay in neutron-production history in Fig. 130.2(c).

Additional variables, including beam energies and shimming, can be employed to optimize the design. The best symmetry for the PD equivalent of design A is obtained with only beam displacements. Beam profiles are predetermined and no combination of beam energies and displacement can improve upon the symmetry of the design shown in Figs. 130.2(a) and 130.2(b). Since it is challenging to achieve adequate equatorial drive in the PD configuration, thinning the DT ice or ablator near the equator or shimming may improve the density uniformity locally near the equator. This is not studied in this work.

The final optimized PD design typically differs somewhat from the original symmetric design because of the retuning of the shocks to achieve adequate uniformity and timing with oblique beams. Since the difference in peak areal density between the original symmetric design (design A) and the PD-optimized design is less than 5%, the original design A is retained as the symmetric equivalent of the optimized PD

design. The predicted PD yield is 27% of the symmetric-drive yield. This reduction is due to the $\ell = 4$ nonuniformity and the reduced implosion velocity in PD relative to symmetric drive. These predictions are similar to observations from warm CH PD implosion experiments.

In warm PD OMEGA implosion experiments, triple-picket laser pulse shapes (Fig. 130.3) irradiate a 9-atm-deuterium-filled, 27-μm-thick CH shell with approximately 13 kJ of laser energy. Full beam smoothing [smoothing by spectral dispersion (SSD)][34] and polarization smoothing (PS)[35] are used in all of the implosions. These implosions are designed to achieve a convergence ratio (CR) of 19, where CR is defined as the ratio of the initial inner shell radius to the hot-spot radius (defined as a radius that is 1/e of peak density) at peak neutron production. It has been shown previously[29] that very good agreement in picket shock velocities and catch-up at the equator is obtained in PD geometry as measured through VISAR (a velocity interferometer system for any reflector)[23] and simulated with *DRACO*.[19] Approximately 100% of the predicted value of areal density (ρR), measured through the energy loss of charged particles,[24] is obtained in these implosions. Since $\rho R \sim \alpha^{-0.6}$ (Ref. 36), this indicates that the predicted adiabat is achieved in the implosion. By comparing the simulated and measured neutron-production time ("bang time" is defined as the time when the neutron rate rises above the experimental noise level), it is estimated that simulations overpredict implosion velocity by ~10%. This will be discussed in the context of CBET (cross-beam energy transfer). The predicted shell asymmetry was well reproduced in these implosions,[29] until the shell converged by a factor of only 7, the latest time at which shell nonuniformity can be reliably inferred from experimental images.

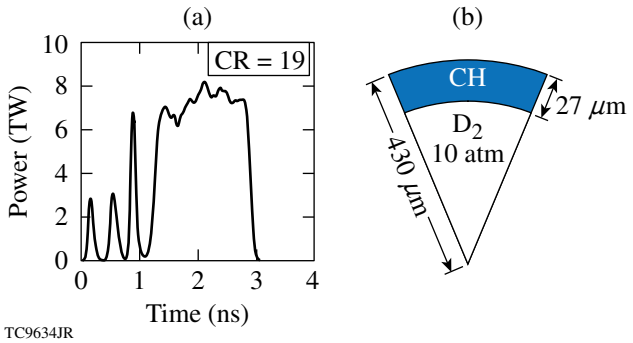

Figure 130.3
(a) Laser pulse shape used to irradiate the target shown in (b) in current OMEGA polar-drive experiments.

The ratio of PD yields to the equivalent energy symmetric-drive yields versus the on-target laser energy is shown in Fig. 130.4(a) for different PD configurations. The average experimental symmetric drive yield is $(1.2\pm0.2) \times 10^{10}$ (averaged over four shots) compared to an average simulated value of $(1.12\pm0.3) \times 10^{11}$. The experimental reduction in the symmetric drive yield is due to nonuniformities such as beam imbalances, including primarily beam mistiming and target-surface rough-

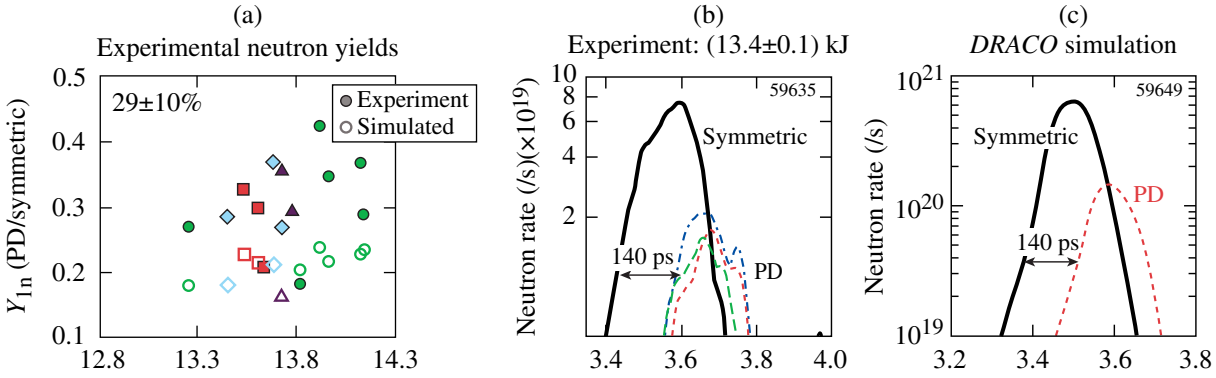

Figure 130.4
(a) Ratio of D_2 neutron yield from PD implosions to symmetric-drive implosions versus laser energy. Each symbol represents a shot. Solid circles represent experimental ratios for PD and symmetric-drive implosions; open circles represent simulated ratios for PD and symmetric-drive implosions. PD configurations are 90 μm, 120 μm, and 120 μm (circles); 90 μm, 150 μm, and 150 μm (squares); 90 μm, 133 μm, and 133 μm (triangles); and 30 μm, 150 μm, and 150 μm (diamonds). The average experimental ratio is 29±10% compared to the average simulated ratio of 20±10%. (b) Measured symmetric drive (solid) neutron rate compared to measured PD (dashed) neutron rates. Different curves correspond to different shots. (c) Simulated neutron rate for symmetric drive (solid) compared to simulated PD (dashed) neutron rate.

ness. Polar-drive yields are further reduced from the symmetric drive yields. The average reduction in the experimental ratio [Fig. 130.4(a)] is (29±10)% compared to the simulated reduction of (20±11)%, which is in good agreement.

The delay in the PD bang time relative to symmetric drive is evident from Fig. 130.4(b). Experimentally the (140±50)-ps delay in the PD bang time relative to the symmetric drive bang time requires a reduction of about 10% in the implosion velocity relative to symmetric drive. Simulations reproduced this delay in bang time [Fig. 130.4(c)]. Using the scaling of the neutron rate with the implosion velocity presented earlier, nearly 80% improvement in the absolute PD neutron yield can be achieved by increasing the implosion velocity by 10%.

The four experimental PD configurations correspond to beam distance displacements of 90 μm, 120 μm, and 120 μm; 30 μm, 150 μm, and 150 μm; 90 μm, 150 μm, and 150 μm; and 90 μm, 133 μm, and 133 μm. The extent of beam repointing in all these configurations is quite significant and results in reduced energy deposited (these repointed configurations also have a significant amount of energy that misses the target, contributing to the reduced energy deposition) and, therefore, reduced hydrodynamic efficiency. To compare these values with those in the NIF ignition design, these numbers are converted to scale invariant angles corresponding to 12°, 16°, and 16°; 4°, 20°, and 20°; 12°, 20°, and 20°; and 12°, 18°, and 18°.

The NIF ignition design also significantly repoints the beams—corresponding to 1.5°, 14.5°, 0°, 38.5°, and 33° for each ring on the NIF,[4] respectively. However, individual laser-spot profiles are optimally designed to prevent energy from going over the horizon of the target; beams are truncated asymmetrically, so that only insignificant beam energy misses the target. Moreover, sufficient energy is available on the NIF to compensate for the reduced hydrodynamic efficiency. Asymmetrically truncated beam profiles are not currently available on OMEGA and, as will be pointed out later, are also not practical for future OMEGA designs. For OMEGA-scale implosions, where the energy is limited, recovering this implosion velocity is important for studying the relative performance of PD and symmetric drive. Better control over the energy deposition in polar angle over the target, by choosing a different spatial beam profile, can make it possible to recover the implosion velocity in OMEGA-scale implosions, as discussed in the next section.

High-Intensity OMEGA Designs

Beam profiles with a relatively high super-Gaussian (SG) order result in a broad deposition region over the target. The spatial beam profiles from individual beams are compared for two different SG orders with δ = 383 μm in Fig. 130.5. The higher SG order (n = 3.7) is characterized by a flat-top in intensity distribution, whereas the lower SG order (n = 2.2) is more center peaked. This center-peaked distribution allows for more-localized on-target intensity when the overlap of all beams within a ring is considered. As a result, the laser irradiation can be more effectively pointed toward the equator with the lower SG order (Fig. 130.6). For the n = 3.7 beam profiles currently on OMEGA, the overlapped-intensity distribution from each ring is broadly incident over a large range of polar angles [Fig. 130.6(a)]. The normalized overlapped intensity (normalized to the maximum value among the three rings, which corresponds to the Ring 1 intensity at the pole) is shown in Fig. 130.6(a) for the un-repointed beam configuration. With the lower SG order, again, for the un-repointed configuration, particularly for Rings 2 and 3, the intensity distribution on target is more peaked toward the equator [Fig. 130.6(b)]. The overlapped intensities from each ring are compared when the beams are repointed [Figs. 130.6(c) and 130.6(d)]. The beam displacements correspond to (16 μm, 21 μm, 68 μm) or (3°, 4°, 13°) values that result in optimized designs, as will be shown below. The equator is under driven by nearly 20% relative to the pole for n = 3.7 [Fig. 130.6(c), dashed lines], whereas the n = 2.2 beam profiles permit nearly the same intensities at the equator and pole [Fig. 130.6(d), dashed lines]. A purely elliptical beam profile described by

$$I_b(x,y) = I_0 e^{-\left[\frac{\sqrt{\eta_3 x^2 + y^2}}{\delta}\right]^n} \quad (5)$$

with ellipticity η_3 = 1.2 for Ring 3 permits greater intensity at the equator relative to a purely circular beam profile in both

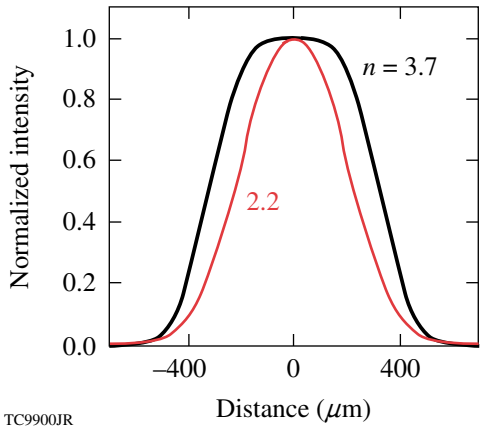

Figure 130.5
Beam profiles for two different super-Gaussian orders: n = 3.7 (black) and n = 2.2 (red).

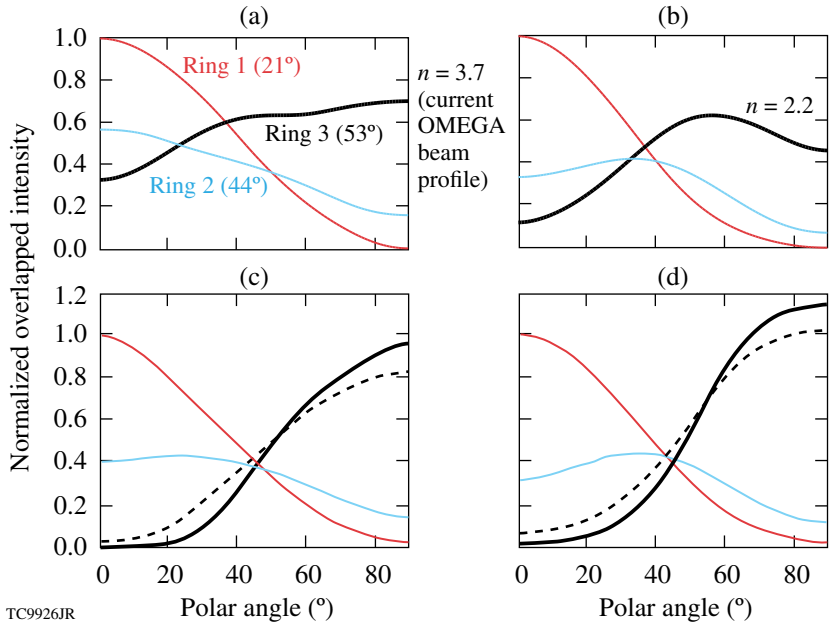

Figure 130.6
On-target normalized overlapped beam intensity attributed to each OMEGA ring versus polar angle: (a) $n = 3.7$ and (b) $n = 2.2$. A lower super-Gaussian order provides a more-localized intensity pattern toward the equator (polar angle = 90°). (c) Overlapped on-target normalized beam intensity attributed to each OMEGA ring versus polar angle for the repointed configuration (16 μm, 21 μm, 28 μm) when only circular $n = 3.7$ beam profiles are used for all rings (solid), when an elliptical profile is used only for Ring 3 with ellipticity $\eta_3 = 1.2$ (dashed), and (d) only circular $n = 2.2$ beam profiles are used for all rings (solid), elliptical profile only for Ring 3 with ellipticity $\eta_3 = 1.2$ (dashed).

cases (solid line). With the same beam displacement, the lower SG order with elliptical beam profiles for Ring 3 is the more-favorable option to compensate for the reduced equatorial drive. This combination irradiates the equator with higher intensity than the pole by nearly 20% compared to the higher SG order.

To increase on-target laser intensity closer to ignition-relevant values, an appropriate value of δ and target radius (R_{target}) is required. The goal is to irradiate the target with NIF-relevant laser quarter-critical intensity. There is no simple scaling argument for the quarter-critical intensity when two different target sizes and laser energies are compared. The NIF target radius is 3 to 4 times that of an OMEGA-scale target, resulting in a proportionately longer coronal density scale length. More absorption occurs in the lower-density corona in the NIF designs because of the longer scale length, leading to a different dependence for the quarter-critical intensity on the incident laser intensity in the NIF designs versus the OMEGA designs. Dimensional scaling relating the required laser energy for a given plasma energy is used as a starting point for a target radius. This is then iteratively adjusted to achieve similar simulated quarter-critical intensity in both designs. Using the scaling for the laser energy E contributing to a given plasma energy, $E \sim R^3$, and typical NIF and OMEGA parameters $R_{\text{NIF}} = 1700$ μm, $E_{\text{NIF}} = 1.5$ MJ, and $E_{\Omega}^{\text{PD}} = 12$ kJ, one gets $R_{\Omega}^{\text{PD}} = 350$ μm. If one instead uses a 15% smaller target radius, the intensity at the quarter-critical surface will increase from 4.5×10^{14} W/cm^2 to 6.5×10^{14} W/cm^2 [Fig. 130.7(a)], a value closer to the PD ignition design value, which varies between 7 and 9×10^{14} W/cm^2 in the polar angle on target [Fig. 130.7(b)]. Higher intensities in the OMEGA designs can be obtained by increasing laser energy (an additional 20% is available for the design as described below) or by further reducing the target radius. The latter approach typically results in lower convergence and is therefore not preferred.

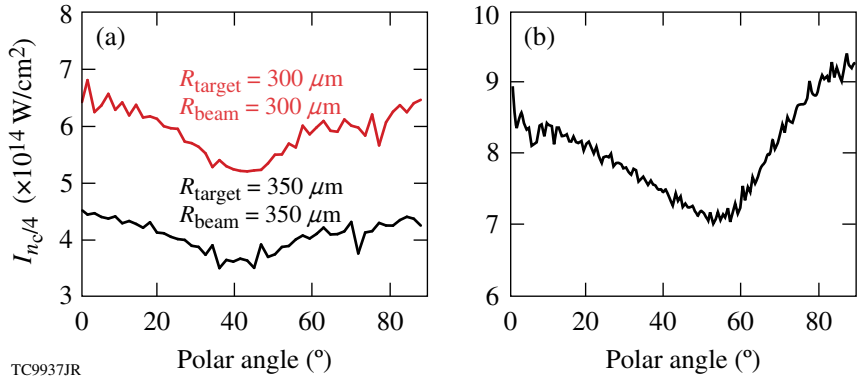

Figure 130.7
(a) Overlapped on-target intensity at the quarter-critical surface at the end of the laser pulse for two different target radii. The beam radius equals the target radius in each case. (b) Overlapped on-target intensity at the quarter-critical surface for the NIF design.[4]

Parameters for the 60-beam OMEGA cryogenic-DT symmetric target designs are shown in Table 130.I. The target has a radius of 300 μm with a 35-μm-thick (design B) or 65-μm-thick (design C) DT layer inside a 9-μm-thick CH shell. This CH thickness is chosen so that only CH is present throughout the laser pulse at the quarter-critical surface in the corona. The presence of DT at the quarter-critical surface is associated with a greater production of energetic electrons from TPD, which can potentially preheat the target.[37] The 65-μm layer thickness corresponds to ongoing symmetric-drive OMEGA cryogenic-DT experiments.[16] With the smaller target radius, initial experiments will be performed using this thicker, more-stable shell. This design deliberately uses only about 80% of the laser energy available on OMEGA; this can be increased by increasing either the intensity, the length of the pulse, or the relative energies of the rings. It is important to note that OMEGA experiments with ignition-relevant intensities are possible at this target radius. The smaller target radius results in a smaller convergence ratio for designs B and C. This can be increased by decreasing the shell adiabat by selecting a main pulse with a step as in Ref. 32. At the values of $I_{n/4}$ accessible in these designs, the TPD threshold parameter η_{TPD} exceeds 1 and has values similar to those in current symmetric-drive OMEGA experiments.[38]

Parameters of the PD design corresponding to the symmetric design C are summarized in Table 130.II. In PD, Ring 3 has 25% more energy than Rings 1 and 2 (parameterized by the variable E_{mod}). An elliptical beam profile [Eq. (5)] is chosen for Ring 3, increasing the equatorial drive (Fig. 130.8). The mass-density profile in Fig. 130.9(a) shows the shock as it breaks out of the DT layer for the 65-μm-thick DT design. The shock front is nonuniform, with the equator being somewhat underdriven compared to the rest of the target. The density contours at peak neutron production indicate a fairly uniform shell [Fig. 130.9(b)]. Little evidence of the underdriven equator is observed at peak neutron production because of shock dynamics. The return shock at the equator is weaker than the shock elsewhere. As a result, the shell at the equator travels a greater distance before it decelerates. Ideally, PD target design should optimize different phases of the implosion. In the NIF design, this is achieved by varying the pulse shapes of each ring independently in time. Picket energies vary between rings relative to the energy in the main pulse to ensure uniformity throughout the implosion. Only overall beam energies can be varied on OMEGA; therefore, only an overall optimization of the implosion is possible.

When beam energies are varied, the equivalency of symmetric drive and PD implosions is less apparent. Here, since Ring 1 is nearly normally incident and the variations in pointing and beam energies relative to symmetric drive for the other rings are used to correct for beam obliquity, Ring 1's picket energies correspond to the equivalent symmetric-drive pulse shape for the optimized PD design. These are the same energies as the original symmetric design C. The peak power in the PD-equivalent symmetric design is appropriately chosen to keep the overall laser energy constant. Nearly 1-D areal density is achieved with a peak-to-valley variation of less than 10% [Fig. 130.10(a)]. The PD design obtains the same bang time as

Table 130.II: Parameters for the nominal high-intensity PD cryogenic OMEGA implosion based on design C in Table 130.I. E_{mod} is the overall energy multiplier to the pulse shape for Design C in Table 130.I; n is the super-Gaussian order for the rings; δ is the $1/e$ radius of the beam profile [Eq. (5)], η is the ellipticity of the beam profiles defined as the ratio of the major to minor axis of the beams (Eq. 5); and Δr is the extent to which the beams are repointed.

	Ring 1	Ring 2	Ring 3
E_{mod}	1.00	1.00	1.25
n	2.2	2.2	2.2
δ	183 μm	183 μm	183 μm
η	1.0	1.0	1.2
Δr	16 μm	21 μm	68 μm

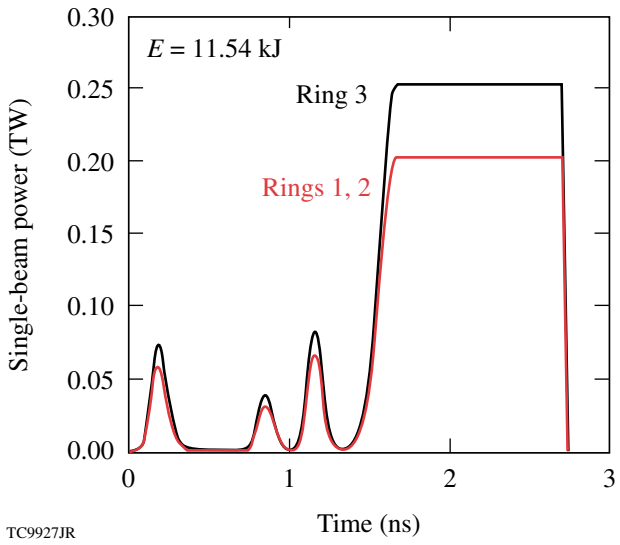

Figure 130.8
Cryogenic target design used with the beam repointing in Fig. 130.6. Laser pulse shapes used for each of the rings irradiating the target in design C.

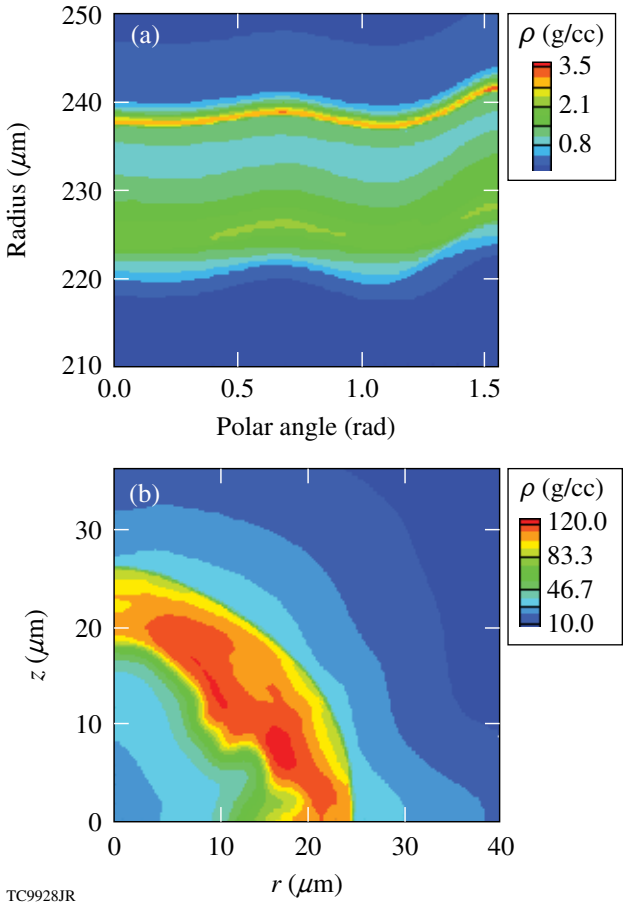

Figure 130.9
(a) Mass-density contours shortly after shock breakout (1.7 ns) for the design in Fig. 130.8 with parameters in Table 130.II. (b) Mass-density contours at peak neutron production (2.8 ns) for the target design shown in Fig. 130.7.

the symmetric design, indicating that the symmetric drive's hydroefficiency is achieved in the PD design [Fig. 130.10(b)]. Nearly 55% of the symmetric drive's yield is obtained in the PD design. This reduction in PD yield is due to the residual nonuniformity, primarily $\ell = 4$.

The OMEGA beam profiles differ from the NIF beam profiles in two respects: The NIF design uses a circular spot modulated by an offset ellipse to provide greater uniformity locally near the equator. In the OMEGA design a similar spot for Ring 3 eliminates the weaker shock near the equator [Fig. 130.9(a)]. This spot is impractical on OMEGA, however, given the dispersion required by SSD. The extent of SSD dispersion (~180 μm) is comparable to the minor radius of the required ellipse, which then necessitates an extremely small (~10 μm) sized pre-SSD ellipse. Such a variation in intensity is impractical to manufacture through a phase plate. The second source of difference is in the beam truncation scheme employed in the NIF design. NIF beam profiles are asymmetrically truncated such that the laser energy spilling over the target horizon is minimized. This allows more energy to couple to the target. On OMEGA, however, this truncation is unnecessary. OMEGA designs require less repointing to achieve optimal symmetry because the beam-port arrangement on OMEGA is more optimal and the smaller-scale targets provide better hydrodynamic efficiency. Beam truncation is required when the repointing is significant since it permits adequate irradiation of the equator without loss of laser energy over the horizon. The optimal beam repointing on OMEGA is small enough that the effect of beam truncation is a simulated unobservable increase of ~2% in the implosion velocity.

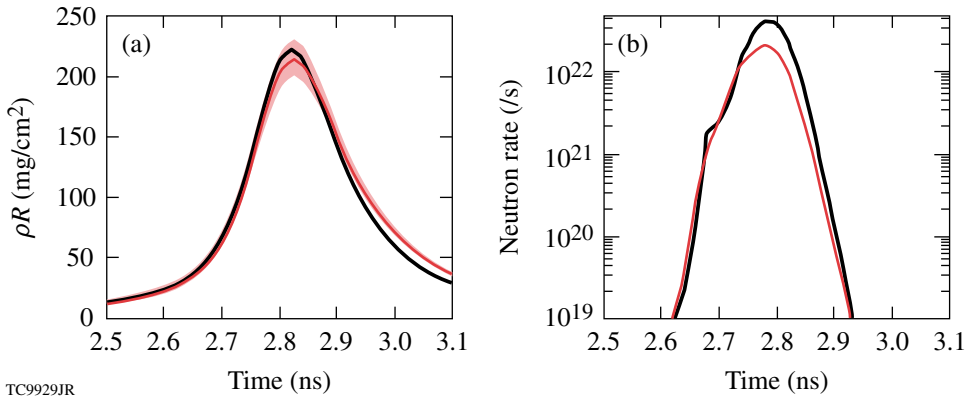

Figure 130.10
(a) Areal-density history for symmetric drive (black) compared to the PD implosion (red). The shaded region indicates the range in areal densities in polar angle. (b) Neutron rate for symmetric drive (black) compared to PD (red). No significant difference in neutron-production timing is calculated indicating that the symmetric-drive implosion velocity is achieved in the PD simulation.

Sensitivities to the OMEGA beam profiles are investigated by systematically varying their parameters (Fig. 130.11). Hot-spot distortion, defined here as the ratio of the standard root-mean-square deviation of the hot-spot radius (defined as the inner 1/*e* location of peak density) to the mean hot-spot radius is used as a measure of implosion quality. This quantity is further broken down into the contribution from the various modes; the ratio of the amplitude of an individual mode to the hot-spot radius is also shown in Fig. 130.11. Super-Gaussian orders of each of the rings and the ring ellipticity are varied individually. As Fig. 130.11 indicates, Legendre modes with $\ell = 2$ and $\ell = 4$ dominate hot-spot distortion. For 10% variations in the SG order, no significant variation in target performance is observed, indicating the robustness of the design. Neutron yields do not change significantly when the beam profile parameters are varied. The parameter that is most sensitive to implosion quality is the ellipticity of the Ring 3 beams' profiles. For Ring 3 ellipticity, the most-sensitive determinant of implosion quality, the neutron yield relative to symmetric drive varies between 58% (for $\eta_3 = 1.0$) and 54% (for $\eta_3 = 1.25$) (see Fig. 130.12).

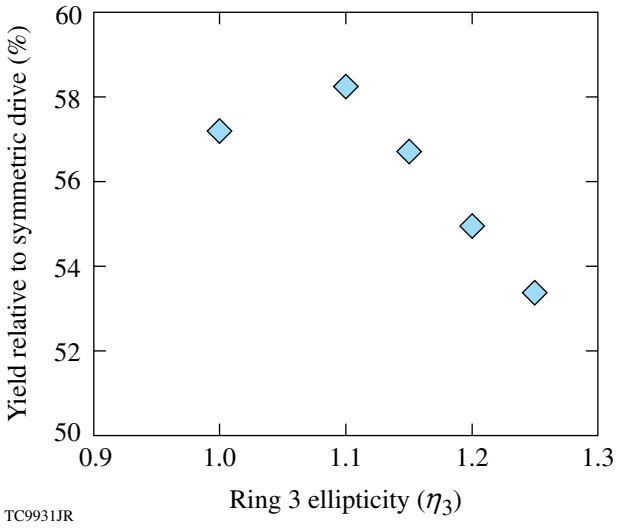

Figure 130.12
Yield relative to symmetric drive versus Ring 3 ellipticity. The PD yield for $\eta_3 = 1.15$ coresponds to 2.3×10^{12}, whereas the symmetric drive yield is 4×10^{12}.

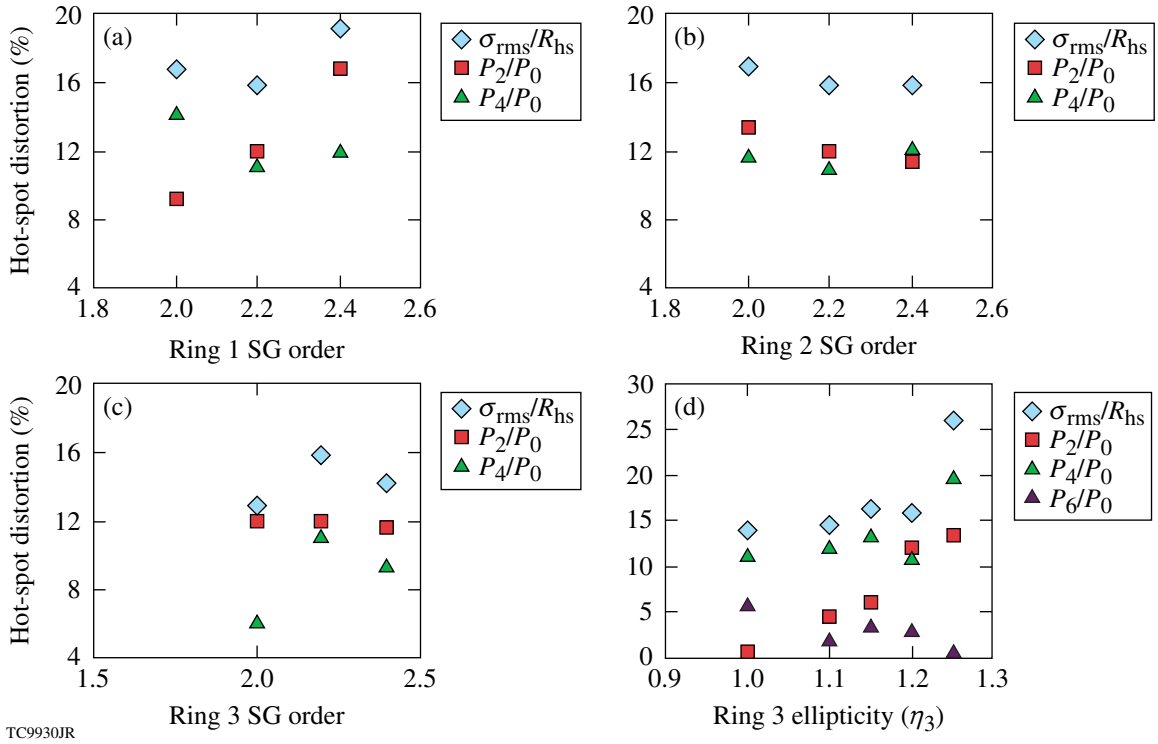

Figure 130.11
(a) Sensitivity of hot-spot distortion to super-Gaussian (SG) order of Ring 1 beams; (b) sensitivity of hot-spot distortion to super-Gaussian order of Ring 2 beams; (c) sensitivity of hot-spot distortion to super-Gaussian order of Ring 3 beams; (d) sensitivity of hot-spot distortion to ellipticity of Ring 3 beams, η_3. Diamonds: ratio of σ_{rms} of hot spot to radius of hot spot (R_{hs} is defined as the 1/*e* of peak density); squares: ratio of amplitude of Legendre-mode P_2 to R_{hs}; green triangles: ratio of amplitude of Legendre-mode P_4 to R_{hs}; dark purple triangles: ratio of amplitude of Legendre-mode P_2 to R_{hs}.

Manufacturing uncertainties introduce variability among phase plates. Such variations can cause the on-target intensity profile to deviate from the pure Legendre mode assumptions used in the design. To constrain the range of acceptable beam profiles, simulations are performed with varying ellipticity for Ring 3 beams. A randomly selected ellipticity for each beam in Ring 3, with η_3 varying uniformly between 1.1 and 1.2, is used in the simulations. The effect of varying ellipticities is bracketed by two different models of the nonuniformity (Fig. 130.13): (1) Only the $m = 0$ modes in the Legendre decomposition of the asymmetry in the 2-D axisymmetric simulation are used as the initial perturbation ampltiudes. (2) The amplitude of the $m \neq 0$ modes is added in quadrature to reach the amplitude of the Legendre mode used in the simulation, where the effect of the 3-D perturbation introduced by beam profile variations can be approximated. The middle point, $\eta_3 = 1.15$, corresponds to a single ellipticity chosen for all the beams in Ring 3. Marginal variations in hot-spot symmetry and neutron yield relative to symmetric drive are modeled in Figs. 130.13(a) and 130.13(b), respectively.

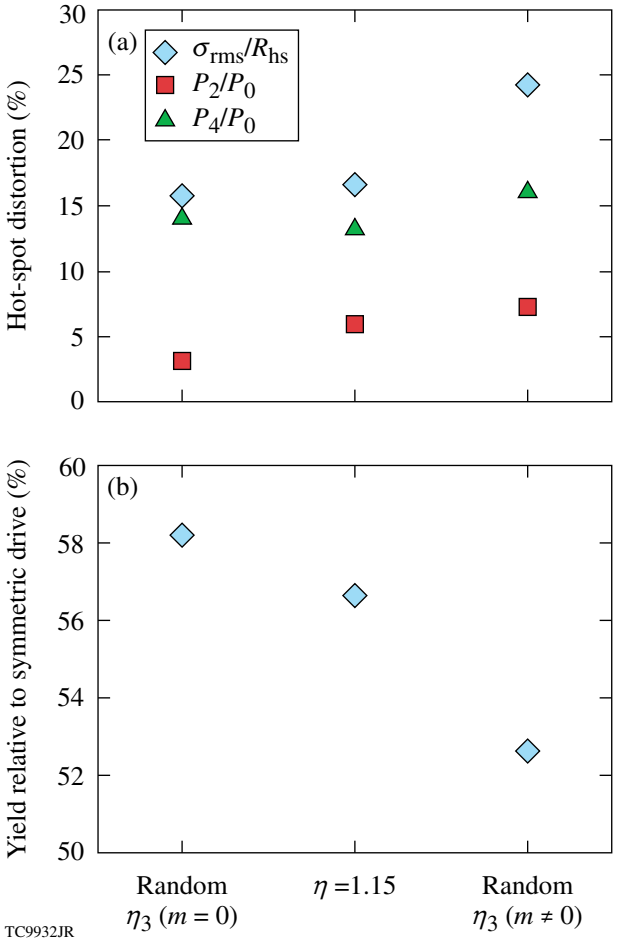

Figure 130.13
(a) Hot-spot distortion for varying ellipticities for each beam in Ring 3. Random ellipticities correspond to a randomly selected ellipticity for each beam in Ring 3 with η_3 varying uniformly between 1.1 and 1.2. Such a variation of ellipticities results in a breakdown of azimuthal symmetry. This is modeled by including only the $m = 0$ modes in the Legendre decomposition of the asymmetry in the 2-D axisymmetric simulation. The middle point, $\eta = 1.15$, corresponds to a single ellipticity chosen for all the beams in Ring 3. The third set of points corresponds to the inclusion of the amplitude of the $m \neq 0$ modes in quadrature in the amplitude of the Legendre mode used in the simulation. (b) Yield relative to symmetric drive for each of the cases in (a).

Warm implosions offer the advantage that frequent, highly repeatable experiments can be conducted to study the relevant coronal physics. A warm CH, PD implosion design also predicts good performance relative to symmetric drive with the same set of beam profiles (Fig. 130.14). As in the cryogenic design, ring energies are varied [Fig. 130.14(a)] to minimize hot-spot distortion [Fig 130.14(b)]. Polar-drive–implosion velocity is very close to the symmetric-drive velocity as shown by the similar bang times between the two simulations [Fig. 130.14(c)].

Effect of Cross-Beam Transfer and Nonlocal Heat Transport in Symmetric and Polar Drives

As mentioned earlier, CBET has been invoked to explain the observed delay in bang time between experiment and simulation for symmetric-drive implosions.[10] The role of CBET in PD implosions is unclear. Experiments to measure scattered light in PD geometry and efforts to model CBET in *DRACO* are ongoing. Similar to symmetric drive, a delay in bang time is observed in warm OMEGA implosion experiments in PD geometry (Fig. 130.15). Bang time is delayed by ~180 ps in PD experiments relative to PD simulations [Fig. 130.15(a)]. This delay is similar for the various PD configurations and also similar to the delay observed for symmetric drive [Fig. 130.15(b)]. CBET's dependence on beam obliquity is also unclear. Apart from an overall delay in the absolute time, observations of shell asymmetry agree with simulations.[29] The latest time at which these measurements can be made is still relatively early, when the shell has converged by a factor of ~7. It is therefore unclear if CBET preferentially compromises laser-energy absorption at some latitudes relative to others. All the 60-beam symmetric designs presented in this article are sensitive to the model of cross-beam transfer[10] and nonlocal transport[13] implemented in *LILAC*. The implosion velocity is reduced by approximately 10% and neutron yield by approximately a factor of 3 when effects of cross-beam transfer are included in *LILAC* simulations. Areal density is also reduced by nearly 10% primarily due to the introduction of a coasting phase in the implosion caused by the driving pressure not being retained until the onset

of deceleration. One possible CBET mitigation strategy is to reduce the beam size relative to the target size; for example, the ratio of ~0.85 improves implosion velocity while imposing optimal levels of nonuniformity on target.[39] With the target radius selected in the previous section, the flexibility can perform such studies in PD. The high-intensity design deliberately uses only about 80% of the maximum energy available on OMEGA; the additional 20% in laser energy is available to drive larger targets, if necessary.

Conclusions

Cryogenic-DT and warm CH polar-drive designs for the OMEGA laser have been presented. Given the available energy on OMEGA, it is challenging to get both ignition-relevant

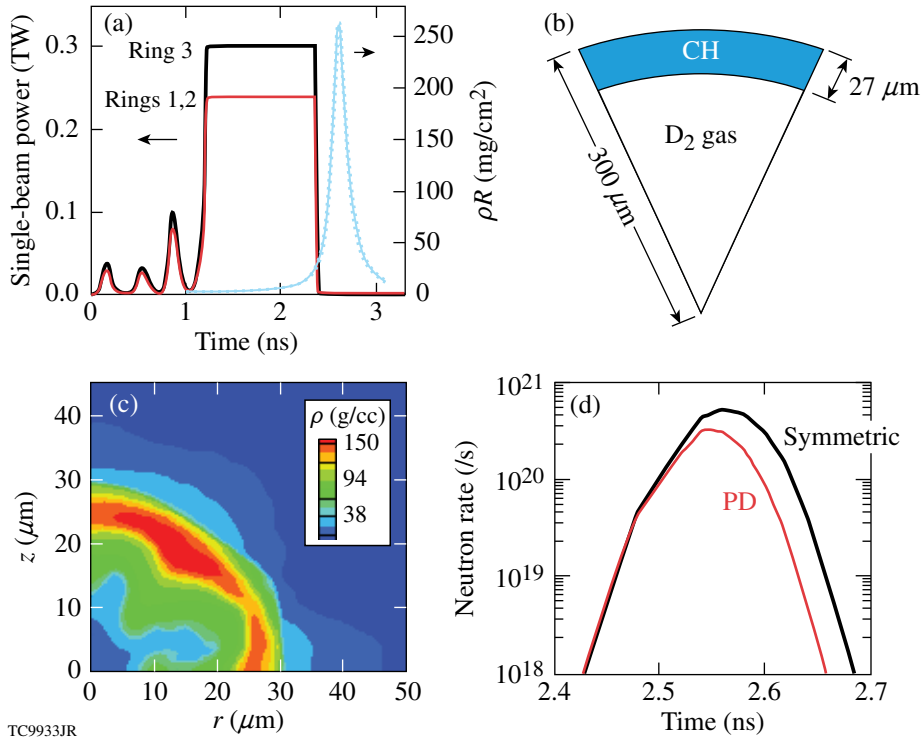

Figure 130.14
(a) Ring pulse shapes (left axis) and areal-density history (right axis) for (b) a warm, plastic-shell target. (c) Mass-density contours at peak neutron production (2.56 ns). (d) Neutron-rate histories for symmetric drive (black) compared to the PD simulation (red). No delay in bang time is observed, indicating that the symmetric-drive–implosion velocity is achieved in the PD simulation.

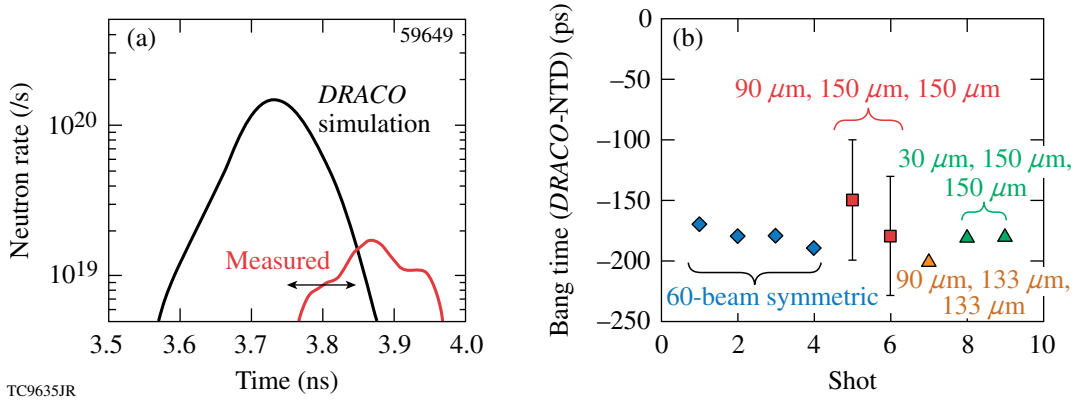

Figure 130.15
(a) Comparison of neutron rates between the measured (red) and the simulated (black) with only collisional absorption and flux-limited heat conduction values in PD configuration. (b) Difference in the simulated and measured bang times for symmetric drive and three different PD configurations. Bang time occurs earlier in the simulations when only collisional absorption of the laser pulse is assumed.

intensity (to study LPI effects and heat conduction) and high in-flight aspect ratio (to study effects of instability growth) in one design. Instead, two designs have been presented, each of which addressed one issue. A low-intensity optimized PD cryogenic DT design using the existing OMEGA phase plates predicts ~27% of the symmetric-drive yield. This yield reduction is due to reduced implosion velocity in PD relative to symmetric drive and the dominant $\ell = 4$ nonuniformity. These predictions are similar to observations from warm CH implosions on OMEGA, where a similar modal nonuniformity is observed and simulated. The observed warm implosion PD yield is reduced relative to spherically symmetric implosion experiments and is due to an inferred loss of ~10% in implosion velocity. High-intensity cryogenic and warm CH designs with smaller targets for future PD experiments on OMEGA have been presented. These designs repoint beams less by making a judicious choice of beam profiles and beam energies, permitting adequate symmetry while reducing the extent of repointed beams. Simulations indicate the recovery of symmetric-drive–implosion velocity in these designs. Weak sensitivity of target performance such as neutron yield and hot-spot distortion on beam profile parameters indicate that the designs are robust. Measurements from current OMEGA PD experiments also indicate an additional loss of ~10% in implosion velocity relative to PD simulations that include only collisional absorption as the mechanism of laser-energy deposition and flux-limited heat conduction. This reduction in implosion velocity is similar to that observed in symmetric drive, where it has been attributed to cross-beam transfer. Mitigation options include reducing the beam size relative to target radius. The beam profile radii chosen for the high-intensity design presented in this article will permit such mitigation studies by varying the target radii. Detailed experimental studies and code development to model the effect of cross-beam transfer in PD geometry are ongoing. Implosion results from the combined set of implosions should yield valuable data to develop and validate models of laser-energy deposition, heat conduction, nonuniformity growth, and fuel assembly in PD geometry.

ACKNOWLEDGEMENT

This work was supported by the U.S. Department of Energy Office of Inertial Confinement Fusion under Cooperative Agreement No. DE-FC52-08NA28302, the University of Rochester, and the New York State Energy Research and Development Authority. The support of DOE does not constitute an endorsement by DOE of the views expressed in this article.

REFERENCES

1. S. Skupsky, J. A. Marozas, R. S. Craxton, R. Betti, T. J. B. Collins, J. A. Delettrez, V. N. Goncharov, P. W. McKenty, P. B. Radha, T. R. Boehly, J. P. Knauer, F. J. Marshall, D. R. Harding, J. D. Kilkenny, D. D. Meyerhofer, T. C. Sangster, and R. L. McCrory, Phys. Plasmas **11**, 2763 (2004).

2. E. Moses, presented at The Seventh International Conference on Inertial Fusion Sciences and Applications, Bourdeaux-Lac, France, 12–16 September 2011.

3. J. Nuckolls *et al*., Nature **239**, 139 (1972).

4. T. J. B. Collins, J. A. Marozas, K. S. Anderson, R. Betti, R. S. Craxton, J. A. Delettrez, V. N. Goncharov, D. R. Harding, F. J. Marshall, R. L. McCrory, D. D. Meyerhofer, P. W. McKenty, P. B. Radha, A. Shvydky, S. Skupsky, and J. D. Zuegel, Phys. Plasmas **19**, 056308 (2012).

5. M. C. Herrmann, M. Tabak, and J. D. Lindl, Nucl. Fusion **41**, 99 (2001).

6. J. D. Lindl, *Inertial Confinement Fusion: The Quest for Ignition and Energy Gain Using Indirect Drive* (Springer-Verlag, New York, 1998).

7. S. E. Bodner, Phys. Rev. Lett. **33**, 761 (1974); H. Takabe *et al*., Phys. Fluids **28**, 3676 (1985); R. Betti, V. N. Goncharov, R. L. McCrory, and C. P. Verdon, Phys. Plasmas **5**, 1446 (1998).

8. P. B. Radha, C. Stoeckl, V. N. Goncharov, J. A. Delettrez, D. H. Edgell, J. A. Frenje, I. V. Igumenshchev, J. P. Knauer, J. A. Marozas, R. L. McCrory, D. D. Meyerhofer, R. D. Petrasso, S. P. Regan, T. C. Sangster, W. Seka, and S. Skupsky, Phys. Plasmas **18**, 012705 (2011).

9. C. D. Zhou and R. Betti, Phys. Plasmas **14**, 072703 (2007).

10. I. V. Igumenshchev, D. H. Edgell, V. N. Goncharov, J. A. Delettrez, A. V. Maximov, J. F. Myatt, W. Seka, A. Shvydky, S. Skupsky, and C. Stoeckl, Phys. Plasmas **17**, 122708 (2010).

11. A. Simon, R. W. Short, E. A. Williams, and T. Dewandre, Phys. Fluids **26**, 3107 (1983).

12. W. Seka, D. H. Froula, D. H. Edgell, J. F. Myatt, R. W. Short, I. V. Igumenshchev, V. N. Goncharov, and A. V. Maximov, Bull. Am. Phys. Soc. **56**, 327 (2011); V. N. Goncharov, T. C. Sangster, R. Epstein, S. X. Hu, I. V. Igumenshchev, D. H. Froula, R. L. McCrory, D. D. Meyerhofer, P. B. Radha, W. Seka, S. Skupsky, C. Stoeckl, D. T. Casey, J. A. Frenje, and R. D. Petrasso, Bull. Am. Phys. Soc. **56**, 240 (2011).

13. V. N. Goncharov, T. C. Sangster, P. B. Radha, R. Betti, T. R. Boehly, T. J. B. Collins, R. S. Craxton, J. A. Delettrez, R. Epstein, V. Yu. Glebov, S. X. Hu, I. V. Igumenshchev, J. P. Knauer, S. J. Loucks, J. A. Marozas, F. J. Marshall, R. L. McCrory, P. W. McKenty, D. D. Meyerhofer, S. P. Regan, W. Seka, S. Skupsky, V. A. Smalyuk, J. M. Soures, C. Stoeckl, D. Shvarts, J. A. Frenje, R. D. Petrasso, C. K. Li, F. Séguin, W. Manheimer, and D. G. Colombant, Phys. Plasmas **15**, 056310 (2008).

14. R. Kishony and D. Shvarts, Phys. Plasmas **8**, 4925 (2001).

15. S. W. Haan, J. D. Lindl, D. A. Callahan, D. S. Clark, J. D. Salmonson, B. A. Hammel, L. J. Atherton, R. C. Cook, M. J. Edwards, S. Glenzer, A. V. Hamza, S. P. Hatchett, M. C. Herrmann, D. E. Hinkel, D. D. Ho, H. Huang, O. S. Jones, J. Kline, G. Kyrala, O. L. Landen, B. J. MacGowan, M. M. Marinak, D. D. Meyerhofer, J. L. Milovich, K. A. Moreno, E. I. Moses, D. H. Munro, A. Nikroo, R. E. Olson, K. Peterson, S. M. Pollaine, J. E. Ralph, H. F. Robey, B. K. Spears, P. T. Springer, L. J. Suter, C. A. Thomas, R. P. Town, R. Vesey, S. V. Weber, H. L. Wilkens, and D. C Wilson, Phys. Plasmas **18**, 051001 (2011).

16. T. C. Sangster, V. N. Goncharov, D. H. Edgell, D. H. Froula, V. Yu. Glebov, D. R. Harding, S. X. Hu, F. J. Marshall, R. L. McCrory, P. W. McKenty, D. D. Meyerhofer, J. F. Myatt, P. B. Radha, W. Seka, C. Stoeckl, B. Yaakobi, J. A. Frenje, M. G. Johnson, and R. D. Petrasso, Bull. Am. Phys. Soc. **56**, 241 (2011).

17. S. P. Obenschain *et al*., Phys. Plasmas **9**, 2234 (2002).

18. T. R. Boehly, D. L. Brown, R. S. Craxton, R. L. Keck, J. P. Knauer, J. H. Kelly, T. J. Kessler, S. A. Kumpan, S. J. Loucks, S. A. Letzring, F. J. Marshall, R. L. McCrory, S. F. B. Morse, W. Seka, J. M. Soures, and C. P. Verdon, Opt. Commun. **133**, 495 (1997).

19. P. B. Radha, V. N. Goncharov, T. J. B. Collins, J. A. Delettrez, Y. Elbaz, V. Yu. Glebov, R. L. Keck, D. E. Keller, J. P. Knauer, J. A. Marozas, F. J. Marshall, P. W. McKenty, D. D. Meyerhofer, S. P. Regan, T. C. Sangster, D. Shvarts, S. Skupsky, Y. Srebro, R. P. J. Town, and C. Stoeckl, Phys. Plasmas **12**, 032702 (2005).

20. F. J. Marshall, J. A. Delettrez, R. Epstein, R. Forties, V. Yu. Glebov, J. H. Kelly, T. J. Kessler, J. P. Knauer, P. W. McKenty, S. P. Regan, V. A. Smalyuk, C. Stoeckl, J. A. Frenje, C. K. Li, R. D. Petrasso, and F. H. Séguin, Bull. Am. Phys. Soc. **48**, 56 (2003).

21. *LLE Review Quarterly Report* **65**, 1, Laboratory for Laser Energetics, University of Rochester, Rochester, NY, LLE Document No. DOE/SF/19460-117, NTIS Order No. DE96011927 (1995).

22. R. A. Forties and F. J. Marshall, Rev. Sci. Instrum. **76**, 073505 (2005).

23. T. R. Boehly, D. H. Munro, P. M. Celliers, R. E. Olson, D. G. Hicks, V. N. Goncharov, G. W. Collins, H. F. Robey, S. X. Hu, J. A. Marozas, T. C. Sangster, O. L. Landen, and D. D. Meyerhofer, Phys. Plasmas **16**, 056302 (2009).

24. F. H. Séguin, C. K. Li, J. A. Frenje, D. G. Hicks, K. M. Green, S. Kurebayashi, R. D. Petrasso, J. M. Soures, D. D. Meyerhofer, V. Yu. Glebov, P. B. Radha, C. Stoeckl, S. Roberts, C. Sorce, T. C. Sangster, M. D. Cable, K. Fletcher, and S. Padalino, Phys. Plasmas **9**, 2725 (2002).

25. C. Stoeckl, R. E. Bahr, B. Yaakobi, W. Seka, S. P. Regan, R. S. Craxton, J. A. Delettrez, R. W. Short, J. Myatt, A. V. Maximov, and H. Baldis, Phys. Rev. Lett. **90**, 235002 (2003).

26. R. A. Lerche, D. W. Phillion, and G. L. Tietbohl, Rev. Sci. Instrum. **66**, 933 (1995).

27. W. Seka, D. H. Edgell, J. P. Knauer, J. F. Myatt, A. V. Maximov, R. W. Short, T. C. Sangster, C. Stoeckl, R. E. Bahr, R. S. Craxton, J. A. Delettrez, V. N. Goncharov, I. V. Igumenshchev, and D. Shvarts, Phys. Plasmas **15**, 056312 (2008).

28. F. J. Marshall, P. W. McKenty, J. A. Delettrez, R. Epstein, J. P. Knauer, V. A. Smalyuk, J. A. Frenje, C. K. Li, R. D. Petrasso, F. H. Séguin, and R. C. Mancini, Phys. Rev. Lett. **102**, 185004 (2009).

29. P. B. Radha, F. J. Marshall, T. R. Boehly, T. J. B. Collins, R. S. Craxton, R. Epstein, V. N. Goncharov, J. A. Marozas, R. L. McCrory, P. W. McKenty, D. D. Meyerhofer, T. C. Sangster, A. Shvydky, S. Skupsky, J. A. Frenje, and R. D. Petrasso, presented at the 7th International Conference on Inertial Fusion Sciences and Applications, Bordeaux, France, 12–16 September 2011.

30. J. A. Marozas, F. J. Marshall, R. S. Craxton, I. V. Igumenshchev, S. Skupsky, M. J. Bonino, T. J. B. Collins, R. Epstein, V. Yu. Glebov, D. Jacobs-Perkins, J. P. Knauer, R. L. McCrory, P. W. McKenty, D. D. Meyerhofer, S. G. Noyes, P. B. Radha, T. C. Sangster, W. Seka, and V. A. Smalyuk, Phys. Plasmas **13**, 056311 (2006).

31. J. Delettrez, R. Epstein, M. C. Richardson, P. A. Jaanimagi, and B. L. Henke, Phys. Rev. A **36**, 3926 (1987).

32. V. N. Goncharov, T. C. Sangster, T. R. Boehly, S. X. Hu, I. V. Igumenshchev, F. J. Marshall, R. L. McCrory, D. D. Meyerhofer, P. B. Radha, W. Seka, S. Skupsky, C. Stoeckl, D. T. Casey, J. A. Frenje, and R. D. Petrasso, Phys. Rev. Lett. **104**, 165001 (2010).

33. C. Stoeckl, P. B. Radha, R. E. Bahr, J. A. Delettrez, D. H. Edgell, V. Yu. Glebov, V. N. Goncharov, I. V. Igumenshchev, T. C. Sangster, W. Seka, J. A. Frenje, and R. D. Petrasso, Bull. Am. Phys. Soc. **56**, 241 (2011).

34. S. Skupsky, R. W. Short, T. Kessler, R. S. Craxton, S. Letzring, and J. M. Soures, J. Appl. Phys. **66**, 3456 (1989).

35. T. R. Boehly, V. A. Smalyuk, D. D. Meyerhofer, J. P. Knauer, D. K. Bradley, R. S. Craxton, M. J. Guardalben, S. Skupsky, and T. J. Kessler, J. Appl. Phys. **85**, 3444 (1999).

36. R. Betti and C. Zhou, Phys. Plasmas **12**, 110702 (2005).

37. T. C. Sangster, V. N. Goncharov, P. B. Radha, V. A. Smalyuk, R. Betti, R. S. Craxton, J. A. Delettrez, D. H. Edgell, V. Yu. Glebov, D. R. Harding, D. Jacobs-Perkins, J. P. Knauer, F. J. Marshall, R. L. McCrory, P. W. McKenty, D. D. Meyerhofer, S. P. Regan, W. Seka, R. W. Short, S. Skupsky, J. M. Soures, C. Stoeckl, B. Yaakobi, D. Shvarts, J. A. Frenje, C. K. Li, R. D. Petrasso, and F. H. Séguin, Phys. Rev. Lett. **100**, 185006 (2008).

38. P. B. Radha, J. P. Knauer, T. C. Sangster, V. N. Goncharov, I. V. Igumenshchev, R. Betti, R. Epstein, D. D. Meyerhofer, and S. Skupsky, Bull. Am. Phys. Soc. **52**, 143 (2007).

39. D. H. Froula, B. Yaakobi, S. X. Hu, P.-Y. Chang, R. S. Craxton, D. H. Edgell, R. Follett, D. T. Michel, J. F. Myatt, W. Seka, R. W. Short, A. Solodov, and C. Stoeckl, Phys. Rev. Lett. **108**, 165003 (2012).

Cryogenic Deuterium and Deuterium–Tritium Direct-Drive Implosions on OMEGA

Introduction

To ignite the deuterium–tritium (DT) fuel in a conventional, hot-spot ignition scheme in inertial confinement fusion (ICF), ion temperature and areal density of the central, lower-density region (hot spot) of the final fuel assembly must be sufficient to create fuel self-heating by alpha particles produced as a result of fusing D and T (Refs. 1 and 2). In addition, the areal density (ρR) of the main fuel must be large enough to provide confinement time sufficient to burn a significant portion of that fuel. A typical target consists of a higher-density shell filled with a lower-density fuel vapor. The shell has an outer layer of ablator material and an inner layer of frozen fuel. To compress the main fuel layer and initiate a burn wave propagating from the vapor through the main fuel, the shell is accelerated inward by a temporally shaped pressure drive created by laser energy that is delivered either directly to the target (direct drive) or indirectly by converting its energy to x rays inside the hohlraum (indirect drive).[1,2] As convergence causes pressure to build up in the vapor, the shell begins to decelerate when the vapor pressure exceeds shell pressure and an outgoing shock wave is launched into the incoming shell. During deceleration, hot-spot areal density and temperature increase as the shell's kinetic energy is converted into internal energy of the hot spot and main fuel. Achieving ignition conditions requires the areal density of the hot spot to exceed the stopping range of the alpha particles produced by fusing D and T. This leads to $(\rho R)_{\rm hs} \geq 0.3$ g/cm^2 (Refs. 1 and 2). In addition, the hot-spot ion temperature $T_{\rm hs}$ must be larger than ~5 keV so that the alpha heating exceeds bremsstrahlung losses.[1,2] Since both hot-spot areal density and temperature depend on in-flight shell kinetic energy, there is a threshold value of this energy below which a target fails to ignite.

A target design starts by calculating how much energy the drive pressure must provide to the shell so ignition requirements are met at stagnation. Numerical simulations give the following expression for the minimum shell kinetic energy required for ignition:[3,4]

$$E_{\rm k,min}({\rm kJ}) = 51\,\alpha^{1.9}\left(\frac{V_{\rm imp}}{3\times 10^7}\right)^{-5.9}\left(\frac{p_{\rm a}}{100\ {\rm Mbar}}\right)^{-0.8}. \quad (1)$$

This expression depends on the following in-flight hydrodynamic parameters, crucial for achieving ignition: (1) the peak in mass-averaged main fuel velocity (implosion velocity) $V_{\rm imp}$; (2) the in-flight fuel adiabat α [defined as the ratio of the shell pressure p to the Fermi-degenerate pressure at shell density ρ; for DT fuel, $p \simeq \mu\alpha\rho^{5/3}$ and $\mu = 2.2\ {\rm Mbar}\big/({\rm g/cm}^{3/5})$]; and (3) the drive (ablation) pressure $p_{\rm a}$. Even though Eq. (1) provides a very useful scaling law, it gives very little insight into the physical processes that determine this scaling. To provide such an insight, a simplified model of hot-spot formation is developed and presented next.

1. A Simple Ignition Model

To calculate minimum shell kinetic energy of an igniting target, nearly all this energy is assumed to be converted into the internal hot-spot and fuel energy at stagnation,

$$E_{\rm k} \sim p_{\rm max}R^3 \sim \left(\rho_{\rm hs}T_{\rm hs}R\right)^3\Big/ p_{\rm max}^2, \quad (2)$$

where $p_{\rm max} \sim \rho_{\rm hs}T_{\rm hs}\big/m_{\rm i}$ is the peak hot-spot pressure and $m_{\rm i}$ is ion mass. Since the minimum value of product $(\rho R)_{\rm hs}T_{\rm hs}$ is 0.3 g/cm$^2 \times$ 5 keV, as described earlier, then[2]

$$E_{\rm k,min} \sim 1\Big/ p_{\rm max}^2 \quad (3)$$

and calculation of $E_{\rm k,min}$ is reduced to determine the peak hot-spot pressure.

The maximum pressure is calculated by assuming that the hot-spot radius at peak convergence is R, and a fraction $f_{\rm shl}$ of shell kinetic energy $E_{\rm k} = MV_{\rm imp}^2\big/2$ has been transferred at that time to the hot-spot internal energy $2\pi p_{\rm max}R^3$, where M is the unablated shell mass. Then, the maximum hot-spot pressure is

$$p_{\rm max} \sim f_{\rm shl}E_{\rm k}\Big/R^3. \quad (4)$$

With the goal of expressing $E_{\rm k,min}$ and $p_{\rm max}$ in terms of in-flight shell parameters, stagnation variables must be related to these at the beginning of shell deceleration. Since the hot spot is adiabatic during deceleration,[4,5] $p_{\rm max}$ can be written in

terms of vapor pressure p_d and radius of vapor region R_d at the beginning of shell deceleration:

$$p_{\max} = p_d\left(R_d/R\right)^5. \tag{5}$$

Equating the right-hand sides of Eqs. (4) and (5) gives a hot-spot convergence ratio during deceleration,

$$\frac{R_d}{R} \sim \sqrt{\frac{f_{\rm shl}E_{\rm k}}{p_d R_d^3}}. \tag{6}$$

Then, using Eqs. (5) and (6) defines the maximum hot-spot pressure as a ratio of the shell's kinetic energy to the internal energy of the vapor at the beginning of deceleration:[5]

$$p_{\max} \sim p_d\left(\frac{f_{\rm shl}E_{\rm k}}{p_d R_d^3}\right)^{5/3} \sim p_d\left(\frac{f_{\rm shl}M}{p_d R_d^3}\right)^{5/2} V_{\rm imp}^5. \tag{7}$$

For $f_{\rm shl} = 1$, Eqs. (3) and (7) give $p_{\max} \sim V_{\rm imp}^5$ and $E_{\rm k,min} \sim V_{\rm imp}^{-10}$, similar to the result of the isobaric model.[6] The fraction $f_{\rm shl}$, however, is smaller than unity and depends on in-flight shell parameters. Keeping in mind that the shell is decelerated by the outgoing shock wave, $f_{\rm shl}$ can be defined as a fraction of the shell mass (an effective mass $M_{\rm eff}$) overtaken by this shock while the hot spot converges inward. In the strong shock limit, the Hugoniot conditions across the shock give

$$M_{\rm eff} \equiv f_{\rm shl}M \sim \sqrt{\rho_{\rm shl}p_{\max}}\,R^2\Delta t, \tag{8}$$

where $\rho_{\rm shl}$ is the shell density ahead of the shock front. The hot-spot time of confinement by the shell inertia is determined by Newton's law, $M_{\rm eff}R/(\Delta t)^2 \sim p_{\max}R^2$, which yields[7]

$$\Delta t \sim \sqrt{M_{\rm eff}/p_{\max}R}. \tag{9}$$

Then, Eqs. (8) and (9) lead to

$$M_{\rm eff} \sim \rho_{\rm shl}R^3. \tag{10}$$

With the help of the latter equation, Eq. (4) yields intuitively simple scaling

$$p_{\max} \sim \rho_{\rm shl}V_{\rm imp}^2. \tag{11}$$

The maximum pressure, however, does not scale as $V_{\rm imp}^2$, as Eq. (11) would suggest, since $\rho_{\rm shl}$ is different from the in-flight shell density. As the unshocked part of the incoming shell keeps converging during deceleration, its density $\rho_{\rm shl}$ increases inversely proportional to the surface area:

$$\rho_{\rm shl} \simeq \rho_d\left(\frac{R_d}{R}\right)^2. \tag{12}$$

Combining Eqs. (5), (11), and (12) defines the hot-spot convergence ratio in terms of in-flight shell quantities

$$\frac{R_d}{R} \sim \left(\frac{V_{\rm imp}^2\rho_d}{p_d}\right)^{1/3}. \tag{13}$$

Substituting Eq. (13) into Eqs. (10) and (12) gives the effective shell mass and $\rho_{\rm shl}$:

$$M_{\rm eff} \sim \rho_d R_d^3\frac{R_d}{R} \sim \rho_d R_d^3\left(\frac{p_d}{\rho_d V_{\rm imp}^2}\right)^{1/3} \tag{14}$$

and

$$\rho_{\rm shl} \sim \rho_d\left(\frac{V_{\rm imp}^2\rho_d}{p_d}\right)^{2/3}. \tag{15}$$

Finally, the scaling for the maximum pressure is obtained by combining Eqs. (7) and (14):

$$p_{\max} \sim \rho_d V_{\rm imp}^2\left(\frac{V_{\rm imp}^2\rho_d}{p_d}\right)^{2/3} = p_d\left(\frac{V_{\rm imp}^2\rho_d}{p_d}\right)^{5/3}. \tag{16}$$

Pressure at the beginning of the deceleration phase is proportional to the drive ablation pressure, $p_d \sim p_{\rm a}$, and shell density is related to the drive pressure through the in-flight shell adiabat α, $p_d({\rm Mbar}) \sim 2.2\,\alpha\rho_d^{5/3}$. This gives

$$p_{\max} \sim \frac{p_{\rm a}^{1/3}V_{\rm imp}^{10/3}}{\alpha}. \tag{17}$$

This scaling of $p_{\max}$ with $V_{\rm imp}$ is similar to that derived using self-similar analysis,[8] which leads to $p_{\max}^{\text{self-similar}} \sim V_{\rm imp}^3$. Substituting Eq. (17) back into Eq. (3) gives a scaling law similar to that obtained using simulation results [see Eq. (1)]:

$$E_{\rm k,min} \sim 1/p_{\max}^2 \sim V_{\rm imp}^{-20/3}p_{\rm a}^{-2/3}\alpha^2. \tag{18}$$

Equation (17) shows that the maximum pressure has a weaker implosion velocity dependence than $V_{\rm imp}^5$ obtained assuming that all kinetic energy of the shell is transferred to the internal energy of the fuel at stagnation. The weaker dependence is due to the fact that the kinetic energy fraction contributing to the fuel's internal energy is proportional to the fraction of the shell mass overtaken by the outgoing shock wave during the hot-spot confinement time. Several competing effects define this fraction: First, the mass flux per unit area across the shock increases with hot-spot convergence since both shell density $\rho_{\rm shl}$ and maximum pressure $p_{\rm max}$ increase with R_d/R [see Eqs. (5) and (12)], so $\sqrt{\rho_{\rm shl}p_{\rm max}} \sim \sqrt{\rho_d p_d}\left(R_d/R\right)^{7/2}$. Multiplied by the surface area of the shock front, the mass flux across the shock is $\sqrt{\rho_{\rm shl}p_{\rm max}}\,R^2 \sim \sqrt{\rho_d p_d}\,R_d^2\left(R_d/R\right)^{3/2}$. The convergence ratio increases with the implosion velocity, as shown in Eq. (13), giving

$$\text{mass flux} \sim \sqrt{\rho_{\rm shl}p_{\rm max}}\,R^2 \sim V_{\rm imp}. \tag{19}$$

The confinement time, on the other hand, decreases with convergence ratio and implosion velocity. Indeed, writing $\Delta t \sim R/V_{\rm imp}$ [this can be obtained by substituting Eqs. (10) and (11) into Eq. (9)] and using Eq. (13) gives

$$\text{confinement time} \sim \frac{R}{V_{\rm imp}} \sim \left(\frac{R_d}{R}\right)^{-5/2} \sim V_{\rm imp}^{-5/3}. \tag{20}$$

Then, the product of mass flux and confinement time gives the effective mass and fraction of kinetic energy that contributes to the stagnation pressure $M_{\rm eff} \sim f_{\rm shl} \sim V_{\rm imp}^{-2/3}$, in agreement with Eq. (14). Negative power in velocity dependence of the effective mass changes pressure scaling from $V_{\rm imp}^5$ to $V_{\rm imp}^{10/3}$.

The maximum pressure, on the other hand, has a stronger dependence on $V_{\rm imp}$ than that given by the dynamic pressure argument $p_{\rm max} \sim \rho_{\rm shl} V_{\rm imp}^{10/2}$. This is due to convergence effects and an increase in the unshocked shell density during deceleration. Since $\rho_{\rm shl}$ rises with convergence ratio, as shown in Eq. (12), the maximum pressure scales as

$$p_{\rm max} \sim \left(\rho_{\text{in flight}} V_{\rm imp}^{2\times 2/3}\right) V_{\rm imp}^2 \sim V_{\rm imp}^{10/3},$$

in agreement with Eq. (17).

Since $E_{\rm k,min}$ is strongly dependent on the implosion velocity, as shown in Eqs. (1) and (18), it is crucial that a shell reaches the designed value of $V_{\rm imp}$ to achieve ignition in an experiment. The minimum $V_{\rm imp}$ can be estimated by the following argument: Balancing a fraction of the kinetic energy of the shell and the internal energy of the fuel yields

$$MV_{\rm imp}^2/2 > 2\pi p_{\rm max} R^3. \tag{21}$$

For fully ionized gas with ion charge Z and ion mass $m_{\rm i}$,

$$p_{\rm max} = (1+Z)\rho_{\rm hs}T_{\rm hs}/m_{\rm i}.$$

For DT fuel this gives $p_{\rm max} \simeq 4\rho_{\rm hs}T_{\rm hs}/m_{\rm p}$, where $m_{\rm p}$ is proton mass. Finally, writing shell mass at stagnation as $M \sim 4\pi R^2 \rho_{\rm fuel}\Delta$ leads to

$$V_{\rm imp} > \sqrt{\frac{4}{5}\frac{(\rho R)_{\rm hs}}{(\rho\Delta)_{\rm fuel}}\frac{T_{\rm hs}}{m_{\rm p}}}, \tag{22}$$

where $\rho_{\rm fuel}$ and Δ are the density and thickness of compressed fuel, respectively. To create a hot spot and trigger burn propagation into the cold fuel, the hot-spot areal density and temperature must exceed, as discussed earlier, $(\rho R)_{\rm hs}T_{\rm hs} > 0.3$ g/cm$^2 \times$ 5 keV. To burn enough cold fuel and achieve gain = fusion energy/laser energy > 1 requires, on the other hand, $(\rho\Delta)$fuel > 1 g/cm^2 (Refs. 1 and 2). Substituting these three conditions back into Eq. (22) gives

$$V_{\rm imp} > 3\times 10^7 \text{ cm/s}. \tag{23}$$

This leads to a requirement on stagnation pressure $p_{\rm max}$. Indeed, the ablation pressure in an ICF implosion is $p_{\rm a} \sim$ 100 Mbar, and the effective dynamic pressure of the accelerated shell at $V_{\rm imp} = 3\times 10^7$ cm/s and $\alpha = 1$ is $\rho V^2 \simeq (100/2.2)^{3/5}$ $[3\times 10^7]^2 \simeq 9$ Gbar. In general, $\rho \simeq \left[p(\text{Mbar})/2.2\,\alpha\right]^{3/5}$ and the dynamic pressure is

$$\text{dynamic pressure}_{\text{in flight}} \simeq$$

$$9\left(\frac{p_{\rm a}}{100\text{ Mbar}}\right)^{3/5}\alpha^{-3/5}\left(\frac{V_{\rm imp}}{3\times 10^7}\right)^2 \text{Gbar}. \tag{24}$$

An additional amplification in dynamic pressure is due to shell convergence during deceleration. As described earlier, unshocked-shell density amplification is proportional to the hot-spot convergence ratio to the second power [see Eq. (12)]. According to Eq. (13), the hot spot converges by a factor of 4.4 during deceleration for $\alpha \sim 1$ and $V_{\rm imp} \sim 3\times 10^7$ cm/s. This

gives an additional increase by a factor of $4.4^2 = 20$ in the dynamic pressure, leading to a maximum hot-spot pressure in an igniting target of $p_{\max} > 200$ Gbar, or for a given implosion velocity and drive pressure,

$$p_{\max} \simeq 180\left(\frac{p_a}{100\ \text{Mbar}}\right)^{1/3}\alpha^{-1}\left(\frac{V_{\text{imp}}}{3\times 10^7}\right)^{10/3}\ \text{Gbar}. \quad (25)$$

Using the numerical factor obtained in Eq. (25), one can recover a numerical factor in Eq. (18) as well:

$$E_{k,\min} \simeq 30\,\alpha^2\left(\frac{V_{\text{imp}}}{3\times 10^7}\right)^{-20/3}\left(\frac{p_a}{100\ \text{Mbar}}\right)^{-2/3}\text{kJ}. \quad (26)$$

The numerical coefficient in Eq. (26) is 40% smaller than that in the fitting formula shown in Eq. (1). This is a consequence of the fact that only a fraction f_{shl} of the total shell kinetic energy is transferred to the fuel at stagnation. Typically, $f_{\text{shl}} \sim 0.5$ to 0.6, which brings the numerical coefficient in Eq. (26) in closer agreement with the numerical result.

2. Sensitivity of Ignition Condition on Implosion Parameters

The minimum shell kinetic energy required for ignition depends strongly on the shell's velocity and adiabat [see Eq. (1)]. When a particular target design is considered for an ignition experiment, one of the important design parameters is margin [this is also referred to as an ignition threshold factor (ITF)][9] defined as the ratio of the shell kinetic energy E_k to its minimum value required for ignition $E_{k,\min}$,

$$\text{ITF} = \frac{E_k}{E_{k,\min}}. \quad (27)$$

In using Eq. (1) to determine $E_{k,\min}$, one must keep in mind that Eq. (1) does not account for asymmetry effects (such as shell and hot-spot nonuniformity growth, mix of ablator material and fuel, etc.). A more-complete analysis using 2-D and 3-D hydrodynamic simulations results in correction factors related to these effects (for details, see Ref. 9). Since the main purpose of this article is to address accuracy in the modeling of average 1-D hydrodynamic parameters, the terms proportional to multidimensional effects will be neglected.

Robustness of a particular design is determined by how much uncertainty in velocity, adiabat, and the drive pressure it can tolerate before the probability of achieving ignition becomes very small. Such maximum uncertainty values depend on ITF.

The target fails to ignite if the shell's kinetic energy E_k in an experiment is lower than the ignition energy threshold $E_{k,\min}$ or the actual energy threshold $E_{k,\min}$ is higher than calculated $E_{k,\min}$ as a result of inaccuracies in modeling of hydro-dynamic quantities. If E_k^{design} and $E_{k,\min}^{\text{design}}$ are design values of the shell's kinetic energy and energy threshold, respectively, and $\text{ITF} = E_k^{\text{design}}\big/E_{k,\min}^{\text{design}}$, then the maximum deviations in V_{imp}, α, and p_a (denoted as δV_{imp}, $\delta\alpha$, and δp_a, respectively) from predictions are determined from the condition $E_k^{\text{limit}}\big/E_{k,\min}^{\text{limit}} = 1$, where $E_k^{\text{limit}} = M\left(V_{\text{imp}} - \delta V_{\text{imp}}\right)^2\big/2$,

$$E_{k,\min}^{\text{limit}} = E_{k,\min}\left(\alpha + \delta\alpha, V_{\text{imp}} - \delta V_{\text{imp}}, p_a - \delta p_a\right),$$

$$E_k^{\text{design}} = MV_{\text{imp}}^2\big/2, \text{ and } E_{k,\min}^{\text{design}} = E_{k,\min}\left(\alpha, V_{\text{imp}}, p_a\right).$$

This reads as

$$1 = \text{ITF}\left(1 - \frac{\delta V_{\text{imp}}}{V_{\text{imp}}}\right)^{7.9}\left(1 + \frac{\delta\alpha}{\alpha}\right)^{-1.9}\left(1 - \frac{\delta p_a}{p_a}\right)^{0.8}. \quad (28)$$

Since it is very difficult to assess the fuel adiabat by a direct measurement, the adiabat increase $\delta\alpha$ is replaced in this analysis with energy deposited in the fuel ΔE that leads to an adiabat increase $\delta\alpha$. This energy is expressed in terms of a fraction ε_E of the shell kinetic energy $\Delta E = \varepsilon_E E_{k,0}$. To relate $\delta\alpha$ and ΔE, we write internal energy as a product of pressure and volume $E = 3/2\ pV$. Replacing pressure by the drive ablation pressure p_a and the fuel volume by fuel mass over shell density, $V = M/\rho$, gives $E = 3p_aM/2\rho$. Shell density is related to the ablation pressure as $\rho \sim \left(p_a\big/\alpha\right)^{3/5}$. Then, collecting all appropriate numerical coefficients leads to

$$E(\text{kJ}) = 1.5\left(\frac{p_a}{100\ \text{Mbar}}\right)^{2/5}\alpha^{3/5}M\left(\text{mg}\right). \quad (29)$$

Fixing shell mass and drive pressure gives $1 + \delta\alpha/\alpha = (1 + \Delta E/E_0)^{5/3}$. Then, Eq. (28) takes the form

$$\left(1 - \frac{\delta V_{\text{imp}}}{V_{\text{imp}}}\right)^{-7.9}\left[1 + \frac{30\,\varepsilon_E\left(V_{\text{imp}}\big/3\times 10^7\right)^2}{\left(p_a\big/100\ \text{Mbar}\right)^{2/5}\alpha^{3/5}}\right]^{3.1}$$

$$\times\left(1 - \frac{\delta p_a}{p_a}\right)^{-0.8} = \text{ITF}. \quad (30)$$

Figure 130.16 plots (a) the reduction in shell velocity, (b) shell preheat as a percentage fraction of the shell's kinetic energy, and (c) reduction in drive pressure that lead to ignition failure in a design with a given value of ITF. Figure 130.16 shows that for NIF-scale ignition designs with ITF ~ 3.5 to 5, ignition fails if velocity reduction is greater than ~15% and the shell is preheated by more than ~1% of the shell's kinetic energy. The drive pressure, according to Fig. 130.16(c), can be reduced as much as 80% before ignition will fail. This number, however, does not account for a reduction in the implosion velocity associated with reduced drive. Therefore, Fig. 130.16(c) must be used in combination with Fig. 130.16(a). In addition to ignition failure caused by a significant deviation from predicted 1-D hydrodynamic parameters (velocity, adiabat, drive pressure), other failure mechanisms are due to asymmetries in an implosion. Nonuniformity sources caused by both target imperfections (such as ice roughness and ablator roughness) and asymmetry in laser illumination are amplified by the Rayleigh–Taylor (RT) and Richtmyer–Meshkov (RM) instabilities[1,2] during an implosion. Nonuniformity growth could either disrupt the shell or lead to significant hot-spot distortions. The distortion region width inside the hot spot exceeding 20% to 40% of the 1-D hot-spot radius is typically sufficient to reduce alpha-particle production and ion temperature and quench the burn.[7]

Even though control of the multidimensional effect is one of the main challenges for any ignition design, validation of code ability to adequately model target-drive efficiency and the amount of the fuel preheat is a primary goal of the ICF experiments. This article will describe how these global hydrodynamic parameters predicted by hydrosimulations were experimentally validated using direct-drive implosions on OMEGA.

Early Direct-Drive Target Designs and Target Stability Properties

1. All-DT, Direct-Drive, NIF-Scale Ignition Target Design

The original direct-drive target design[10,11] for the National Ignition Facility (NIF) Laser System[12] is a 350-μm-thick, solid-DT layer inside a very thin (~3-μm) plastic shell (shown in Fig. 130.17). Because the plastic shell ablates early in the pulse and the DT layer acts as both the main fuel and ablator, this design is referred to as an "all-DT" design. The fact that the ablator and the main fuel are the same material (DT) has several advantages: (1) It eliminates the interface between the fuel and ablator. Any mismatch in density or opacity between two neighboring materials in the shell usually leads to an enhancement in the early-time perturbation growth or the RT instability growth factor.[13] (2) Because of its initial low density, DT gives both the lowest in-flight aspect ratio (IFAR)

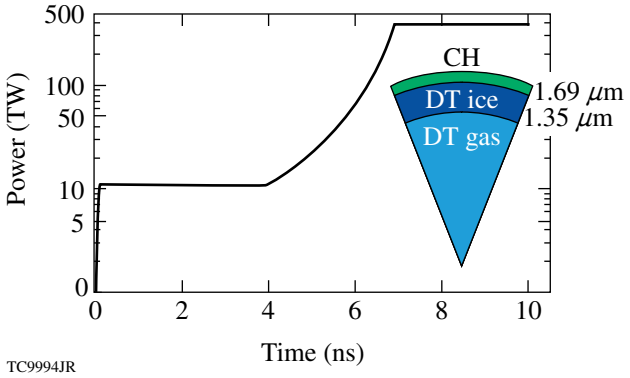

Figure 130.17
An α = 3, "all-DT," 1.5-MJ, direct-drive–ignition target design with a 1-D gain of 45.

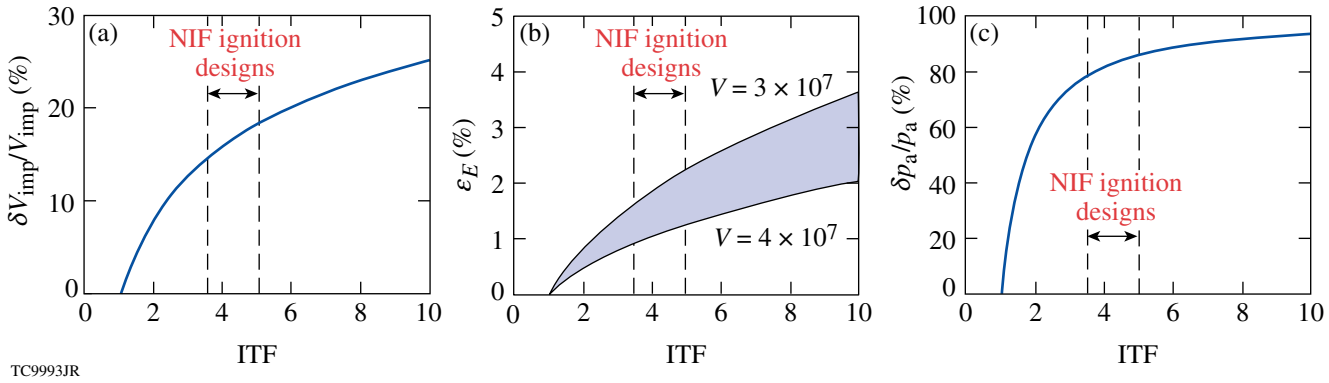

Figure 130.16
(a) Maximum velocity reduction, (b) maximum preheat energy as fractions of the shell's kinetic energy, and (c) maximum pressure reduction versus ITF.

for the same shell mass and the largest ablative stabilization factor in the RT instability growth rate formula compared to other ablator materials [see **Rayleigh–Taylor Instability** below for more details on design stability properties]. The biggest downside of using DT as an ablator, as demonstrated in OMEGA experiments, is the low absorption fraction caused by inverse bremsstrahlung and low threshold for the two-plasmon-decay (TPD) instability,[14] which generates suprathermal electrons that preheat the fuel. Currently, there is no experimental demonstration of low-adiabat, high fuel compression in direct-drive designs with DT or D_2 ablators driven at ignition-relevant intensities above 5×10^{14} W/cm^2 (this will be discussed further in **Cryogenic D_2 Implosions on the OMEGA Upgrade Laser System from 2001 Until Mid-2008**, p. 85). In the design presented in Fig. 130.17, the fuel is accelerated by 1.5 MJ of laser energy to a peak velocity of $V_{\rm imp} = 4.3 \times 10^7$ cm/s at adiabat $\alpha = 3$. The target ignites and gives a 1-D gain of 45 with an ITF of 5. This design uses a continuous pulse shape (as opposed to the picket pulse described in the next section), launching the initial shock that sets the in-flight shell adiabat. Later, at $t = 4$ ns, the intensity gradually rises, launching a compression wave. The head of this wave catches up with the first shock in the vapor region, soon after it breaks out of the shell. Timing the first shock and compression wave breaking out of the fuel and preventing the compression wave from turning into a shock inside the fuel are crucial to achieving ignition in this design.

2. Target Stability Properties: Rayleigh–Taylor Instability Growth and Target IFAR

A shell kinetic energy required to ignite DT fuel in an ICF implosion is strongly dependent on the maximum shell velocity. According to Eq. (1), increasing the shell's velocity to well above the minimum value of $V_{\rm imp} \sim 3 \times 10^7$ cm/s is beneficial for reducing the laser-energy requirement. Increasing implosion velocity, however, must be achieved without compromising the the shell's integrity due to hydrodynamic instability growth.

To understand how $V_{\rm imp}$ scales with target parameters, we start by writing

$$V_{\rm imp} \sim g t_{\rm accel}, \tag{31}$$

where g is shell acceleration and $t_{\rm accel}$ is the acceleration time. The acceleration is determined from Newton's law,

$$M_{\rm shell}\, g \sim 4\pi R^2 p_{\rm a} \longrightarrow g \sim 4\pi \frac{p_{\rm a} R^2}{M_{\rm shell}}, \tag{32}$$

where $M_{\rm shell}$ is the initial shell mass, R is shell radius, and $p_{\rm a}$ is ablation pressure. The acceleration time for a given laser energy $E_{\rm laser}$ and drive intensity I is

$$t_{\rm accel} \sim \frac{E_{\rm laser}}{4\pi R^2 I}. \tag{33}$$

Substituting Eqs. (32) and (33) into Eq. (31) gives

$$V_{\rm imp} \sim p_{\rm a} E_{\rm laser} \big/ M_{\rm shell} I.$$

Results of simulations lead to a numerical factor of 0.8 in the latter equation. Therefore,

$$V_{\rm imp} \simeq 0.8 \frac{p_{\rm a} E_{\rm laser}}{M_{\rm shell} I}. \tag{34}$$

Since $p_{\rm a} \sim I^{0.8}$ to $I^{0.7}$ (Refs. 1 and 2), implosion velocity increases, for a given shell mass and laser energy, by reducing drive intensity. This intuitively contradictory result can be explained by noting that a lower laser drive is overcompensated by the duration of the shell's acceleration, as shown in Eq. (33). The acceleration distance is longer for lower-intensity drives: $R \sim V_{\rm imp} t_{\rm accel} \sim p_{\rm a} E_{\rm laser}^2 \big/ M_{\rm shell} I^2 R^2$, so $R^3 \sim p_{\rm a} E_{\rm laser}^2 \big/ M_{\rm shell} I^2 \sim I^{-1.2}$. The implosion velocity can also be increased, according to Eq. (34), by reducing shell mass. An increase in $V_{\rm imp}$, however, is beneficial for reducing $E_{\rm k,min}$ only up to the point where multidimensional effects (asymmetry growth) start to affect target performance. Hydrodynamic instabilities put severe constraints on target designs, limiting the values of the shell mass and adiabat used in a robust target design. To determine such constraints, we next identify target parameters that affect the target stability.

a. Rayleigh–Taylor instability. The dominant hydrodynamic instability in an ICF implosion is the Rayleigh–Taylor (RT) instability.[1,2] The RT instability develops in systems where the heavier fluid is accelerated by the lighter fluid.[15] In an ICF implosion, the heavier shell material is accelerated by the lighter blowoff plasma, creating the condition for RT instability. This instability amplifies shell distortions, seeded by both the ablator and ice roughness, and laser illumination nonuniformities (laser "imprint"[13]). Excessive growth of these perturbations leads to shell breakup during acceleration, limiting the final compression and hot-spot temperature. An example of a direct-drive implosion simulation is shown in Fig. 130.18. Shell distortions developed due to the RT instability during

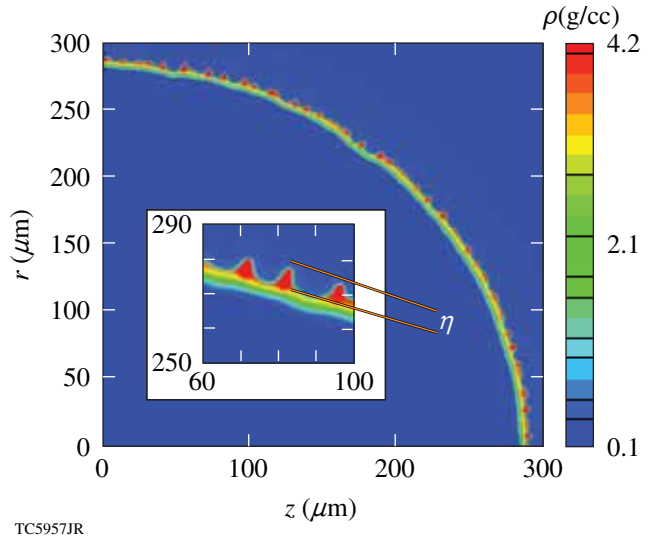

Figure 130.18
Two-dimensional simulation of a direct-drive implosion using the hydrocode *DRACO*. Rayleigh–Taylor instability causes shell distortions with amplitude η to grow in time.

acceleration are clearly visible in this simulation. The small initial perturbation amplitude η_0 grows in time as

$$\eta \sim \eta_0 e^{\gamma_{\mathrm{RT}} t}, \tag{35}$$

where γ_{RT} is the growth rate. In the classical RT configuration where a heavier fluid with density ρ_2 is supported by a lighter fluid of density ρ_1 in a gravitational field g directed from heavier to lighter fluids, the RT growth rate is[15]

$$\gamma_{\mathrm{RT,classical}} = \sqrt{A_T k g}, \quad A_T = \frac{\rho_2 - \rho_1}{\rho_2 + \rho_1}, \tag{36}$$

where A_T is Atwood number, $k = 2\pi/\lambda$ is the perturbation wave number, and λ is the perturbation wavelength. In an ICF implosion, the thermal conduction (electron dominant in direct-drive implosions and x-ray radiation dominant in indirect-drive implosions) that drives the ablation process significantly reduces the growth rate from its classical value.[16] The full expression for the growth rate in this case is rather complicated and can be found in Ref. 17. Here, we show the growth rate in the limit $kL_0 < 1$, where L_0 is the effective thickness of the ablation front,

$$\begin{aligned} \gamma_{\mathrm{RT,ICF}} &\simeq \sqrt{kg - \Omega_{\mathrm{bl}}^2 + \Omega_{\mathrm{a}}^2} - \Omega_{\mathrm{a}}, \\ \Omega_{\mathrm{bl}} &= k\sqrt{V_{\mathrm{a}} V_{\mathrm{bl}}}, \\ \Omega_{\mathrm{a}} &= 2kV_{\mathrm{a}}, \end{aligned} \tag{37}$$

where V_{a} and V_{bl} are the ablation and blowoff velocities, respectively (for the definition of V_{bl}, see Ref. 17). Because mass density in the plasma blowoff region is much smaller than shell density, $A_T \simeq 1$ for modes with $kL_0 < 1$. There are two stabilizing terms in $\gamma_{\mathrm{RT,ICF}}$: the first is proportional to Ω_{bl} and the other to Ω_{a}. Both of them are due to the mass ablation driven by thermal conduction; physical mechanisms of the two, however, are different.

The ablation process is characterized by the ablation velocity V_{a}, defined as the ratio of the mass ablation rate per unit area of target surface, $\left(\mathrm{d}M/\mathrm{d}t\right)\Big/\left(4\pi R^2\right)$, and the shell density at the ablation front $\rho_{\mathrm{shell,abl}}$ (see Fig. 130.19),

$$V_{\mathrm{a}} = \frac{\mathrm{d}M}{\mathrm{d}t}\Big/\left(4\pi R^2 \rho_{\mathrm{shell,abl}}\right), \tag{38}$$

where R is the ablation-front radius. When mass ablation is included, several physical mechanisms reduce the ablation-front perturbation growth and, in some cases, totally suppress it. These are illustrated in Fig. 130.20. First, different plasma blowoff velocities at different parts of the corrugated ablation region create modulation in the dynamic pressure or "rocket effect" that leads to a stabilizing restoring force.[13,18,19] Indeed,

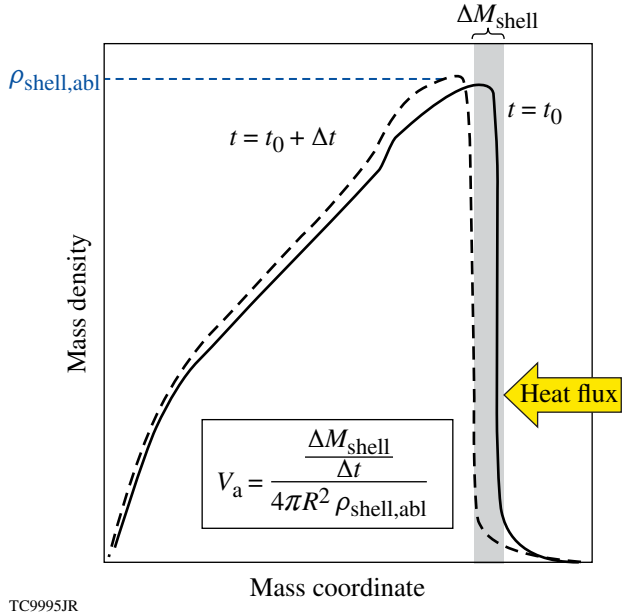

Figure 130.19
Ablation velocity is defined as mass ablation rate, $\Delta M/\Delta t \simeq \mathrm{d}M/\mathrm{d}t$, divided by the ablation region surface area $4\pi R^2$ and the shell density at the ablation front $\rho_{\mathrm{shell,abl}}$.

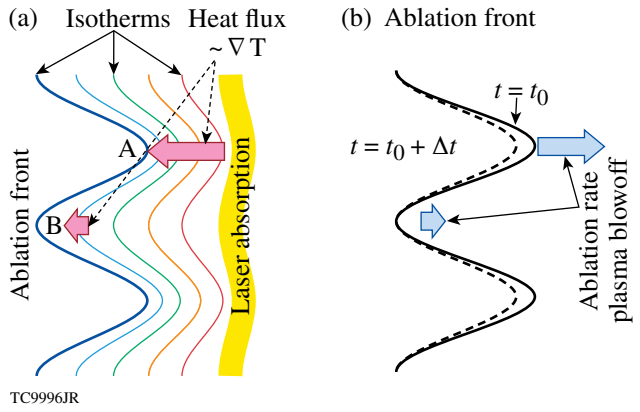

Figure 130.20
(a) Ablation-front modulation creates stronger temperature gradients at perturbation peaks (A) and weaker gradients at valleys (B). Since heat flux is proportional to such gradients, this leads to a slightly enhanced heat flux at A and a reduced heat flux at B. (b) Modulation in heat flux results in modulation in the mass ablation rate. The mass removed by ablation at point A is larger than that at point B, leading to both a fire-polishing effect and a restoring force caused by dynamic overpressure.

as a result of the perturbation growth, the peaks [point A in Fig. 130.20(a)] of the ablation-front ripple protrude into the hotter plasma corona, and the valleys [point B in Fig. 130.20(a)] recede toward the colder shell material. Since the temperature is uniform along the ablation front,[16] the temperature gradients and the heat fluxes are slightly enhanced at the peaks and reduced at the valleys, as shown in Fig. 130.20(a). An excess/deficiency in the heat flux speeds up/slows down the ablation front. This is illustrated in Fig. 130.20(b), where the solid and dashed lines indicate the positions of the ablation front at two instances in time separated by Δt. The ablation front at the peaks (point A) propagates further into the shell than at the valleys (point B). This increases velocity of the blowoff material ("exhaust" velocity, if an analogy of the ablatively driven shell with a rocket is used) at point A and reduces it at point B. A modulation in the blowoff velocity leads to a modulation in the dynamic pressure, creating a restoring force and reducing perturbation growth [see terms with Ω_{bl}^2 in Eq. (37)]. The second stabilizing mechanism caused by ablation is an increased mass ablation rate at the perturbation peaks in comparison with the valley. This leads to faster mass removal at point A and slower removal at point B (so-called "fire-polishing" effect). The latter effect gives the stabilizing terms proportional to Ω_a in Eq. (37).

Since the ablation and blowoff velocities are inversely proportional to the shell density at the ablation front, and density and ablation pressure are related as $\rho_{\text{shell,abl}} \sim \left(p_a/\alpha_{\text{abl}}\right)^{3/5}$, the velocities scale with the adiabat near the ablation front α_{abl} as

$$V_a \sim V_{bl} \sim \alpha_{\text{abl}}^{3/5}. \tag{39}$$

Equation (39) shows that reducing shell density or increasing shell adiabat at the ablation front enhances shell stability.

b. Target in-flight aspect ratio (IFAR). The other important parameter characterizing shell stability is the shell's in-flight aspect ratio (IFAR) defined as the ratio of the shell's radius R to the in-flight shell thickness $\Delta_{\text{in flight}}$ (see Fig. 130.21). Designs with thicker shells are less sensitive to the instability growth because they break up at a larger distortion amplitude and have smaller seeding of the deceleration RT instability. Such an instability develops as lower-density vapor pushes against the higher-density shell. During the shell acceleration, perturbations feed through from the unstable ablation front to the inner shell $\eta_{\text{inner}} \sim \eta_{\text{ablation}} e^{-k\Delta_{\text{in flight}}}$. As the shell decelerates, the inner surface distortions start to grow from η_{inner}, leading to hot-spot deformation at peak compression. Therefore, the thicker the shell, the smaller the feedthrough factor, and the smaller the finite hot-spot deformation.

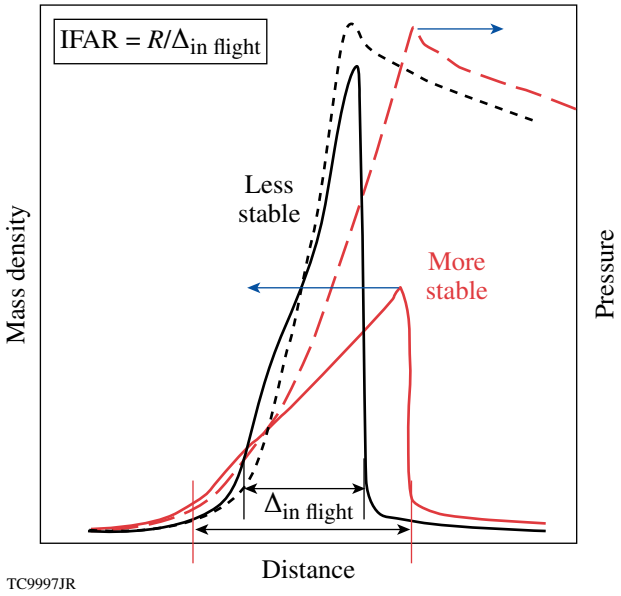

Figure 130.21
In-flight aspect ratio is defined as the ratio of the shell's radius to the in-flight shell thickness. Designs with smaller IFAR are less sensitive to the shell's distortion growth since they break up at larger distortion amplitudes.

Next, we find a scaling of IFAR with implosion parameters. As defined, IFAR = $R/\Delta_{\text{in flight}}$. The in-flight shell thickness is the initial shell thickness Δ_0 reduced by shell compression during acceleration (effect of mass ablation is neglected in this analysis),

$$\Delta_{\text{in flight}} \simeq \Delta_0 \frac{\rho_0}{\langle\rho\rangle_{\text{in flight}}} \frac{R_0^2}{R^2}, \tag{40}$$

where ρ_0 and $\langle\rho\rangle$ are initial and average in-flight shell densities, respectively, and R_0 is the initial shell radius. For the all-DT design where the shell consists mainly of DT, $\langle\rho\rangle_{\text{in flight}} = \left[p_a(\text{Mbar})/2.2\langle\alpha\rangle\right]^{3/5}$, where $\langle\alpha\rangle$ is the mass-averaged shell adiabat. This gives

$$\text{IFAR} = \frac{R}{\Delta_{\text{in flight}}}$$

$$\simeq 10\frac{R_0}{\rho_0\Delta_0}\left(\frac{R}{R_0}\right)^3\left(\frac{p_a}{100\ \text{Mbar}}\right)^{3/5}\langle\alpha\rangle^{-3/5}. \tag{41}$$

Multiplying the numerator and denominator of Eq. (41) by $4\pi R_0^2$ and replacing $4\pi R_0^2\Delta_0\rho_0$ with the shell mass M_{shell} yields

$$\text{IFAR} = 10\left(\frac{4\pi R_0^3}{M_{\text{shell}}}\right)\left(\frac{R}{R_0}\right)^3\left(\frac{p_a}{100\ \text{Mbar}}\right)^{3/5}\langle\alpha\rangle^{-3.5}. \tag{41a}$$

Initial shell radius in an optimized design is proportional to shell's velocity times acceleration time, $R_0 \sim V_{\text{imp}} t_{\text{accel}}$ and the required shell mass is given by Newton's law $MR_0/t_{\text{accel}}^2 \sim 4\pi p_a R_0^2$. Eliminating t_{accel} from the latter two equations gives

$$\frac{4\pi R_0^3}{M} = \frac{V^2}{p_a}. \tag{42}$$

Combining Eqs. (41a) and (42) leads to

$$\text{IFAR} = 90\frac{R^3}{R_0^3}\left(\frac{V_{\text{imp}}}{3\times 10^7}\right)^2\left(\frac{p_a}{100\ \text{Mbar}}\right)^{-2/5}\langle\alpha\rangle^{-3/5}. \tag{43}$$

Equation (43) shows that IFAR's value decreases as the shell implodes (the ratio R/R_0 gets smaller), reaching its peak value at the beginning of the shell's acceleration, when drive intensity reaches its peak value. Then, the stability property of a design is characterized by this peak IFAR value. Fit to the results of numerical simulations gives[20]

$$\max(\text{IFAR}) \simeq 60\left(\frac{V_{\text{imp}}}{3\times 10^7}\right)^2\left(\frac{p_a}{100\ \text{Mbar}}\right)^{-2/5}\langle\alpha\rangle^{-3/5}, \tag{44}$$

which can be recovered from Eq. (43) by using $R \simeq 0.9R_0$. Numerical simulations of directly driven cryogenic implosions (both on OMEGA and the NIF) show that to keep the shell from breaking up because of the short-scale perturbation growth during the acceleration, IFAR should not exceed

$$\text{IFAR}_{\max} \simeq 40. \tag{45}$$

Using Eq. (44), we conclude that increasing implosion velocity by reducing the drive intensity alone, as Eq. (34) suggests, is not the best strategy from a stability point of view since two factors cause IFAR in this case to increase: (1) an increase in V_{imp} and (2) a reduction in p_a. The fact that reduction in drive pressure increases IFAR is a consequence of the larger traveled distances required to accelerate a shell to a given V_{imp} if the drive pressure is lower. Larger acceleration distances mean larger initial shell radius and higher IFAR. This is illustrated in Fig. 130.22, where initial shell dimensions are schematically shown for different drive intensities. The smallest drive intensity requires the largest initial and in-flight aspect ratios.

Increasing the implosion velocity by reducing shell mass has a lesser effect on IFAR since the latter increases only as a

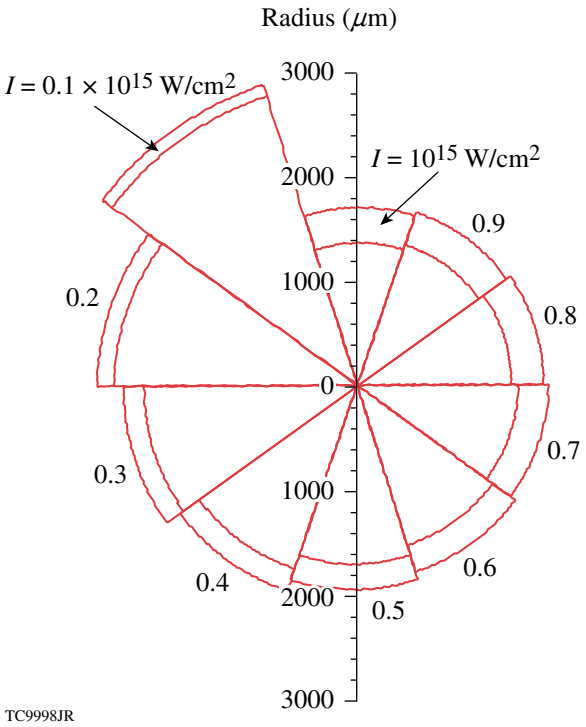

Figure 130.22
Initial shell dimensions for all-DT designs driven at indicated intensities using $E_{\text{laser}} = 1.5$ MJ.

result of larger V_{imp} [see Eq. (43)]. This approach, however, has limited beneficial effects: As the IFAR exceeds the maximum value set by the stability considerations, the target performance begins to degrade. Improving shell stability while reducing shell mass can be accomplished, according to Eq. (44), by increasing the average shell adiabat $\langle\alpha\rangle$. This must be done, however, without raising the adiabat of the unablated fuel since that is set by the condition on maximum fuel pressure at stagnation, as shown in Eq. (25). An adiabat-shaping technique[21] was proposed and implemented in the direct-drive designs to raise the adiabat only at the outer part of the shell, without degrading the adiabat at the inner part of the fuel. The designs with adiabat shaping will be discussed in **Cryogenic D_2 Implosions on the OMEGA Upgrade Laser System from 2001 Until Mid-2008**, p. 85).

Experimental Cryogenic Program on OMEGA

The experimental cryogenic program on OMEGA is designed to study fundamental physics of direct-drive ICF implosions. In particular, the following key questions are addressed:

(1) Is a low-adiabat compression of cryogenic fuel possible in a spherical implosion driven by direct laser illumination?

(2) Can cryogenic fuel be accelerated to velocities in excess of 3×10^7 cm/s in such implosions?

(3) At what drive intensities does the laser drive become inefficient in accelerating low-adiabat fuel, creating an excessive amount of fuel preheat because of suprathermal electrons, and scattering a significant fraction of the incident laser light as a result of laser–plasma interaction?

(4) Can asymmetry growth be controlled during an implosion, so

   (a) the short-scale perturbations with wavelength $\lambda \sim \Delta_{\text{in flight}}$ do not compromise shell integrity, and

   (b) hot-spot deformation is not severe enough to significantly reduce hot-spot ion temperature and quench the yield?

To answer these questions, various experimental techniques were developed and used to diagnose OMEGA implosions. Selecting a specific technique is based on measurement accuracy, which must be high enough to be able to tune the physics models and to meet the predictive accuracy goals discussed in **Sensitivity of Ignition Condition on Implosion Parameters** (p. 75). Next, we list the experimental techniques that are used to address these key questions.

1. Adiabat

The shell adiabat during an implosion can be inferred from shell density and temperature measurements. Two techniques have been developed and used on OMEGA implosions to measure these quantities: spectrally resolved x-ray scattering[22,23] and time-resolved x-ray absorption spectroscopy.[24] X-ray scattering requires large scattering volumes to keep signal-to-noise ratio at acceptable levels. This significantly limits the accuracy of measuring the adiabat at inner parts of the shells in designs with spatial adiabat gradients. The x-ray absorption technique, on the other hand, is designed to be much more local since the temperature and density are inferred by analyzing the spectral shapes of a backlighter source attenuated by a buried mid-Z tracer layer inside the shell. Hydrodynamic instabilities developed during shell implosion, however, redistribute the signature layer material throughout the shell, making temperature and density measurements dependent on the accuracy of mix models.

A significant progress in understanding how to infer the fuel adiabat in a spherical implosion was made after Ref. 21 demonstrated that the peak in areal density in an optimized implosion depends mainly on laser energy and the average adiabat of the unablated mass,

$$\max\left(\rho R\right)_{\text{optimized}} \simeq 2.6\frac{\left[E_{\text{laser}}(\text{MJ})\right]^{1/3}}{\alpha^{0.54}}. \tag{46}$$

This scaling can be understood based on the following consideration: The unablated mass at the beginning of shell deceleration can be written as

$$M \sim \rho_d \Delta_d R_d^2, \tag{47}$$

where $\Delta_d = R_d/A_d$ is the shell thickness and A_d is the shell aspect ratio at the start of shell deceleration, respectively. The mass is related to drive pressure (or shell pressure at the beginning of deceleration, p_d) using Newton's law,

$$M\frac{R_d}{t_{\text{accel}}^2} \sim p_d R_d^2 \longrightarrow M \sim p_d R_d t_{\text{accel}}^2, \tag{48}$$

where t_{accel} is defined in Eq. (33). Equating the right-hand sides of Eqs. (47) and (48) yields

$$R_d \sim t_{\text{accel}} \sqrt{\frac{p_d}{\rho_d} A_d} \sim \left(\frac{E_{\text{laser}}}{V_{\text{imp}}^2 I}\right)^{1/3} \sqrt{\frac{p_d}{\rho_d} A_d}. \tag{49}$$

At peak compression, the main contribution to areal density is given by the shock-compressed region. Therefore, rewriting Eq. (14) as

$$M_{\text{eff}} \sim (\rho\Delta)_{\text{shocked}} R^2 \sim \rho_d R_d^2 \frac{R}{R_d} \tag{50}$$

leads to

$$\max(\rho R) \sim (\rho\Delta)_{\text{shocked}} \sim \rho_d R_d \left(\frac{R_d}{R}\right). \tag{51}$$

Substituting Eqs. (49) and (13) into Eq. (51) results in

$$\max(\rho R) \sim p_d \left(\frac{\rho_d}{p_d}\right)^{5/6} \frac{E_{\text{laser}}^{1/3}}{I^{1/3}} \sqrt{A_d}. \tag{52}$$

Finally, replacing ρ_d with $\sim \left(p_{\text{a}}/\alpha\right)^{3/5}$

$$\max(\rho R) \sim \frac{p_d^{2/3}}{I^{1/3}} \sqrt{A_d} \frac{E_{\text{laser}}^{1/3}}{\sqrt{\alpha}}. \tag{53}$$

Shell aspect ratio at the start of the deceleration phase has a weak dependence on implosion parameters: For an implosion with a higher shell adiabat, the shell is thicker but the deceleration phase starts while the shell is at larger radius, so the ratio R_d/Δ_d is approximately a constant $A_d \simeq 2$ for all implosion conditions. For a well-tuned implosion when the drive pressure keeps pushing the shell up to the beginning of shell deceleration (shell coasting is minimized), $p_d \sim p_{\text{a}}$. Since $p_{\text{a}} \sim I^{2/3}$, Eq. (53) becomes

$$\max(\rho R)_{\text{optimized}} \sim I^{1/9} \sqrt{A_d} \frac{E_{\text{laser}}^{1/3}}{\sqrt{\alpha}}, \tag{54}$$

which agrees with the numerical fit shown in Eq. (46), taking into account the weak dependence of $\sqrt{A_d} I^{1/9}$ on implosion parameters. When ablation drive is terminated early and the shell starts to decompress during the coasting phase, p_d drops, reducing the maximum areal density [see Eq. (53)].

Equation (53) shows that the adiabat of an unablated mass in an implosion without a significant coasting phase can be inferred by measuring the areal density close to the shell's peak convergence. The areal density in an ICF implosion is measured using either x-ray backlighting,[25] Compton radiography,[26] or charged-particle spectrometry.[27,28] While the first two techniques are still under development, the areal density in current cryogenic experiments is inferred by measuring the spectral shapes of fusion-reaction products. Areal density in D_2 fuel is determined from energy downshift in secondary protons[27] created in D–^{3}He reactions [primary reaction creates a neutron and ^{3}He ion, D + D ⟶ n(2.45 MeV) + ^{3}He (0.82 MeV), and a secondary reaction creates an α particle and a proton, ^{3}He + D ⟶ α (6.6–1.7 MeV) + p (12.6–17.5 MeV)]. This is shown in Fig. 130.23.

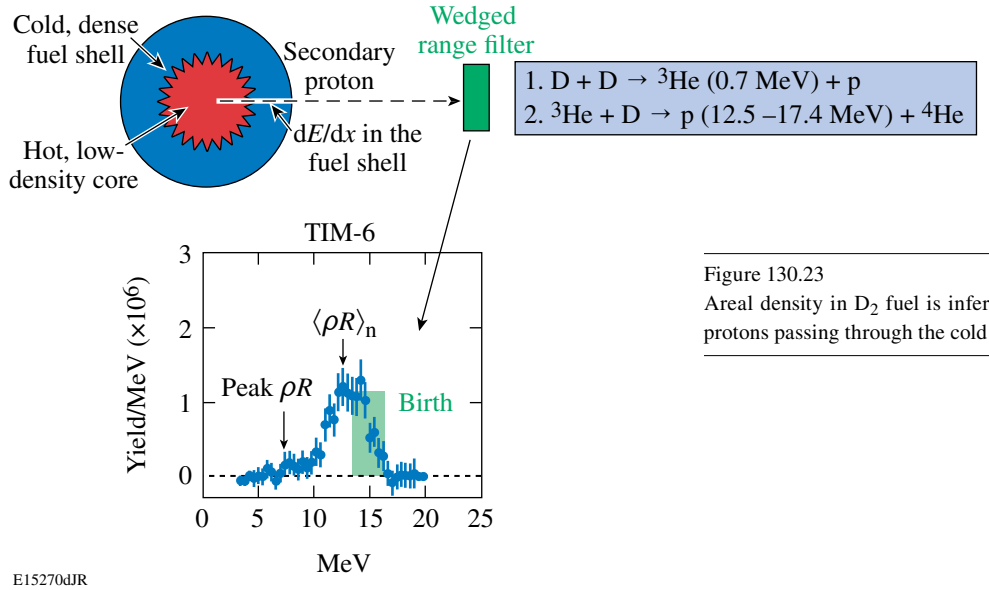

Figure 130.23
Areal density in D_2 fuel is inferred from energy attenuation of secondary protons passing through the cold shell material.

For DT fuel, the areal density is inferred by using a magnetic recoil spectrometer (see Fig. 130.24) that measures the fraction of neutrons down-scattered from fuel deuterons and tritons[28] (this fraction is directly proportional to the fuel ρR).

The main advantage to using charged-particle spectrometry to measure areal densities is that the peak in the reaction rate and peak fuel compression are not far apart (for OMEGA implosions they are separated by 20 to 30 ps with the peak in neutron production being earlier), so the reaction products sample areal density close to its peak value. The fusion rates are affected, on the other hand, by the nonuniformity growth that reduces both the fuel ion temperature and fuel "clean" volume where reactions take place. This changes timing and sampling of areal density by fusion-reaction products. The sensitivity of areal density measurement to neutron-production timing can be shown by noting that areal density evolves on a time scale $\Delta t_{\rho R} \sim 2\Delta t$, where Δt is the confinement time defined in Eq. (9). For OMEGA-scale targets this gives

$$\Delta t_{\rho R} \sim 2\frac{R}{V_{\rm imp}} \sim 2\frac{2\times 10^{-3}\ {\rm cm}}{3\times 10^{7}\ {\rm cm/s}} \simeq 130\ {\rm ps}, \qquad (55)$$

while the temporal width of neutron production in a spherically symmetric implosion is twice less,

$$\Delta t_{\rm n} \simeq \Delta t \simeq 70\ {\rm ps}. \qquad (56)$$

The areal density and neutron production histories for a typical cryogenic-DT target are shown in Fig. 130.25. Since the temporal scale of ρR evolution is short, the effect of perturbation growth on neutron-production timing and duration must be taken into account when comparing the experimentally inferred ρR values with the predictions.

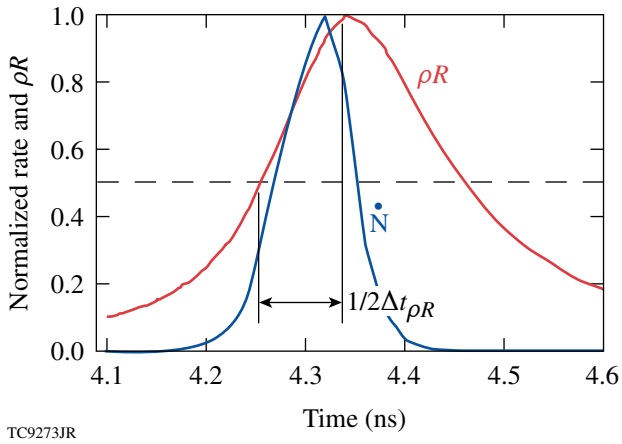

Figure 130.25
Areal density and neutron-production–rate evolution for a typical cryogenic implosion on OMEGA.

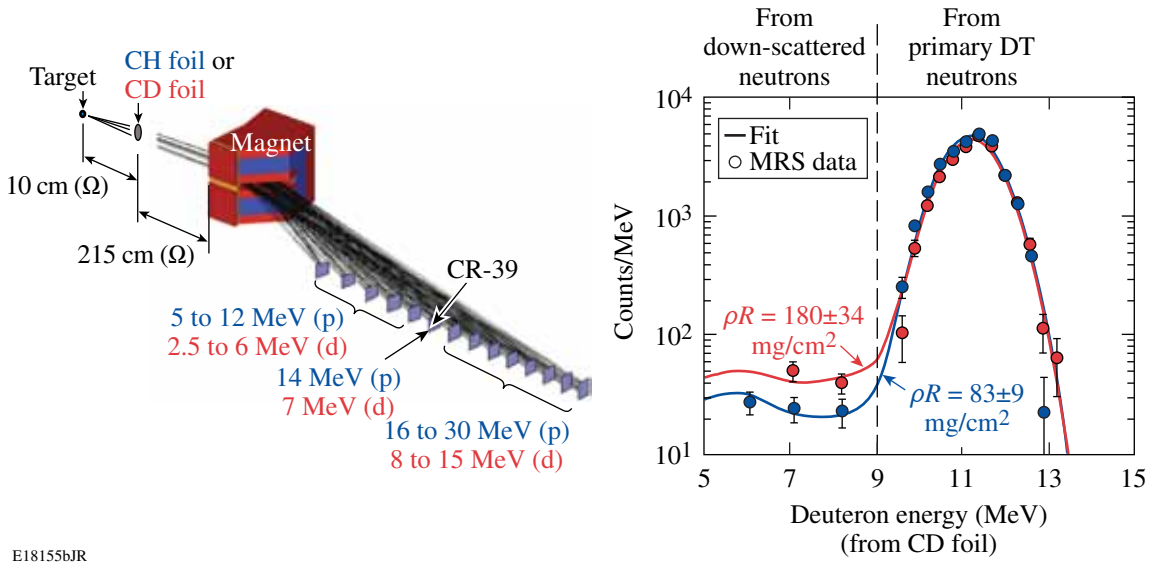

Figure 130.24
Areal density in DT fuel is inferred from measurements of the down-scattered fraction of primary neutrons produced in a D + T reaction.

2. Implosion Velocity

Implosion velocity is the key parameter that determines how much kinetic energy the fuel must acquire to ignite [see Eq. (1)]. Shell velocity can be inferred from trajectory measurements using either time-resolved x-ray–backlit images[29] of an imploding shell or time-resolved self-emission images.[25,30] The most-accurate measurement (although indirect) of hydrocoupling efficiency in implosions on OMEGA is done by measuring the onset of neutron production. Temporal history of the neutron rate is measured on OMEGA using neutron temporal diagnostics (NTD).[31] The absolute timing of NTD is calibrated to better than ±50 ps, which is equivalent to a spread in the implosion velocity of ±3.5% for OMEGA-scale targets. Figure 130.26 illustrates the sensitivity of neutron-production timing to the variation in shell velocity. Here, the shell velocity (dashed lines) and neutron rate (solid lines) histories are calculated using two different laser-deposition models. The implosion velocity predicted with the less-efficient drive (red lines) is 5% lower than that predicted for higher-efficiency drive (blue lines), resulting in a 200-ps delay in neutron production. Such a delay is easily observed in an experiment since this time difference is well outside the measurement error bar.

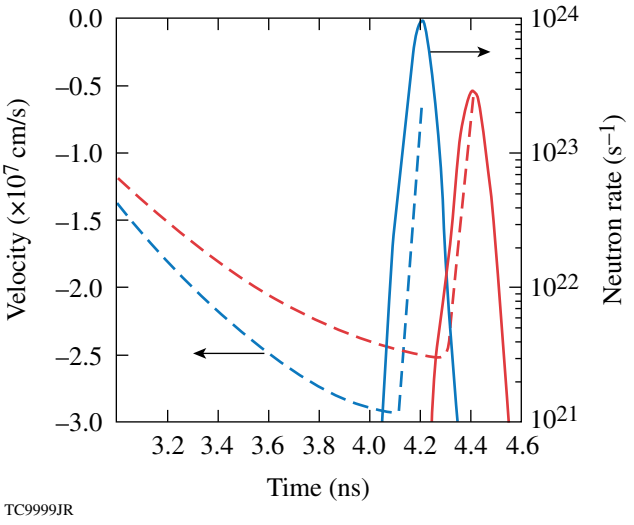

Figure 130.26
Shell velocity (left axis, dashed lines) and neutron production rates (right axis, solid lines) calculated for an OMEGA cryogenic design using two different laser-deposition models. The less-efficient laser absorption (red lines) predicts smaller shell velocity and later neutron-production timing.

3. Ion Temperature at Time of Peak Neutron Production

The fuel ion temperature at peak neutron production depends on the shell's kinetic energy during the acceleration phase of implosion and on the growth of the hot-spot distortions while the shell decelerates. The ion temperature in an implosion is inferred by measuring the temporal width of the primary-neutron signal.[32] The thermal broadening of the neutron energy distribution ΔE_{FWHM} is related to the local ion temperature T_{i} as[33]

$$\Delta E_{\mathrm{FWHM}} = 177\sqrt{T_{\mathrm{i}}}, \tag{57}$$

where both ΔE_{FWHM} and T_{i} are measured in keV. Then, measuring the neutrons' time of flight (TOF) from the target to a detector, TOF = $72.3\, L/\sqrt{E_{\mathrm{n}}}$, the neutron-averaged ion temperature is inferred relating TOF broadening Δ_{TOF} with ΔE and using Eq. (57),

$$\left\langle T_{\mathrm{i}}\right\rangle_{\mathrm{n,exp}} = 68\frac{\Delta^2_{\mathrm{TOF}}}{L^2}, \tag{58}$$

where L is the distance from detector to target in meters, E_{n} = 14.1 is the energy (in MeV) of primary neutrons in the D + T reaction, and TOF is measured in nanoseconds. Strictly speaking, the neutron spectral width is determined not only by thermal broadening, but also by gradients in the bulk fluid velocity of the reacting fuel. The latter contribution is not very important in a spherically symmetric implosion since the peak in neutron production occurs while the fuel is close to stagnation. When drive and target nonuniformities are taken into account, however, fuel flow caused by asymmetry growth can make a significant contribution to neutron spectral width. Therefore, comparing $\langle T_{\mathrm{i}}\rangle_{\mathrm{n,exp}}$ with calculations, the bulk fluid motion must be taken into account in this case. To generalize Eq. (57), including the effect of bulk motion, we start with Eq. (29) of Ref. 33 and write the neutron kinetic energy as

$$E_{\mathrm{n}} \simeq \frac{m_\alpha}{m_{\mathrm{n}}+m_\alpha}Q + \left(\mathbf{V}\cdot\mathbf{e}_{\mathrm{n}}\right)\sqrt{\frac{2m_{\mathrm{n}}m_\alpha Q}{m_{\mathrm{n}}+m_\alpha}}, \tag{59}$$

where Q is nuclear energy released in a fusion reaction (Q = 17.6 MeV for D + T reaction), m_{n} and m are masses of reaction products (neutron and alpha-particle mass, respectively, for DT), $\mathbf{V}$ is the velocity of the center of mass of reaction products, and $\mathbf{e}_{\mathrm{n}}$ is a unit vector in the direction of neutron velocity (and direction to a neutron detector). If $\mathbf{V_f}$ is the fluid velocity, then averaging over thermal motion gives

$$\left\langle E_{\mathrm{n}}\right\rangle \simeq E_0 + V_f\cos\theta_{\mathrm{n}}\sqrt{2m_{\mathrm{n}}E_0}, \tag{60}$$

where $E_0 = m_\alpha/\left(m_{\mathrm{n}}+m_\alpha\right)Q$ (E_0 = 14.1 MeV for DT), and θ_{n} is the angle between fluid flow and neutron velocity. Next, using Eq. (36) of Ref. 33, the neutron distribution at a particular location in a plasma with ion temperature T_{i} becomes

$$f_{\rm n}(E) = e^{-\left(\frac{E-E_0}{\Delta E} - M_a \cos\theta_{\rm n}\right)^2}, \quad \Delta E = 2\sqrt{\frac{m_{\rm n} T_{\rm i} E_0}{m_{\rm n} + m_\alpha}}, \qquad (61)$$

where $M_a = V_f / c_s$ is the flow Mach number $c_s = \sqrt{T_{\rm i}/m_{\rm i}}$ is the ion sound speed, and $m_{\rm i} = \left(m_{\rm n} + m_\alpha\right)/2$ is the average fuel ion mass. According to Eq. (61), a fluid velocity, uniform in the direction of the neutron detector, affects only the position in the peak of the distribution function, but not its width. Averaging the distribution function over the fuel volume gives

$$\left\langle f_{\rm n}(E)\right\rangle_V = \frac{\int {\rm d}V n^2 \left\langle\sigma v\right\rangle e^{-\left[\alpha(E) - M_a \mu\right]^2}}{\int {\rm d}V n^2 \left\langle\sigma v\right\rangle}, \qquad (62)$$

where $\mu = \cos\theta$, $\left\langle\sigma v\right\rangle$ is reaction cross section, n is ion density, $\alpha(E) = \left(E - E_0\right)/\Delta E$. Taking the integral over the angles assuming spherical symmetry in Eq. (62) yields

$$\left\langle f_{\rm n}(E)\right\rangle_V =$$

$$\sqrt{\pi}\,\frac{\int_0^R {\rm d}r r^2 n^2 \left\langle\sigma v\right\rangle \left\{{\rm erf}\left[\alpha(E) + M_a\right] - {\rm erf}\left[\alpha(E) - M_a\right]\right\}}{4 M_a \int_0^R {\rm d}r r^2 n^2 \left\langle\sigma v\right\rangle}, \qquad (63)$$

where erf is the error function. Integrating Eq. (63) over the neutron-production time and fitting the result with a Gaussian with FWHM = $\Delta E_{\rm fit}$,

$$\int {\rm d}t \left\langle f_{\rm n}(E)\right\rangle_V \xrightarrow{\rm fit} \exp\left[-4\ln 2\left(\frac{E-E_0}{\Delta E_{\rm fit}}\right)^2\right],$$

defines an effective temperature $\left\langle T_{\rm i}\right\rangle_{\rm n,fit} = \left(\Delta E_{\rm fit}/177\right)^2$ to be compared with the measurements [see Eq. (58)]. A bulk flow with velocity distribution not pointing in the same direction broadens the neutron spectrum, leading to a higher effective ion temperature. This is illustrated by evaluating the angular integral in Eq. (62), assuming $M_a \ll 1$ and spherical symmetry,

$$\frac{1}{2}\int_{-1}^{1} {\rm d}\mu e^{-\alpha^2 + 2\alpha M_a \mu} \simeq \frac{e^{-\alpha^2}}{2}\int_{-1}^{1} d\mu \left[1 + 2\left(\alpha M_a\right)^2 \mu^2\right]$$

$$\simeq e^{-\alpha^2}\Big/\left(1 + 2M_a^2/3\right). \qquad (64)$$

Equation (64) gives

$$\left\langle T_{\rm i}\right\rangle_{\rm fit} = T_{\rm i}\left(1 + \frac{2}{3}M_a^2\right) = T_{\rm i} + \frac{2}{3} m_{\rm i} V_f^2.$$

For a spherically symmetric flow, $\left\langle T_{\rm i}\right\rangle_{\rm fit}$ tracks $T_{\rm i}$ within a few percent since the fuel is close to stagnation at the neutron-production time. When significant asymmetries are present, bulk flow can lead to a significant contribution to $\left\langle T_{\rm i}\right\rangle_{\rm fit}$, making an inferred ion temperature larger than the actual thermodynamic value.

Early Experiments on the OMEGA-24 Laser

The first experiments with layered DT targets were performed on the OMEGA-24 Laser System[34] in the late 1980s (Refs. 35 and 36). The targets were spherical 3- to 5-μm-thick glass shells with outer radii of 100 to 150 μm. The cryogenic, 5- to 10-μm-thick solid DT layers were produced using a fast-freeze technique.[37] These targets were driven with 1 to 1.2 kJ of UV energy delivered with 650-ps Gaussian pulses (with a peak in drive intensity of up to 6×10^{14} W/cm^2). The target and drive pulse are shown in Fig. 130.27(a). The predicted convergence ratios in these implosions were relatively high, $C_r \sim 20$ (C_r is defined as the ratio of the initial to the minimum radius of the fuel–glass interface) with a peak DT density of ~300 g/cm^3 and a peak fuel areal density of 150 mg/cm^2. For comparison, the all-DT ignition design described in **All-DT, Direct-Drive, NIF-Scale Ignition Target Design** (p. 76) has $C_r = 27$. Targets were held inside the U-shaped cradle using three to five spider silks. These early designs were highly susceptible to the RT instability since the peak of the in-flight aspect ratio (IFAR) approached 70, a much higher value than currently considered to be acceptable for a robust design, IFAR < 40 (see **Target In-Flight Aspect Ratio**, p. 79). The areal densities in these experiments were directly measured (the first such measurement performed in an ICF implosion at that time) by counting the down-scattered fraction of deuterium and tritium atoms.[38] Even though the inferred fuel areal density and mass density were the highest measured to date, they were lower than predictions by 40% to 60%. Figure 130.27(b) plots the predicted value of fuel areal density using the 1-D hydrocode *LILAC*[39] and inferred areal densities using knock-on statistics. A significant deviation in the predicted value has occurred for an effective fuel adiabat $\alpha < 4$. This is not surprising considering the high IFAR of these shells. If perturbation growth causes a shell to break up during acceleration, it creates a low-density precursor ahead of the imploding shell, which causes the shell to stagnate at a larger radius with a smaller peak areal density.

Cryogenic D_2 Implosions on the OMEGA Upgrade Laser System from 2001 Until Mid-2008

The fast-freezing technique employed to make cryogenic targets on OMEGA-24 could not be used to produce thicker fuel layers required for ignition-relevant OMEGA-scaled designs.

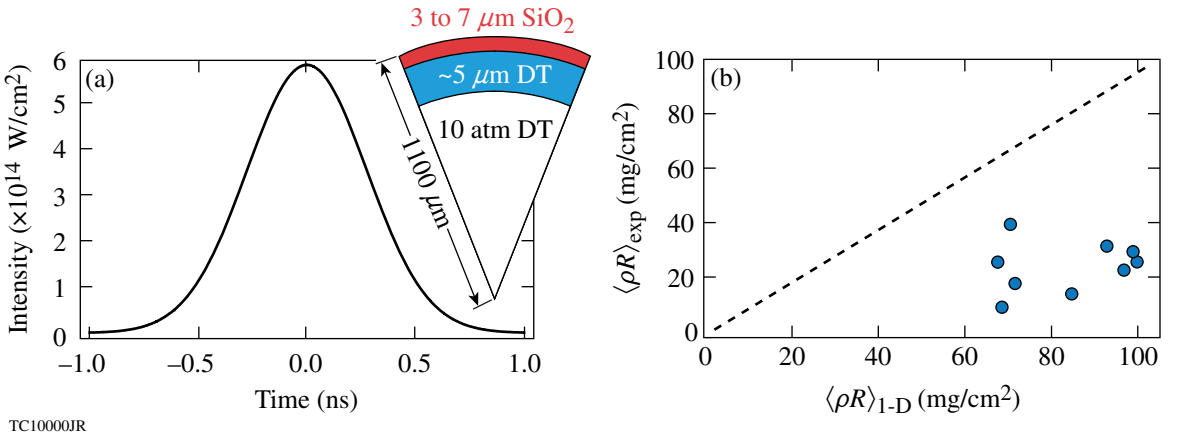

Figure 130.27
(a) Pulse shape and target and (b) predicted and inferred fuel areal densities for cryogenic implosions on the OMEGA-24 Laser System.

Novel techniques for producing smooth DT and D_2 layers were introduced in the 1980s and 1990s. A "β-layering" was demonstrated to make uniform solid DT layers,[40] and IR radiation was shown to produce layer smoothing in cryogenic D_2 fuel by exciting the vibration–rotation band.[41] The newly developed cryogenic system[42] on the OMEGA Upgrade (30 kJ of UV energy, 60-beam system)[43] employed both these techniques for cryogenic target production. Cryogenic experiments on the new system started in 2000 by imploding D_2 targets.[44] DT was introduced in February 2006, after completion of an extensive system readiness review associated with the radiological impact of using tritium.[45] Since target production was on a learning path to improving D_2-layer quality, the first implosions used a square laser drive pulse with laser energy ~23 kJ to set the cryogenic fuel on a high adiabat $\alpha \sim 25$ (see green dashed line in Fig. 130.28). The acceleration phase in this design was very short so the impact of the RT growth on target performance was minimal. The yields, areal densities (30 to 60 mg/cm^2), and timing of neutron production were consistent with 1-D and 2-D hydrocode simulations.[44,46]

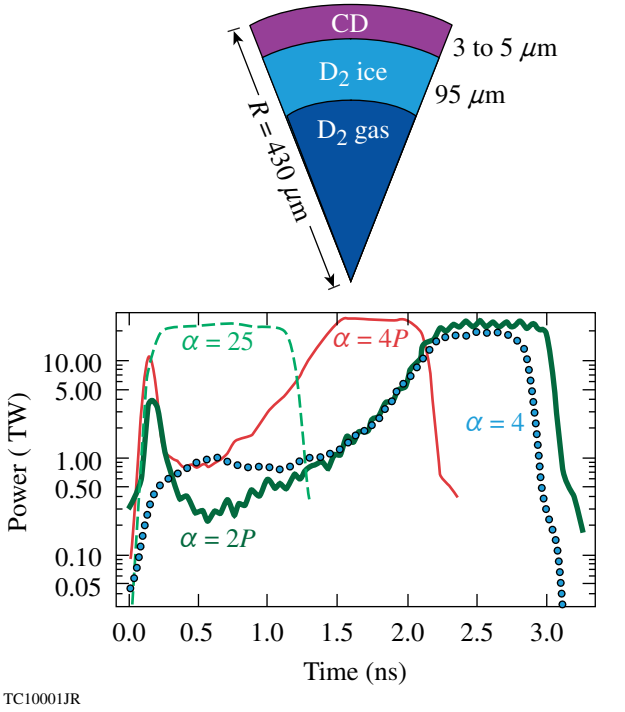

Figure 130.28
Pulse shapes and target for $\alpha = 25$ (dashed), $\alpha = 4$ (red solid and blue dotted lines), and $\alpha = 2$ (thick green line) designs on OMEGA. The designs with the decaying-shock adiabat shaping are shown with solid lines.

As the uniformity of ice layers dramatically improved from σ_{rms} = 9 to 15 μm down to 1 to 3 μm in 2002, experiments began using designs that approached the OMEGA-scaled version of the all-DT ignition designs.[47] These were 3- to 5-μm-thick CD shells overcoated over 95- to 100-μm-thick D_2 ice layers driven at $I \sim 10^{15}$ W/cm^2 on $\alpha = 4$ adiabat (see dotted line in Fig. 130.28). These shells were somewhat thicker than required for hydrodynamic scaling (<1 μm) since fill time was shorter and overall long-wavelength shell nonuniformities were smaller. By the middle of 2005, a large data set of these implosions was built sufficient to conclude that the measured areal densities were significantly lower than predicted, as shown with solid circles in Fig. 130.29. For the lowest adiabat (highest ρR) in this series, degradation in areal density was up to 50%, which is equivalent to adiabat degradation [according to Eq. (46)], by up to 70%! The 2-D calculations using the hydrocode *DRACO*[48] and results of the stability postproces-

sor[49] indicated that the shells in the low-adiabat implosions were sufficiently stable (the ratio of the mix width to the shell thickness did not exceed 50%, where the short-scale mix at the ablation front, seeded mainly by laser imprint, was amplified by the RT instability). Measurements of the imprint efficiencies made earlier on planar targets,[50] however, suggested that calculations could be underestimating imprint amplitude as much as by a factor of 2, and the shell in low-adiabat implosions could be broken by the imprint growth. Since shell stability was a main concern at that time, LLE was working on perturbation growth mitigation strategies. A novel technique for reducing the RT growth was proposed in 2002. The idea was to shape the adiabat through the shell (adiabat-shaping designs[20]). This can be accomplished either by launching a shock wave of decaying strength [decaying-shock (DS) design] through the shell[20] or by relaxing the shell material with a short-duration picket and recompressing it later with the shaped main pulse [adiabat shaping by relaxation (RX) design].[51] This sets the outer part of the ablator on a higher adiabat, keeping the inner part of the shell on a lower adiabat. The higher adiabat at the ablation front increases the ablation velocity, mitigating the impact of the RT instability on target performance, as described in **Rayleigh–Taylor Instability**, p. 77.

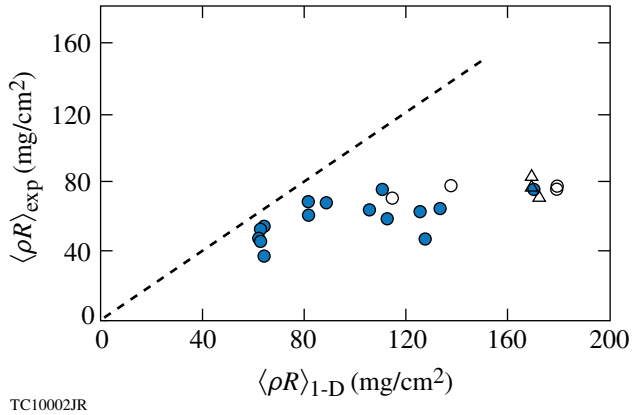

Figure 130.29
Measured and predicted areal densities for cryogenic-D_2 implosions using the $\alpha = 4$ pulses shown in Fig. 130.28 (solid circles) and $\alpha = 4P$ (open circles).

Pulse shapes, similar to ones shown in Fig. 130.28 with thin and thick solid lines, were used to implement adiabat-shaping designs on OMEGA. Calculations predicted a significant improvement in shell stability in designs with adiabat shaping in comparison with the original flat-foot designs (see Fig. 130.30). The experiments, however, did not show any significant improvement in measured areal densities, which continued to saturate at ~80 mg/cm^2. These are shown as open circles in Fig. 130.29. To further support the conclusion that the short-scale mix caused by the RT growth at the ablation front was not the main contributor to the observed ρR degradation, a series of implosions were performed with an enhanced laser-imprint level by turning off the smoothing by spectral dispersion (SSD).[52] The target yield dropped by a factor of 2 in these implosions, but the areal density remained unchanged (see open triangles in Fig. 130.29).

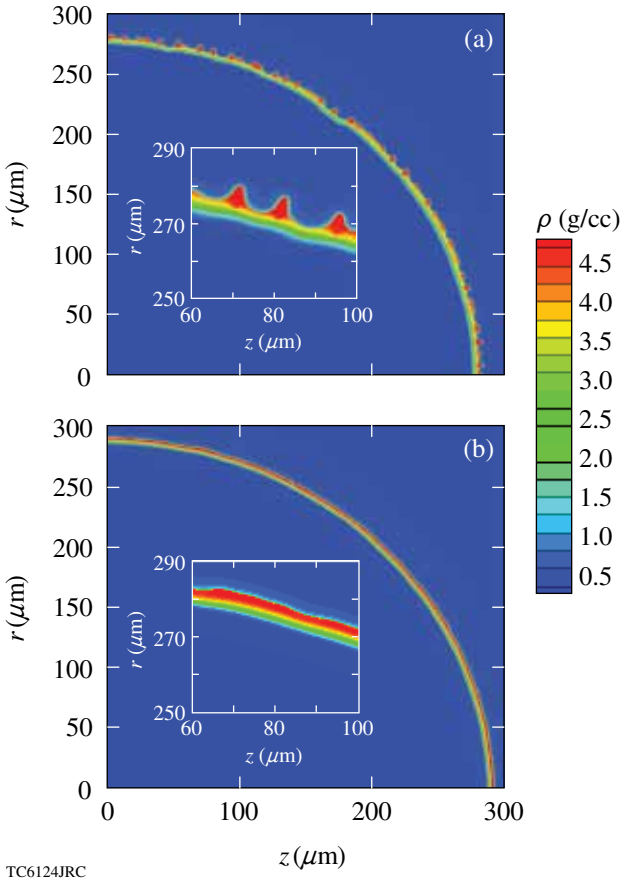

Figure 130.30
In-flight shell density contours in designs (a) without and (b) with adiabat shaping.

Since the source of excessive shell heating, not accounted for in a hydrosimulation, was unknown at the time, several scenarios explaining the areal-density deficiency were considered: Excessive shell heating could have been due to (1) suprathermal electrons with $T_{hot} > 40$ keV, (2) radiation, or (3) shock waves. Next, we describe how each of these possibilities were addressed in OMEGA experiments.

1. Suprathermal Electrons

Suprathermal electrons are always present in a plasma because of high-energy tails in the electron distribution function. In addition, laser–plasma interaction processes, such as

two-plasmon-decay (TPD) instability and stimulated Raman scattering (SRS),[53] can generate electrons with energies above 20 keV. These electrons can penetrate the ablator and fuel in OMEGA designs and deposit their energy close to the inner part of the fuel, degrading peak ρR. The electrons in the energetic tails of the distribution function will be addressed first.

a. Electron distribution tails and nonlocal thermal transport. To model electron thermal transport in ICF experiments, a flux-limited model[54] is conventionally used in hydrocode simulations. Thermal conduction in such a model is calculated using the Spitzer expression[55] q_{sp}, which is derived assuming that the electron mean free path is much shorter than the gradient scale-length of hydrodynamic variables.[56] In a narrow region, near the peak of the laser deposition, the temperature profile is steep enough to break the validity condition of the Spitzer formula. The heat flux in this case is calculated as a fraction $f < 1$ of the free-stream conduction $q_{fs} = nTv_T$, where n and T are electron density and temperature, respectively, $v_T = \sqrt{T/m}$ is the electron thermal velocity, and m is electron mass. The limiting factor f is referred to as "flux limiter." The flux-limiter value of $f = 0.06$ is typically used to simulate direct-drive experiments.

Although it was successfully applied to simulate many experimental observables,[57] the flux-limited thermal transport model neglects the effect of finite electron-stopping ranges and cannot be used to access the amount of shell preheat from the energetic electrons in plasma. To account for this effect, a simplified thermal transport model was developed and implemented in the 1-D hydrocode *LILAC*. The model used the Krook-type approximation[58] to the collisional operator to solve the Boltzmann equation without making the high collisionality approximation used in the "classical" Chapman–Enskog method.[56] The modified energy-dependent Krook-type operator[57] conserves particles and energy by renormalizing local electron density and electron temperature (which depend on gradients in hydrodynamic profiles) in the symmetric part of the distribution function (Maxwellian modified to include effects of the laser electric field[59]). When applied to the OMEGA experimental data, the nonlocal model showed no significant inner fuel preheat caused by the energetic electrons in the distribution tail (see Fig. 130.31). These electrons, instead, preheated the ablation front region [see how electron temperature in the calculation using the nonlocal model (thick dashed line in Fig. 130.31) increases toward the ablation front], leading to a greater ablative stabilization of the RT growth. This preheat of the outer region of the shell can explain very little sensitivity of the measured ρR to variation in the source of short-scale perturbations described earlier in this section. Ablation-front preheating from the nonlocal electrons is also consistent with the short-wavelength stabilization of the RT growth observed in experiments with accelerated planar foils.[60]

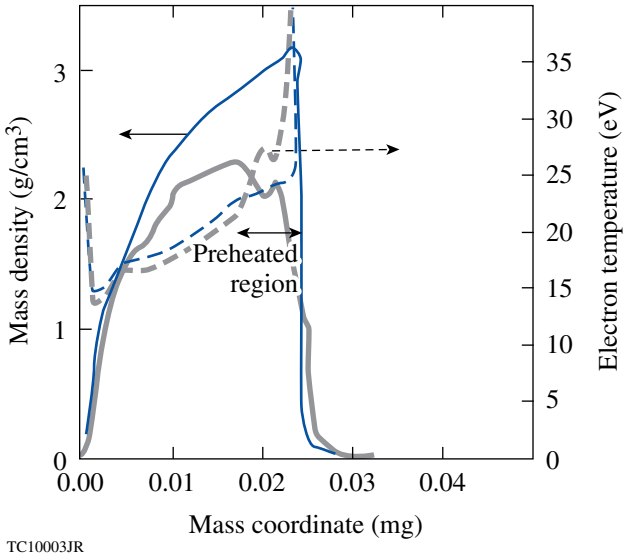

Figure 130.31
In-flight shell density (solid lines) and electron temperature (dashed) with (thin lines) and without (thick lines) nonlocal effects in electron thermal conduction.

In addition to the ablation region preheating, the strength of the first shock and a compression wave were significantly modified in calculations using the nonlocal electron-transport model.[57] At the beginning of the laser drive, where the hydrodynamic scale lengths are short, the shock strength predicted using the nonlocal model was larger compared to the results of the flux-limited model. This effectively led to shock mistiming and an adiabat degradation prior to the shell acceleration. Experimental validation of the nonlocal model predictions by direct shock-velocity measurement in spherical geometry was not available at that time (the experimental platform was developed in 2008). The existing shock-velocity data in planar geometry, on the other hand, were not very sensitive to differences in predictions using the nonlocal and flux-limited models.[57] Measurements of early-time perturbation evolution (ablative Richtmyer–Meshkov instability[61]), however, clearly indicated that the higher heat fluxes, predicted by the nonlocal model at the beginning of the pulse, are consistent with the observations.[62] In addition, the absorption measurements of Gaussian pulses with FWHM of 200 ps and peak laser intensity varied from 5×10^{13} to 1.2×10^{15} W/cm^2 (Ref. 63) were in much closer agreement with the results of the nonlocal heat-transfer model. These are shown in Fig. 130.32. In addition to the inverse bremsstrahlung, the resonance absorption[53] resulting from tunneling of the laser electric field from the

turning point to the critical surface and exciting plasma waves was included in these simulations.[57,64] The resonant absorption effects were important only early in the pulse when the density scale length is short.

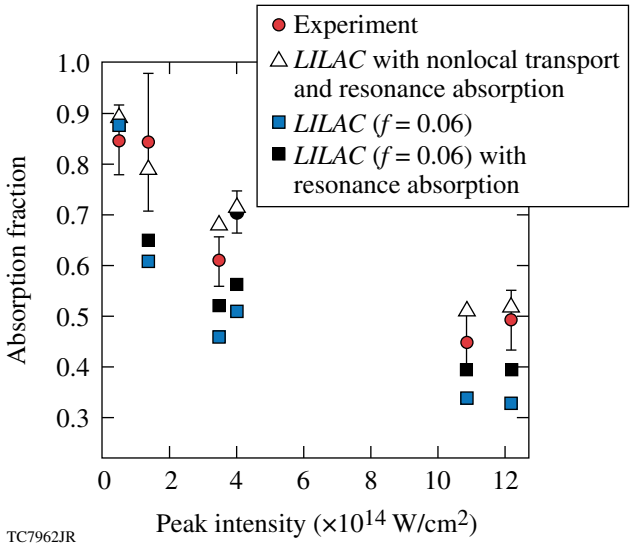

Figure 130.32
Absorption fraction of the incident laser energy for a 20-μm-thick CH shell driven by a 200-ps Gaussian pulse at different peak intensities.

When the nonlocal model was used, the calculated areal densities were in closer agreement with the data compared to the results of the flux-limited model (see Fig. 130.33). Nevertheless, some discrepancies in ρR, especially for implosions with the lowest adiabat, still remained.

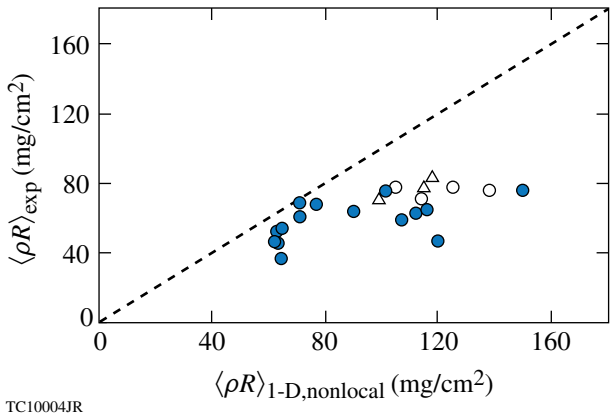

Figure 130.33
Same as in Fig. 130.29, except these calculations were performed using the nonlocal thermal transport model.

The next step in the cryogenic campaign was to redesign the drive pulse design, taking into account modified coupling efficiency early in the pulse, as predicted by the new thermal transport model. Both the RX and DS designs driven at peak intensities of ~6×10^{14} W/cm^2 were used in this "retuning" campaign. The experimental ρR values have marginally improved from 80 up to 100 mg/cm^2 (looking at this result with the knowledge that we have now, this 20% increase in areal density was mainly due to a reduction in peak intensity from 9 to 6×10^{14} W/cm^2, which also reduced the strength of secondary hydrodynamic waves launched by the pulse) but fell short of predicted values that were in the range of 150 to 170 mg/cm^2. Even though this campaign did not succeed in significantly increasing areal densities, it revealed a very interesting trend: the measured areal densities showed very strong dependence on CD shell thickness. These results are plotted in Fig. 130.34. Such a dependence was not predicted in hydrocode simulations. Among the hypotheses explaining

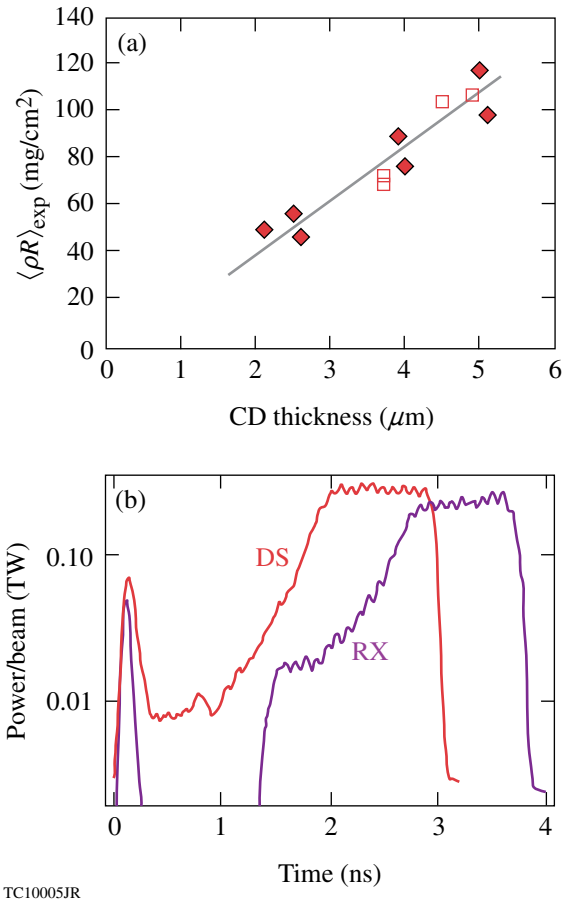

Figure 130.34
(a) Measured areal densities as a function of CD shell thickness and (b) pulse shapes used in this series. DS: decaying shock; RX: relaxation.

this trend are radiation preheat caused by mix at the CD–D_2 interface (as discussed in **Radiation Preheat**, p. 91), increased preheat as a result of suprathermal electron generation by the TPD instability, or short-scale magnetic-field generation at the CH–D_2 interface as the latter travels through the ablation front and conduction zone. None of these hypotheses, however, could account for a factor-of-2.5 reduction in areal density when the CD thickness decreased from 5 to 2.5 μm. The true explanation of this observation is still not found.

b. Suprathermal electrons generated by two-plasmon-decay (TPD) instability. In parallel to the study of the effect of nonlocal thermal transport on implosion performance, a different cryogenic design was proposed and used on OMEGA experiments to address a possible preheat issue caused by the suprathermal electrons created by the TPD instability. The threshold factor for the absolute TPD instability[65] is

$$\eta = \frac{I_{14} L_n(\mu\text{m})}{230\, T_{\text{keV}}}. \tag{65}$$

It exceeds unity in direct-drive implosions on OMEGA when drive intensities are above $\sim 3 \times 10^{14}$ W/cm^2. Here, I_{14} is the laser intensity at quarter-critical surface in units of 10^{14} W/cm^2, L_n is the electron-density scale length in microns, and T is the electron temperature in keV. At these intensities, hard x-ray bremsstrahlung radiation, emitted by suprathermal electrons as they slow down in the plasma, is observed in OMEGA implosions[66] (see dotted line in Fig. 130.35). To prove that the preheat signal has its origin in the TPD instability, the measured hard x-ray signal must correlate with 3/2ω and ω/2 emission.[63] An example of such a correlation in a cryogenic implosion with a 5-μm CD shell is shown in Fig. 130.35. Here, an ω/2 signal is shown with a thick green solid line. Both signals are observed when the calculated threshold parameter (shown by the dashed line marked "Threshold η") exceeds unity. The scale length for OMEGA spherical implosions, $L_n \simeq 150$ μm, is set by the target size. Therefore, the main parameter that controls the TPD instability in an experiment is the laser intensity. Since the hard x-ray emission increases with laser intensity,[66] as plotted in Fig. 130.36, a "low-intensity" series of cryogenic implosions were designed with peak laser intensity reduced to below 3×10^{14} W/cm^2. Lowering drive intensity eliminates a possibility of fuel preheating caused by the suprathermal electrons.[67] The first results of this campaign, shown in Fig. 130.37(a) by three solid circles, were very encouraging: for the first time the areal density measured in a low-adiabat ($\alpha \sim 3$) cryogenic implosion agreed with the simulation result! This initial success in the ability to accurately predict fuel compression in a cryogenic implosion, however, was short lived. With the goal of increasing areal density in a low-drive design, the first picket energy was reduced and the intensity foot was reduced and extended in time [see dashed line in Fig. 130.37(b)]. The measurements, however, showed no areal density increase predicted in simulations [see open circles in Fig. 130.37(a)]. Instead, the data followed the same trend observed in higher-intensity

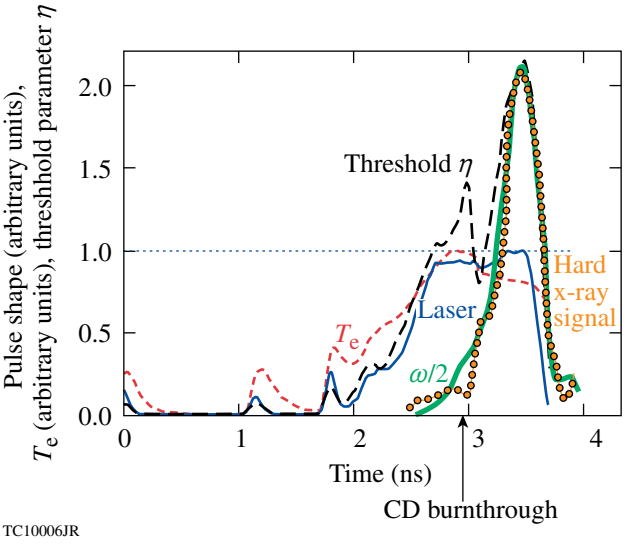

Figure 130.35
Laser pulse shape (thin solid line), electron temperature at quarter-critical surface (short-dashed line), TPD instability threshold factor (long-dashed line), measured hard x-ray signal (dotted line), and measured ω/2 signal (green solid line) for a cryogenic implosion with a 5-μm-thick CD shell.

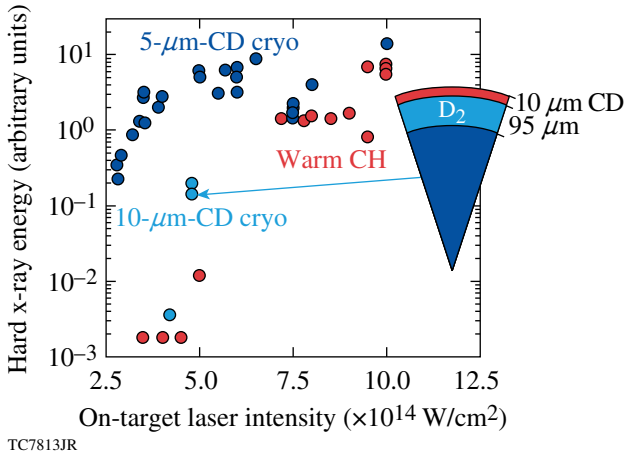

Figure 130.36
Measured energy of hard x rays (above 40 keV) as a function of incident laser intensity for a variety of OMEGA implosions.

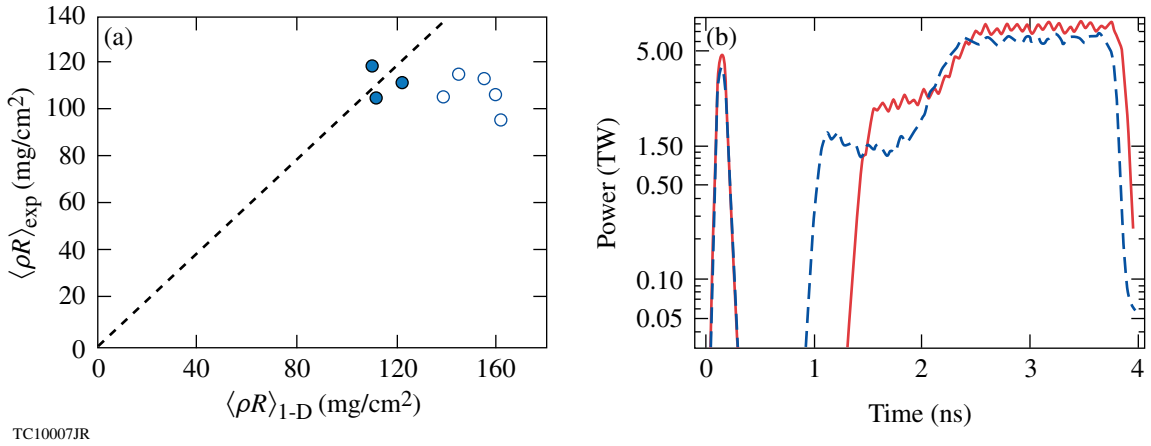

Figure 130.37
(a) Measured and (b) predicted areal densities for low-intensity RX drive pulses. Solid symbols correspond to the design shown with the solid red line in (b). The open symbols correspond to the lower-adiabat design shown with the dashed line in (b).

implosions: areal density saturated at a value independent of the predicted adiabat.

Additional evidence supporting the conclusion that the suprathermal electrons alone cannot explain the areal density degradation (as shown in Fig. 130.33) was obtained using a "dropping-intensity" design, where the drive intensity was reduced from its peak value of 5×10^{14} down to 3×10^{14} W/cm^2 starting from the time of onset of the suprathermal electron generation. This design and its comparison with the original flat-top design are shown in Fig. 130.38. While the suprathermal electron preheat signal was substantially reduced, the dropping-intensity design has also failed to achieve areal densities above the saturation value of 80 to 100 mg/cm^2.

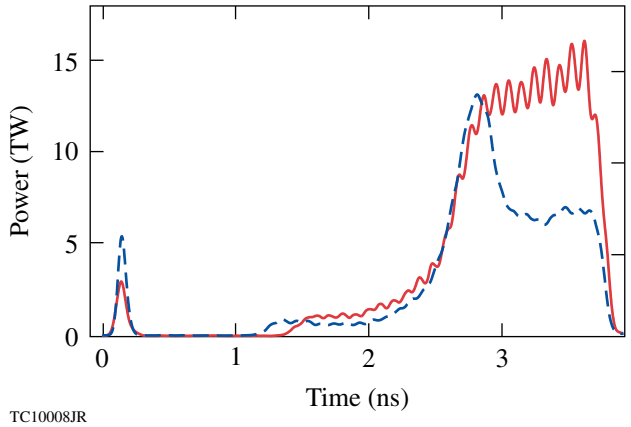

Figure 130.38
The original (solid red line) and modified (dashed line) design to reduce suprathermal electron production.

c. Radiation preheat. In addressing the second scenario for ρR degradation, excessive radiation preheating of the main fuel, the radiation x-ray power from plasma corona was measured using Dante.[68] Figure 130.39(a) shows the total radiated x-ray power as a function of time for cryogenic implosion with a 5-μm-thick CD shell. The result of a *LILAC* simulation is also plotted. The measured radiation power starts to deviate from the predictions at 3 ns. An x-ray radiation spectrum, plotted in Figs. 130.39(b) and 130.39(c), also shows agreement with calculations early in the pulse. The spectrum deviates from calculations at t = 3.48 ns in the energy range from 100 eV to 1 keV. The plastic shell is totally ablated by that time, and the CD–D_2 interface starts to move into the plasma corona. Radiation in the hydrocode calculation diminishes at this time because a higher-Z carbon is replaced by a lower-Z hydrogen in the x-ray–emitting region. Experimental data, on the other hand, showed a persistent signal after the burnthrough time. One plausible explanation of this effect is the mix of carbon and hydrogen at the CD–D_2 interface. This would cause carbon to stay longer at the higher-density region and significantly enhance the radiated x-ray power. An estimated 200 J was irradiated from the plasma corona in this experiment in excess of hydrocode predictions. Based on these observations, a new target design was proposed for cryogenic implosions on OMEGA.

d. Thick plastic cryogenic designs. Observations of an enhanced x-ray emission showed that increasing the CD shell thickness from 5 to 10 μm is beneficial. The thicker shell is predicted to ablate just at the end of the pulse, protecting the fuel layer from any excessive radiation in the corona. Thicker plastic ablators also increase the threshold factor of the TPD instabil-

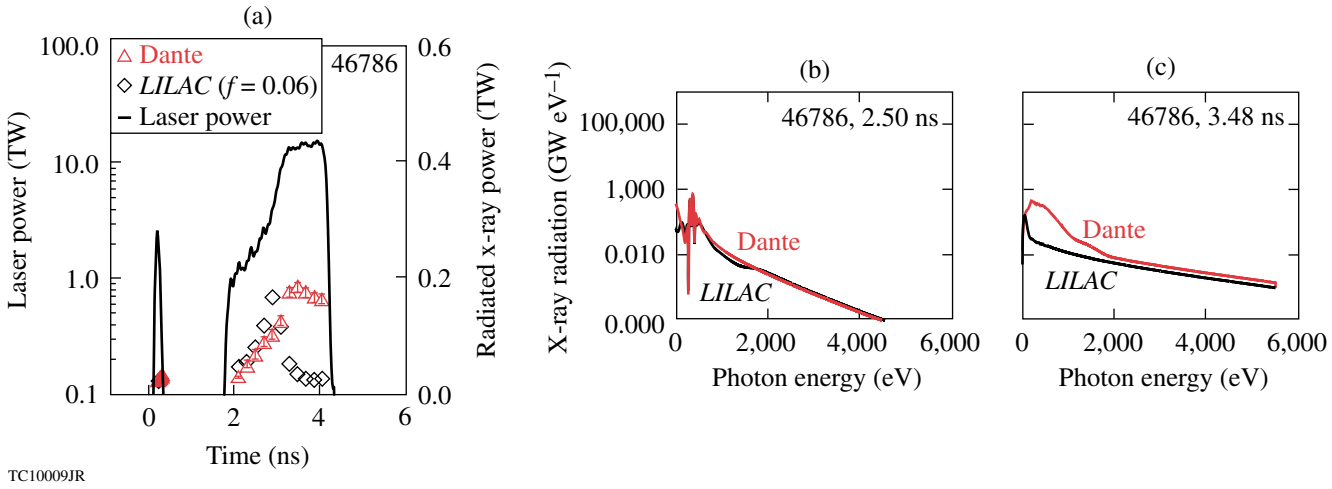

Figure 130.39
(a) Total radiated x-ray power and pulse shape and (b) x-ray radiation spectrum as measured using Dante at t = 2.5 ns and (c) t = 3.48 ns.

ity later in the pulse by raising the temperature in the plasma corona. Such a temperature increase is caused by a larger laser absorption fraction caused by the presence of higher-Z carbon in the absorption region. A higher absorption fraction farther away in the corona also reduces irradiation intensity that reaches a quarter-critical surface. Both these effects lead to a reduction in η [see Eq. (65)]. The cryogenic design with a 10-μm-thick CD ablator driven at $\sim 5 \times 10^{14}$ W/cm^2 is shown in Fig. 130.40. Four shots with this design produced areal densities 200 mg/cm^2, matching code predictions.[57,69] Figure 130.41 shows predicted and measured spectra of down-scattered secondary protons, confirming prediction accuracy. The areal densities and fuel compression in these implosions were the highest ever achieved in an ICF implosion. As expected, both the hard x-ray signal (see points marked "10-μm-CD cryo" in Fig. 130.36) and x-ray energy below 1 keV, emitted in excess to the predicted value, were significantly reduced in these experiments.

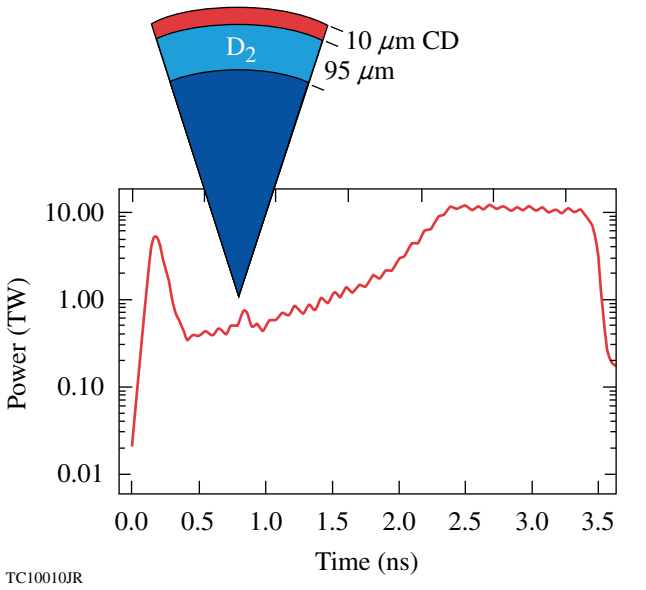

Figure 130.40
Pulse shape and target dimensions for the thick plastic cryogenic design.

Even though the designs with a thicker ablator demonstrated high compression, the drive intensity and implosion velocity $V_{imp} \sim 2.2 \times 10^7$ cm/s were smaller than required for a robust direct-drive–ignition design, $I \sim 8 \times 10^{14}$ W/cm^2 and $V_{imp} > 3.5 \times 10^7$ cm/s, respectively (see **A Simple Ignition Model**, p. 72). The next step was to increase both the drive intensity and the implosion velocity (by reducing the shell mass). This turned out to be a very challenging task. Figure 130.42(a) shows modifications made to the pulse shape in an attempt to increase the drive intensity. Raising the intensity also increases the electron preheat signal. Figure 130.42(b) shows measured areal densities as a function of the preheat signal (solid symbols). The measured areal density decreased dramatically even for minor variations in the laser pulse with very little or no sensitivity to the preheat signal. Reducing the thickness of the frozen D_2 layer from 95 to 80 μm also resulted in a decreased measured areal density (the predictions were ~200 mg/cm^2 for all cases). This is shown with open symbols in Fig. 130.42(b) . These results demonstrated that the continuous-pulse designs cannot be easily extended to the ignition-relevant drive intensities and implosion velocities.

e. Shock heating. The breakthrough in understanding cryogenic target performance came in 2008 when the shock-velocity

measurement technique matured enough to give information on the formation of shock and compression waves in spherical geometry.[70] These measurements addressed the third scenario for explaining areal-density degradation—excessive shock heating. Accuracy of shock timing was verified by measuring the velocity of the leading shock wave using the velocity interferometry system for any reflector (VISAR).[71] The targets in these experiments were spherical, 5- or 10-μm-thick CD shells fitted with a diagnostic cone. The shell and cone were filled with liquid deuterium. An example of VISAR measurement performed using the continuous pulse design is shown in Fig. 130.43. The measured shock velocity, as a function of

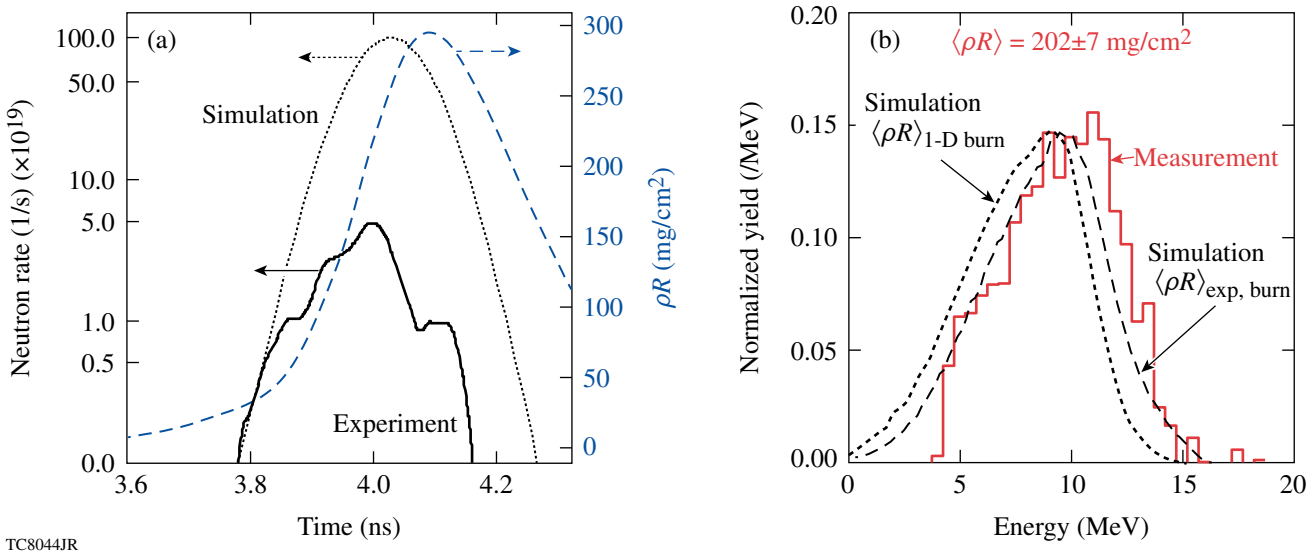

Figure 130.41
(a) The neutron-production history measured (solid line) and predicted (dotted line) for the design shown in Fig. 130.40. The ρR evolution calculated using the 1-D code *LILAC* (dashed line, right axis) is also shown. (b) Measured secondary-proton spectrum (solid line). The dotted line shows the calculated spectrum averaged over the predicted 1-D neutron production, and the dashed line represents the calculated spectrum averaged over the experimental neutron-production history.

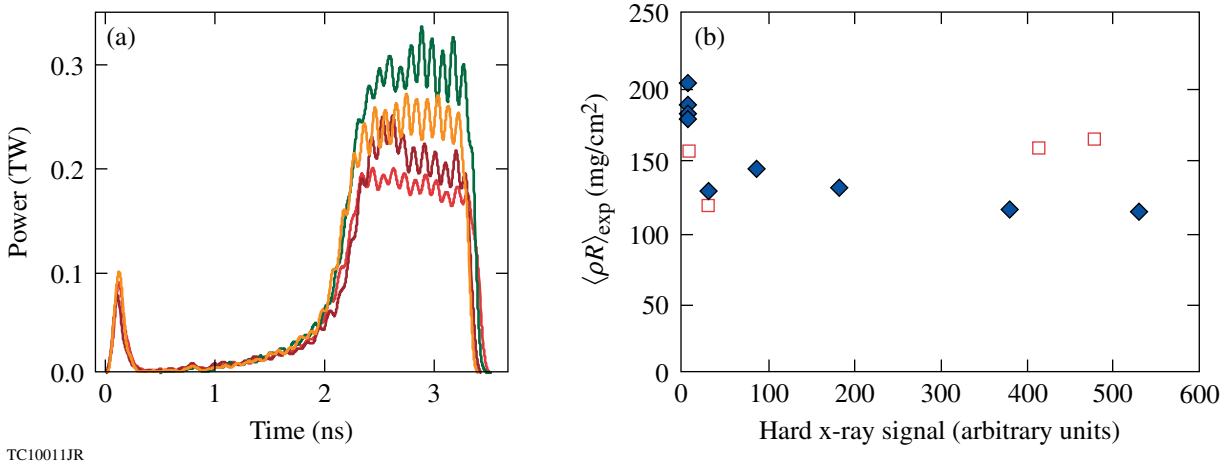

Figure 130.42
(a) Variation to the target design shown in Fig. 130.40 and (b) resulting measured areal densities for designs with 95-μm (solid symbols) and 80-μm (open symbols) D_2 ice thickness.

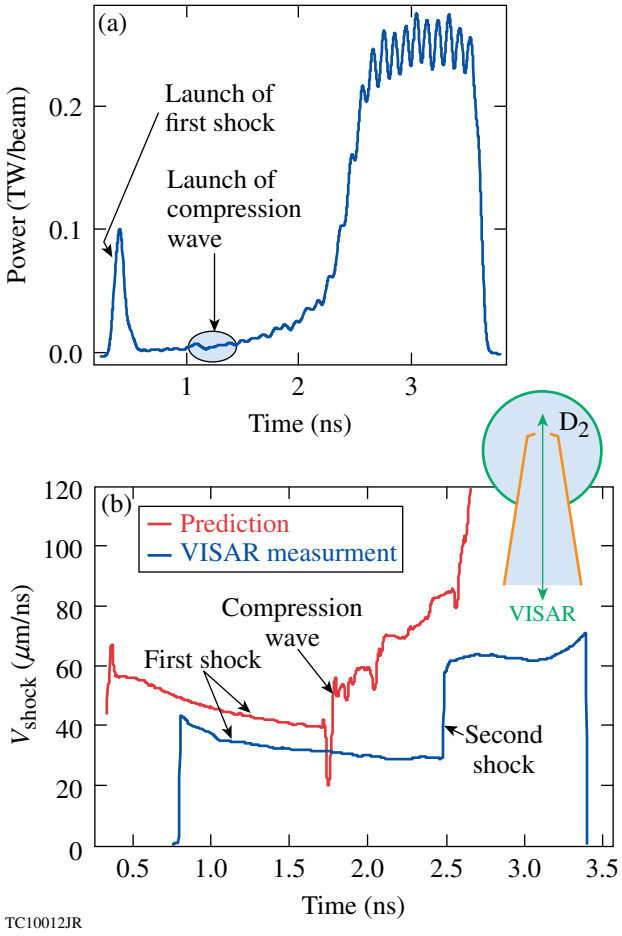

Figure 130.43
(a) Pulse shape and (b) leading shock velocity measured (lower curve) and predicted (upper curve).

time, is compared with 1-D predictions obtained using a *LILAC* simulation. An intensity picket at the beginning of the drive pulse sends a shock wave of decaying strength. As the drive intensity starts to rise from its minimum value, a compression wave is launched into the ablator at $t \simeq 1$ ns. After the head of the compression catches up with the first shock, strength and velocity of the leading shock increase gradually in time. The measured velocity history, however, shows a much steeper velocity increase that takes place later in the pulse, indicating that the compression wave turns into a shock prior to its coalescence with the first shock. Such a transition from adiabatic to shock compression raises the fuel adiabat at the inner part of the shell, limiting the final target convergence and peak fuel ρR. Since the effect of the compression wave steepening into a shock, not predicted by a simulation, is exacerbated by an increasing peak drive pulse or changing the shell thickness, difficulty in tuning continuous-pulse designs can be explained by excessive shock heating.

After obtaining the VISAR results, the cryogenic program at LLE quickly moved to multiple-picket designs[72] by introducing double-picket and, later, triple-picket pulses (see Fig. 130.44). To set the fuel on a low adiabat $\alpha \sim 1$ to 3, the double-picket design still requires a moderate-intensity foot (1/4 to 1/3 of peak intensity) and a gradual intensity increase to compress the fuel adiabatically (dashed line in Fig. 130.44). The triple-picket design (solid line in Fig. 130.44), on the other hand, does not rely on an adiabatic compression and requires a short step at the beginning of the main pulse to control the strength of the main shock.

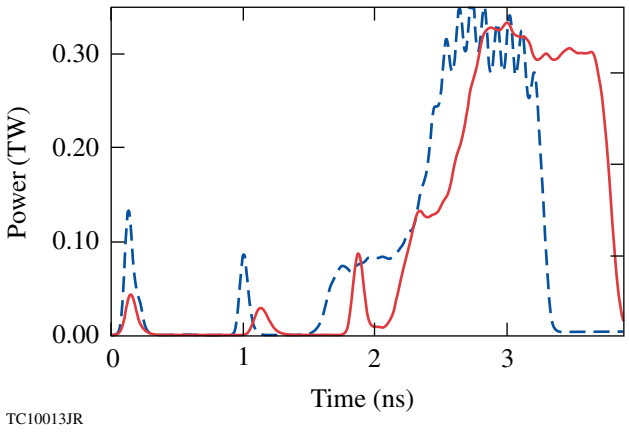

Figure 130.44
Two- (dashed line) and three-picket (solid line) cryogenic OMEGA target designs.

Current Triple-Picket Cryogenic-DT Implosions

The main advantage in using multiple-picket designs is the ability to control all hydrodynamic waves launched by the drive pulse.[72] As described in **All-DT, Direct-Drive, NIF-Scale Ignition Target Design** (p. 76), designs with continuous pulses rely on adiabatic fuel compression while the drive pressure increases by a factor of 50 or more. The observed premature steepening of the adiabatic compression wave into a shock inside the shell makes it impractical to experimentally tune the shell adiabat in these designs. In the multiple-picket designs shown in Fig. 130.44, the required increase in drive pressure from a few Mbar to ~100 Mbar is accomplished by launching a sequence of shocks that can be well controlled by adjusting the timing and energy of each individual intensity picket. Two types of the triple-picket pulse shapes are used in current cryogenic implosions on OMEGA. The laser power in the first design, shown in Fig. 130.45(a), consists of three pickets and the main drive in the form of a square pulse. To control the strength of the main shock, a short intensity step is introduced at the beginning of the main drive in the second design [shown

in Fig. 130.45(b)]. The stronger main shock launched in the first design sets the fuel on α = 2.5 to 3. A weaker shock in the second design reduces the adiabat to α = 2 to 2.5. Next, we describe how shock tuning was accomplished in these designs using OMEGA experiments.

1. Shock Tuning

Accuracy in predicting shock timing is verified by measuring the velocity of the leading shock wave using VISAR. The targets in these experiments were spherical, 5- or 10-μm-thick CD shells fitted with a diagnostic cone.[73] The shell and cone were filled with liquid deuterium. For an optimized design,[72] all shocks should coalesce within 100 ps, soon after they break out of the shell. For the purpose of code validation, the time separation between shock coalescence events was increased in these experiments to accurately infer leading shock velocity after each coalescence. An example of such a measurement is shown in Fig. 130.46. Because of radiation precursor, the shock is not visible to VISAR early in time while it travels through the plastic layer. Then, at $t \sim 300$ ps, the shock breaks out of CD into D_2 with a velocity of ~60 μm/ns. The shock is not supported by the laser at this time (picket duration is ~80 ps). Therefore, the shock strength and its velocity decrease with time. Then, the second shock is launched at t = 1.1 ns. It travels through

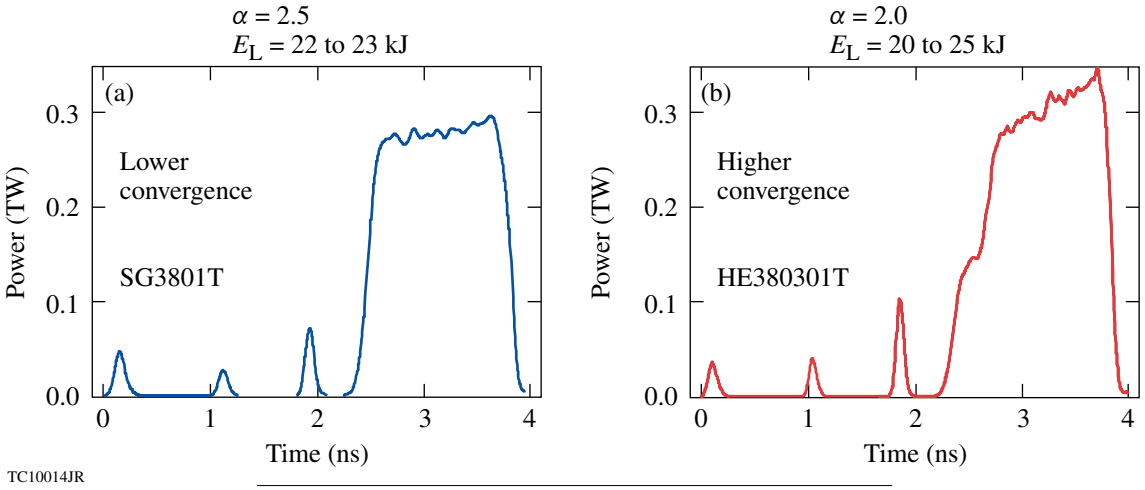

Figure 130.45
Two triple-picket target designs used in cryogenic implosions on OMEGA.

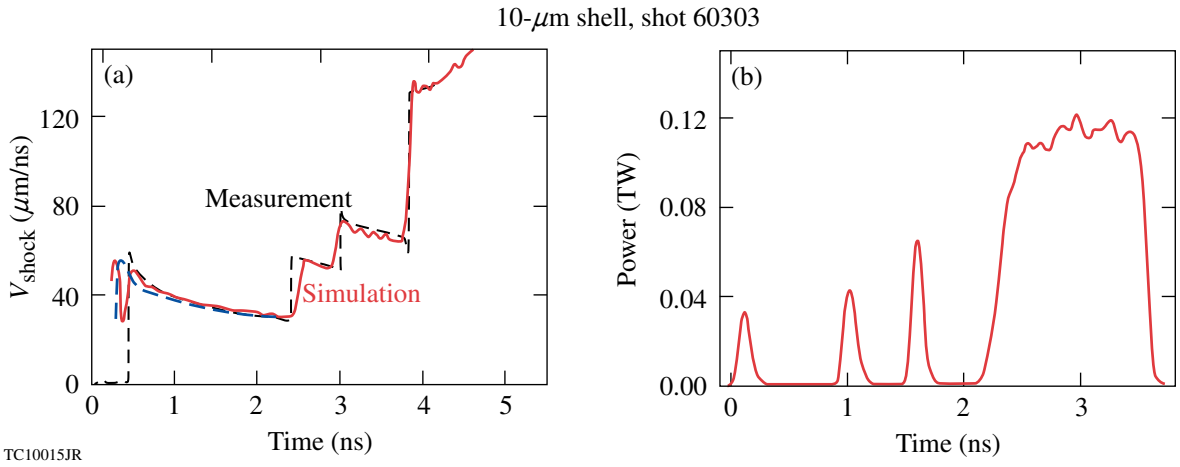

Figure 130.46
(a) Measured (dashed line) and predicted (solid line) leading shock velocity in (b) a triple-picket design.

the relaxed density and pressure profiles established by the first shock. At $t = 2.5$ ns the second shock catches up with the first, resulting in a jump in leading shock velocity from 35 up to 60 μm/ns. The third picket and the main pulse launch two additional shocks that coalesce with the leading shock at $t =$ 3.0 and 3.9 ns, respectively.

Matching both shock velocities and coalescence times is a good test of a thermal-conduction model used in a hydrocode simulation. The thermal conduction affects hydrodynamic profiles that determine energy coupling. The flux-limited model with $f = 0.06$ predicts a lower laser-absorption fraction than that calculated using the nonlocal thermal transport model, leading to a slower shock. The difference between two transport models increases with the energy in the first picket. The comparison between model predictions and experimental data is shown in Fig. 130.47. As seen in this figure, agreement between prediction and measurement improves when the nonlocal thermal-transport model is used in the simulations.

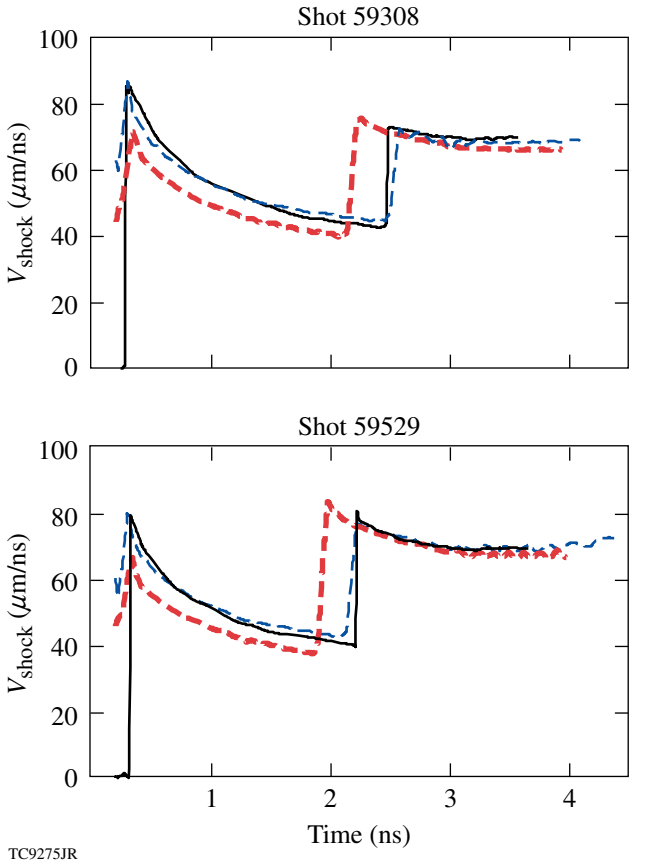

Figure 130.47
Measured (solid lines) and predicted leading shock velocity using the flux-limited (thick red dashed lines) and nonlocal (thin dashed lines) electron thermal-transport models for two shots.

Matching the predicted and measured shock velocities and coalescence times ensures that the shock heating is properly modeled. The in-flight shell adiabat, set by the shocks, can be degraded during the implosion by electron or radiation preheat as well as by secondary shock waves. As described in **Adiabat** (p. 81), the in-flight adiabat can be inferred from areal-density measurements if no significant shell decompression is induced by the prolonged coasting phase [see discussion after Eq. (53)]. The extended coasting phase could result from a loss in hydro-efficiency during shell acceleration. The latter would reduce shell implosion velocity and delay the time of neutron production. Therefore, to connect any observable degradation in areal density with fuel preheat or any other effects that enhance in-flight adiabat, one must verify that hydrodynamic efficiency is accurately modeled and no extended coasting phase is present in the implosion. This will be addressed in the next subsection.

2. Laser Coupling and Hydrodynamic Efficiency

Accurate modeling of hydrodynamic efficiency of an imploding shell (defined as the ratio of the peak in shell kinetic energy to the total laser energy) is crucial for optimizing high-convergence target designs, since a loss in the shell's implosion velocity and kinetic energy leads to shell coasting after the laser drive turns off. During such coasting, both shell density and pressure drop. This reduces ρR [see Eq. (53)] and gives a lower fuel ion temperature at the time of neutron production. One of the diagnostics that is most sensitive to deviations in the shell's implosion velocity is a measurement of timing and temporal shape of primary neutrons produced as a result of fusion reactions. This is accomplished by using NTD (see discussion in **Implosion Velocity**, p. 84). Currently, NTD is calibrated on OMEGA to ~50-ps absolute timing accuracy with ~10-ps shot-to-shot timing variation. In addition to the neutron-production timing, the laser-absorption measurement is performed using two full-aperture backscattering stations (FABS).[63] Time-resolved scattered-light spectroscopy and time-integrated calorimetry in these stations are used to infer the absorption of laser light. Laser absorption, however, is not a direct measurement of hydrodynamic efficiency since only a small fraction of the incident laser energy (~5%) is converted (through the mass ablation) into the shell's kinetic energy and the majority of the absorbed energy goes into heating the underdense plasma corona. Also, some fraction of laser energy can be deposited into plasma waves that accelerate suprathermal electrons and do not directly contribute to the drive.

Figures 130.48(a) and 130.48(b) compare the measured scattered laser light and Fig. 130.48(c) compares neutron production history with the predictions (blue solid lines represent

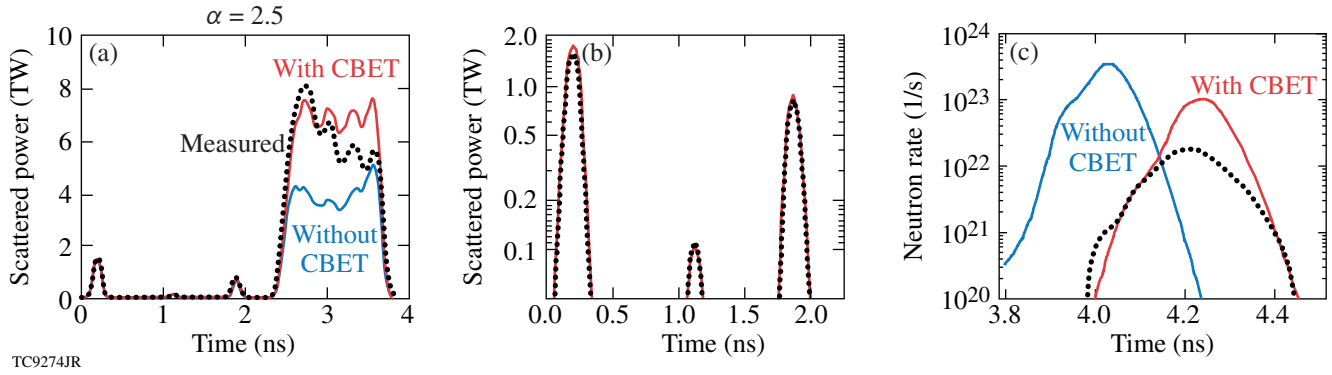

Figure 130.48
[(a) and (b)] Measured (dotted lines) and predicted (solid lines) scattered-light data. (c) Neutron-production history for the $\alpha = 2.5$ design shown in Fig. 130.45(a).

without CBET) for an $\alpha = 2.5$ design. As seen in Fig. 130.48(b), calculations are in very good agreement with the measured scattered-light data (dotted line) for the picket portion of the pulse. At the main drive, however, the predicted laser absorption overestimates the data, especially at the beginning of the drive. Higher predicted laser coupling results in an earlier bang time, as shown in Fig. 130.48(c). On average, the rise of the neutron rate is earlier in simulations by 200 ps. Since calculations fail to accurately reproduce the laser-absorption fraction and neutron-production timing, an additional mechanism explaining a reduced laser coupling must be present in the experiments.

Such a mechanism, as discussed in a recent publication,[74] is due to the cross-beam energy transfer (CBET).[75] In the geometric optics approximation where each laser beam is subdivided into rays, the incoming ray in the central part of the beam interacts (through the ion-acoustic waves) with the outgoing ray on the outer edge of the beam, transferring its energy to that ray. This is illustrated in Fig. 130.49. Since the central part of the beam propagates closest to the target, CBET reduces the fraction of the beam energy that reaches the higher-density plasma corona, decreasing overall laser absorption. Because CBET reduces the total laser absorption, and, furthermore, the absorbed energy is deposited in corona farther away from the target surface, the hydroefficiency of laser drive in directly driven implosions is degraded by 15% to 20% in OMEGA implosions. When implemented into the hydrocode *LILAC*, a CBET model predicts a 10% to 15% reduction in the absorbed energy, in agreement with experimental data. Shown in Fig. 130.48 solid lines marked "with CBET" are (a) the scattered light and (c) neutron-production rate calculated using a combination of the nonlocal thermal transport and CBET models. The neutron-production timing matches data very well. The scattered-light power, however, deviates from the measurements at later times. This late-time discrepancy is likely due

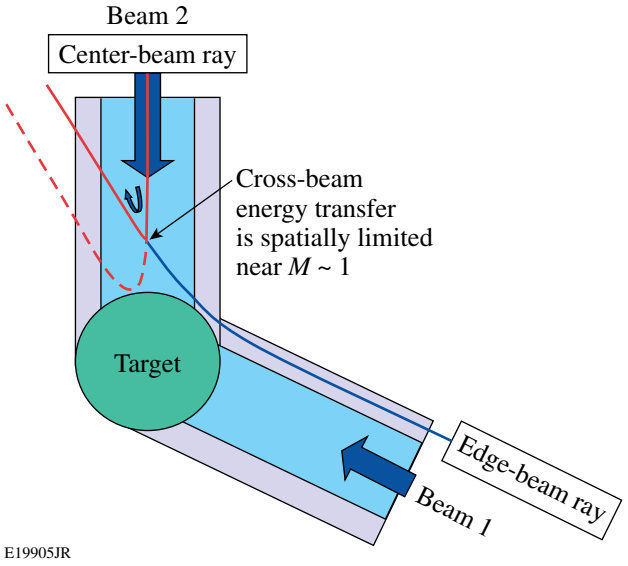

Figure 130.49
The incoming ray in the central part of Beam 2 interacts with the outgoing ray on the outer edge of Beam 1, transferring its energy to that ray.

to extra absorption of laser energy by plasma waves excited by the TPD instability.[14] Figure 130.50 shows the drive pulses and threshold parameters for $\alpha = 2.5$ designs. The threshold parameter first oscillates around $\eta = 1$ and then rises above unity at $t \sim 3.2$ to 3.3 ns. This matches the time when the experimental scattered light starts deviating from the predictions. To further support the assertion that the observable fraction of laser energy is being deposited into plasma waves, the scattered-light measurement and prediction are plotted in Fig. 130.51 for an implosion at a slightly higher drive intensity where the TPD instability threshold is exceeded at the beginning of the main drive [see Fig. 130.51(b)]. The calculated scattered-light power starts deviating from measurements earlier in this case, which is consistent with the timing of η exceeding unity.

Incorporating the CBET model into hydrocode simulations shows only a marginal reduction (on average by ~5%) in neutron-averaged areal densities. This confirms that the areal densities in cryogenic implosions on OMEGA are affected mainly by the in-flight shell adiabat and the effect of shell decompression during the coasting phase is small.

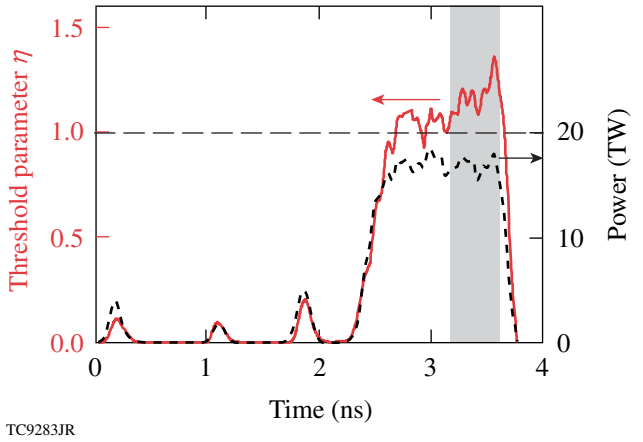

Figure 130.50
Pulse shape (dashed line) and threshold parameter η of TPD instability.

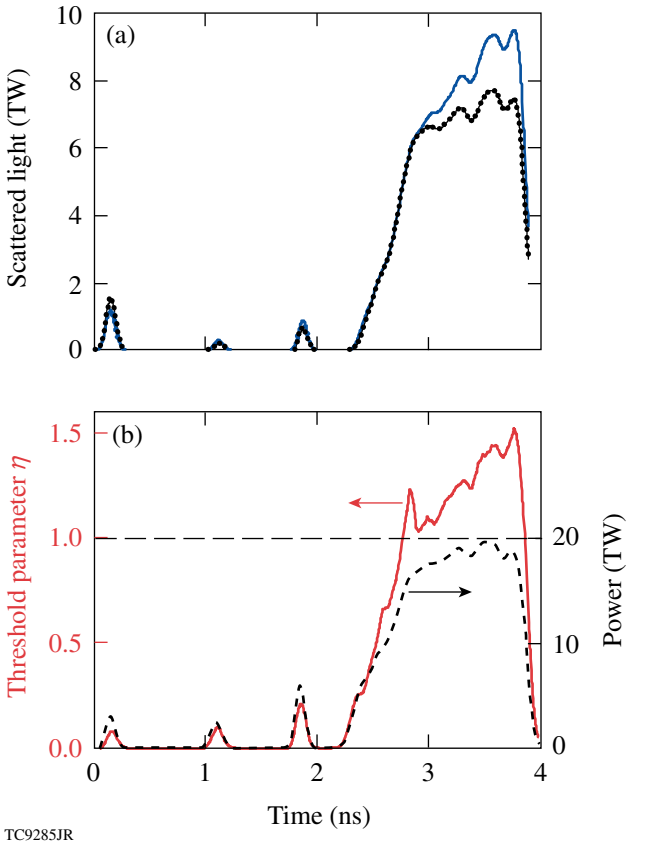

Figure 130.51
(a) Measured (dotted line) and predicted scattered power. (b) Pulse shape (dashed line) and threshold parameter η of TPD instability (solid line).

3. Areal Densities in a Triple-Picket Cryogenic Implosions

In this section we compare the calculated neutron-averaged areal density $\langle \rho R \rangle_n$ with the measurements. Since the predicted $\langle \rho R \rangle_n \sim 150$ to 200 mg/cm^2 for $\alpha = 2.5$ and $\langle \rho R \rangle_n \sim 220$ to 300 mg/cm^2 for $\alpha = 2$, the areal density is currently inferred using a single-view measurement with a magnetic recoil spectrometer (MRS).[28] The MRS measures the number of primary neutrons and the number of neutrons scattered in the dense DT fuel. The ratio of these two is proportional to the fuel areal density during the neutron production. Two charged-particle spectrometers (CPS's) were also used to measure the spectrum of knock-on deuterons, elastically scattered by primary DT neutrons. These measurements, however, are insensitive to $\langle \rho R \rangle_n >$ 180 mg/cm^2 and were used to assess low-ℓ-mode ρR asymmetries for implosions where areal density along the CPS's line of sight is below 180 mg/cm^2. Such asymmetries arise from errors in target positioning (offset) and ice roughness amplified during shell implosion. Since only a single-view MRS measurement is used for ρR analysis, it is important to take long-wavelength asymmetries into account when comparing the simulated and measured areal densities for high-convergence implosions. Strictly speaking, even a single MRS measurement averages fuel ρR over a solid angle of ~1.5π since the down-scattered neutrons have a finite spectral width and neutrons with different energies sample different parts of the shell (see Fig. 130.52). The scattering angle θ of a primary neutron (marked with "n" in Fig. 130.52) depends on down-scattered neutron ("n′") energy. MRS is sensitive to 8- to 13-MeV neutrons. The minimum scattering angle $\theta_{min} = 29°$ and 23° correspond to 13-MeV neutrons scattered by tritons and deuterons, respectively. The maximum angle $\theta_{max} = 80°$ and 62° corresponds to 8-MeV neutrons. The dark shell region in Fig. 130.52 corresponds to a region sampled by the down-scattered neutrons in a single-view MRS measurement on OMEGA. Taking into account such averaging, Fig. 130.53 plots a calculated variation in areal density as would be observed by the MRS in a single-view measurement taken along a different direction with respect to the target offset. The results are shown for the offset values of $\Delta_{offset} = 10$ μm (black line) and 30 μm (green line). The calculations were performed by post-processing results of 2-D *DRACO* simulations[76] using the Monte Carlo–based particle transport code *IRIS*. The error bars in Fig. 130.53 represent counting statistics errors in a typical cryogenic implosion on OMEGA. These calculations show that the $\langle \rho R \rangle_n$ variation across the target can be approximated by a linear function of the offset,

$$\frac{\max\langle\rho R\rangle_{\rm n} - \min\langle\rho R\rangle_{\rm n}}{\langle\rho R\rangle_{\rm n}}\% \simeq \Delta_{\rm offset}(\mu{\rm m}). \qquad (66)$$

In addition to the target offset, the low-ℓ modes ($\ell \le 2$) seeded by the ice roughness also lead to an azimuthal variation in the measured areal density. In plotting the predicted $\langle\rho R\rangle_{\rm n}$, we assign the error bar for each point taking into account the ρR variation caused by target offset and low-mode ice roughness measured for each target. The result is shown in Fig. 130.54 (see also Ref. 72), where squares and circles correspond to $\alpha = 2$ and $\alpha = 2.5$ designs, respectively. In general, there is good agreement between the experimental data and calculations. This confirms that the adiabat is modeled accurately in low-adiabat cryogenic implosions on OMEGA using the triple-picket designs.

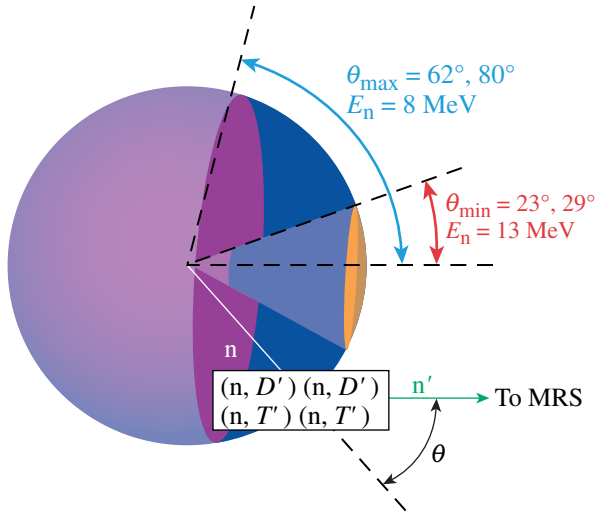

Figure 130.52
The scattering angle θ of a primary neutron (marked with "n") depends on down-scattered neutron ("n′") energy. MRS is sensitive to neutrons with energies between 8 and 13 MeV. The minimum scattering angles $\theta_{\rm min} = 29°$ and 23° correspond to 13-MeV neutrons scattered by tritons and deuterons, respectively. The maximum angles $\theta_{\rm max} = 80°$ and 62° correspond to 8-MeV neutrons. The dark shell region corresponds to a region sampled by the down-scattered neutrons in a single-view MRS measurement on OMEGA.

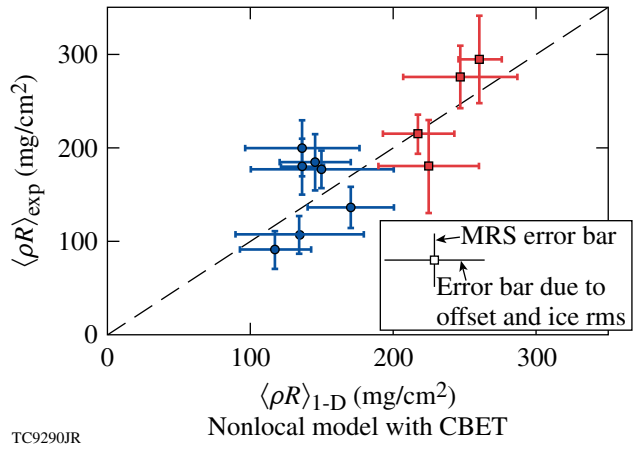

Figure 130.54
Measured versus predicted areal densities for triple-picket cryogenic implosions on OMEGA.

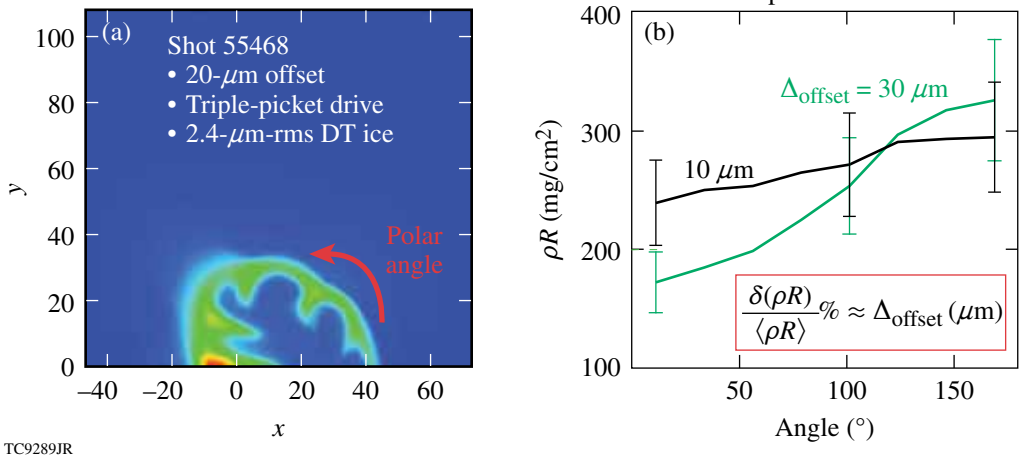

Figure 130.53
(a) Density contour of 2-D *DRACO* simulation of a cryogenic implosion on OMEGA (shot 55468) with a target offset of 20 μm. (b) Predicted variation in areal density as would be observed by the MRS in a single-view measurement taken along a different direction with respect to the target offset.

Based on the good performance of the triple-picket design on OMEGA, this design was extended to a 1.5-MJ direct-drive–ignition design[72] for the National Ignition Facility (see Fig. 130.55). Driven at a peak intensity of 8×10^{14} W/cm^2, the shell reaches $V_{imp} = 3.5$ to 4×10^7 cm/s, depending on the thickness of the fuel layer. This design is predicted to ignite with a gain $G = 48$.

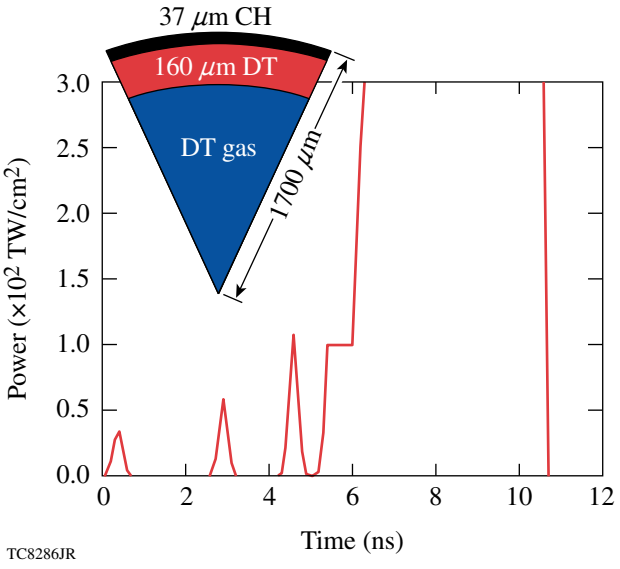

Figure 130.55
Triple-picket, symmetric direct-drive design for the NIF.

ACKNOWLEDGEMENT

This work was supported by the U.S. Department of Energy Office of Inertial Confinement Fusion under Cooperative Agreement No. DE-FC52-08NA28302, the University of Rochester, and the New York State Energy Research and Development Authority. The support of DOE does not constitute an endorsement by DOE of the views expressed in this article.

REFERENCES

1. J. D. Lindl, *Inertial Confinement Fusion: The Quest for Ignition and Energy Gain Using Indirect Drive* (Springer-Verlag, New York, 1998).
2. S. Atzeni and J. Meyer-ter-Vehn, *The Physics of Inertial Fusion: Beam Plasma Interaction, Hydrodynamics, Hot Dense Matter*, International Series of Monographs on Physics (Clarendon Press, Oxford, 2004).
3. M. C. Herrmann, M. Tabak, and J. D. Lindl, Phys. Plasmas **8**, 2296 (2001).
4. R. Betti, K. Anderson, V. N. Goncharov, R. L. McCrory, D. D. Meyerhofer, S. Skupsky, and R. P. J. Town, Phys. Plasmas **9**, 2277 (2002).
5. V. N. Goncharov, in *Laser-Plasma Interactions*, edited by D. A. Jaroszynski, R. Bingham, and R. A. Cairns, Scottish Graduate Series (CRC Press, Boca Raton, FL, 2009), pp. 409–418.
6. J. Meyer-ter-Vehn, Nucl. Fusion **22**, 561 (1982).
7. R. Betti, P. Y. Chang, B. K. Spears, K. S. Anderson, J. Edwards, M. Fatenejad, J. D. Lindl, R. L. McCrory, R. Nora, and D. Shvarts, Phys. Plasmas **17**, 058102 (2010).
8. A. Kemp, J. Meyer-ter-Vehn, and S. Atzeni, Phys. Rev. Lett. **86**, 3336 (2001).
9. S. W. Haan, J. D. Lindl, D. A. Callahan, D. S. Clark, J. D. Salmonson, B. A. Hammel, L. J. Atherton, R. C. Cook, M. J. Edwards, S. Glenzer, A. V. Hamza, S. P. Hatchett, M. C. Herrmann, D. E. Hinkel, D. D. Ho, H. Huang, O. S. Jones, J. Kline, G. Kyrala, O. L. Landen, B. J. MacGowan, M. M. Marinak, D. D. Meyerhofer, J. L. Milovich, K. A. Moreno, E. I. Moses, D. H. Munro, A. Nikroo, R. E. Olson, K. Peterson, S. M. Pollaine, J. E. Ralph, H. F. Robey, B. K. Spears, P. T. Springer, L. J. Suter, C. A. Thomas, R. P. Town, R. Vesey, S. V. Weber, H. L. Wilkens, and D. C Wilson, Phys. Plasmas **18**, 051001 (2011).
10. C. P. Verdon, Bull. Am. Phys. Soc. **38**, 2010 (1993).
11. P. W. McKenty, V. N. Goncharov, R. P. J. Town, S. Skupsky, R. Betti, and R. L. McCrory, Phys. Plasmas **8**, 2315 (2001).
12. J. Paisner *et al.*, Laser Focus World **30**, 75 (1994).
13. V. N. Goncharov, S. Skupsky, T. R. Boehly, J. P. Knauer, P. McKenty, V. A. Smalyuk, R. P. J. Town, O. V. Gotchev, R. Betti, and D. D. Meyerhofer, Phys. Plasmas **7**, 2062 (2000).
14. W. L. Kruer, *The Physics of Laser–Plasma Interactions*, Frontiers in Physics, Vol. 73, edited by D. Pines (Addison-Wesley, Redwood City, CA, 1988), Chap. 4, p. 81.
15. S. Chandrasekhar, in *Hydrodynamic and Hydromagnetic Stability*, International Series of Monographs on Physics (Clarendon Press, Oxford, 1961), p. 428.
16. J. Sanz, Phys. Rev. Lett. **73**, 2700 (1994); V. N. Goncharov, R. Betti, R. L. McCrory, P. Sorotokin, and C. P. Verdon, Phys. Plasmas **3**, 1402 (1996).
17. R. Betti, V. N. Goncharov, R. L. McCrory, and C. P. Verdon, Phys. Plasmas **5**, 1446 (1998).
18. J. Sanz, Phys. Rev. E **53**, 4026 (1996).
19. V. N. Goncharov, O. V. Gotchev, E. Vianello, T. R. Boehly, J. P. Knauer, P. W. McKenty, P. B. Radha, S. P. Regan, T. C. Sangster, S. Skupsky, V. A. Smalyuk, R. Betti, R. L. McCrory, D. D. Meyerhofer, and C. Cherfils-Clérouin, Phys. Plasmas **13**, 012702 (2006).
20. V. N. Goncharov, J. P. Knauer, P. W. McKenty, P. B. Radha, T. C. Sangster, S. Skupsky, R. Betti, R. L. McCrory, and D. D. Meyerhofer, Phys. Plasmas **10**, 1906 (2003).
21. H. Sawada, S. P. Regan, D. D. Meyerhofer, I. V. Igumenshchev, V. N. Goncharov, T. R. Boehly, R. Epstein, T. C. Sangster, V. A. Smalyuk, B. Yaakobi, G. Gregori, S. H. Glenzer, and O. L. Landen, Phys. Plasmas **14**, 122703 (2007).
22. D. Zhou and R. Betti, Phys. Plasmas **14**, 072703 (2007).
23. A. L. Kritcher *et al.*, Phys. Rev. Lett. **107**, 015002 (2011).

24. H. Sawada, S. P. Regan, P. B. Radha, R. Epstein, D. Li, V. N. Goncharov, S. X. Hu, D. D. Meyerhofer, J. A. Delettrez, P. A. Jaanimagi, V. A. Smalyuk, T. R. Boehly, T. C. Sangster, B. Yaakobi, and R. C. Mancini, Phys. Plasmas **16**, 052702 (2009).

25. F. J. Marshall, P. W. McKenty, J. A. Delettrez, R. Epstein, J. P. Knauer, V. A. Smalyuk, J. A. Frenje, C. K. Li, R. D. Petrasso, F. H. Séguin, and R. C. Mancini, Phys. Rev. Lett. **102**, 185004 (2009).

26. R. Tommasini, S. P. Hatchett, D. S. Hey, C. Iglesias, N. Izumi, J. A. Koch, O. L. Landen, A. J. MacKinnon, C. Sorce, J. A. Delettrez, V. Yu. Glebov, T. C. Sangster, and C. Stoeckl, Phys. Plasmas **18**, 056309 (2011).

27. F. H. Séguin, C. K. Li, J. A. Frenje, D. G. Hicks, K. M. Green, S. Kurebayashi, R. D. Petrasso, J. M. Soures, D. D. Meyerhofer, V. Yu. Glebov, P. B. Radha, C. Stoeckl, S. Roberts, C. Sorce, T. C. Sangster, M. D. Cable, K. Fletcher, and S. Padalino, Phys. Plasmas **9**, 2725 (2002).

28. J. A. Frenje, C. K. Li, F. H. Séguin, D. T. Casey, R. D. Petrasso, T. C. Sangster, R. Betti, V. Yu. Glebov, and D. D. Meyerhofer, Phys. Plasmas **16**, 042704 (2009); J. A. Frenje, D. T. Casey, C. K. Li, F. H. Séguin, R. D. Petrasso, V. Yu. Glebov, P. B. Radha, T. C. Sangster, D. D. Meyerhofer, S. P. Hatchett, S. W. Haan, C. J. Cerjan, O. L. Landen, K. A. Fletcher, and R. J. Leeper, Phys. Plasmas **17**, 056311 (2010).

29. D. G. Hicks, B. K. Spears, D. G. Braun, R. E. Olson, C. M. Sorce, P. M. Celliers, G. W. Collins, and O. L. Landen, Phys. Plasmas **17**, 102703 (2010).

30. J. P. Knauer, K. Anderson, R. Betti, T. J. B. Collins, V. Yu. Glebov, V. N. Goncharov, F. J. Marshall, D. D. Meyerhofer, P. B. Radha, S. P. Regan, C. Stoeckl, J. A. Frenje, C. K. Li, R. D. Petrasso, and F. H. Séguin, Bull. Am. Phys. Soc. **50**, 113 (2005).

31. C. Stoeckl, V. Yu. Glebov, S. Roberts, T. C. Sangster, R. A. Lerche, R. L. Griffith, and C. Sorce, Rev. Sci. Instrum. **74**, 1713 (2003).

32. T. J. Murphy *et al*., Rev. Sci. Instrum. **66**, 930 (1995).

33. H. Brysk, Plasma Phys. **15**, 611 (1973).

34. J. M. Soures, R. J. Hutchison, S. D. Jacobs, L. D. Lund, R. L. McCrory, and M. C. Richardson, in *Proceedings of the 10th Symposium on Fusion Engineering* (IEEE, New York, 1983), p. 1392.

35. F. J. Marshall, S. A. Letzring, C. P. Verdon, S. Skupsky, R. L. Keck, J. P. Knauer, R. L. Kremens, D. K. Bradley, T. Kessler, J. Delettrez, H. Kim, J. M. Soures, and R. L. McCrory, Phys. Rev. A **40**, 2547 (1989).

36. R. L. McCrory, J. M. Soures, C. P. Verdon, F. J. Marshall, S. A. Letzring, S. Skupsky, T. J. Kessler, R. L. Kremens, J. P. Knauer, H. Kim, J. Delettrez, R. L. Keck, and D. K. Bradley, Nature **335**, 225 (1988).

37. D. L. Musinski *et al*., J. Appl. Phys. **51**, 1394 (1980).

38. S. Kacenjar, L. M. Goldman, A. Entenberg, and S. Skupsky, J. Appl. Phys. **56**, 2027 (1984); S. Skupsky and S. Kacenjar, J. Appl. Phys. **52**, 2608 (1981).

39. J. Delettrez, R. Epstein, M. C. Richardson, P. A. Jaanimagi, and B. L. Henke, Phys. Rev. A **36**, 3926 (1987).

40. J. K. Hoffer and L. R. Foreman, Phys. Rev. Lett. **60**, 1310 (1988); A. J. Martin, R. J. Simms, and R. B. Jacobs, J. Vac. Sci. Technol. A **6**, 1885 (1988).

41. G. W. Collins *et al*., J. Vac. Sci. Technol. A **14**, 2897 (1996).

42. *LLE Review Quarterly Report* **81**, 6, Laboratory for Laser Energetics, University of Rochester, Rochester, NY, LLE Document No. DOE/SF/19460-335 (1999).

43. T. R. Boehly, D. L. Brown, R. S. Craxton, R. L. Keck, J. P. Knauer, J. H. Kelly, T. J. Kessler, S. A. Kumpan, S. J. Loucks, S. A. Letzring, F. J. Marshall, R. L. McCrory, S. F. B. Morse, W. Seka, J. M. Soures, and C. P. Verdon, Opt. Commun. **133**, 495 (1997).

44. C. Stoeckl, C. Chiritescu, J. A. Delettrez, R. Epstein, V. Yu. Glebov, D. R. Harding, R. L. Keck, S. J. Loucks, L. D. Lund, R. L. McCrory, P. W. McKenty, F. J. Marshall, D. D. Meyerhofer, S. F. B. Morse, S. P. Regan, P. B. Radha, S. Roberts, T. C. Sangster, W. Seka, S. Skupsky, V. A. Smalyuk, C. Sorce, J. M. Soures, R. P. J. Town, J. A. Frenje, C. K. Li, R. D. Petrasso, F. H. Séguin, K. Fletcher, S. Padalino, C. Freeman, N. Izumi, R. Lerche, and T. W. Phillips, Phys. Plasmas **9**, 2195 (2002).

45. T. C. Sangster, R. Betti, R. S. Craxton, J. A. Delettrez, D. H. Edgell, L. M. Elasky, V. Yu. Glebov, V. N. Goncharov, D. R. Harding, D. Jacobs-Perkins, R. Janezic, R. L. Keck, J. P. Knauer, S. J. Loucks, L. D. Lund, F. J. Marshall, R. L. McCrory, P. W. McKenty, D. D. Meyerhofer, P. B. Radha, S. P. Regan, W. Seka, W. T. Shmayda, S. Skupsky, V. A. Smalyuk, J. M. Soures, C. Stoeckl, B. Yaakobi, J. A. Frenje, C. K. Li, R. D. Petrasso, F. H. Séguin, J. D. Moody, J. A. Atherton, B. D. MacGowan, J. D. Kilkenny, T. P. Bernat, and D. S. Montgomery, Phys. Plasmas **14**, 058101 (2007).

46. P. W. McKenty, T. C. Sangster, M. Alexander, R. Betti, R. S. Craxton, J. A. Delettrez, L. Elasky, R. Epstein, A. Frank, V. Yu. Glebov, V. N. Goncharov, D. R. Harding, S. Jin, J. P. Knauer, R. L. Keck, S. J. Loucks, L. D. Lund, R. L. McCrory, F. J. Marshall, D. D. Meyerhofer, S. P. Regan, P. B. Radha, S. Roberts, W. Seka, S. Skupsky, V. A. Smalyuk, J. M. Soures, K. A. Thorp, M. Wozniak, J. A. Frenje, C. K. Li, R. D. Petrasso, F. H. Séguin, K. A. Fletcher, S. Padalino, C. Freeman, N. Izumi, J. A. Koch, R. A. Lerche, M. J. Moran, T. W. Phillips, G. J. Schmid, and C. Sorce, Phys. Plasmas **11**, 2790 (2004).

47. F. J. Marshall, R. S. Craxton, J. A. Delettrez, D. H. Edgell, L. M. Elasky, R. Epstein, V. Yu. Glebov, V. N. Goncharov, D. R. Harding, R. Janezic, R. L. Keck, J. D. Kilkenny, J. P. Knauer, S. J. Loucks, L. D. Lund, R. L. McCrory, P. W. McKenty, D. D. Meyerhofer, P. B. Radha, S. P. Regan, T. C. Sangster, W. Seka, V. A. Smalyuk, J. M. Soures, C. Stoeckl, S. Skupsky, J. A. Frenje, C. K. Li, R. D. Petrasso, and F. H. Séguin, Phys. Plasmas **12**, 056302 (2005).

48. P. B. Radha, V. N. Goncharov, T. J. B. Collins, J. A. Delettrez, Y. Elbaz, V. Yu. Glebov, R. L. Keck, D. E. Keller, J. P. Knauer, J. A. Marozas, F. J. Marshall, P. W. McKenty, D. D. Meyerhofer, S. P. Regan, T. C. Sangster, D. Shvarts, S. Skupsky, Y. Srebro, R. P. J. Town, and C. Stoeckl, Phys. Plasmas **12**, 032702 (2005).

49. V. N. Goncharov, P. McKenty, S. Skupsky, R. Betti, R. L. McCrory, and C. Cherfils-Clérouin, Phys. Plasmas **7**, 5118 (2000).

50. T. R. Boehly, V. N. Goncharov, O. Gotchev, J. P. Knauer, D. D. Meyerhofer, D. Oron, S. P. Regan, Y. Srebro, W. Seka, D. Shvarts, S. Skupsky, and V. A. Smalyuk, Phys. Plasmas **8**, 2331 (2001).

51. K. Anderson and R. Betti, Phys. Plasmas **11**, 5 (2004).

52. S. Skupsky, R. W. Short, T. Kessler, R. S. Craxton, S. Letzring, and J. M. Soures, J. Appl. Phys. **66**, 3456 (1989).

53. W. L. Kruer, *The Physics of Laser-Plasma Interactions*, Frontiers in Physics, Vol. 73, edited by D. Pines (Addison-Wesley, Redwood City, CA, 1988).

54. R. C. Malone, R. L. McCrory, and R. L. Morse, Phys. Rev. Lett. **34**, 721 (1975).

55. L. Spitzer, Jr. and R. Härm, Phys. Rev. **89**, 977 (1953).

56. S. Chapman and T. G. Cowling, *The Mathematical Theory of Non-Uniform Gases; An Account of the Kinetic Theory of Viscosity, Thermal Conduction and Diffusion in Gases*, 3rd. ed. (Cambridge University Press, Cambridge, England, 1970).

57. V. N. Goncharov, T. C. Sangster, P. B. Radha, R. Betti, T. R. Boehly, T. J. B. Collins, R. S. Craxton, J. A. Delettrez, R. Epstein, V. Yu. Glebov, S. X. Hu, I. V. Igumenshchev, J. P. Knauer, S. J. Loucks, J. A. Marozas, F. J. Marshall, R. L. McCrory, P. W. McKenty, D. D. Meyerhofer, S. P. Regan, W. Seka, S. Skupsky, V. A. Smalyuk, J. M. Soures, C. Stoeckl, D. Shvarts, J. A. Frenje, R. D. Petrasso, C. K. Li, F. Séguin, W. Manheimer, and D. G. Colombant, Phys. Plasmas **15**, 056310 (2008).

58. N. A. Krall and A. W. Trivelpiece, *Principles of Plasma Physics* (San Francisco Press, Inc., San Francisco, 1986).

59. V. N. Goncharov and G. Li, Phys. Plasmas **11**, 5680 (2004).

60. V. A. Smalyuk, S. X. Hu, V. N. Goncharov, D. D. Meyerhofer, T. C. Sangster, D. Shvarts, C. Stoeckl, B. Yaakobi, J. A. Frenje, and R. D. Petrasso, Phys. Rev. Lett. **101**, 025002 (2008).

61. V. N. Goncharov, Phys. Rev. Lett. **82**, 2091 (1999).

62. O. Gotchev, V. N. Goncharov, J. P. Knauer, T. R. Boehly, T. J. B. Collins, R. Epstein, P. A. Jaanimagi, and D. D. Meyerhofer, Phys. Rev. Lett. **96**, 115005 (2006).

63. W. Seka, D. H. Edgell, J. P. Knauer, J. F. Myatt, A. V. Maximov, R. W. Short, T. C. Sangster, C. Stoeckl, R. E. Bahr, R. S. Craxton, J. A. Delettrez, V. N. Goncharov, I. V. Igumenshchev, and D. Shvarts, Phys. Plasmas **15**, 056312 (2008).

64. I. V. Igumenshchev, V. N. Goncharov, W. Seka, D. Edgell, and T. R. Boehly, Phys. Plasmas **14**, 092701 (2007).

65. A. Simon, R. W. Short, E. A. Williams, and T. Dewandre, Phys. Fluids **26**, 3107 (1983).

66. C. Stoeckl, V. Yu. Glebov, D. D. Meyerhofer, W. Seka, B. Yaakobi, R. P. J. Town, and J. D. Zuegel, Rev. Sci. Instrum. **72**, 1197 (2001).

67. V. A. Smalyuk, D. Shvarts, R. Betti, J. A. Delettrez, D. H. Edgell, V. Yu. Glebov, V. N. Goncharov, R. L. McCrory, D. D. Meyerhofer, P. B. Radha, S. P. Regan, T. C. Sangster, W. Seka, S. Skupsky, C. Stoeckl, B. Yaakobi, J. A. Frenje, C. K. Li, R. D. Petrasso, and F. H. Séguin, Phys. Rev. Lett. **100**, 185005 (2008).

68. H. N. Kornblum, R. L. Kauffman, and J. A. Smith, Rev. Sci. Instrum. **57**, 2179 (1986); K. M. Campbell *et al*., Rev. Sci. Instrum. **75**, 3768 (2004).

69. T. C. Sangster, V. N. Goncharov, P. B. Radha, V. A. Smalyuk, R. Betti, R. S. Craxton, J. A. Delettrez, D. H. Edgell, V. Yu. Glebov, D. R. Harding, D. Jacobs-Perkins, J. P. Knauer, F. J. Marshall, R. L. McCrory, P. W. McKenty, D. D. Meyerhofer, S. P. Regan, W. Seka, R. W. Short, S. Skupsky, J. M. Soures, C. Stoeckl, B. Yaakobi, D. Shvarts, J. A. Frenje, C. K. Li, R. D. Petrasso, and F. H. Séguin, Phys. Rev. Lett. **100**, 185006 (2008).

70. T. R. Boehly, D. H. Munro, P. M. Celliers, R. E. Olson, D. G. Hicks, V. N. Goncharov, G. W. Collins, H. F. Robey, S. X. Hu, J. A. Marozas, T. C. Sangster, O. L. Landen, and D. D. Meyerhofer, Phys. Plasmas **16**, 056302 (2009).

71. L. M. Barker and R. E. Hollenbach, J. Appl. Phys. **43**, 4669 (1972); P. M. Celliers *et al*., Appl. Phys. Lett. **73**, 1320 (1998).

72. V. N. Goncharov, T. C. Sangster, T. R. Boehly, S. X. Hu, I. V. Igumenshchev, F. J. Marshall, R. L. McCrory, D. D. Meyerhofer, P. B. Radha, W. Seka, S. Skupsky, C. Stoeckl, D. T. Casey, J. A. Frenje, and R. D. Petrasso, Phys. Rev. Lett. **104**, 165001 (2010).

73. T. R. Boehly, V. N. Goncharov, W. Seka, M. A. Barrios, P. M. Celliers, D. G. Hicks, G. W. Collins, S. X. Hu, J. A. Marozas, and D. D. Meyerhofer, Phys. Rev. Lett. **106**, 195005 (2011).

74. I. V. Igumenshchev, D. H. Edgell, V. N. Goncharov, J. A. Delettrez, A. V. Maximov, J. F. Myatt, W. Seka, A. Shvydky, S. Skupsky, and C. Stoeckl, Phys. Plasmas **17**, 122708 (2010).

75. C. J. Randall, J. R. Albritton, and J. J. Thomson, Phys. Fluids **24**, 1474 (1981).

76. S. X. Hu, V. N. Goncharov, P. B. Radha, J. A. Marozas, S. Skupsky, T. R. Boehly, T. C. Sangster, D. D. Meyerhofer, and R. L. McCrory, Phys. Plasmas **17**, 102706 (2010).

Experimental Reduction of Laser Imprinting and Rayleigh–Taylor Growth in Spherically Compressed, Medium-*Z*–Doped Plastic Targets

Introduction

The performance of inertial confinement fusion (ICF) ignition targets[1,2] can be compromised by implosion asymmetries caused by hydrodynamic instabilities. If the target deformation is large enough, it causes mixing of the inner hot area of the target ("hot spot") with the outer colder shell, quenching the fusion reactions. The Rayleigh–Taylor (RT) instability[3] is the primary hydrodynamic instability that develops during the compression of an ICF capsule. Small nonuniformities, seeded at the outer ablation interface by imperfections in the laser irradiation and/or by target surface roughness, are amplified during the acceleration phase, feed through the shell, and seed the RT growth at the inner surface of the shell, which becomes unstable during the stagnation phase.

Because of the paramount importance of this instability to the success of ICF, a great amount of theoretical and experimental research has been devoted to reducing the seed nonuniformities and mitigating the instability growth. To reduce the initial beam imprint and improve the laser radiation uniformity, LLE's OMEGA Laser System[4] employs 60 beams on the surface of a spherical capsule augmented by advanced nonuniformity reduction techniques such as laser-beam two-dimensional (2-D) smoothing by spectral dispersion (SSD),[5] distributed phase plates (DPP's),[6] polarization smoothing (DPR),[7] and temporal shaping of the laser pulse.[8,9]

Techniques for RT mitigation such as coating the target with a high-*Z* material and the shell's volumetric doping with impurities have been studied elsewhere.[10–13] Radiation preheat, enhanced by impurities, reduces the peak density, increases the ablation velocity, and increases the density-gradient scale length; all of which decrease the RT growth rate.[14] Expansion of the ablated doped plasma reduces the laser imprint by increasing the separation between the absorption region and the ablator surface. Experiments with planar targets in the Nike facility demonstrated reduction of the instability for targets coated with thin Pd or Au layers.[11] On OMEGA, coating deuterium-filled plastic spherical capsules with a thin layer of palladium resulted in a twofold increase in the neutron yield.[12] Capsules volumetrically doped with Si and Ge were imploded and their neutron yield doubled as well.[13]

This article presents time-resolved measurements of the RT growth of target areal-density modulations during the spherical implosion of thin plastic shells volume doped with Si and Ge. The targets were imploded with 48 laser beams with a low-adiabat, triple-picket laser pulse shape[8] with an intensity of 4×10^{14} W/cm^2 and a duration of 2.5 ns. To seed the initial nonuniformities, SSD[5] was turned off. The targets were backlit with x rays generated by irradiating a Ta backlighter target with six overlapping beams with the same pulse shape. The x rays passing through the shell were recorded by a fast framing camera,[15] and the density (areal density) perturbation of the shell was inferred from the x-ray absorption.[16] The results indicate that the initial perturbation amplitude at the beginning of the compression phase was reduced by a factor of 2.5±0.5 for CH [4.3% Si] targets and by a factor of 3±0.5 for CH [7.4% Si] and CH [3.9% Ge] targets. At the end of compression the reduction factor in the density modulation became 3±0.5 and 5±0.5, respectively. The instability growth rate was reduced by a factor of 1.5 in doped targets in comparison to undoped ones. These results agree with simulations using the 2-D, radiation–hydrodynamics code *DRACO*.[17]

This article is organized as follows: The experimental configuration is described; the main results are presented; and the discussion is summarized.

Experimental Configuration

The experimental configuration, diagnostics, and data analysis are similar to those described in Refs. 16, 18, and 19. The experimental setup is illustrated in Fig. 130.56. The targets were smooth spherical plastic (CH) shells with an outer diameter of 860 μm and a shell thickness of 22 μm. Pure plastic shells and plastic shells volumetrically doped with Si (4.3% and 7.4%) and Ge (3.9%) were used. The targets were irradiated with 48 OMEGA beams (out of the remaining 12 beams, six beams were used for backlighter irradiation and six beams incident on the diagnostic hole in the target were not used) with

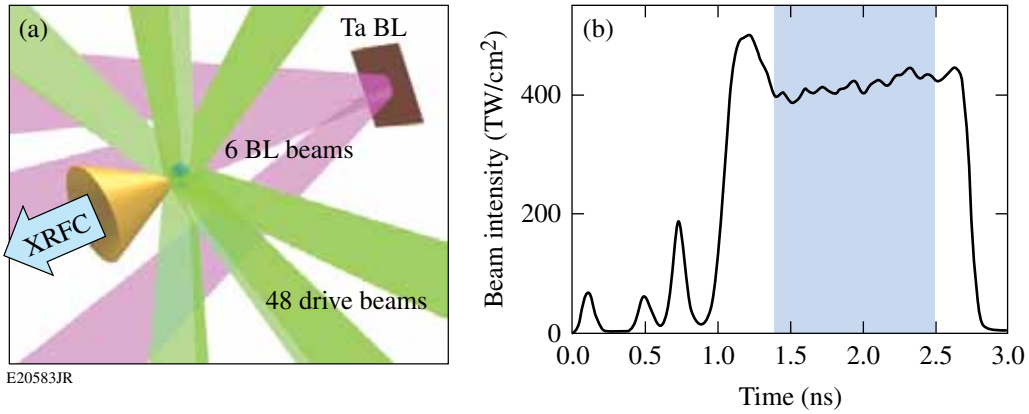

Figure 130.56
(a) Experimental setup. A spherical plastic shell was imploded by 48 beams (green) and the Ta backlighter (BL) was irradiated by 6 beams (violet). The shells had an outer diameter of 860 μm and a thickness of 22 μm. Each shell had a round opening with a diameter of 400 μm into which was inserted a gold cone shield with a tip opening of 400 μm, a height of 3 mm, and an opening angle of 53°. A Ta foil backlighter ($500 \times 500 \times 20$ μm^3) was placed 9 mm from the target. The target was x-ray radiographed by an x-ray framing camera (XRFC) during a time interval of 1.4 ns to 2.5 ns. (b) Laser power shape. The measurement interval from 1.4 ns to 2.5 ns is highlighted.

the triple-picket pulse laser shape at a total energy of 14.4 kJ (300 J per beam) and a main drive time duration of 2.5 ns. To seed the initial nonuniformities, SSD was turned off. The shells were backlit by x rays from a Ta foil backlighter ($500 \times 500 \times 20$ μm^3) placed 9 mm from the target and irradiated with six beams with the same pulse shape.

Similar to Ref. 19, the shells had a round opening with a diameter of 400 μm through which one could monitor the transmission of the x rays through the shell. To shield the opening and the line of sight against direct x-ray exposure from the coronal plasma, a gold cone with a tip opening of 400 μm, a height of 3 mm, and an opening angle of 53° was inserted into the shell's opening.

The x rays, with a peak energy of about 2.8 keV, were recorded with a fast x-ray framing camera (XRFC),[15] and the shell's areal-density variation was inferred from spatial modulation of the x-ray transmission. The camera's 16-pinhole array was situated at 3 cm from the target and the images were recorded with a charge-coupled device (CCD) situated at a distance of 36 cm from the pinhole array. The pinholes had a diameter of 10 μm, and the CCD had 2048×2048 pixels with a size of 18 μm $\times$ 18 μm each. This viewing geometry resulted in a magnification of 12 and provided a field of view at the shell's surface of approximately 400 μm in diameter. The modulation transfer function (MTF) of the imaging system was 50% at a wavelength of approximately 20 μm and 10% at a wavelength of approximately 10 μm, the latter representing the limit of spatial resolution. The framing camera was triggered at 1.4 ns, and 16 images were recorded during a time interval of 1.4 ns to 2.5 ns [highlighted in Fig. 130.56(b)] with a frame-to-frame time interval of ~60 ps.

Experimental Results

1. X-Ray Absorption

Attenuation of x rays with a reasonably narrow spectrum (the measured spectrum had a relative width $\Delta E/E \approx 20\%$) can be described as $I = I_{\mathrm{BL}} \exp\left(-\bar{\mu}\rho\delta\right)$, where ρ and δ are correspondingly the shell's mass density and thickness, $\bar{\mu}$ is the spectrum-averaged mass attenuation coefficient, and I_{BL} is the backlighter intensity. To measure the x-ray absorption in the shell, a series of shots were conducted using undriven shells that had laser-drilled, round, 200-μm-diam openings facing the backlighter. In a single shot, within the 400-μm field of view set by the framing camera, the intensities of x rays passing unattenuated through the 200-μm opening and attenuated through the shell were compared. The mass attenuation coefficient was calculated as $\bar{\mu} = (\rho\delta)^{-1} \ln\left(I_{\mathrm{open}}/I_{\mathrm{shell}}\right)$, where I_{open} and I_{shell} are, respectively, the x-ray intensities passing through the opening and the shell and δ is the shell thickness. The values for the mass attenuation coefficients obtained are given in Table 130.III. To simplify further notations, the bar sign over $\bar{\mu}$ will be omitted.

2. Areal-Density Modulation

For the shell-density modulation measurement, SSD beam smoothing was turned off so the laser beams' speckle created a broadband spectrum of seed-density perturbation at the time of the first picket. The areal-density modulation was determined

Table 130.III: Measured mass attenuation coefficient for undoped (CH) and doped shells. The amount and type of doping were 4.3% Si, 7.4% Si, and 3.9% Ge.

	CH	CH [4.3% Si]	CH [7.4% Si]	CH [3.9% Ge]
(g/cm^3)	1.02	1.07	1.29	1.34
$\bar{\mu}\left(\mathrm{cm}^2/\mathrm{g}\right)$	110±26	317±50	420±67	517±62

by taking a natural logarithm of the modulation of the image intensity I:

$$\ln I = \ln I_{\mathrm{BL}} - \mu\rho r, \tag{1}$$

where I_{BL} is the backlighter intensity. The product $\mu\rho r$ is commonly called optical density (OD). A typical image of the natural ln of XRFC intensity taken at $t = 2.12$ ns is shown in Fig. 130.57. A CH target doped with 3.4% of Si was used.

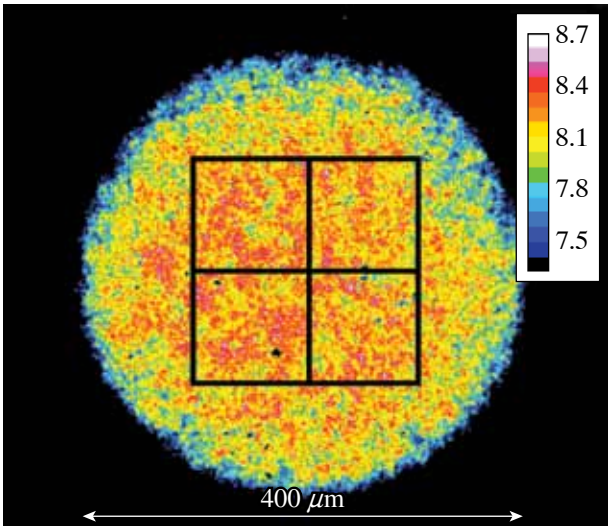

E20584JR

Figure 130.57
An XRFC image of ln(I) for a CH target doped with 4.3% Si taken in t = 2.12 ns. The size of the image is approximately 400 μm. The large 192 × 192-μm^2 square (128 × 128 pixels) was used to calculate modulation rms. The four 96 × 96-μm^2 subregions were used to calculate error.

As the first step of data analysis, high-frequency digital noise in the XRFC signal was reduced by smoothing over two CCD pixels, equivalent to filtering out spatial frequencies higher than 300 mm^{-1}. Large-scale variations of the backlighter intensity were removed using 2-D, fourth-order polynomial fitting to ln$I$ (Ref. 18). Equation (1) describes the remaining fine-scale spatial modulation of the areal density ρr and the optical density (OD) $\mu\rho r$.

One way to characterize the density modulation is to calculate its rms (root-mean-square) value averaged over a certain area. A region of interest (ROI) of 128 × 128 pixels selected in each image corresponds to a 192 × 192-μm^2 area at the shell's surface (Fig. 130.57). Each ROI was subdivided into four smaller ROI's, 64 × 64 pixels each, and the rms calculation (described below) was repeated for each subregion. The standard deviation of results obtained for each subregion is considered as the measurement error represented by the "error bars" in the figures that follow.

The modulation of the backlighter intensity and the shell density are assumed to be uncorrelated. Therefore, the rms of the signal intensity fluctuations is comprised of the rms of the shell's optical-density modulation added in quadrature to the rms of the backlighter modulation:

$$\sigma^2_{\ln I} = \sigma^2_{\mathrm{OD}} + \sigma^2_{\ln I_{\mathrm{BL}}}. \tag{2}$$

The second term in the right-hand side of Eq. (2) can be treated as the background or the noise floor of the measurement and is subtracted from the signal rms to obtain the true rms of the areal-density modulation. Because the backlighter intensity varies with time for each shot and changes from shot to shot, the background subtraction must be done carefully. To scale the background noise with the mean intensity of the transmitted x rays, a series of shots with undriven shells was performed, so the density fluctuation was absent and any fluctuation of the signal resulted from modulation of the backlighter intensity (and statistical noise). This dependence (shown in Fig. 130.58) is fitted by a power fit $\sigma^2_{\ln I_{\mathrm{BL}}} = 0.46\,\bar{I}^{-0.59}$, where $\bar{I}$ is the mean value of the transmitted intensity. Using Eq. (2) the rms of the areal-density modulation is

$$\sigma_{\rho r} = \mu^{-1}\sigma_{\mathrm{OD}} = \mu^{-1}\sqrt{\sigma^2_{\ln I} - 0.46\,\bar{I}^{-0.59}}. \tag{3}$$

The time evolution of the areal-density perturbation for undoped and doped targets is shown in Fig. 130.59 and compared with simulations using the 2-D, radiation–hydrodynamics code *DRACO*[17] (shown as solid lines). Cross-beam energy

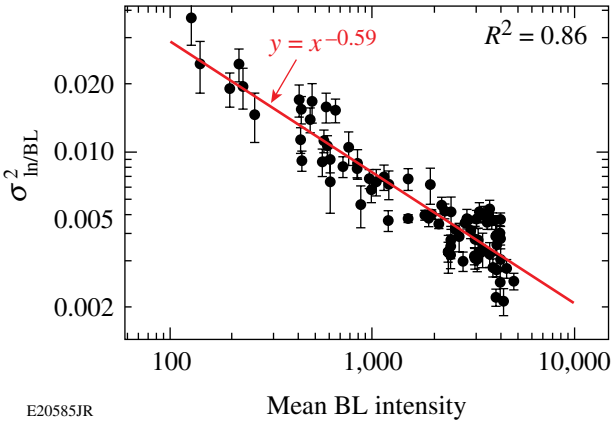

Figure 130.58
Measured rms of backlighter intensity as a function of mean backlighter intensity. A power fit is shown as the red line.

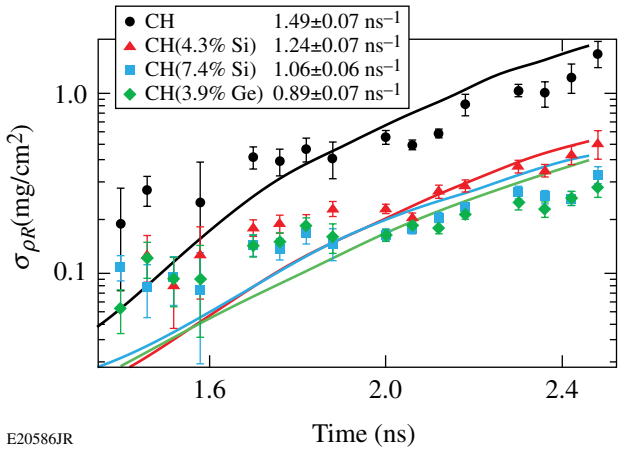

Figure 130.59
The time evolution of the areal-density perturbation amplitude for undoped and doped targets. The symbols are the measured data and the solid lines of the same color are the *DRACO* calculations. The corresponding measured growth rates, calculated as the slopes of the respective exponential fits, are shown in the legend box.

transfer (CBET)[20] was taken into account, providing a slightly reduced drive.

The initial perturbation amplitude at the beginning of the acceleration phase was reduced by a factor of 2.5±0.5 for CH [4.3% Si] targets and by a factor of 3±0.5 for CH [7.4% Si] and CH [3.9% Ge] targets. At the end of compression the reduction factor in the density modulation becomes 3±0.5 and 5±0.5, correspondingly. All targets exhibit exponential perturbation growth, and their growth rates are calculated as the slopes of the respective exponential fits. The doped targets demonstrate a reduction in the growth rate from ≈1.5 ns^{-1} for pure-CH targets to ≈0.9 ns^{-1} for targets doped with 3.9% Ge. The reduction in the growth rate also agrees well with the growth rates for the dominant wavelengths calculated by *DRACO*: 1.46 ns^{-1} for pure-CH targets and 0.92 ns^{-1} for targets doped with 3.9% Ge. A more-detailed comparison can be found in Ref. 21.

The 2-D simulations reproduce the experimental trend of reduction in modulation and the growth rate reasonably well except at the beginning of acceleration when the measured perturbations are somewhat larger than predicted by *DRACO*. The discrepancy could be caused by a small signal amplitude and a large noise contribution at the beginning of acceleration. A similar deviation was observed in earlier spherical compression experiments.[19] At the end of the acceleration phase, the signal is much larger and agreement with numerical simulations is much better.

3. Spectral Composition

To gain insight into the structure of the shell's density modulation, its spatial power spectrum is calculated by performing 2-D, MTF-corrected Fourier decomposition. Typical power spectra for driven and undriven CH spherical targets are shown in Fig. 130.60 as functions of the spatial frequency. As expected, the driven and undriven spectra merge at a frequency corresponding to the MTF-limited resolution. The difference between the two power spectra is the spectrum of the areal-density fluctuation. The power spectra of the optical-density modulation for CH [3.9% Ge] targets at different times are shown in Fig. 130.61. The power spectra calculated by *DRACO* are shown in the same plots and are in reasonable agreement

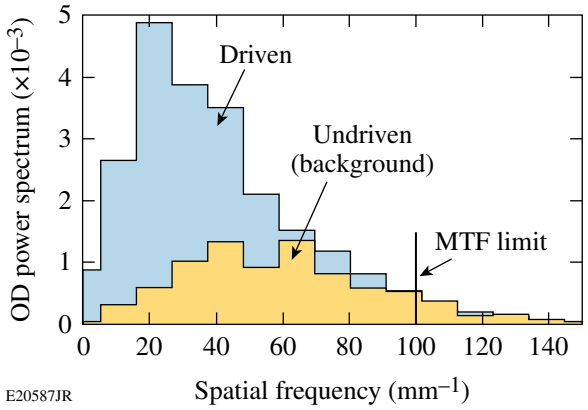

Figure 130.60
Spatial power spectra of optical-density modulation for undriven and driven spherical CH targets at t = 2.4 ns. The undriven target's modulation is caused by the nonuniformities in the backlighter radiation and is subtracted from the driven target's modulation to obtain the modulation in the shell's areal density.

with the measured spectra. The results indicate that during the acceleration phase, the spectral power is shifting from high spatial frequencies (short wavelengths) at the beginning to shorter spatial frequencies (long wavelengths) later in time, similar to what was observed for planar targets.[22,23]

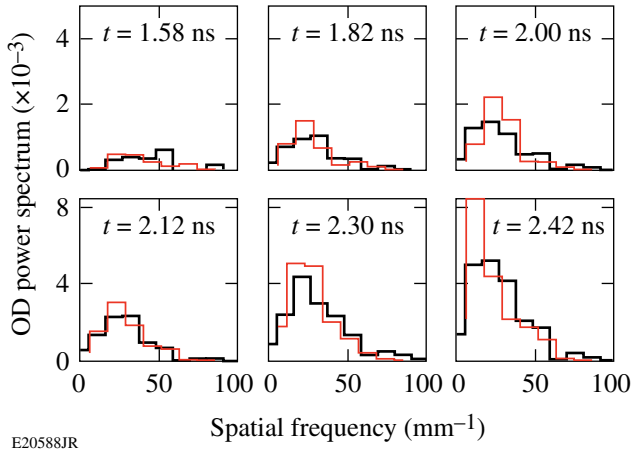

Figure 130.61
Plots of OD power spectra for CH [3.9% Ge] spherical targets at different times. The measured spectra are shown as thick (black) lines and the calculated spectra are shown as thin (red) lines.

Discussion and Conclusions

The experiments have demonstrated that doping plastic shells with a several-percent concentration of medium-Z impurity such as Si or Ge substantially decreases the initial imprint and the growth rate, leading to a significant reduction of the shell's areal-density perturbation. The initial perturbation amplitude at the beginning of the compression phase was reduced by a factor of 2.5±0.5 for CH [4.3% Si] targets and by a factor of 3±0.5 for CH [7.4% Si] and CH [3.9% Ge] targets. At the end of compression the reduction factor in the density modulation becomes 3±0.5 and 5±0.5, correspondingly. The doped targets demonstrate a reduction in the growth rate from ≈1.5 ns^{-1} for pure-CH targets to ≈0.89 ns^{-1} for targets doped with 3.9% Ge. The results agree well with numerical simulations using *DRACO*. From the analysis of the simulation results described in Ref. 21, the main mechanisms of the growth suppression are (a) an increase in the stand-off distance between the laser-absorption region to the ablation front and (b) enhanced coronal radiation preheating in doped shells. The simulations show that the ablation velocity increases from V_a = 5.95 μm/s for CH targets to V_a = 13.5 μm/s for CH [3.9% Ge] targets, which reduces the RT linear growth rate according to the fitting formula[14] $\gamma_k = 0.94\sqrt{kg/(1+kL_n)} - 1.5\,kV_a$, where k is the modulation wave vector, g is the acceleration, and L_n is the gradient length. Ignition-scale direct-drive target designs would require doping only the outer half of the ablator material to prevent excessive radiation preheating of the main fuel. Future experiments will address the imprint reduction effects in shells with the dopant introduced only into the outer layer of the ablator.

ACKNOWLEDGMENT

This work was supported by the U.S. Department of Energy Office of Inertial Confinement Fusion under Cooperative Agreement No. DE-FC52-08NA28302, the University of Rochester, and the New York State Energy Research and Development Authority. The support of DOE does not constitute an endorsement by DOE of the views expressed in this article.

REFERENCES

1. J. D. Lindl, *Inertial Confinement Fusion: The Quest for Ignition and Energy Gain Using Indirect Drive* (Springer-Verlag, New York, 1998).
2. J. D. Lindl, R. L. McCrory, and E. M. Campbell, Phys. Today **45**, 32 (1992).
3. S. Chandrasekhar, in *Hydrodynamic and Hydromagnetic Stability*, International Series of Monographs on Physics (Clarendon Press, Oxford, 1961).
4. T. R. Boehly, D. L. Brown, R. S. Craxton, R. L. Keck, J. P. Knauer, J. H. Kelly, T. J. Kessler, S. A. Kumpan, S. J. Loucks, S. A. Letzring, F. J. Marshall, R. L. McCrory, S. F. B. Morse, W. Seka, J. M. Soures, and C. P. Verdon, Opt. Commun. **133**, 495 (1997).
5. S. Skupsky, R. W. Short, T. Kessler, R. S. Craxton, S. Letzring, and J. M. Soures, J. Appl. Phys. **66**, 3456 (1989).
6. Y. Lin, T. J. Kessler, and G. N. Lawrence, Opt. Lett. **20**, 764 (1995).
7. T. R. Boehly, V. A. Smalyuk, D. D. Meyerhofer, J. P. Knauer, D. K. Bradley, R. S. Craxton, M. J. Guardalben, S. Skupsky, and T. J. Kessler, J. Appl. Phys. **85**, 3444 (1999).
8. V. N. Goncharov, J. P. Knauer, P. W. McKenty, P. B. Radha, T. C. Sangster, S. Skupsky, R. Betti, R. L. McCrory, and D. D. Meyerhofer, Phys. Plasmas **10**, 1906 (2003).
9. J. P. Knauer, K. Anderson, R. Betti, T. J. B. Collins, V. N. Goncharov, P. W. McKenty, D. D. Meyerhofer, P. B. Radha, S. P. Regan, T. C. Sangster, V. A. Smalyuk, J. A. Frenje, C. K. Li, R. D. Petrasso, and F. H. Séguin, Phys. Plasmas **12**, 056306 (2005).
10. N. Ohnishi *et al.*, J. Quant. Spectrosc. Radiat. Transf. **71**, 551 (2001).
11. S. P. Obenschain *et al.*, Phys. Plasmas **9**, 2234 (2002).
12. A. N. Mostovych, D. G. Colombant, M. Karasik, J. P. Knauer, A. J. Schmitt, and J. L. Weaver, Phys. Rev. Lett. **100**, 075002 (2008).
13. V. N. Goncharov, T. C. Sangster, P. B. Radha, R. Betti, T. R. Boehly, T. J. B. Collins, R. S. Craxton, J. A. Delettrez, R. Epstein, V. Yu. Glebov, S. X. Hu, I. V. Igumenshchev, J. P. Knauer, S. J. Loucks, J. A. Marozas, F. J. Marshall, R. L. McCrory, P. W. McKenty, D. D. Meyerhofer, S. P. Regan, W. Seka, S. Skupsky, V. A. Smalyuk, J. M.

Soures, C. Stoeckl, D. Shvarts, J. A. Frenje, R. D. Petrasso, C. K. Li, F. Séguin, W. Manheimer, and D. G. Colombant, Phys. Plasmas **15**, 056310 (2008).

14. R. Betti, V. N. Goncharov, R. L. McCrory, and C. P. Verdon, Phys. Plasmas **5**, 1446 (1998).

15. D. K. Bradley, P. M. Bell, O. L. Landen, J. D. Kilkenny, and J. Oertel, Rev. Sci. Instrum. **66**, 716 (1995).

16. V. A. Smalyuk, T. R. Boehly, L. S. Iwan, T. J. Kessler, J. P. Knauer, F. J. Marshall, D. D. Meyerhofer, C. Stoeckl, B. Yaakobi, and D. K. Bradley, Rev. Sci. Instrum. **72**, 635 (2001).

17. P. B. Radha, V. N. Goncharov, T. J. B. Collins, J. A. Delettrez, Y. Elbaz, V. Yu. Glebov, R. L. Keck, D. E. Keller, J. P. Knauer, J. A. Marozas, F. J. Marshall, P. W. McKenty, D. D. Meyerhofer, S. P. Regan, T. C. Sangster, D. Shvarts, S. Skupsky, Y. Srebro, R. P. J. Town, and C. Stoeckl, Phys. Plasmas **12**, 032702 (2005).

18. J. P. Knauer, R. Betti, D. K. Bradley, T. R. Boehly, T. J. B. Collins, V. N. Goncharov, P. W. McKenty, D. D. Meyerhofer, V. A. Smalyuk, C. P. Verdon, S. G. Glendinning, D. H. Kalantar, and R. G. Watt, Phys. Plasmas **7**, 338 (2000).

19. V. A. Smalyuk, S. X. Hu, J. D. Hager, J. A. Delettrez, D. D. Meyerhofer, T. C. Sangster, and D. Shvarts, Phys. Rev. Lett. **103**, 105001 (2009).

20. I. V. Igumenshchev, D. H. Edgell, V. N. Goncharov, J. A. Delettrez, A. V. Maximov, J. F. Myatt, W. Seka, A. Shvydky, S. Skupsky, and C. Stoeckl, Phys. Plasmas **17**, 122708 (2010).

21. S. X. Hu, G. Fiksel, V. N. Goncharov, S. Skupsky, D. D. Meyerhofer, and V. A. Smalyuk, "Mitigating Laser Imprints in Direct-Drive ICF Implosions with High-*Z* Dopants," submitted to Physical Review Letters.

22. V. A. Smalyuk, T. R. Boehly, D. K. Bradley, V. N. Goncharov, J. A. Delettrez, J. P. Knauer, D. D. Meyerhofer, D. Oron, and D. Shvarts, Phys. Rev. Lett. **81**, 5342 (1998).

23. V. A. Smalyuk, O. Sadot, J. A. Delettrez, D. D. Meyerhofer, S. P. Regan, and T. C. Sangster, Phys. Rev. Lett. **95**, 215001 (2005).

Shell-Trajectory Measurements from Direct-Drive–Implosion Experiments

In direct-drive inertial confinement fusion (ICF), laser beams are focused directly onto a fusion capsule that is imploded to reach thermonuclear ignition. The laser beams ablate the target surface and, through the rocket effect, drive the shell to high velocities. Accurate velocity measurements are critical since the minimum total laser energy for ignition is proportional to V_{imp}^{-6}, where V_{imp} is the implosion velocity.[1] Hydrodynamic models show 10% differences in the velocity (~200 km/s) for typical direct-drive implosions on OMEGA.[2,3] To distinguish among models, the velocity must be measured to within an accuracy of 2%. To achieve this accuracy over 200 ps, the radius and time must be measured to within accuracies of ~1 μm and ~5 ps, respectively.

X-ray radiography has long been applied to ICF experiments[4,5] to measure the shell's velocity, but this technique requires backlighter beams that are taken from the 60 OMEGA drive beams, which reduces the available drive beams, thereby reducing the drive symmetry and efficiency. The accuracy of the radial measurements is often dominated by errors in Abel inversion. X-ray radiography is typically possible only when the laser is turned off because the self-emission adds significant noise to the measurements.

In this article, we present a technique[2,3] where the soft x-ray self-emission of a directly driven target is measured with an x-ray framing camera (XRFC)[6,7] and used to determine the trajectory of the imploding shell. A coronal plasma extending from the ablation surface of the imploding shell to the underdense plasma produces a ring of soft x rays that are imaged to the diagnostic plane. With the proper choice of filtration, a combination of the limb effect and an optically thick shell produces an instrument-limited (~5-μm) emission gradient. This steep gradient and the ability to average over many angles enables one to measure the radius of the imploding shell to an accuracy of better than 1 μm. Combined with the well-characterized XRFC timing (an accuracy of ~5 ps over 200 ps), a 2% velocity measurement is obtained.

The diagnostic obtains 16 radial measurements of the shell during the implosion by imaging the x-ray self-emission of the target integrated along the direction of the diagnostic [Fig. 130.62(a)]. A high contrast is observed between the intensity of the surrounding part and the inner part of the images [Fig. 130.62(a)]. The maximum intensity corresponds to the limb effect produced by the x rays emitted by the coronal plasma. When the cold shell reaches significant convergence, it becomes optically thick, absorbing radiation coming from the back of the sphere, which further enhances the contrast. The radius measurement (corresponding to the position of the sharp intensity gradient at the inner circle) is obtained without knowledge of the path-integrated x-ray emission through plasma and absorption through the shell (i.e., no Abel inversion is required and the measurement is insensitive to the x-ray emission profile).

An array of 16 6-μm-diam pinholes are used to produce 16 x-ray images of the target on a four-strip XRFC.[6,7] For optimum resolution, 12× magnification was used with a distance between the target and the detector plane of 38.1 cm. The resolution of the system was calculated by convolving the pinhole with a multichannel plate (MCP)[8] using the ray-tracing program FRED,[9] resulting in an edge spread function that increases from 10% to 90% over 5 μm. The MCP integration time was 40 ps (Ref. 7). The interstrip timing was 200 ps and determined within 5 ps using the Multi-Terawatt laser.[10]

To determine the optimum filtering, Spect3D[11] was used to post-process hydrodynamic simulations of a 20-μm plastic shell implosion and obtain the x-ray emission at the diagnostic plane. Figure 130.62(b) shows the calculated spectrum, at the detector plane, along a line extending from the center of the target (R = 0) to beyond the coronal plasma ($R \approx 400$ μm). Three distinct x-ray emission regions are observed with varying contrast: (1) for low photon energies (<250 eV), a narrow, ~50-μm emission region with a medium contrast is observed; (2) for medium photon energies (250 to 500 eV), three distinct

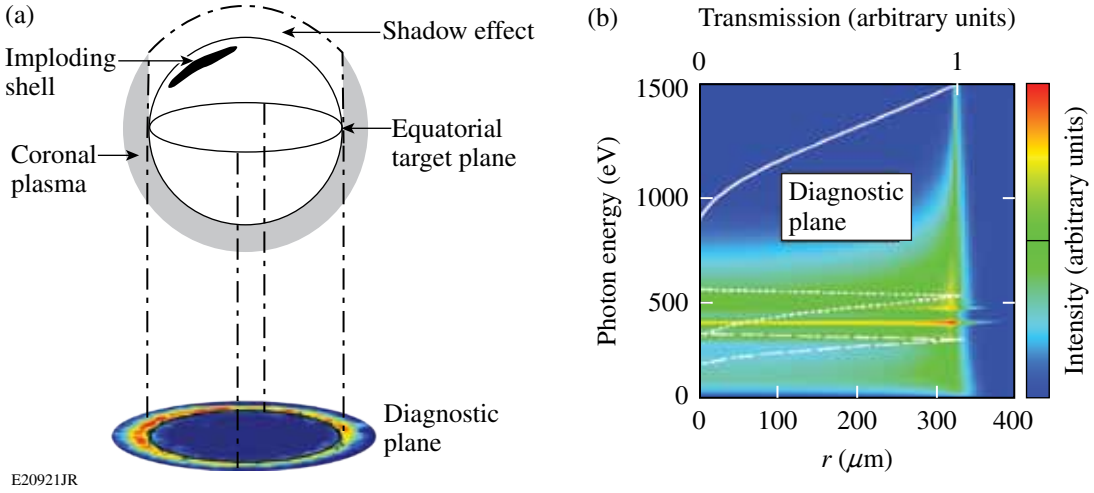

Figure 130.62
(a) Schematic of the limb and shadow effects; (b) simulated spectrally resolved emission at the diagnostic plane integrated along the diagnostic line of sight. The normalized spectral transmission of the low-photon-energy filter (dashed curve), the medium-photon-energy filter (dotted curve), and the high-photon-energy filter (solid curve).

spectral features corresponding to the line emission of the carbon and a low contrast are observed; and (3) for high photon energies (>800 eV), a very thin emission region with a high contrast is observed.

Figure 130.63 shows the results of an experiment performed to investigate the three x-ray-emission regions. The normalized filter transmissions are plotted in Fig. 130.62(b). The low-photon-energy filter used a 3° reflection from Al and transmission through 5-μm-thick parylene N to create a passband filter at ~200 eV. The medium-photon-energy filter used a 3° reflection from Al and transmission through 1-μm-thick vanadium to create a passband filter at ~400 eV. The high-photon-energy filter used 25.4-μm-thick beryllium to create a high-pass filter at ~100 eV. Figure 130.63(c) shows the optimal filtering (with high photon energy) with high contrast, leading to a sharp inner edge to the x-ray emission.

Figure 130.64(a) compares the simulated x-ray emission, spectrally integrated after passing through the high-photon-energy filter, with the corresponding measurements. The location of the middle intensity point in the sharp inner gradient [black curve in Fig. 130.64(c)] is used to determine the shell's radius. After moderate compression, the shell becomes

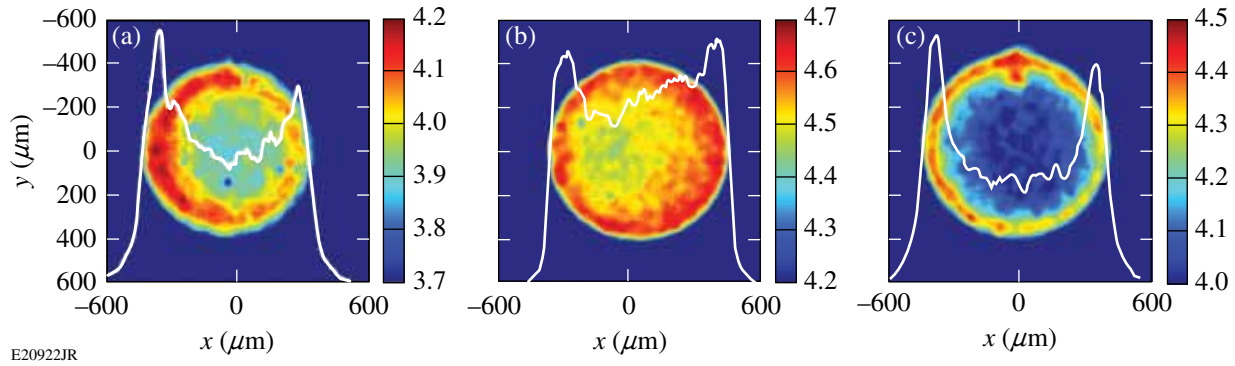

Figure 130.63
Self-emission images and lineouts (white) obtained with the XRFC with a 4× magnification using three different filters: (a) low photon energy; (b) medium photon energy; and (c) high photon energy.

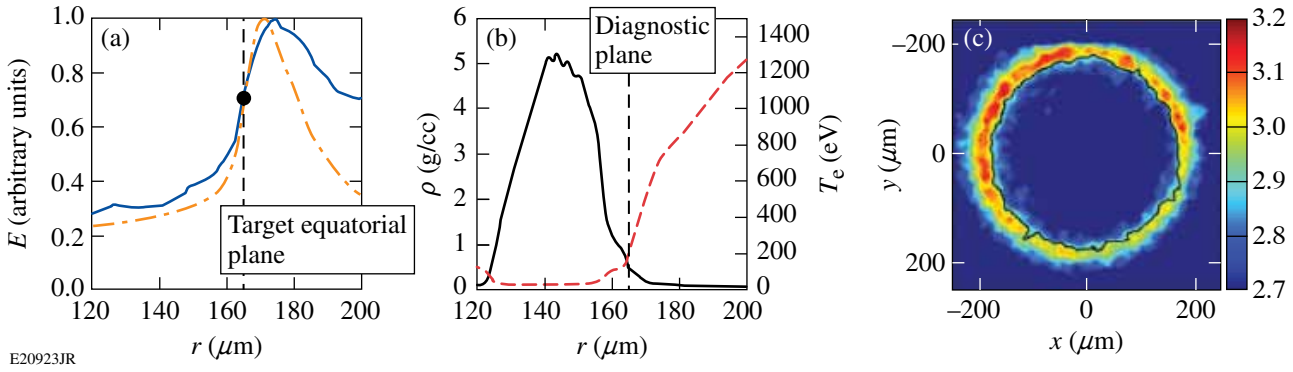

Figure 130.64
(a) Emission at the diagnostic plane obtained by post-processing hydrodynamic simulations and passing through a high-energy filter (orange dashed/dotted line) and experimental emission measured with the XRFC (blue line). The curves are normalized to their maximum values. (b) The calculated electron density (solid black line) and temperature (red dashed line) in the target equatorial plane. (c) Example of an experimental image measured with the XRFC; the black curve corresponds to the curve of the inner gradient, middle intensity point for different angles.

optically thick to x rays above 500 eV, removing the emission from the back of the shell, reducing the signal in the center of the image by a factor of 2, and enhancing the inner gradient [shadow effect represented in Fig. 130.62(a)]. When the laser is on, the middle intensity point corresponds to the ablation surface [Fig. 130.64(b)]. The ablation front follows the mass average point [Fig. 130.65].

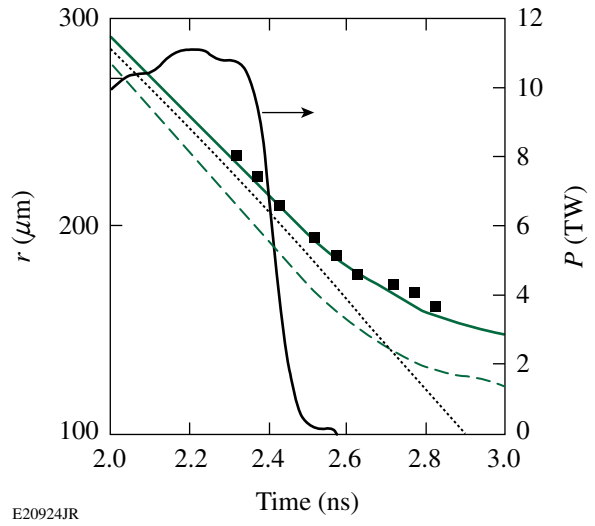

Figure 130.65
Temporal evolution of the laser beams (black solid curve, right axis), shell radius post-processed with Spect3D for simulations with (green solid curve) and without (green dashed curve) cross-beam energy transfer (CBET) and experimental shell trajectories (black squares). For reference, the shell mass averaged point is plotted for the simulations that include CBET (dotted curve). At the end of the laser pulse, the plasma is no longer heated, which results in a decoupling of the x-ray absorption and the shell position.

The accuracy in determining the radius of the middle intensity point is ~3 μm given by σ_n/ρ, where σ_n is the standard deviation of the photon intensity noise and ρ is the slope of the gradient. A standard deviation from the average radius obtained from different angular measurements is 3.5 μm. An accuracy of <1 μm is obtained when averaging the measurements over different angles; this increases the accuracy by a factor of $1/\sqrt{N}$, where N is the number of independent measurements of the radius along different chords passing through the center of the shell (for a shell radius of 150 μm, $\sqrt{N} \sim 10$).

As an example of a use of the diagnostic technique described above, Fig. 130.65 compares the measured and simulated shell trajectories with and without cross-beam energy transfer (CBET) (the experiment is described in detail in Ref. 3). The diagnostic measurements validate the CBET model in *LILAC* simulations.[3] The averaged shell velocity is measured between 2.3 and 2.5 ns to be 200±2 km/s.

ACKNOWLEDGMENT

This work was supported by the U.S. Department of Energy Office of Inertial Confinement Fusion under Cooperative Agreement No. DE-FC52-08NA28302, the University of Rochester, and the New York State Energy Research and Development Authority. The support of DOE does not constitute an endorsement by DOE of the views expressed in this article.

REFERENCES

1. M. C. Herrmann, M. Tabak, and J. D. Lindl, Nucl. Fusion **41**, 99 (2001).

2. D. H. Froula, I. V. Igumenshchev, D. T. Michel, D. H. Edgell, R. Follett, V. Yu. Glebov, V. N. Goncharov, J. Kwiatkowski, F. J. Marshall, P. B. Radha, W. Seka, C. Sorce, S. Stagnitto, C. Stoeckl, and T. C. Sangster, Phys. Rev. Lett. **108**, 125003 (2012).

3. I. V. Igumenshchev, W. Seka, D. H. Edgell, D. T. Michel, D. H. Froula, V. N. Goncharov, R. S. Craxton, L. Divol, R. Follett, J. H. Kelly, T. Z. Kosc, P. Michel, R. L. McCrory, A. V. Maximov, D. D. Meyerhofer, J. F. Myatt, T. C. Sangster, A. Shvydky, S. Skupsky, and C. Stoeckl, "Crossed-Beam Energy Transfer in Direct-Drive Implosions," to be published in Physics of Plasmas.

4. D. G. Hicks, B. K. Spears, D. G. Braun, R. E. Olson, C. M. Sorce, P. M. Celliers, G. W. Collins, and O. L. Landen, Phys. Plasmas **17**, 102703 (2010).

5. F. J. Marshall, P. W. McKenty, J. A. Delettrez, R. Epstein, J. P. Knauer, V. A. Smalyuk, J. A. Frenje, C. K. Li, R. D. Petrasso, F. H. Séguin, and R. C. Mancini, Phys. Rev. Lett. **102**, 185004 (2009).

6. D. K. Bradley, P. M. Bell, J. D. Kilkenny, R. Hanks, O. Landen, P. A. Jaanimagi, P. W. McKenty, and C. P. Verdon, Rev. Sci. Instrum. **63**, 4813 (1992).

7. D. K. Bradley *et al*., Rev. Sci. Instrum. **66**, 716 (1995).

8. V. A. Smalyuk, T. R. Boehly, D. K. Bradley, J. P. Knauer, and D. D. Meyerhofer, Rev. Sci. Instrum. **70**, 647 (1999).

9. Photon Engineering, accessed 9 April 2012, http://www.photonengr.com.

10. V. Bagnoud, I. A. Begishev, M. J. Guardalben, J. Puth, and J. D. Zuegel, Opt. Lett. **30**, 1843 (2005).

11. J. J. MacFarlane *et al*., High Energy Density Phys. **3**, 181 (2007).

Spherical Shock-Ignition Experiments with the 40 + 20-Beam Configuration on OMEGA

Introduction

Shock ignition (SI)[1] is a promising new concept in direct-drive inertial confinement fusion (ICF) that achieves thermonuclear ignition and burn by a strong focusing shock wave in a precompressed DT shell.[2] Shock ignition, as described in Ref. 1, is a two-step scheme designed to enhance the hot-spot compression with respect to the single-step conventional hot-spot ignition.[3] SI uses a moderate-intensity assembly laser pulse followed by a subnanosecond high-intensity spike that launches a strong shock wave (the ignitor shock) into the imploding shell. It is important to emphasize that SI does not use a shock wave to directly ignite the dense fuel;[4] instead, it relies on the collision of the ignitor and the rebound shock waves at the inner shell surface to raise the hot-spot pressure.[1] A non-isobaric fuel assembly with a centrally peaked pressure profile makes SI more energy efficient by lowering the ignition threshold compared to isobaric assemblies.[1] Thick-shell targets containing more fuel can be compressed on a low adiabat with a low implosion velocity, which promises high fusion gains[1,2,5–7] at moderate laser energies. One-dimensional (1-D) simulations[7,8] have described igniting SI designs with as low as ~300 kJ of total laser energy. The SI requirements for laser pulse shaping are more demanding than in conventional hot-spot–ignition designs but are still within the pulse-shaping capabilities of currently operating laser systems like the National Ignition Facility (NIF).[9] Proof-of-principle experiments on the NIF were recently proposed;[10] also, SI is considered to be a viable option[8] for the European direct-drive HiPER project.[11]

The intensity of the spike pulse is expected to be a few times of 10^{15} W/cm^2. At these high intensities, parametric plasma instabilities[12] such as stimulated Brillouin scattering (SBS), stimulated Raman scattering (SRS), and the two-plasmon-decay (TPD) instability are of concern in an ignition target design for two reasons: The instabilities generate energetic electrons that might preheat the shell with the consequence of reducing the final core compression and they increase the back-reflection of the laser light from the target, degrading the laser-energy coupling to the capsule. SI designs typically apply lower laser intensity during the main part of the drive than in hot-spot designs, so these issues might be less important during the early compression phase. Strong growth of laser–plasma instabilities and significant transfer of laser energy to hot electrons are expected during the high-intensity ignitor spike. The areal density increases during the implosion, and if the range of the hot electrons is less than the shell thickness, the electrons are stopped in the outer regions of the shell and do not considerably increase the adiabat of the inner part of the shell.[13] The hot electrons might then be advantageous for SI because they improve the shock strength. The effect of hot electrons on a NIF-scale SI target[13] was modeled in 1-D for a marginal igniting target using a multigroup diffusion model[14] for the hot electrons. The ignition (time) window for shock launching is considerably wider when the effects of moderate-energy hot electrons are included. The simulations[13] show that a NIF-scale target can efficiently stop up to 150-keV electrons that are generated during the spike pulse. Hot electrons can be beneficial for SI as long as their range is shorter than the shell's thickness. Important parameters are therefore the hot-electron temperature, the amount of laser energy that is transferred into electrons, and the time of generation.

This article presents SI experiments on the OMEGA laser[15] that use a novel beam configuration called the 40 + 20-beam configuration. Preliminary results with this configuration are discussed in Ref. 16. It uses 40 of the 60 OMEGA beams to implode the target with a low-intensity laser pulse, and the remaining 20 beams are tightly focused to launch a late shock into the imploding shell. Compared to the highly symmetric 60-beam implosions, irradiation nonuniformity with normal-incidence beams is higher in the 40 + 20 configuration. The implosion performance was also studied with a beam configuration with repointed beams. The experiments demonstrated significant improvement in implosion performance (higher neutron yield, higher areal density, and rounder core in x-ray images) with repointed beams. Two-dimensional (2-D) hydrodynamic simulations were performed for the repointed beam configuration. A similar concept, using a dedicated group of beams with a low-intensity pulse to implode the capsule and a second group of beams with a short high-intensity pulse for the

ignitor shock wave, might be implemented on the NIF.[17] The 40 + 20 configuration makes it possible to study high-intensity coupling on OMEGA and to measure hot-electron production and laser backscattering for intensities that are SI relevant. Previous spherical target SI experiments[18] on OMEGA studied the fuel assembly with 60-beam symmetric implosions. In those experiments, the shock wave was launched by a spike at the end of the pulse on all 60 beams with a maximum intensity of $\sim 7 \times 10^{14}$ W/cm^2. OMEGA cannot produce the requisite SI intensity with a compression pulse using the symmetric 60-beam configuration on a standard target because it leads to intensities that are too low to study laser–plasma instabilities. Switching to the 40 + 20-beam configuration allows one to use two separate pulse shapes with high-intensity beams tightly focused to reach intensities up to $\sim 8 \times 10^{15}$ W/cm^2. While the surface-averaged intensity is still rather low ($\sim 9 \times 10^{14}$ W/cm^2), the single-beam intensities are sufficiently high to study laser–plasma interactions at shock-ignition–relevant intensities. The objectives of this work are to study the implosion performance in the 40 + 20-beam configuration, the coupling of laser energy from high-intensity beams into a spherically imploding capsule, and the laser–plasma instabilities at SI-relevant laser intensities.

This article is organized as follows: the beam configurations are presented; the targets, laser pulse shapes, and diagnostics are described; the areal-density measurements and neutron measurements, including 2-D hydrodynamic simulations, are discussed; and the time-resolved hard x-ray and laser backscatter measurements are presented.

Beam Configurations

OMEGA is a 60-beam laser that was built for direct-drive experiments operating at the third harmonic (λ = 351 nm) of the Nd:glass laser wavelength. The 60 beams are symmetrically distributed around the target chamber in a soccer-ball geometry with the beams located at the vertices of hexagons and pentagons. OMEGA consists of three laser legs, each feeding two clusters with ten beams per cluster; leg 1 feeds clusters 1 and 4, leg 2 feeds clusters 2 and 5, and leg 3 feeds clusters 3 and 6. It is possible to use two independent pulse shapes: one pulse shape in one of the legs and the other pulse shape in the other two legs. For SI studies with a spherical target, this opens up the opportunity to use two separate pulse shapes with independent control over the two beam groups. One pulse shape in two legs implodes the capsule and a short high-intensity spike pulse in the third leg drives a late shock. Two different beam-pointing configurations were used; they are designated A and B in the following configurations. Configuration A used clusters 1, 3, 4, and 6 for the drive and clusters 2 and 5 for the spike with all beams pointed to target center. The configuration with this particular choice of clusters resulted in significant target illumination nonuniformity because of the spatial and temporal separation between both beam groups. The pattern of the 40 drive beams is not as regular as in a standard 60-beam implosion, and, assuming perfect power balance, the irradiation nonuniformity was calculated to be ~11% root-mean-square (rms) variation compared to less than ~1% in a standard 60-beam spherically symmetric case.[19] A beam profile with a super-Gaussian shape given by $I(r_\mu) = I_0 \exp\left[-(r_\mu/352)^{4.1}\right]$ (where r_μ is the radius in microns) was assumed in the 40 drive beams. The focal spot for the 40 drive beams is obtained with distributed phase plates[20] with a super-Gaussian intensity distribution of fourth order, and the laser light was smoothed with polarization smoothing.[21] In configuration B, clusters 1, 2, 4, and 5 were used for the drive and clusters 3 and 6 for the spike. The irradiation nonuniformity in the 40 drive beams was ~7% rms in this configuration, which was lower than in the previous configuration. It was further improved to ~3% rms by repointing the beams. Most of the 40 drive beams were moved individually, as shown in Fig. 130.66, with the arrows representing direction and amount of shift for each beam.

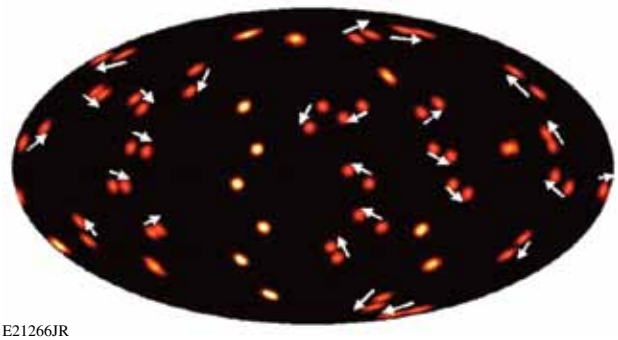

Figure 130.66
Aitoff representation of the original beam positions and repointed positions of the 40 drive beams. Arrows indicate the direction and amount of displacement. Some beams were not moved. The configuration with repointed beams is referred to as configuration B, while in configuration A all beams are pointed to target center.

Figure 130.67 shows the intensity variation of the 40 repointed drive beams in (a) an Aitoff presentation and (b) a 3-D rendering. The illumination pattern in Fig. 130.67(b) was averaged over the azimuthal angle, which resulted in the axisymmetric illumination pattern shown in Fig. 130.67(c) that was used as input in 2-D cylindrical symmetric simulations with the radiation–hydrodynamic code CHIC.[22] Figure 130.68 shows the laser-intensity variation of the axisymmetric irradia-

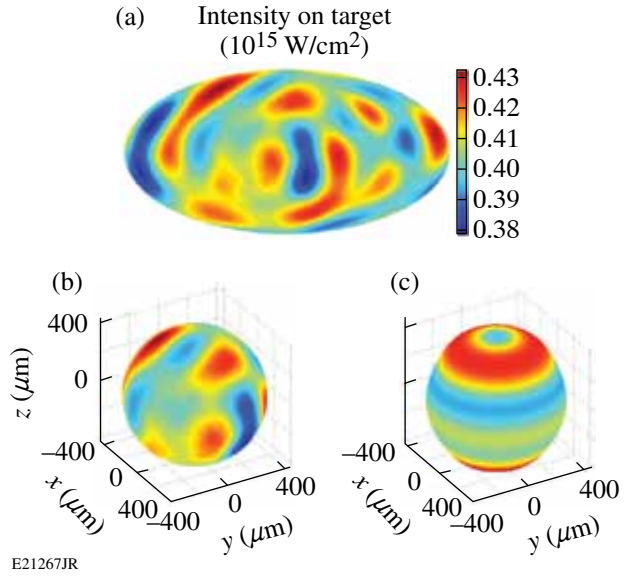

Figure 130.67
Intensity variation of 40 repointed drive beams (configuration B) in (a) an Aitoff representation and (b) a 3-D rendering. (c) The azimuthally averaged intensity distribution was used as input in 2-D cylindrical symmetric hydrodynamic simulations with the code CHIC.[22]

tion pattern versus polar angle and a Legendre-mode analysis, indicating that the modes $\ell = 2$, 4, 6, and 7 are dominant. In addition, a robustness study with respect to power imbalance was performed. A power imbalance of about ±8% on the illumination was assumed. From six random power configurations, the results show that the nonuniformity increases by ~25% to ~3.5% rms. Besides the Legendre mode $\ell = 2$, the odd modes 1 and 3 are considerably increased in the presence of power imbalance. Moreover, the maximum of the $\ell = 1$ amplitude is equivalent to a target offset of 5 μm, which further indicates that the 40-beam configuration is sensitive to power imbalance.

To achieve best symmetry in configuration B, a beam repointing from target center was also performed for the 20 spike beams, as shown in Fig. 130.69. The 20 beams were moved to the vertices of a dodecahedron pattern. This means that the beams were repointed on four rings at the following polar angles: 37.4°, 79.2°, 100.8°, and 142.6°. Figure 130.69 shows that each of the 20 spike beams was moved individually, where the arrows represent the direction and the amount of shift of each beam. Significantly larger shifts were used in the 20 spike beams.

The single-beam laser intensity of the 20 spike beams on target was controlled by changing the radial beam's focal position. It is important to make a clear distinction between the average intensity $\langle I_{\text{spike}} \rangle$ and the single-beam intensity (SBI) of the spike beams on the capsule surface. The SBI ranges from $I_{\text{spike}} \sim 0.5 \times 10^{15}$ to $\sim 8 \times 10^{15}$ W/cm^2, while the average intensity on target is not affected as much by the focusing and is $\langle I_{\text{spike}} \rangle \sim 0.5 \times 10^{15}$ W/cm^2. The average intensity is the relevant quantity to determine the shock strength and the

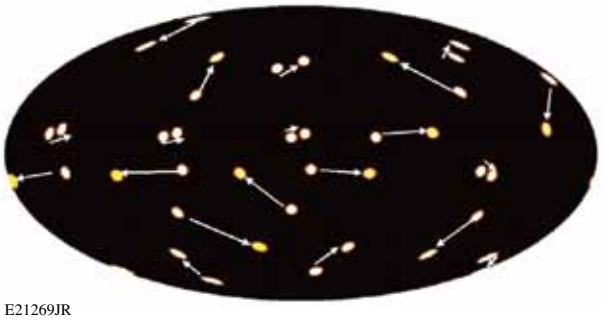

Figure 130.69
Aitoff representation of the original beam positions and repointed positions of the 20 spike beams. Arrows indicate the direction and amount of displacement.

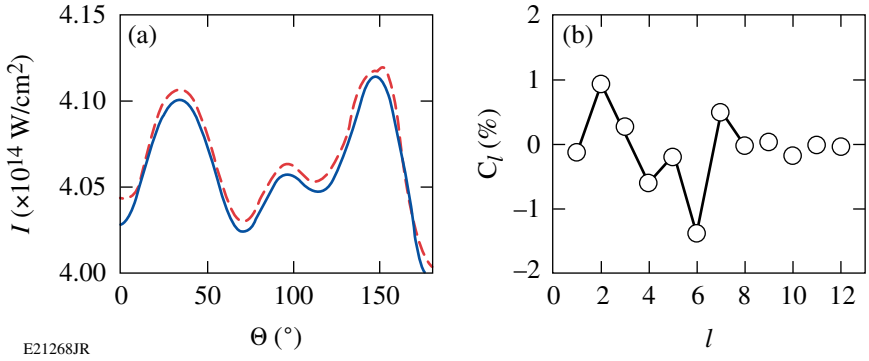

Figure 130.68
Laser-intensity variation on target of the axisymmetric irradiation pattern from Fig. 130.67(c) as a function of (a) polar angle (solid curve—initial irradiation; dashed curve—Legendre polynomial representation) and (b) Legendre-mode analysis of the pattern for ℓ below 12. Dominant modes are $\ell = 2$, 4, 6, and 7.

equivalent pressure from the spike beams. The nominal single-beam laser intensity is quoted for vacuum at the location of the critical-density plasma surface at the time when the spike pulse was launched during the implosion as calculated by simulations with the radiation–hydrodynamic codes *LILAC*[14] and CHIC. The distance from the critical-density surface to the capsule center was ~0.3 mm at 2.7 ns. At best focus, the diameter of the spike beams was estimated with ~80 μm, which gave an SBI of ~8×10^{15} W/cm^2 in vacuum. The actual intensity might be different as a result of plasma effects. Figure 130.70 shows the intensity pattern of the 20 spike beams for the following spot sizes: ~140 μm (SBI ~ 2.5×10^{15} W/cm^2), ~220 μm (SBI ~ 1×10^{15} W/cm^2), and ~580 μm (SBI ~ 0.5×10^{15} W/cm^2) without the drive beams. The foci of the 20 spike beams did not overlap at the critical-density surface for most lens positions. Only at the lowest intensity for an ~580-μm spot size did the beams partially overlapped. This created local peak intensities of ~0.7×10^{15} W/cm^2 in some regions where several beams overlapped. Except for some shots with small-spot phase plates,[23] phase plates were not used in the spike beams for most of the shots.

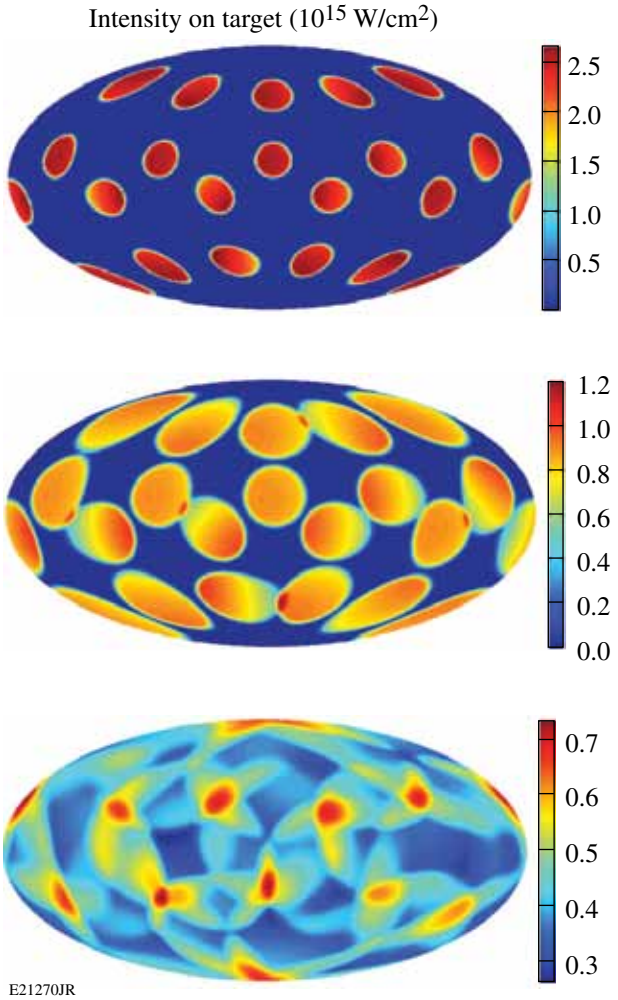

Figure 130.70
Intensity variations of the 20 repointed spike beams (configuration B), on the dodecahedron vertices in an Aitoff representation. Different lens defocus positions resulted in single-beam spike intensities of ~2.5×10^{15} W/cm^2, ~1×10^{15} W/cm^2, and ~0.5×10^{15} W/cm^2, respectively (from top to bottom).

Targets, Pulse Shapes, and Diagnostics

The targets were ~34- to 36-μm-thick, ~430-μm-outer-radius, deuterated plastic shells coated outside with a 0.1-μm layer of aluminum. They were filled with D_2 gas at a pressure of ~25 atm. The capsules were imploded on a low adiabat ($\alpha \sim$ 2.4) with a drive pulse shape that is shown for a single beam by the solid curve in Fig. 130.71. The adiabat α is defined as the ratio of the plasma pressure to the Fermi pressure of a degenerate electron gas. The pulse shape contained ~14 kJ of laser energy in 40 beams. Standard 60-beam implosions with the same pulse shape and similar targets, but higher drive energy, are discussed in Refs. 18 and 24. The drive pulse consists of an ~100-ps full-width-at-half-maximum (FWHM) picket pulse preceding a shaped main drive portion with a total duration of 2.7 ns. The 20 spike beams delivered a total energy of ~5 kJ on target and used an ~600-ps FWHM square pulse (dashed curve in Fig. 130.71).

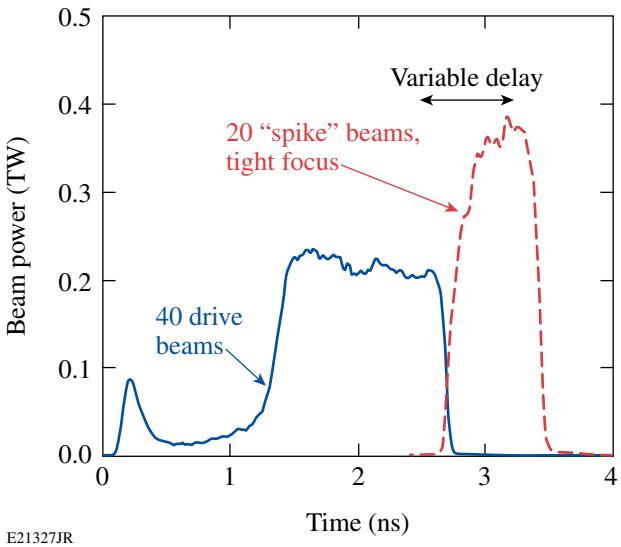

Figure 130.71
Single-beam power versus time of the drive-pulse shape (solid) for the 40 beams and the high-intensity pulse (dashed) for the 20 spike beams. Beam delay and spike intensity were varied.

The experimental observables were the spatially resolved x-ray emission from pinhole cameras,[25] the neutron yield,[26] the neutron-rate,[27] the backscattered laser energy,[28] the hard x-ray signal,[29] and the neutron-rate–averaged areal density (ρR).[30] The laser light reflected back from the imploded capsule was measured from two adjacent beam ports (a spike-beam and a drive-beam port), which were equipped with a full-aperture backscatter station (FABS).[28] Time-resolved spectra were recorded by two streaked spectrometers covering the wavelength ranges of 351±3 nm for SBS and 450 to 700 nm for SRS. The total backscattered energy in either of these spectral ranges was measured by calorimeters with an uncertainty of ±10%. The hard x-ray (HXR) signals were measured with ~100-ps temporal resolution by the HXR detector with four channels measuring x rays >20, >40, >60, and >80 keV, respectively.[29] The HXR measurements were used to infer the hot-electron temperature.[29]

Areal-Density Measurements and CHIC Simulations

Close to stagnation of the imploded shell, secondary deuterium fusion reactions in the central hot-spot region produce protons that pass through the dense, cold shell, where they lose energy. Measurement of the downshifted kinetic-energy spectrum provides information about the shell's areal density. This technique makes it possible to accurately reconstruct the proton spectrum and to infer ρR, as discussed in detail in Ref. 30. Figure 130.72(a) shows two spectra taken at an SBI of $\sim 3 \times 10^{15}$ W/cm^2. Each spectrum represents the average over several spectra from various lines of sight. The solid histogram is from an implosion with configuration A and the dashed histogram is from configuration B. Lower proton energy indicates a higher ρR. The corresponding ρR from the different lines of sight versus the target chamber polar angle is plotted in Fig. 130.72(b) with cross and circle symbols. The corresponding lines represent the average value. The ρR is almost a factor of 2 higher with configuration B, showing that repointing the beams significantly improved the implosion performance. The ρR varies with the observation direction, indicating considerable modulation in ρR, which is primarily due to illumination nonuniformities.

Two-dimensional simulations with the code CHIC studied the density and temperature modulations of the imploded capsule at stagnation for configuration B [see Fig. 130.73(a)]. Figure 130.73(b) shows simulated (curves) and measured (circles) areal density as a function of the polar angle. The black solid curve is from the 2-D simulation while the dashed line is from a 1-D simulation. The squares mark the 2-D–simulated values at those polar angles used in the measurement. The

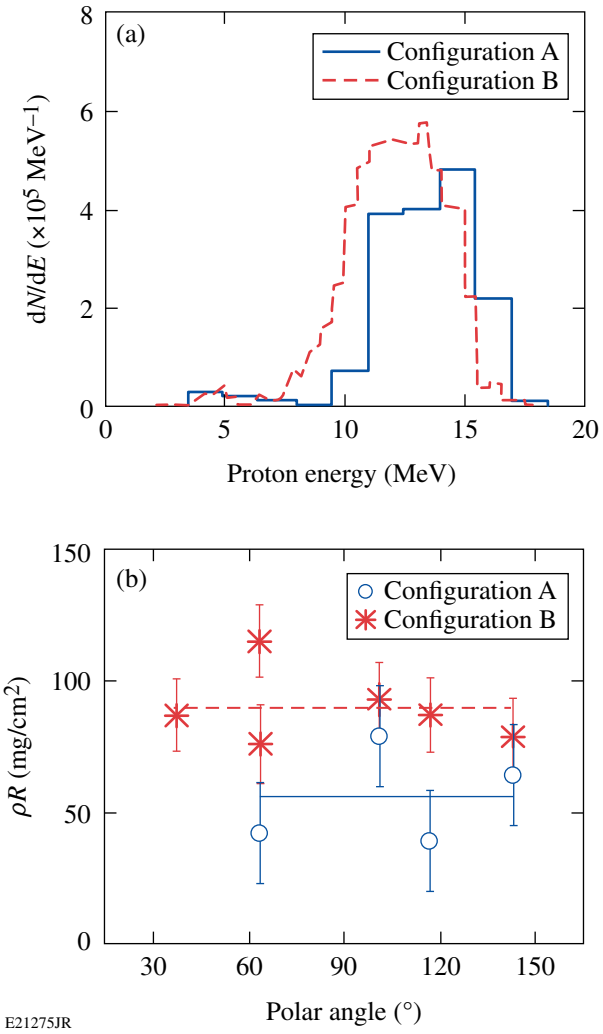

Figure 130.72
(a) Secondary proton spectra from an implosion with beam configuration A (solid) and for configuration B (dashed) under similar conditions with SBI ~ 3×10^{15} W/cm^2 and spike onset at ~2.3 ns. A lower proton energy spectrum indicates higher areal density. (b) Corresponding neutron-rate–averaged areal densities from different lines of sight are plotted versus the target chamber polar angle.

dotted line is the averaged experimental value. Note that the simulation values are higher because they represent ρR at peak neutron production, while the experimental values are temporally averaged over the neutron-production rate.

The ρR was measured for various onsets of the spike beams with respect to the start of the drive pulse and various SBI. The spike onset was varied from 2.1 to 2.8 ns (see Fig. 130.71). Figure 130.74 shows the measured angular-averaged ρR. The symbols represent 40 + 20 implosions, and the line in Fig. 130.74(b) represents a 40-beam implosion with no spike and ~14 kJ of

energy. In configuration A [Fig. 130.74(a)], the proton yield from implosions with only 40 beams was too low to provide a ρR measurement. The ρR values are consistently higher in configuration B [see Fig. 130.74(b)], showing improved implosion performance. For SBI > 1.5×10^{15} W/cm^2 there is a tendency of lower ρR for early spike onset. The lower ρR is correlated with a higher hard x-ray signal [see Fig. 130.74(c)], which could indicate preheating by hot electrons.

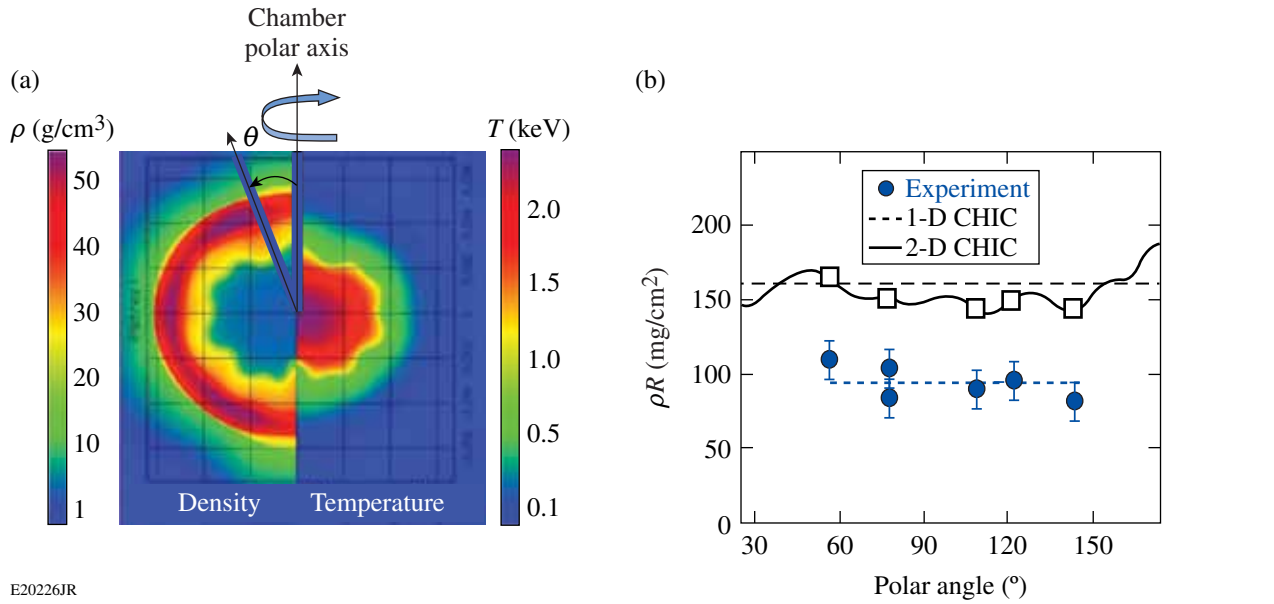

Figure 130.73
Two-dimensional (2-D) CHIC[22] simulations show significant modulations in the compressed shell. (a) Simulated density and temperature map of a 40 + 20-beam implosion close to stagnation. (b) Simulated (solid and dashed curves, squares) and measured areal density (circles) as functions of the polar angle. The SBI was ~3×10^{15} W/cm^2 and spike onset was at ~2.6 ns.

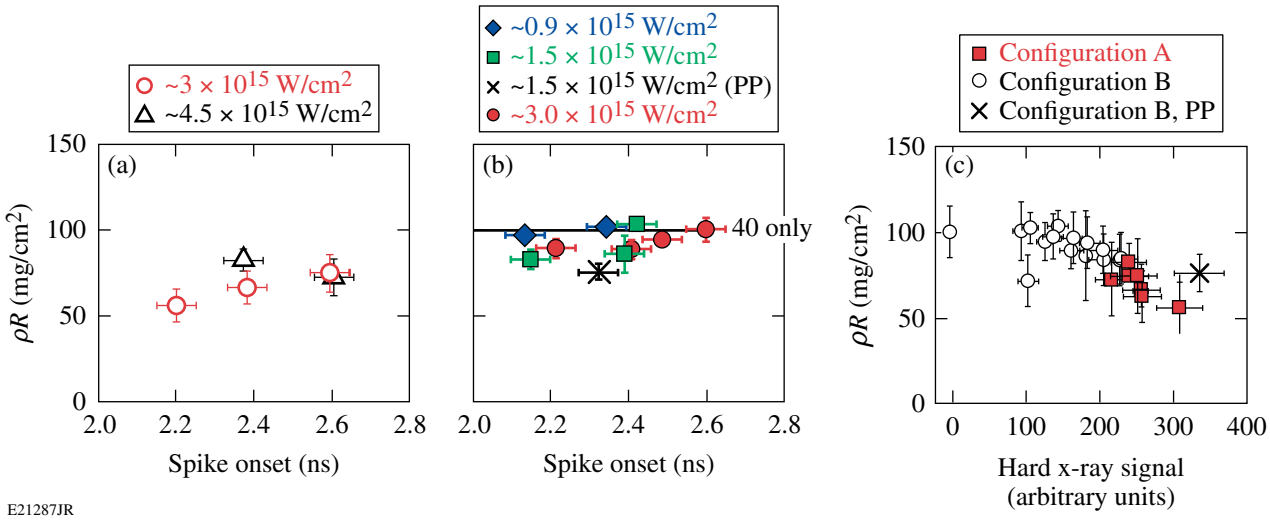

Figure 130.74
Measured areal densities from 40 + 20 implosions for (a) configuration A, (b) configuration B, and (c) both configurations versus the measured hard x-ray signal. The solid line in (b) represents the measured areal density of a 40-beam implosion. The spike onset and SBI were varied. The solid squares and open circles in (c) represent the measurements in configurations A and B, respectively, and × represents the measurement with phase plates in the spike beams in configuration B.

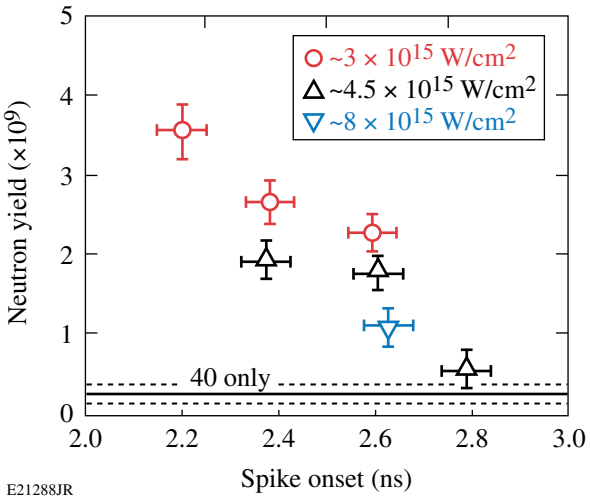

Figure 130.75
Measured neutron yield in 40 + 20-beam implosions for various spike-onset times and single-beam intensities for configuration A.

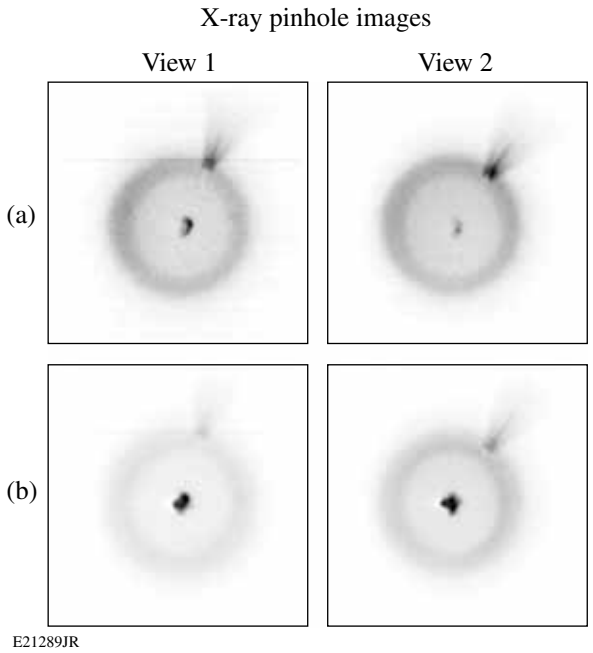

Figure 130.76
Measured time-integrated x-ray pinhole images for configuration A. Two views from different directions are shown in each row. (a) The top row represents a 40-beam implosion and (b) the lower row a 40 + 20 implosion. The V-shaped feature in the top right is the emission from the target stalk.

Neutron Measurements and CHIC Simulations

Figure 130.75 shows the measured neutron yield for beam configuration A for various spike-onset times and single-beam intensities. A maximum yield of ~3.5×10^9 was measured for the shortest time delay. Two reference implosions with only the 40 drive beams produced neutron yields of 1.4×10^8 and 3.7×10^8; the solid line in Fig. 130.75 represents the average of those yields. The low yield of the 40-beam implosion is caused by the large illumination nonuniformity in configuration A, which was also seen in a strongly perturbed core in x-ray pinhole camera images. The x-ray images[25] from two different views are shown in Fig. 130.76(a). The recorded x-ray emission is from the 2- to 7-keV range and comes from the outer-shell region, the target stalk, and the core region. Adding the spike beams mitigated the nonuniformities, leading to less core distortions [Fig. 130.76(b)] and an ~14× increase in neutron yield for the shortest spike onset. This shows that a significant amount of the energy from the high-intensity beams was coupled into the capsule. The large illumination nonuniformity in configuration A was partially mitigated by the spike beams, which led to the recovery of the neutron yield. At high intensities, the experimental yield may be affected by a high plasma reflectivity (see **Backscatter Measurements**, p. 124), which lowers the coupling efficiency. With later spike onset, there was less temporal overlap between the drive and the spike pulse and a lower neutron signal was measured. The drive and spike pulses were completely separated at 2.8 ns, which is when the lowest neutron yield was measured in the 40 + 20 implosions. For configuration A, neutron yields were strongly affected by 3-D effects in a highly perturbed core.

Similar implosions were performed with configuration B, where the illumination uniformity was significantly improved. This was demonstrated by a much rounder core in the x-ray pinhole camera images [compare Fig. 130.77(a) to Fig. 130.76(a)]. Adding the 20 spike beams did not further improve the roundness of the core emission. Figures 130.77(b) and 130.77(c) show corresponding images using (b) no phase plates and (c) small spot phase plates in the 20 spike beams, respectively. Core distortions are even slightly worse than in Fig. 130.77(a). A stronger x-ray emission is observed in Fig. 130.77(c) with phase plates. Figure 130.78 shows the (a) measured and (b) simulated neutron yields for these implosions. Implosions with repointed 40 drive beams produced neutron yields of ~1.5×10^9 [solid line in Fig. 130.78(a)], which is a factor of ~6 higher than in the implosions where beams were pointed to target center. Adding the 20 spike beams, and therefore more energy on target, enhances the yield further by a factor of up to 2.3, with a trend of slightly lower yields at longer times. With 20 spike beams, the overall neutron yield is very similar to configuration A. The neutron yield shows no significant dependence on the spike intensity. A similar trend is observed in the predicted neutron yield from 1-D CHIC simulations [Fig. 130.78(b)]. There the enhancement is up to a factor of ~3.5 when the spike beams are added, slightly more than what was measured. Configuration B

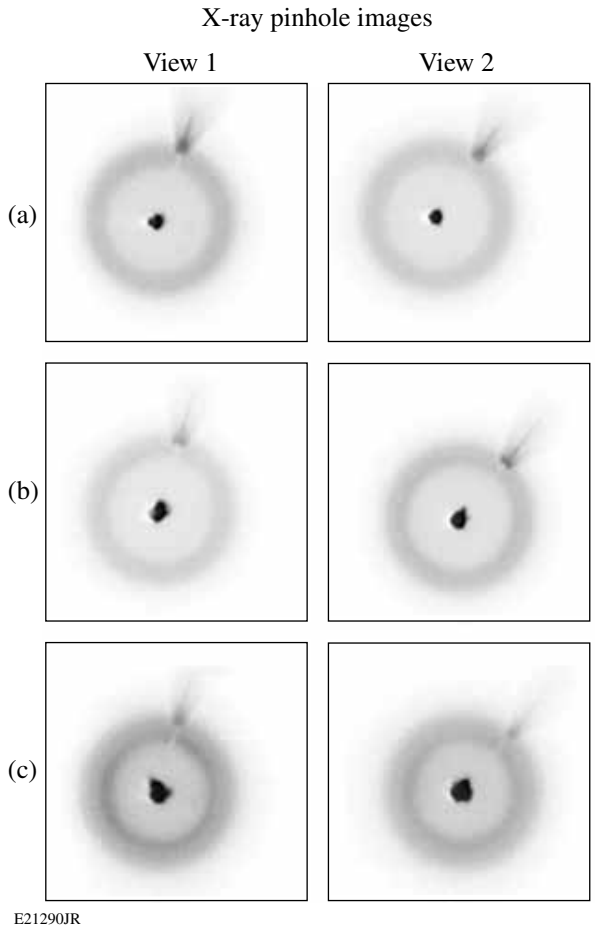

Figure 130.77
Measured time-integrated x-ray pinhole images for configuration B. Two views from different directions are shown in each row. (a) The top row represents a 40-beam implosion, (b) the middle row a 40 + 20 implosion (no phase plates in the spike beams), and (c) the lower row a 40 + 20 implosion with phase plates in the spike beams.

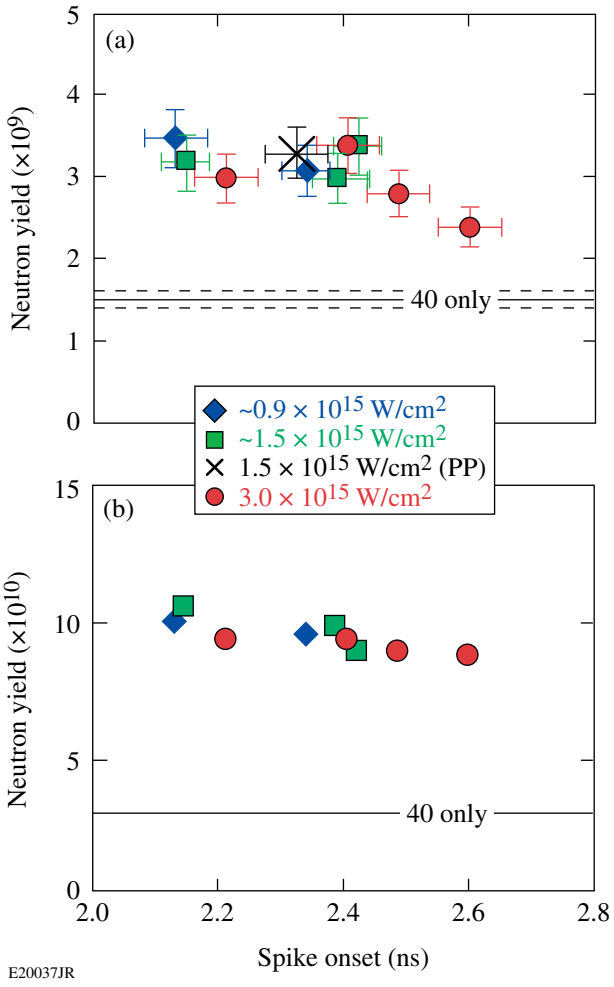

Figure 130.78
(a) Measured and (b) 1-D–simulated neutron yields for configuration B.

starts with a good illumination pattern in the 40 drive beams, but the 20 spike beams probably increased nonuniformities, which is seen in the x-ray pinhole images in Figs. 130.77(b) and 130.77(c). This might explain why the yield increase is less than predicted. The yield-over-clean (YOC) ratio, defined as the measured-to-predicted neutron number, is 3% to 5% for these experiments. The low YOC can be explained by a strong Rayleigh–Taylor instability growth during the acceleration phase in these low-velocity plastic-shell implosions and a substantial shell–fuel mixing that quenches fusion reactions.[18]

The neutron temporal diagnostic[27] recorded the fusion reaction-rate history in most of the implosions, provided that the neutron yield was above ~1×10^9. The signals were noisy and the peak of the measured neutron rate or "bang time" was obtained by fitting a Gaussian curve to the signals. The error in determining the bang time is estimated with ~50 ps. The bang time versus spike onset is plotted in Fig. 130.79(a). Bang times are earlier in configuration A for a given spike onset. The general trend for both data sets is that the bang time is later with a later onset of the spike pulse. The gray band marks the range of measured bang times from 40 drive beam implosions in configuration B. The solid line is a linear fit through the squares. The slope of this line is ~1.6× larger than the slope of the dashed line, which is a linear fit through the circles. This indicates a stronger effect of the spike pulse in configuration A. However, the earliest bang time (~3.59 ns) was measured in one 40 + 20 shot with phase plates in the spike beams and in configuration B. This is ~200 ps earlier than in the 40-drive-beam implosions. Figure 130.79(b) shows that it is not so much the particular beam configuration that is important for the bang time; the amount of hot electrons that are generated (see **Hard**

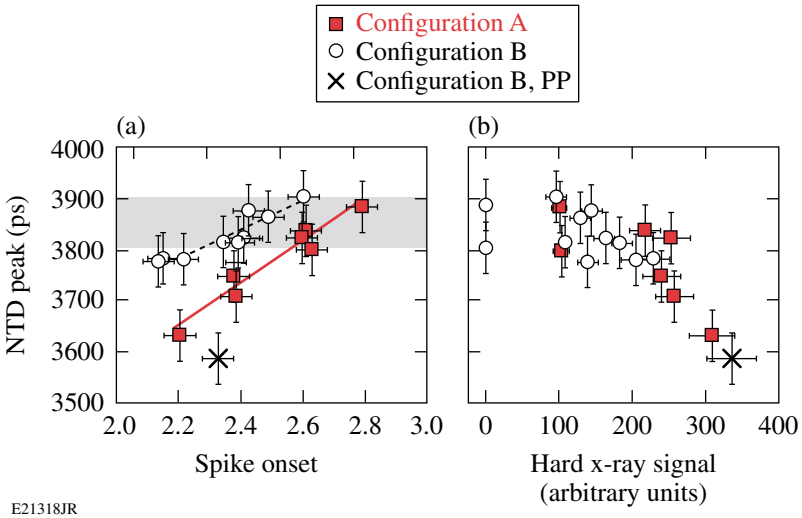

Figure 130.79
Measured neutron bang time versus (a) the spike onset time and (b) the hard x-ray signal. The solid squares and open circles represent the measurements in configurations A and B, respectively, and × represents the measurement with phase plates in the spike beams in configuration B. The gray band in (a) denotes the range of measured bang times in 40-beam implosions.

X-Ray Measurements, p. 122) is more important. A clear correlation of the bang time with the measured hard x-ray signal is observed. An earlier bang time correlates with a higher x-ray signal, indicating that the hot electrons responsible for the hard x-ray emission affect the hydrodynamic implosion.

Figure 130.80 shows electron-temperature and pressure maps obtained from various 2-D CHIC simulations for configuration B. Hot electrons were not included in the simulations. This is probably justified for most of the shots in configuration B without phase plates since those shots are less affected by hot electrons (see Fig. 130.79). Figure 130.80(a) shows the case without a spike pulse. The 40-beam illumination corresponds to that rendered in Fig. 130.67(c). In this case the corona temperature and pressure are isotropic during the shell implosion, and the shock pressure is about 50 Mbar at the end of the drive pulse ($t = 2.6$ ns). Figures 130.80(b)–130.80(d) show 2-D simulations 300 ps after the spike onset for different focusing conditions of the spike beams (see Fig. 130.70), i.e., with different SBI. The temperature in Fig. 130.80(d) shows weak laser imprint in the corona from the spike illumination pattern, while with lower intensity the temperature becomes more symmetric because of a better spatial overlap of the 20 spike beams. Independent of the spike intensity on target, however, the pressure remains fairly symmetric with the same value of ~75 Mbar. Some slight pressure modulations are observed at the highest intensity. The simulations show that the temperature in the conduction layer is always symmetric, which explains why the spike pressure keeps the same values in all the cases. For all focus conditions, the equivalent pressure can be estimated from the average spike intensity, which is $\langle I_{\text{spike}} \rangle \sim 0.5 \times 10^{15}$ W/cm^2. The total intensity on target is the sum of the spike intensity and the compression intensity ($I_{\text{comp}} = \sim 0.4 \times 10^{15}$ W/cm^2). For a laser absorption of about 70%, the absorbed intensity is

$$I_{\text{abs}} = \sim 0.7\left(I_{\text{comp}} + \langle I_{\text{spike}} \rangle\right) = \sim 0.6 \times 10^{15} \text{ W/cm}^2,$$

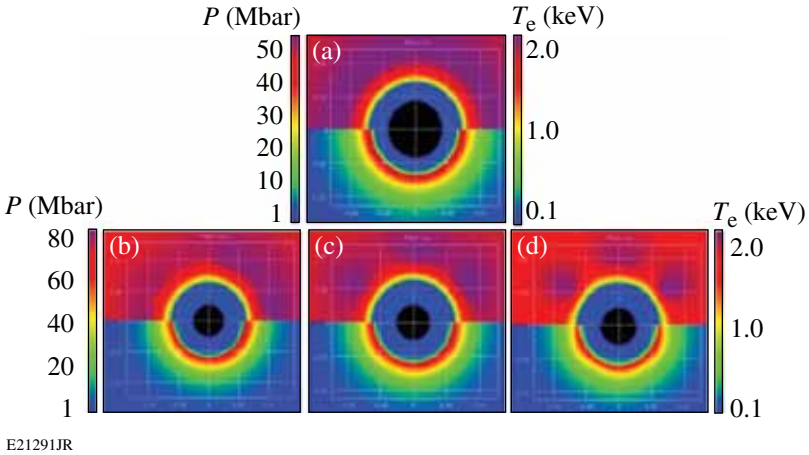

Figure 130.80
Two-dimensional CHIC simulations. Electron temperature (top half) and pressure (bottom half): (a) without a spike at the end of the drive pulse (2.6 ns) and with a spike, 300 ps after the spike onset (2.9 ns) with (b) SBI = 0.5×10^{15} W/cm^2, (c) SBI = 1×10^{15} W/cm^2, and (d) SBI = 2.5×10^{15} W/cm^2. The temperature and pressure scales are the same for (b)–(d).

and the expected pressure is ~80 Mbar for this intensity from a simple scaling law model,[31] in agreement with the simulated value. The 2-D simulations explain why for all SBI's, the spike pressure remains constant, as does, consequently, the neutron yield. This argument applies only for the experiments with configuration B, while for configuration A, the neutron yields are dominated by the illumination nonuniformities and their mitigation by the spike beams.

Hard X-Ray Measurements

The hard x-ray (HXR) detector provides information on the temperature of the electron distribution. The measured time-resolved hard x-ray pulse from the >40-keV channel is shown in Fig. 130.81 for various spike-onset times. The hard x-ray pulse correlates with the spike laser pulse, with respect to both the onset and its duration. The hard x rays and, therefore, the hot electrons are predominantly produced by the high-intensity laser spike and are negligible when only the 40 low-intensity drive beams are used.

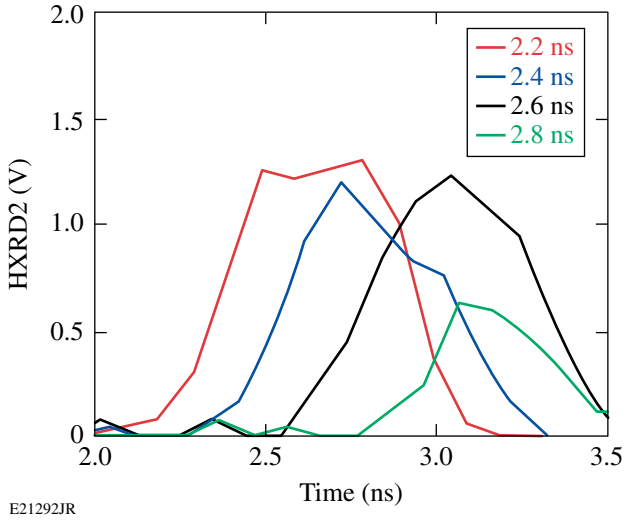

Figure 130.81
Measured time-resolved hard x-ray pulses for energies >40 keV. The times in the legend indicate the onset of the spike pulse. The hard x-ray pulse is clearly correlated with the spike pulse, in both onset and duration.

The hot-electron temperature for configuration A [Fig. 130.82(a)] was determined by fitting estimated values from the convolution of an exponentially decaying hard x-ray spectrum with the sensitivity of the different channels of the HXR detector to the three measured higher-energy channels.[29] The lowest-energy channel was excluded from the fit. A hot-electron–energy distribution with a temperature of ~30 keV was measured, independent of laser intensity and timing. Large-scale, collisional, 1-D particle-in-cell (PIC) simulations[32] for

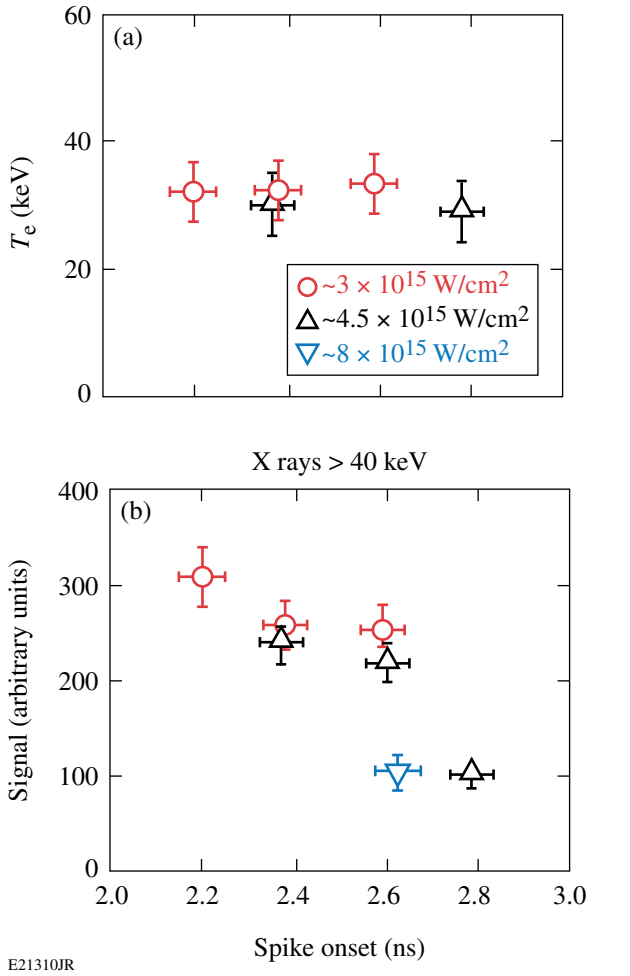

Figure 130.82
(a) Inferred hot-electron temperature and (b) measured, time-integrated hard x ray signal >40 keV for configuration A.

laser intensities of 10^{15} to 10^{16} W/cm^2 using very similar plasma parameters, as in these experiments, reported hot-electron temperatures of ~25 keV, with the primary source for hot electrons being SRS. Remarkably, the simulations[32] predict a relatively low, constant hot-electron temperature that will not change with laser intensity, in agreement with the experimental observation.

Figure 130.82(b) shows the time-integrated hard x-ray yield of the >40-keV channel. It is interesting to note that for implosions in configuration A, there is a clear correlation between the measured neutron signal (Fig. 130.75) and the hard x-ray signal [Fig. 130.82(b)], which suggests that the yield increase from adding the spike beams was partially due to hot electrons coupled into the outer regions of the compressing target. It can be excluded that hard x ray interfered with the neutron-yield measurements because of proper shielding of the diagnostics and time-resolved measurements. Hard x rays are measured

during the time of the spike pulse, while the neutron time-of-flight signal is measured much later in time. As mentioned before, the neutron signal is very sensitive to the condition of the target illumination. Adding the 20 spike beams in configuration A probably mitigated the nonuniformities, resulting in a much-higher (×14) neutron yield when the 20 spike beams were added. This indicates that the spike beam's energy is partially coupled by hot electrons that slowed down in the dense shell.

Higher hard x-ray signals were measured for early spike onset, probably caused by a longer temporal overlap between drive and spike pulse, which suggests that electron plasma waves seeded by the drive pulse are amplified by the high-intensity spike. More overlap provides a longer time period when the electron-plasma waves are driven; therefore, more hot electrons and higher hard x-ray signals are generated. Hot-electron generation is caused by the SRS and TPD instabilities.[33] The foci of the 20 spike beams did not overlap at the critical density for those measurements, so effects from overlapping beams[33] are not expected and the hot-electron production is dominated by single-beam interactions with the target. At 2.6 ns, there are three shots with different intensities. The hard x-ray signal decreases with higher intensity. Two causes might explain this effect: First, the backscatter losses increase from ~10% to ~35% (see below) with higher intensity, reducing the coupling efficiency of the spike beams. Second, since the SBI was varied through the focus size w-hile holding the energy constant, a higher intensity corresponds to a smaller spot size. This affects the total number of generated hot electrons and the hard x-ray signal. The number of hot electrons is proportional to the plasma volume intercepted by the high-intensity beams. When normalizing the measured hard x-ray signal by the estimated laser beam area at quarter-critical density, the yield actually increases with laser intensity (see Fig. 130.83). This shows that the hot-electron production per area increases with laser intensity, presumably because of a larger growth of laser–plasma instabilities. As in previous experiments performed under similar conditions,[33] the hard x-ray signal saturates at intensities above ~2×10^{15} W/cm^2.

Similar measurements were performed for beam configuration B (see Fig. 130.84). Here, the SBI was varied between 0.9×10^{15} and ~3×10^{15} W/cm^2. In contrast to the previous experiment, the foci of the spike beams were large enough at the lowest intensity so that they partially overlapped [see Fig. 130.70(c)]. Not surprising, the lowest hard x-ray signal was measured for the lowest intensity. The inferred temperature was

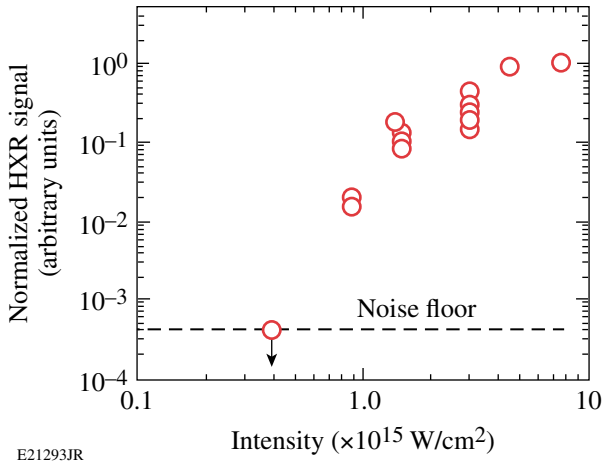

Figure 130.83
Hard x-ray signal divided by the estimated laser-beam area at quarter-critical density as a function of SBI. The maximum signal was normalized to unity. Data from both configurations are plotted.

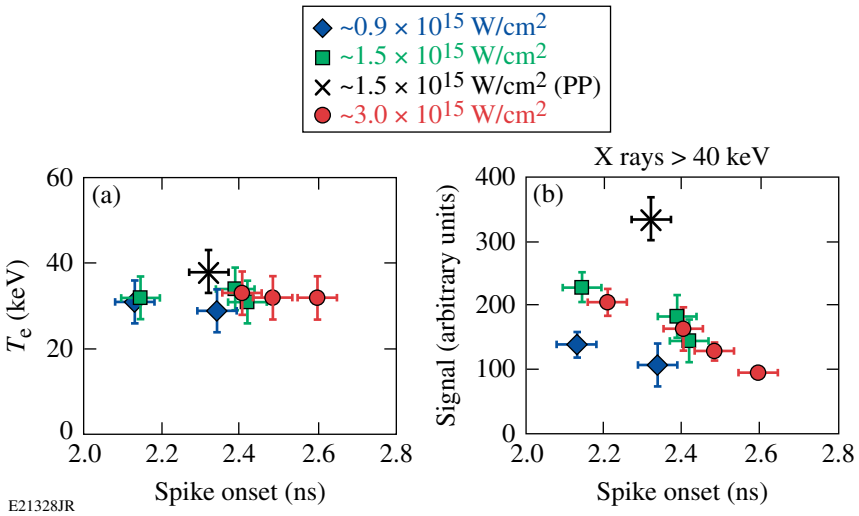

Figure 130.84
(a) Inferred hot-electron temperature and (b) measured hard x-ray signal for configuration B.

~30 keV for all the shots without phase plates, independent of laser intensity and timing, which is very similar to the temperature in configuration A. A slightly higher temperature of ~40 keV was measured with phase plates, which also produced the highest hard x-ray signal for this beam configuration. Less backscattering (see **Backscatter Measurements** below) and less beam filamentation are expected with phase plates,[34] which should lead to higher laser intensity at quarter-critical density. It is expected that the laser–plasma instabilities are driven harder, which could then lead to a hotter electron population and more electrons. Only for this shot with phase plates, a measureable 3/2-harmonic signal[33] was present; the 3/2 signal was absent in all other shots without phase plates. The hotter electron distribution might therefore be caused by some contribution from TPD, while the shots without phase plates were dominated by SRS instability (see **Backscatter Measurements** below).

For beam configuration B, there is no clear correlation between the neutron signal [Fig. 130.78(a)] and hard x-ray signal [Fig. 130.84(b)]. This can be explained by the fact that in configuration B a relatively uniform 40-beam implosion is distorted when the 20 spike beams are added. The 20 spike beams impose a dodecahedron imprint pattern and seed modulations [see Fig. 130.80(d)] that increase the core deformation at peak compression (Fig. 130.73). Larger core distortions were also observed in x-ray pinhole images when the spike beams were added [Figs. 130.77(b) and 130.77(c)]. This led to more Rayleigh–Taylor instability growth and reduced the neutron yields despite the additional energy that was coupled into the imploding shell. In general, adding laser energy from the spike beams should help to compress the shell more and boost the neutron yield, but there is a trade-off between more energy coupled into the target and more seeds for instabilities.

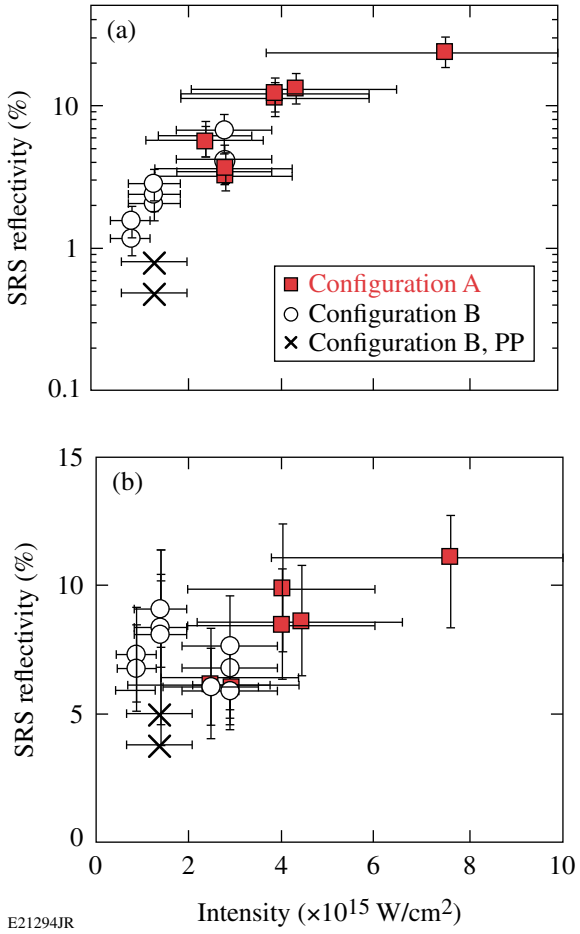

Figure 130.85
Percentage of back-reflected laser light in a spike beam port by (a) SRS and (b) SBS as a function of SBI. Most of the high-intensity shots were done with configuration A denoted by the full symbols. The open symbols represent repointed beams (configuration B). The lowest reflectivity was measured with configuration B and phase plates (cross).

Backscatter Measurements

The plasma reflectivity was measured for various laser intensities. Figure 130.85 shows the percentage of back-reflected light in the (a) SRS and (b) SBS channels of one of the spike beams. The SRS signal increased in intensity by more than a factor of ~10 to up to 24% and dominated the backscattering at the highest intensity, while SBS increased moderately from ~5% to 12%. A very low level of SRS backscattering (~0.5%) was measured at $\sim 1.5 \times 10^{15}$ W/cm^2 with phase plates in the spike beams. The simultaneously measured back-reflection through the neighboring drive-beam port, i.e., one of the 40 beam ports delivering the assembly pulse, was low and remained constant at the same level as in implosions without the 20 spike beams for all timings and intensities (see Fig. 130.86). In the drive beam, SRS stayed below 1% and SBS stayed in the 2% to 4% range. This shows that the light from the spike beams was scattered back in a narrow cone and did not spill over into adjacent ports.

It has been shown[35,36] that smoothing the intensity distribution in the focal spot with spatial, temporal, and polarization smoothing schemes can substantially reduce the backscattering. This is attributed to a reduction of filamentation.[34] In most of the shots, no phase plates were used in the spike beams, which could explain the high levels of backscattering. The sum of SBS and SRS backscatter was lowest (~6%) with phase plates, while without phase plates, the reflectivity increased from ~8% at $\sim 0.9 \times 10^{15}$ W/cm^2 to ~36% at $\sim 8 \times 10^{15}$ W/cm^2. Most of the high-intensity shots were done with configuration A, but some shots were taken at 3×10^{15} W/cm^2 with both beam configurations. The backscatter was the same within the measurement

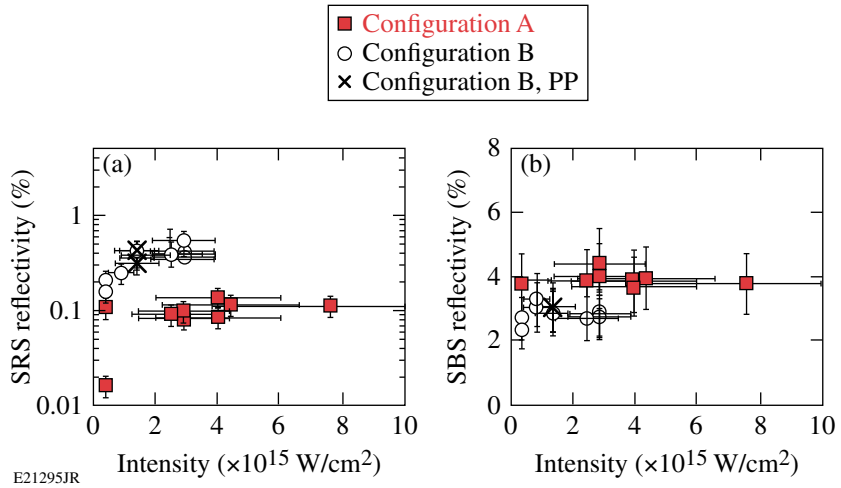

Figure 130.86
Percentage of reflected laser light in a drive beam port by (a) SRS and (b) SBS as a function of SBI. See Fig. 130.85 for an explanation of the different symbols.

uncertainty. In contrast to the experiment, collisional PIC simulations[32] for similar plasma conditions predict that the calculated reflected laser energy should remain constant at ~35% when the laser intensity increases from 1×10^{15} W/cm^2 to 8×10^{15} W/cm^2. The simulations show that the fraction of energy absorbed by the collisionless processes significantly increased with intensity, while the collisional absorption decreased proportionally.

A 2-D radiation–hydrodynamics code *DRACO*[37] simulation was performed to study the heating and profile modification of the plasma under the interaction of a single high-intensity (~5×10^{15} W/cm^2) spike beam with the imploding shell on the pole. The simulation shows the formation of a density depression in the underdense plasma and the steepening of the density profile at the critical density. Figure 130.87(a) shows axial density profiles for various times during the spike interaction. Figure 130.87(b) shows the density scale length at the critical density n_c (circles) and at $n_c/4$ (squares) along with the spike pulse's profile (dashed). Profile steepening at n_c occurs during the spike interaction, and the density scale length is reduced from ~20 μm to ~2 μm. In contrast, the scale length at $n_c/4$ does not change significantly and remains ~170 μm until the end of the spike pulse. As a result of this density profile modification, the spike pulse creates a channel through the underdense plasma. Scattered light is guided by this channel and is dominantly reflected back into the incident beam with very little sidescattering. This is supported by the small amount of scatter in the drive beam (Fig. 130.86) and the negligible amount of sidescattering shown by the near-backscatter diagnostic around the spike beam.

Time-resolved spectra of the SBS back-reflected light were recorded. Figure 130.88 shows two examples of the SBS sig-

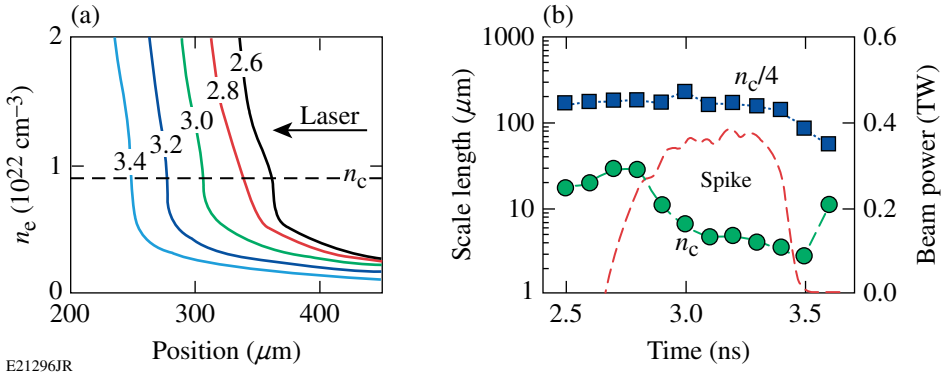

Figure 130.87
(a) Density profiles from a 2-D hydrodynamics code *DRACO*[37] simulation along the channel axis of a high-intensity spike beam interacting with the imploding shell. The numbers indicate the time in nanoseconds. The critical density is marked by the dashed line. (b) Density scale length at critical (circles) and quarter-critical (squares) density. Profile steepening occurs when the spike pulse (dashed) interacts.

nal for a medium- and high-intensity shot. The white curve represents the composite pulse shape of the drive and spike pulses. The SBS signal is produced only during the spike curve. The frequency spectrum of the SBS light is affected by the plasmas temperature and the Doppler shift with respect to the incident laser light. The amount of blue shift is given by $\omega - \omega_0 = 2k_0 c_s (M-1)\sqrt{1 - n_e/n_c}$ (Ref. 38), where ω and ω_0 are the angular frequencies of the scattered and incident light, respectively, k_0 is the wave number of the incident light, c_s is the ion sound velocity, and M is the Mach number. Supersonic movement of the plasma region where SBS occurs will cause a blue shift of the SBS spectrum. The experiment shows that the blue shift is reduced with increasing laser intensity, indicating that SBS originates from plasma regions with lower flow velocities. A comparison with 2-D hydro simulations shows that lower flow velocities occur at higher plasma densities. The corresponding plasma density is indicated in Fig. 130.88 by the ratio of electron density to n_c. For an intensity of ~2.5×10^{15} W/cm^2, the SBS active region is located at a plasma density of ~$0.03\, n_c$.

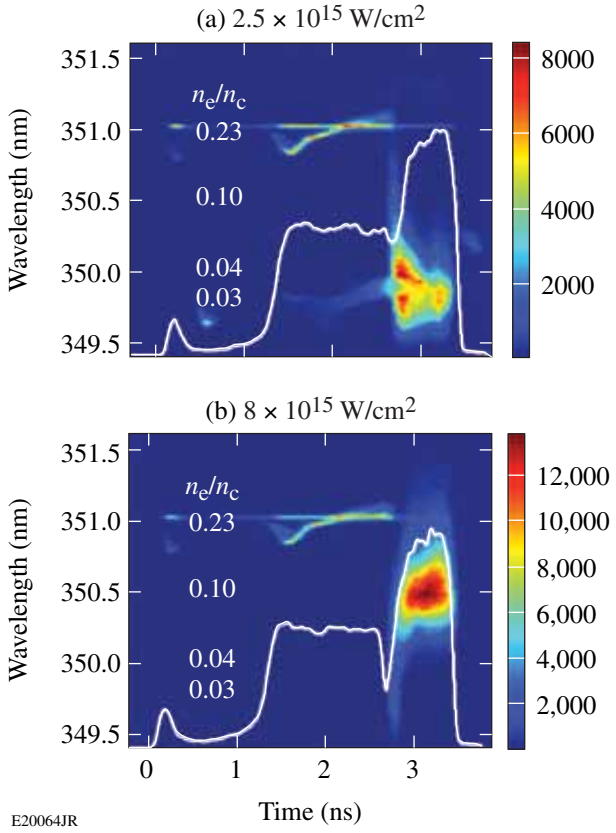

Figure 130.88
Streaked SBS spectra for (a) medium (SBI = 2.5×10^{15} W/cm^2) and (b) high (SBI = 8×10^{15} W/cm^2) spike intensity. The numbers in the figures indicate the plasma density normalized to the critical density. The white curve is the composite pulse shape of the drive and spike pulses.

For ~4.5×10^{15} W/cm^2 (not shown), the peak emission shifted to ~$0.05\, n_c$ with a weak SBS signal coming from up to ~$n_c/4$ later in time. At the highest intensity [Fig. 130.88(b)], the SBS active region shifts up to ~0.1 to $0.2\, n_c$ with a clear indication of a signal coming from above $n_c/4$. The laser-intensity threshold for SBS can be estimated with

$$I_{SBS} \approx \left(T_{keV}/L_v \lambda_\mu\right) \times \left(n_c/n_e\right) \times 7 \times 10^{15} \text{ W/cm}^2 \text{ (Ref. 39)},$$

where T_{keV}, L_v, and λ_μ are the electron temperature in keV, scale length of the Mach number profile in microns, and the laser wavelength in microns, respectively. The resulting threshold is $I_{SBS} \approx 5 \times 10^{14}$ W/cm^2 for the current plasma conditions and $n_e/n_c = 0.04$. The drive-pulse intensity is below the threshold, while the spike intensity is above the threshold.

The laser-intensity threshold for the TPD instability can be estimated from $I_{TPD} \approx \left(82 \times T_{keV}/L_\mu \lambda_\mu\right) \times 10^{14}$ W/cm^2 (Ref. 40), where L_μ is the density scale length in microns and λ_μ is the laser wavelength in microns. For SRS, the threshold at around $\sim n_c/4$ is given by

$$I_{SRS} \approx \left(T_{keV}/L_\mu^{4/3} \lambda_\mu^{2/3}\right) \times 5 \times 10^{16} \text{ W/cm}^2 \text{ (Ref. 39)}.$$

DRACO simulations predict $T_{keV} \approx 1.8$, which results in $I_{TPD} \approx 2.5 \times 10^{14}$ W/cm^2 and $I_{SRS} \approx 2 \times 10^{14}$ W/cm^2 for the current plasma conditions. The thresholds are lower than the peak intensity in the drive beams, but no SRS or TPD signatures were measured with only the 40 drive beams. With increasing intensity, a strong reduction in the TPD instability is observed, which is evident by the reduction in optical emission at the half-harmonic ($\omega/2$) of the laser wavelength. The $\omega/2$ signal decreased by more than two orders of magnitude in the applied intensity range. At the maximum intensity, the $\omega/2$ signal was below the detection threshold, indicating no significant contribution of TPD to the hot-electron production. This and the relatively low hot-electron temperature of ~30 keV support the conjecture that SRS plays the dominant role in hot-electron production in these experiments. The strong reduction of TPD with intensity, together with the observed shift of the SBS active region to $\sim n_c/4$, might indicate that driven ion-acoustic waves at $\sim n_c/4$ play a role in the reduction of TPD.

Conclusions

Spherical shock-ignition experiments were performed on OMEGA by using a beam configuration that separates low-intensity compression beams and high-intensity spike beams. D_2-filled plastic shells were compressed on a low adiabat by 40 of the 60 OMEGA beams, and the remaining 20 spike beams

were delayed and tightly focused onto the imploding shell to deliver a late shock. This article studied the implosion performance with the new beam configuration and used the platform to measure hot-electron production and laser backscattering for laser intensities that are relevant for shock ignition. Two different beam-pointing configurations were used: one that used the standard pointing to target center and another in which the beams were repointed to improve target illumination uniformity. Significant improvement in areal density and neutron yield and a rounder core in x-ray images were observed for the repointed beam configuration. The coupling of high-intensity spike beam energy into the imploding capsule was studied in experiments and simulations. Implosions in the standard configuration show a correlation between the measured neutron yield and the hard x-ray signal, which suggests that the yield increase was partially due to hot electrons coupled into the compressing target. The spike beams mitigated the large beam illumination nonuniformities in this configuration, which led to the recovery of the neutron yield by a factor of ~14. Several indications suggest that when spike beams are equipped with phase plates, a stronger coupling of the spike beam energy into the imploding shell is achieved. With phase plates the following observations were made: lower backscatter losses, stronger x-ray emission in the 2- to 7-keV and >20-keV ranges, lower ρR, and an earlier bang time. This indicates that higher coupling is achieved through increased thermal and hot-electron components. Two-dimensional hydrodynamic simulations were performed and show significant modulation in areal density. Similar modulations were observed in the experiments. Laser–plasma instabilities were studied for single-beam peak laser intensities of up to $\sim 8 \times 10^{15}$ W/cm^2, measuring backscattering of laser energy of up to 36% at the highest intensity. Hard x-ray measurements reveal a relatively low hot-electron temperature of ~30 keV, which is independent of intensity and spike onset time. With increasing laser intensity, the region where stimulated Brillouin scattering occurs shifts to higher densities. At the highest intensity it occurs near and above the quarter-critical density. With higher intensity the two-plasmon-decay instability is suppressed and hot-electron production is dominated by stimulated Raman scattering.

These experiments measured a low hot-electron temperature, not too high backscatter losses, and a good coupling of spike beam energy into an imploding capsule at laser intensities of up to $\sim 8 \times 10^{15}$ W/cm^2, which is encouraging for the shock-ignition concept. A low hot-electron temperature is beneficial since these electrons are stopped in the outer layer of the imploding target, augmenting the strong hydrodynamic shock. Further shock-ignition experiments are required, however, to study laser–plasma instabilities and hot-electron production at plasma conditions with longer density scale lengths and higher electron temperatures that are closer to those of an ignition design.

ACKNOWLEDGMENT

This work was supported by the U.S. Department of Energy Office of Fusion Energy Sciences under contract DE-FC02-04ER54789 and by the Office of Inertial Confinement Fusion under Cooperative Agreement No. DE-FC52-08NA28302, the University of Rochester, and the New York State Energy Research and Development Authority. The support of DOE does not constitute an endorsement by DOE of the views expressed in this article. This work was partially supported by the Aquitaine Region Council and the European Union's Seventh Framework Program: the HiPER project #211737.

REFERENCES

1. R. Betti, C. D. Zhou, K. S. Anderson, L. J. Perkins, W. Theobald, and A. A. Solodov, Phys. Rev. Lett. **98**, 155001 (2007).
2. R. L. McCrory, D. D. Meyerhofer, R. Betti, R. S. Craxton, J. A. Delettrez, D. H. Edgell, V. Yu Glebov, V. N. Goncharov, D. R. Harding, D. W. Jacobs-Perkins, J. P. Knauer, F. J. Marshall, P. W. McKenty, P. B. Radha, S. P. Regan, T. C. Sangster, W. Seka, R. W. Short, S. Skupsky, V. A. Smalyuk, J. M. Soures, C. Stoeckl, B. Yaakobi, D. Shvarts, J. A. Frenje, C. K. Li, R. D. Petrasso, and F. H. Séguin, Phys. Plasmas **15**, 055503 (2008).
3. J. D. Lindl, *Inertial Confinement Fusion: The Quest for Ignition and Energy Gain Using Indirect Drive* (Springer-Verlag, New York, 1998).
4. V. A. Shcherbakov, Sov. J. Plasma Phys. **9**, 240 (1983).
5. R. Betti and C. Zhou, Phys. Plasmas **12**, 110702 (2005).
6. X. Ribeyre *et al*., Plasma Phys. Control. Fusion **50**, 025007 (2008).
7. A. J. Schmitt, J. W. Bates, S. P. Obenschain, S. T. Zalesak, D. E. Fyfe, and R. Betti, Fusion Sci. Technol. **56**, 377 (2009).
8. X. Ribeyre *et al*., Plasma Phys. Control. Fusion **51**, 015013 (2009).
9. E. I. Moses *et al*., Phys. Plasmas **16**, 041006 (2009).
10. L. J. Perkins, R. Betti, K. N. LaFortune, and W. H. Williams, Phys. Rev. Lett. **103**, 045004 (2009).
11. M. Dunne, Nat. Phys. **2**, 2 (2006); HiPER, accessed 7 May 2012, http://www.hiper-laser.org/index.asp.
12. W. L. Kruer, *The Physics of Laser-Plasma Interactions*, Frontiers in Physics, Vol. 73, edited by D. Pines (Addison-Wesley, Redwood City, CA, 1988).
13. R. Betti, W. Theobald, C. D. Zhou, K. S. Anderson, P. W. McKenty, S. Skupsky, D. Shvarts, V. N. Goncharov, J. A. Delettrez, P. B. Radha, T. C. Sangster, C. Stoeckl, and D. D. Meyerhofer, J. Phys., Conf. Ser. **112**, 022024 (2008).
14. J. Delettrez, R. Epstein, M. C. Richardson, P. A. Jaanimagi, and B. L. Henke, Phys. Rev. A **36**, 3926 (1987); M. C. Richardson, P. W. McKenty, F. J. Marshall, C. P. Verdon, J. M. Soures, R. L. McCrory, O. Barnouin,

R. S. Craxton, J. Delettrez, R. L. Hutchison, P. A. Jaanimagi, R. Keck, T. Kessler, H. Kim, S. A. Letzring, D. M. Roback, W. Seka, S. Skupsky, B. Yaakobi, S. M. Lane, and S. Prussin, in *Laser Interaction and Related Plasma Phenomena*, edited by H. Hora and G. H. Miley (Plenum Publishing, New York, 1986), Vol. 7, pp. 421–448.

15. T. R. Boehly, D. L. Brown, R. S. Craxton, R. L. Keck, J. P. Knauer, J. H. Kelly, T. J. Kessler, S. A. Kumpan, S. J. Loucks, S. A. Letzring, F. J. Marshall, R. L. McCrory, S. F. B. Morse, W. Seka, J. M. Soures, and C. P. Verdon, Opt. Commun. **133**, 495 (1997).

16. W. Theobald, K. S. Anderson, R. Betti, R. S. Craxton, J. A. Delettrez, J. A. Frenje, V. Yu. Glebov, O. V. Gotchev, J. H. Kelly, C. K. Li, A. J. Mackinnon, F. J. Marshall, R. L. McCrory, D. D. Meyerhofer, J. F. Myatt, P. A. Norreys, P. M. Nilson, P. K. Patel, R. D. Petrasso, P. B. Radha, C. Ren, T. C. Sangster, W. Seka, V. A. Smalyuk, A. A. Solodov, R. B. Stephens, C. Stoeckl, and B. Yaakobi, Plasma Phys. Control. Fusion **51**, 124052 (2009).

17. R. S. Craxton, L. Tucker, T. Mo, K. S. Anderson, R. Betti, L. J. Perkins, G. P. Schurtz, X. Ribeyre, and C. A. Casner, Bull. Am. Phys. Soc. **55**, 26 (2010).

18. W. Theobald, R. Betti, C. Stoeckl, K. S. Anderson, J. A. Delettrez, V. Yu. Glebov, V. N. Goncharov, F. J. Marshall, D. N. Maywar, R. L. McCrory, D. D. Meyerhofer, P. B. Radha, T. C. Sangster, W. Seka, D. Shvarts, V. A. Smalyuk, A. A. Solodov, B. Yaakobi, C. D. Zhou, J. A. Frenje, C. K. Li, F. H. Séguin, R. D. Petrasso, and L. J. Perkins, Phys. Plasmas **15**, 056306 (2008).

19. F. J. Marshall, J. A. Delettrez, R. Epstein, R. Forties, R. L. Keck, J. H. Kelly, P. W. McKenty, S. P. Regan, and L. J. Waxer, Phys. Plasmas **11**, 251 (2004).

20. Y. Lin, T. J. Kessler, and G. N. Lawrence, Opt. Lett. **21**, 1703 (1996).

21. T. R. Boehly, V. A. Smalyuk, D. D. Meyerhofer, J. P. Knauer, D. K. Bradley, R. S. Craxton, M. J. Guardalben, S. Skupsky, and T. J. Kessler, J. Appl. Phys. **85**, 3444 (1999).

22. P.-H. Maire *et al*., SIAM J. Sci. Comput. **29**, 1781 (2007).

23. S. P. Regan, T. C. Sangster, D. D. Meyerhofer, W. Seka, R. Epstein, S. J. Loucks, R. L. McCrory, C. Stoeckl, V. Yu. Glebov, O. S. Jones, D. A. Callahan, P. A. Amendt, N. B. Meezan, L. J. Suter, M. D. Rosen, O. L. Landen, E. L. DeWald, S. H. Glenzer, C. Sorce, S. Dixit, R. E. Turner, and B. MacGowan, J. Phys., Conf. Ser. **112**, 022077 (2008).

24. C. D. Zhou, W. Theobald, R. Betti, P. B. Radha, V. A. Smalyuk, D. Shvarts, V. Yu. Glebov, C. Stoeckl, K. S. Anderson, D. D. Meyerhofer, T. C. Sangster, C. K. Li, R. D. Petrasso, J. A. Frenje, and F. H. Séguin, Phys. Rev. Lett. **98**, 025004 (2007).

25. F. J. Marshall, T. Ohki, D. McInnis, Z. Ninkov, and J. Carbone, Rev. Sci. Instrum. **72**, 713 (2001).

26. V. Yu. Glebov, D. D. Meyerhofer, C. Stoeckl, and J. D. Zuegel, Rev. Sci. Instrum. **72**, 824 (2001).

27. R. A. Lerche, D. W. Phillion, and G. L. Tietbohl, Rev. Sci. Instrum. **66**, 933 (1995).

28. W. Seka, D. H. Edgell, J. P. Knauer, J. F. Myatt, A. V. Maximov, R. W. Short, T. C. Sangster, C. Stoeckl, R. E. Bahr, R. S. Craxton, J. A. Delettrez, V. N. Goncharov, I. V. Igumenshchev, and D. Shvarts, Phys. Plasmas **15**, 056312 (2008).

29. C. Stoeckl, V. Yu. Glebov, D. D. Meyerhofer, W. Seka, B. Yaakobi, R. P. J. Town, and J. D. Zuegel, Rev. Sci. Instrum. **72**, 1197 (2001).

30. F. H. Séguin, J. A. Frenje, C. K. Li, D. G. Hicks, S. Kurebayashi, J. R. Rygg, B.-E. Schwartz, R. D. Petrasso, S. Roberts, J. M. Soures, D. D. Meyerhofer, T. C. Sangster, J. P. Knauer, C. Sorce, V. Yu. Glebov, C. Stoeckl, T. W. Phillips, R. J. Leeper, K. Fletcher, and S. Padalino, Rev. Sci. Instrum. **74**, 975 (2003).

31. S. Atzeni and J. Meyer-ter-Vehn, *The Physics of Inertial Fusion: Beam Plasma Interaction, Hydrodynamics, Hot Dense Matter*, International Series of Monographs on Physics (Clarendon Press, Oxford, 2004), p. 225.

32. O. Klimo *et al*., Phys. Plasmas **18**, 082709 (2011).

33. C. Stoeckl, R. E. Bahr, B. Yaakobi, W. Seka, S. P. Regan, R. S. Craxton, J. A. Delettrez, R. W. Short, J. Myatt, A. V. Maximov, and H. Baldis, Phys. Rev. Lett. **90**, 235002 (2003).

34. C. Labaune *et al*., Phys. Fluids B **4**, 2224 (1992).

35. B. J. MacGowan *et al*., Phys. Plasmas **3**, 2029 (1996).

36. J. D. Moody *et al*., Phys. Rev. Lett. **86**, 2810 (2001).

37. P. B. Radha, T. J. B. Collins, J. A. Delettrez, Y. Elbaz, R. Epstein, V. Yu. Glebov, V. N. Goncharov, R. L. Keck, J. P. Knauer, J. A. Marozas, F. J. Marshall, R. L. McCrory, P. W. McKenty, D. D. Meyerhofer, S. P. Regan, T. C. Sangster, W. Seka, D. Shvarts, S. Skupsky, Y. Srebro, and C. Stoeckl, Phys. Plasmas **12**, 056307 (2005).

38. T. P. Hughes, in *Laser-Plasma Interactions*, edited by R. A. Cairns and J. J. Sanderson (SUSSP Publications, Edinburgh, 1980), p. 44.

39. H. A. Baldis, E. M. Campbell, and W. L. Kruer, in *Handbook of Plasma Physics*, edited by A. Rubenchik and S. Witkowski, Physics of Laser Plasma, edited by M. N. Rosenbluth and R. Z. Sagdeev (North-Holland, Amsterdam, 1991), Vol. 3, p. 377.

40. A. Simon, R. W. Short, E. A. Williams, and T. Dewandre, Phys. Fluids **26**, 3107 (1983).

A Single-Shot, Multiwavelength Electro-Optic Data-Acquisition System for Inertial Confinement Fusion Applications

Introduction

On large inertial confinement fusion (ICF) laser systems like the National Ignition Facility (NIF),[1] the signals from diagnostic instruments originate in an environment where the ionizing radiation and electromagnetic interference (EMI) can significantly degrade the signal-to-noise ratio (SNR) of the measurement or even damage the recording equipment. In addition, there are many recording channels to which these considerations must apply. The cost of the recording system can be reduced if the signals from several detectors can be multiplexed together onto a single, protected oscilloscope channel. Modern high-bandwidth oscilloscopes have nearly infinite record lengths that make this serial multiplexing possible. The prototype system described here is focused on the set of 36 vacuum x-ray photodiodes (XRD's) of the NIF Dante instruments[2] that produce temporally resolved x-ray spectra.

In high-EMI environments, an electro-optic (EO) data-acquisition system is desirable. Fiber optics provide a means of isolating the recording equipment from the harsh detector environment. The signals from the XRD's are converted into the optical domain with fiber-optic Mach–Zehnder modulators (MZM's).[3] The MZM's are typically built to telecom specifications that make it possible for them to survive not only voltage transients of 250 V for 1 μs (Ref. 4), but also the EMI in an ICF environment and the maximum output of an XRD. Once the signals are in the optical domain, they can propagate on single-mode optical fiber that provides high-bandwidth (BW) transmission over long distances. The BW of the fibers is much larger than the signals being recorded, so arbitrarily long fiber delays can be added to the signal paths. These long delays, coupled with wavelength-selective fiber-coupling techniques, allow one to serially combine multiple signals onto a single photodetector.

The system described here was designed as a prototype for the NIF Dante instruments. These instruments use XRD's to measure the x-ray spectra of ICF implosions. There are 36 channels spread over two instruments. The specifications require that signals be acquired in a temporal window at least 200 ns long. The response time of the XRD's is 120 ps, so the system requires a minimum BW of 2.75 GHz. The system was actually designed to a 6-GHz BW to accommodate multifringe events, which will be discussed later. The XRD's can deliver a maximum unsaturated signal of 200 V. The minimum meaningful signal is 50 mV and the desired SNR at this level is 5, which implies a dynamic range (DR) of greater than 4000:1. This DR exceeds the capabilities of the current electronics. With this newly adopted requirement the instrument will be able to record signals without changing any radio-frequency (rf) attenuators.

Experimental

This data-acquisition system is designed to operate in the near-IR optical C band with wavelengths from 1530 nm to 1560 nm, which are used by the telecommunications industry. A layout of the system is shown in Fig. 130.89. The optical carriers are provided by continuous-wave (cw), fiber-coupled laser diodes (LD's) that use distributed-feedback Bragg gratings to maintain narrow-bandwidth operation. The International Telcommunication Union (ITU) has specified a standard set of wavelengths separated by approximately 1.6 nm (200 GHz) around which telecom components are fabricated.[5] The output power of these types of devices ranges from 20 to 100 mW (13 to 20 dBm) with a typical noise figure of –140 dB/Hz. The prototype system used a 20-mW LD at 1552 nm and a 60-mW LD at 1557 nm. The 20-mW version is less expensive and more readily available at all wavelengths on the ITU 200 grid. The 60-mW laser is better suited to compensate for losses in the system. However, cw illumination is inappropriate for this application because of the requirement to multiplex signals. The cw wings of the serially combined signals would overlap, thereby overwhelming the photodetector or forcing a reduction of the signal amplitude by *N*, the number of serially overlapped signals.

The cw lasers are converted into pulsed lasers via acousto-optic modulators (AOM's). These optical modulators have very high contrast ratios (50 dB) with a rise time of 10 ns. They also allow for both digital and analog modulation. In the prototype described here, the AOM's produced pulses that were 40 ns

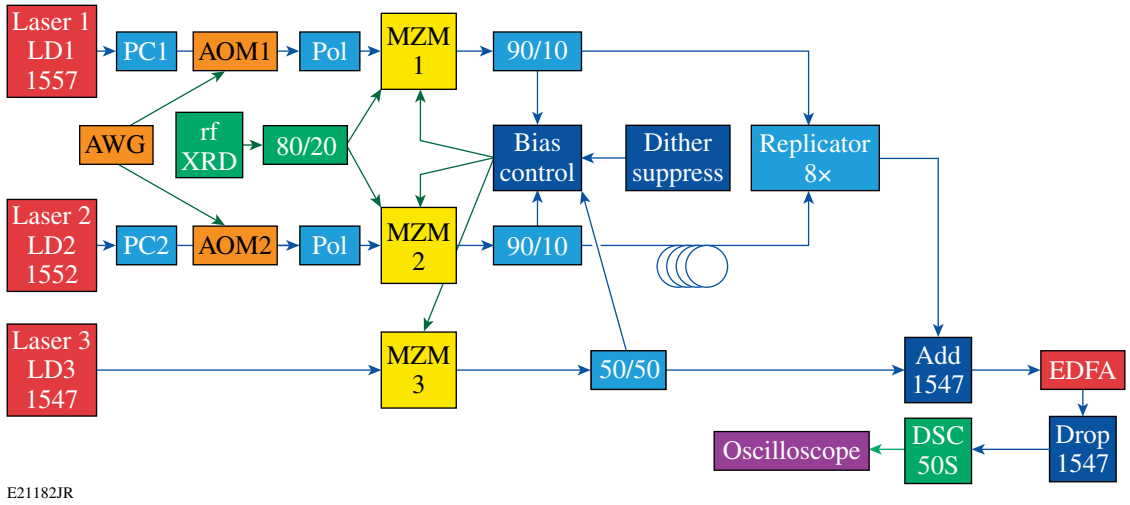

Figure 130.89
In the EO data-acquisition system, the cw outputs of LD1 and LD2 are pulse shaped with an AOM with the shaping pulse provided by the arbitrary waveform generator (AWG). The light is polarized (pol) before being modulated by the MZM. The MZM's are driven by a single XRD through an 80/20 splitter. The 90/10 splitters provide an optical feedback signal to the bias control loop. The signals from the two MZM's are combined at the input of the 8× replicator. After the replicator, another cw source (LD3) is added to provide a cw input to the EDFA. The LD3 signal is removed before detection by the photodiode (DSC50s) and oscilloscope.

wide (10% width) with a 20-ns flattop acquisition window. This window is sufficient for tests performed on the OMEGA Dante system.

For this prototype we chose to multiplex the signal from two MZM's, which was sufficient to demonstrate all concepts that will be incorporated into the final system. To further enhance the DR, the same rf signal was used to drive both MZM's. The single signal is fed to an rf splitter with a BW of 18 GHz and a 4:1 power split ratio. The asymmetric split means that the optical signal from one modulator will be 4× more sensitive to low-voltage signals, thereby extending the lower edge of the dynamic range. On the other hand, the attenuated channel can be subjected to a 4×-higher signal without exceeding $V_\pi/2$ of the modulator. Exceeding this voltage would generate a fringe jump in the sinusoidal response of the MZM. When combined, these two signals will have an enhanced DR.

The MZM's are from EOSpace and have a –3-dB EO response of between 12 GHz and 14 GHz. The modulators were chosen because they have a low V_π of 3.6 V at 1 GHz. A dc bias was applied to the MZM such that it operated quadrature point (50% transmission) with a negative slope, $Q-$. This gives a linear response at low voltage. Conversely, the sensitivity is low at the extrema, $V = \pm MV_\pi/2$, where M is an odd integer. In the low-signal regime, the modular sensitivity is approximately inversely proportional to V_π, so the low V_π values enhance the DR at the lower end of the range. However, the bias points of MZM's are prone to drift with time. To maintain the operating point, a commercial monitoring circuit was employed. This circuit applied a 20-mV, 1-kHz dither to the dc bias. This dither voltage introduces harmonics of the dither frequency on the transmitted optical signal.[6] Ten percent of the light, after the MZM, is split off with a fiber-optic splitter. This signal was used to monitor the harmonics, therefore enabling the controller to maintain the $Q-$ operating point. However, this scheme works only if the light through the MZM is cw, which it is not. Using the analog modulation capabilities of the AOM, an optical pulse shape was constructed that was at a quasi-cw level of 5% of the peak intensity. To accommodate the optical replicator, which will be described later, the cw level was turned off 2 μs before the 40-ns pulse described above was formed at the 100% transmission level. After the pulse, the AOM output was again blanked for 2 μs before returning to the 5% level. The quasi-cw light was used for the dither control. Any dither voltage that occurred during the 40-ns pulse would look like a baseline drift in the signal; therefore, the commercial controller was modified to suppress the dither voltage during the 4-μs cw blanking window.

There are two options for multiplexing the signals from the two MZM's onto a single optical fiber for additional processing and detection. A dense wavelength-division multiplexer (DWDM) with eight channels on the ITU 200 grid was used

to combine the two wavelengths. This means that in the final system, up to eight MZM's could be multiplexed onto a photodiode attached to a single oscilloscope channel. However, the DWDM has a loss of –2.5 dB or a transmission of 56% plus two additional fiber connections with their associated losses (85% transmission). Since the prototype has only two wavelengths, a lower-loss option was to use the two inputs of the next component in the system—the optical replicator.

The optical replicator is a set of 2×2, 3-dB fused-fiber splitters, as shown in Fig. 130.90 (Ref. 7). Optical interference at the output of the fused-fiber splitters causes half of the light from each of the two input fibers to be distributed equally between the two output fibers. The splitting is independent of the wavelength over the operational band of the device. The outputs of the first 2×2 are connected to inputs of the second with an extra 12 m of fiber (60 ns) inserted into one of the connections. The output of the second 2×2 is then two identical optical pulses separated by 60 ns. The output of the second 2×2 is fed into the third 2×2 with the additional delay increased by a factor of 2 to 120 ns. This process was repeated until eight copies of the original pulse were spread over 480 ns. The input pulse cannot extend beyond 60 ns; otherwise, the tails of the pulses will overlap in time in the 2×2 splitters and produce interference with 100% modulation. This is why the AOM was configured to produce 40-ns pulses. The future version to be deployed on the NIF will require longer delays.

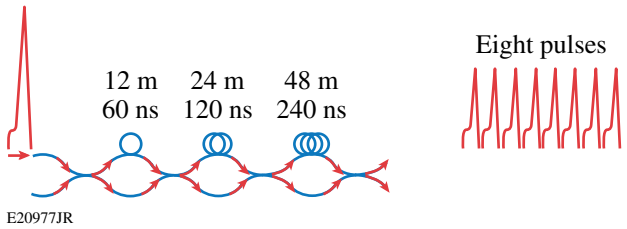

Figure 130.90
The replicator is constructed with 2×2 optical splitters. The outputs of the three stages are connected to the inputs of the subsequent stage with one of the connections having an additional length of fiber. Therefore, the eight replicated pulses arrive at the output at different times.

When detected by the photodiode, each of the optical replicas constitutes an independent measurement of the optical pulse from the MZM. These measurements can be averaged together to produce a measurement with the SNR improved by $\sqrt{N}$, where N is the number of replicas. For this prototype we expect an improvement in the SNR of 2.8. However, if there is any noise imprinted on the optical pulse before the replicator, e.g., noise from the LD, that noise will not average out. Since each XRD is optically encoded with two MZM's and two LD's, any noise arising before the replicator is reduced by $\sqrt{2}$.

The replicator is a passive device, so creating eight replicas reduces the amplitude of each pulse by a factor of 8, without taking into account the coupling losses between each splitter. Therefore, increasing the number of replicas improves the SNR, but it may also decrease the signal below the detection threshold of the photodiode.

The sensitivity of the InGaAs photodiodes is approximately 0.8 A/W. When coupled into the 50-Ω input of the oscilloscope, the sensitivity can be rewritten as 40 mV/mW. At the input of the system, either 20 mW or 60 mW of optical power is available at 1552 nm or 1557 nm, respectively. In an ideal system, this power is simply gated in time and passed through to the output with analog modulation imposed. Distributing the power over eight pulses, the maximum signals that could be expected at the oscilloscope would be 100 mV and 300 mV. The system is not ideal and each component has intrinsic losses associated with it. In addition many of the components were joined together with fiber connectors rather than fusion splicing to maintain the flexibility to reconfigure the system. Table 130.IV lists the major components in the system and the associated losses in decibels (dB).

Table 130.IV: Losses in the system.

Component	Loss (dB)
Acousto-optic modulator (AOM)	–6
Polarizer	–0.6
Mach–Zehnder modulator (MZM)	–2
10/90 splitter	–1
Wavelength-division multiplexer (WDM)	–1
Miscellaneous coupling losses	–2.6
Total	–13.2

The total losses are approximately 13.2 dB or a factor of 21, which reduces the maximum-possible signals to 5 and 14 mV, respectively. Signals that are this small seriously compromise the DR of the oscilloscope measurements because they represent only a small fraction of the full-scale range, even on the most-sensitive settings. To achieve a DR of 4000:1, the optical signal must be amplified. The signal was amplified by a commercial Er-doped fiber amplifier (EDFA). This device can provide 20 db of linear gain over a wide spectral range center at 1547 nm.

The detector was a highly linear DSC50S from Discovery Semiconductor. This 50-μm detector is large with respect to the core of the optical fiber (7 μm) so it will collect all of the light from the single-mode fiber. The photodiodes have a linear response down to the dark-current limit of 10 nA. Because the system operates at the negative quadrature point of the MZM, the dark current does not affect the low-voltage sensitivity. The photodiode has a 3-dB cutoff frequency of 12 GHz.

The oscilloscope that was used to record the data was a Tektronix TDS6604 with a 6-GHz analog BW and a sampling rate of 20 GS/s, providing a temporal resolution of 50 ps. The oscilloscope has an 8-bit digitizer, nominally providing a DR of 256, which is typical for modern digitizing oscilloscopes. Unfortunately, at full BW, digitizing noise reduces this to approximately 6 bits for a DR of about 64 in single-shot mode. This is insufficient for the NIF Dante requirements and is the primary reason the optical replicas were introduced into the system.

Data-Reduction Method

Several calibration steps are necessary to convert the complicated data record at the photodetector. Figure 130.91 shows the full pulse train at the photodetector. First, the replicator output without an rf signal applied to the MZM is recorded to determine relative positions of the 16 optical pulses. The individual elements of the two sets of eight pulses are nominally identical. Their relative timing can be determined by extracting a window around each pulse and aligning the windows via a cross-correlation. These relative timings are fixed so they may be recorded for future analysis. The eight pulses, aligned in time, are then averaged together to generate an average pulse shape: $I_{J,0}(t)$. The subscript J indicates the number of the MZM. Next a small rf signal $V_{\rm rf}(t)$ is applied to the MZM and $I_{J,{\rm rf}}(t)$ is recorded along with $V_{\rm rf}(t)$. The eight modulated pulses are then averaged together to produce a low-noise version of the MZM output. At each point in time, eight independent measurements are averaged. The standard deviation is given by the root-mean-square (rms) variation about the mean of the eight light pulses, $\Delta I_{J,{\rm opt}}(t)$. The SNR at each point is easily determined as $I_{J,{\rm opt}}(t)/\Delta I_{J,{\rm opt}}(t)$. The MZM transmission is given by

$$I_J(t) = I_{J,0}\sin\left\{\frac{\pi\left[V_{\rm rf}(t)+V_{J,0}\right]}{V_{J,\pi}}\right\} + I_{J,d}, \qquad (1)$$

where the parameter $V_{J,\pi}$ is the half-wave voltage, $V_{J,0}$ is the phase-equivalent, bias-point voltage, and $I_{J,d}$ is the combined optical leakage and bias. These values are approximately known. The manufacturer specifies $V_{J,\pi}$. The Q– operating point implies $V_{J,0}$ is $1.5 \times V_\pi$ and $I_{J,d} \sim I_{J,0}$. For $V_{\rm rf}(t) \ll V_{J,\pi}$, the response is essentially linear and Eq. (1) can be easily inverted over a time window that encompasses the flattop portion of the optical pulse without having to account for multifringe effects. The clean, optically measured $V_{\rm rf}(t)$ can then be compared with the applied, electronically measured $V_{\rm rf}(t)$ and cross-correlated to determine the relative phase. Using the averaged pulse shape makes it less likely that the cross-correlation will be biased by noisy data. Once the temporal alignment is established, the magnitude of $V_{\rm rf}(t)$ can be increased to values greater than $V_\pi/2$ to map out the entire transmission function. The algorithm specified in IEEE standard 1240 (Ref. 8) is used to determine the best-fit values for the constants for the system calibration. Each MZM is now calibrated with a baseline optical transmission curve and three scalar constants. The system is now ready to measure arbitrary rf signals.

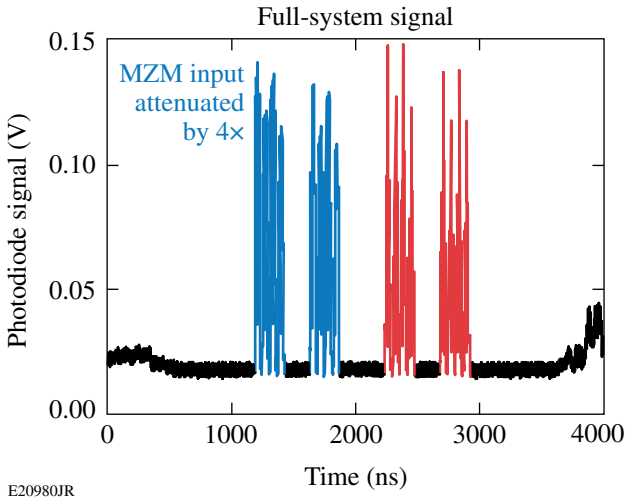

Figure 130.91
The optical signal detected at the oscilloscope at the output of the instrument has 16 serially combined pulses, eight from each Mach–Zehnder modulator (MZM).

The baseline optical transmission with $V_{\rm rf}(t) = 0$ should be reacquired shortly before the actual data are taken to account for drifts in the performance of the many EO components in the system. The arbitrary rf signal is then measured. The eight pulses from the MZM with highest attenuation (J = 1, λ_1 = 1557 nm) are averaged and then converted using calibrated sinusoidal transmittance of the modulator. Ideally, the attenuation is set such that the voltage applied to $\rm MZM_1$ never exceeds $V_{1,\pi}$. The unfolded $V_{1,{\rm rf}}(t)$ from the first MZM is used in conjunction with the calibrated $V_{2,\pi}$ of the lowest-attenu-

ation MZM to determine when the voltage applied to MZM_2 exceeded $V_{2,\pi}/2$. Normally, the arcsine function is calculated on the interval from $(M + 1/2)\pi$ to $(M + 1.5)\pi$, where M is an integer. Note that the sign flips between adjacent intervals. By noting whether M is even or odd, the multivalued unfolding can be made unambiguously single valued.

The averaged and unfolded signals from the two MZM's can be cross-correlated to determine the temporal alignment. The next step is to combine the two EO measured signals. As described above, the SNR can be calculated at each temporal point of the two waveforms. These SNR's can be quite different between the two curves, particularly when MZM_2 reaches the vicinity of $V_{2,\pi}/2$. The slope of the transmission function is zero at this point. The unfolding function has the form

$$V_{\mathrm{rf}}(t) = \frac{V_{J,\pi}}{\pi} \sin^{-1}\left[\frac{I_J(t) - I_{J,d}}{I_{J,0}}\right] - V_{J,0}. \tag{2}$$

Taking the derivative with respect to I_{opt} and multiplying by $\Delta I_{\mathrm{opt}}(t)$, the standard deviation of the optical measurements at each point, the variation in $V_{\mathrm{rf}}(t)$ as a function of $I_{\mathrm{opt}}(t)$ and $\Delta I_{\mathrm{opt}}(t)$ can be determined.

$$\Delta V_{J,\mathrm{rf}}(t) = \Delta I_J(t)\frac{\mathrm{d}V_{J,\mathrm{rf}}}{\mathrm{d}I_J} = \frac{V_{J,\pi}\Delta I_J(t)}{I_{J,0}\pi\sqrt{1 - \left[\dfrac{I_J(t) - I_{J,d}}{I_{J,0}}\right]^2}}, \tag{3}$$

when $V_{\mathrm{rf}}(t)$ equals $V_{J,\pi}/2$, $I_{J,\mathrm{opt}}(t)$ is approximately zero, and the derivative diverges. Small errors in the measurement $\Delta I_{J,\mathrm{opt}}(t)$ lead to large changes in the variation of the EO measured rf voltage $\Delta V_{J,\mathrm{rf}}(t)$. A weighted average based on standard deviations of the two signals was used to combine the two MZM's. To calculate the standard deviation, the rms deviation of the light pulses $\Delta I_{J,\mathrm{opt}}(t)$, was fed into Eq. (2) as

$$I_{J,\mathrm{opt}^+}(t) = I_{J,\mathrm{opt}}(t) + \Delta I_{J,\mathrm{opt}}(t) \tag{4a}$$

and

$$I_{J,\mathrm{opt}^-}(t) = I_{J,\mathrm{opt}}(t) - \Delta I_{J,\mathrm{opt}}(t). \tag{4b}$$

These substitutions generated $\Delta V_{J,\mathrm{rf}^+}(t)$ and $\Delta V_{J,\mathrm{rf}^-}(t)$, respectively. The rms variation in $V_{J,\mathrm{rf}}(t)$ was then defined as

$$\Delta V_{J,\mathrm{rf}}(t) = \left[\Delta V_{J,\mathrm{rf}^+}(t) + \Delta V_{J,\mathrm{rf}^-}(t)\right]/2. \tag{5}$$

The weighting function for the averaging was taken as the inverse of the standard deviation of the raw data $1/\Delta I_{J,\mathrm{opt}}(t)$ normalized by the sum of all the weights:

$$W_J(t) = \left[1/\Delta I_{J,\mathrm{opt}}(t)\right]/\sum\left[1/\Delta I_{J,\mathrm{opt}}(t)\right]; \tag{6}$$

$$\left\langle V_{\mathrm{rf}}(t)\right\rangle = \sum\left[V_{J,\mathrm{rf}} W_J(t)\right]. \tag{7}$$

Likewise, the final rms variation at each point is the weighted rms sum or the variations from each modulator:

$$\Delta\left\langle V_{\mathrm{rf}}(t)\right\rangle = \sqrt{\sum \Delta V_{J,\mathrm{rf}}(t)\Delta V_{J,\mathrm{rf}}(t) W_J(t)} \tag{8}$$

and the SNR is $\left\langle V_{\mathrm{rf}}(t)\right\rangle / \Delta\left\langle V_{\mathrm{rf}}(t)\right\rangle$.

With the hardware and signal-processing algorithms in place, the system was incorporated into the Dante instrument on LLE's OMEGA laser. An rf splitter was used to tap off half of the signal feeding one of the Dante SCD5000 transient digitizers. In this way we could directly compare the current system and the prototype. Figure 130.92 shows the averaged optical output of the two MZM's. Each averaged output is bracketed by curves representing +1 and –1 standard deviation. The data from the highly attenuated modulator vaguely resemble an inverted copy of the output of the XRD. The low-attenuation MZM output is highly distorted because the voltage exceeded $V_{\pi}/2$. This signal required the unfolded signal from the highly attenuated MZM to remove the multivalue ambiguities. This procedure is fully automated. Figure 130.93 shows the combined average of the two MZM's and the purely electrical measurement from the SCD5000. The average rms difference between the two waveforms is 2.6%. Another way to compare the measurements from the different instruments is to look at the spectral content. Figure 130.94 shows the fast Fourier transform (FFT) of both waveforms. The spectra match out to a frequency of about 3.5 GHz. The rise time of the XRD's is approximately 120 ps, giving a maximum frequency of 2.75 GHz. Therefore, we expect the EO acquisition system to capture all of the frequency delivered by the XRD.

Using an offline electronic pulse generator to simulate the NIF Dante XRD's, signals as large as 18 V were measured with the prototype system. Using the analysis described above, the SNR was calculated and is plotted against unfolded and averaged signals in Fig. 130.95. The peak SNR was approximately 500:1. The horizontal line is at an SNR of 1 and represents the minimum signal detectable by the instrument. The measured

points cross this line at 30 mV, so the demonstrated DR is 600:1. The relevance of Fig. 130.95 is illustrated in Fig. 130.96, where the system output for a 30-mV input pulse is plotted. The output is very noisy and just barely discernible.

Conclusions

A prototype EO acquisition system, the NIF Dante, has been built and tested. The system has a DR of 600:1 and a peak SNR of 500:1. The prototype has demonstrated that the concept works, but not all of the specifications of the NIF Dante upgrade have been met. In particular, the DR demonstrated so far is too small. On the high end, the maximum signal is limited to the voltage that drives both MZM's beyond $V_{\pi}/2$. At that point the automated reduction routines cannot define a unique unfolding. The solution to this problem is to add an additional MZM with still-higher attenuation on its rf input. Other strategies must be employed to reach an SNR of 5 at a signal of 50 mV over a 200-ps interval. We now have an SNR of 1 at 30 mV over

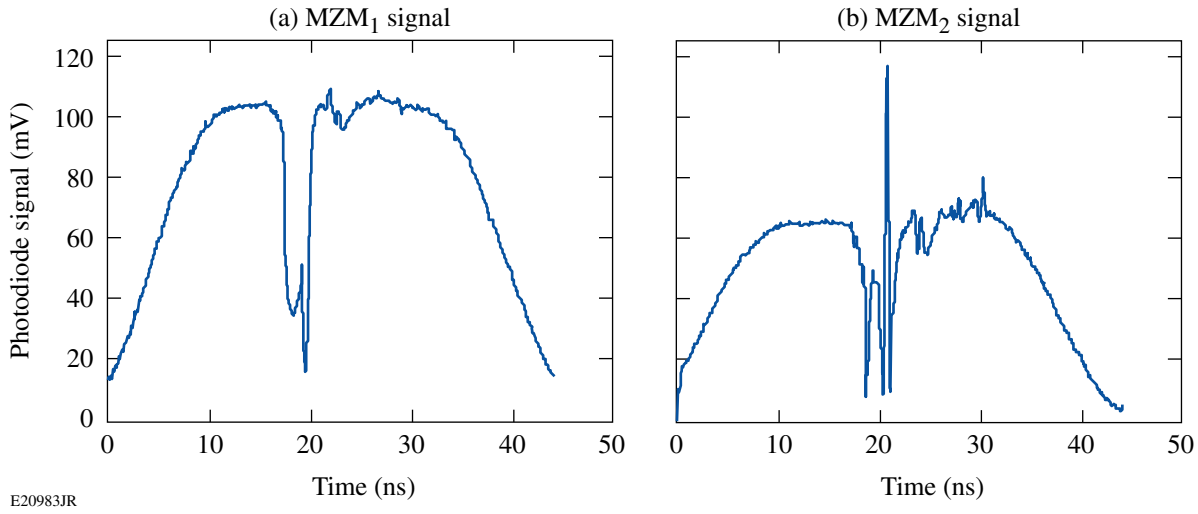

Figure 130.92
The averaged output of the two MZM's. (a) The signal from MZM_1 is approximately an inverted replica of the radio frequency (rf) input. (b) The signal from MZM_2 is highly distorted as a result of fringe shifts.

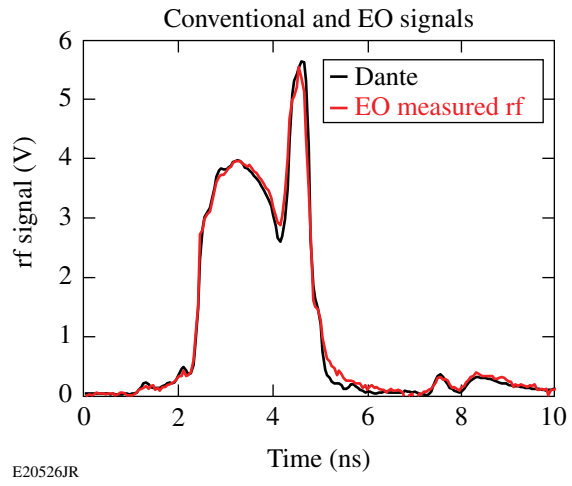

Figure 130.93
The electro-optic (EO) measurement agrees with that of a high-dynamic-range digitizer.

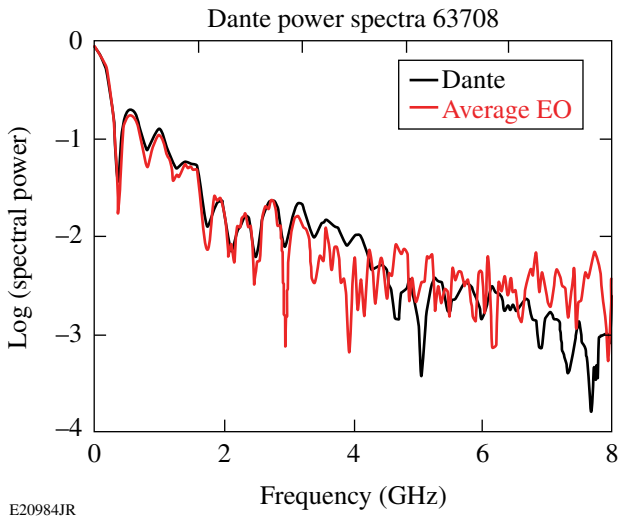

Figure 130.94
The frequency content of the SCD5000 and the EO measurements match out to 3.75 GHZ, which is greater than the bandwidth of the x-ray photodiode.

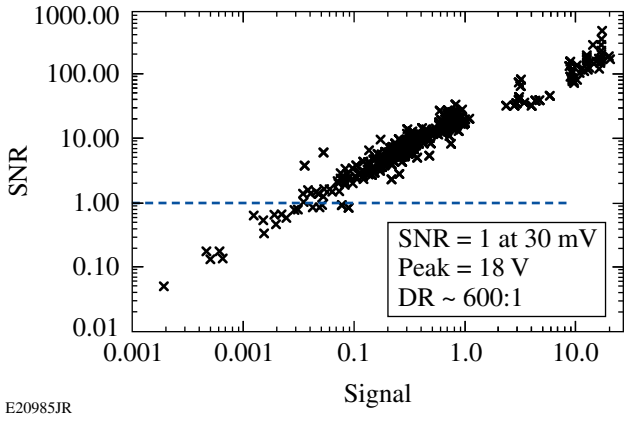

Figure 130.95
The signal-to-noise ratio (SNR) plotted against the EO measured signal clearly shows that the minimum-detectable signal occurs at 30 mV, where the SNR crosses the horizontal line. The DR is ~600:1.

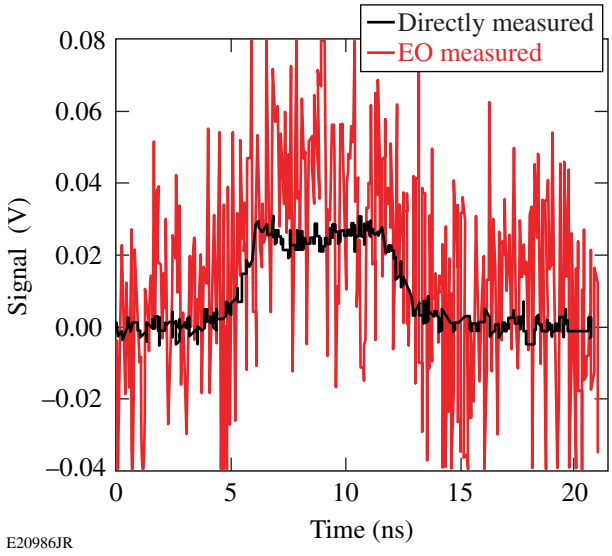

Figure 130.96
At 30 mV, the EO measured output (red curve) is noisy with respect to the directly measured radio frequency (black curve).

a 50-ps time interval. Figure 130.95 implies an SNR of 1.7 at 50 mV. Averaging four points to get to the 200-ps interval will improve the SNR by a factor of 2, giving an SNR of 3.4, which almost meets the specification. The number of replicas can probably be increased to 32 without adding an undue burden of optical fiber management on the system. This will increase the SNR by a factor of 2, and, therefore, will meet the specification. Using a 12-GHz, 40-GS/s oscilloscope will accomodate an eight-point temporal smoothing that could increase the SNR by $\sqrt{8}$. Beyond that, it will be necessary to explore using quieter lasers and an EDFA with lower noise figures.

ACKNOWLEDGMENT

This work was supported by the U.S. Department of Energy Office of Inertial Confinement Fusion under Cooperative Agreement No. DE-FC52-08NA28302, the University of Rochester, and the New York State Energy Research and Development Authority. The support of DOE does not constitute an endorsement by DOE of the views expressed in this article.

REFERENCES

1. E. I. Moses, Fusion Sci. Technol. **54**, 361 (2008).
2. E. L. Dewald *et al.*, Rev. Sci. Instrum. **75**, 3759 (2004).
3. E. L. Wooten *et al.*, IEEE J. Sel. Top. Quantum Electron. **6**, 69 (2000).
4. *Generic Reliability Assurance Requirements for Optoelectronic Devices Used in Telecommunications Equipment*, Telcordia Technologies, Inc., Piscataway, NJ, Document No. GR-468-CORE, Issue 2 (September 2004).
5. Fiberdyne Labs, Inc., accessed 26 April 2012, http://www.fiberdyne.com/products/itu-grid.html.
6. E. I. Ackerman and C. H. Cox III, in *International Topical Meeting on Microwave Photonics, 2000* (IEEE, New York, 2000), pp. 121–124.
7. W. R. Donaldson, J. R. Marciante, and R. G. Roides, IEEE J. Quantum Electron. **46**, 191 (2010).
8. *IEEE Std. 1241-2000, IEEE Standard for Terminology and Test Methods for Analog-to-Digital Converters* (IEEE, New York, 2001).

Publications and Conference Presentations

Publications

D. H. Froula, I. V. Igumenshchev, D. T. Michel, D. H. Edgell, R. Follett, V. Yu. Glebov, V. N. Goncharov, J. Kwiatkowski, F. J. Marshall, P. B. Radha, W. Seka, C. Sorce, S. Stagnitto, C. Stoeckl, and T. C. Sangster, "Increasing Hydrodynamic Efficiency by Reducing Cross-Beam Energy Transfer in Direct-Drive-Implosion Experiments," Phys. Rev. Lett. **108**, 125003 (2012).

M. Guziewicz, W. Słysz, M. Borysiewicz, R. Kruszka, Z. Sidor, M. Juchniewicz, K. Golaszewska, J. Z. Domagała, W. Rzodkiewicz, J. Ratajczak, J. Bar, M. Węgrzecki, and R. Sobolewski, "Technology of Ultrathin NbN and NbTiN Films for Superconducting Photodetectors," Acta Phys. Pol A **120**, A76 (2011).

J. F. Myatt, J. Zhang, J. A. Delettrez, A. V. Maximov, R. W. Short, W. Seka, D. H. Edgell, D. F. DuBois, D. A. Russell, and H. X. Vu, "The Dynamics of Hot-Electron Heating in Direct-Drive-Implosion Experiments Caused by Two-Plasmon-Decay Instability," Phys. Plasmas **19**, 022707 (2012).

P. M. Nilson, J. R. Davies, W. Theobald, P. A. Jaanimagi, C. Mileham, R. K. Jungquist, C. Stoeckl, I. A. Begishev, A. A. Solodov, J. F. Myatt, J. D. Zuegel, T. C. Sangster, R. Betti, and D. D. Meyerhofer, "Time-Resolved Measurements of Hot-Electron Equilibration Dynamics in High-Intensity Laser Interactions with Thin-Foil Solid Targets," Phys. Rev. Lett. **108**, 085002 (2012).

A. V. Okishev, C. Dorrer, Y. Fisher, and M. Pavia, "A Multi-wavelength, Variable-Pulse-Width, Diode-Pumped Laser System," in *Solid State Lasers XXI: Technology and Devices*, edited by W. A. Clarkson and R. K. Shori (SPIE, Bellingham, WA, 2012), Vol. 8235, Paper 82350Y.

C. Stoeckl, G. Fiksel, D. Guy, C. Mileham, P. M. Nilson, T. C. Sangster, M. J. Shoup III, and W. Theobald, "A Spherical Crystal Imager for OMEGA EP," Rev. Sci. Instrum. **83**, 033107 (2012).

A. Trajkovska Petkoska and S. D. Jacobs, "The Manufacture, Characterization and Manipulation of Polymer Cholesteric Liquid Crystal Flakes and Their Possible Applications," J. Mater. Sci. Eng. A **2**, 137 (2012).

B. Yaakobi, P.-Y. Chang, A. Solodov, C. Stoeckl, D. H. Edgell, R. S. Craxton, S. X. Hu, J. F. Myatt, F. J. Marshall, W. Seka, and D. H. Froula, "Fast-Electron Generation in Long-Scale-Length Plasmas," Phys. Plasmas **19**, 012704 (2012).

Forthcoming Publications

J. Bromage, C. Dorrer, and R. K. Jungquist, "Temporal Contrast Degradation at the Focus of Ultrafast Pulses from High-Frequency Spectral Phase Modulation," to be published in the Journal of the Optical Society of America B.

T. J. B. Collins, J. A. Marozas, K. S. Anderson, R. Betti, R. S. Craxton, J. A. Delettrez, V. N. Goncharov, D. R. Harding, F. J. Marshall, R. L. McCrory, D. D. Meyerhofer, P. W. McKenty, P. B. Radha, A. Shvydky, S. Skupsky, and J. D. Zuegel, "A Polar-Drive–Ignition Design for the National Ignition Facility," to be published in Physics of Plasmas.

D. H. Froula, B. Yaakobi, S. X. Hu, P.-Y. Chang, R. S. Craxton, D. H. Edgell, R. Follett, D. T. Michel, J. F. Myatt, W. Seka, R. W. Short, A. A. Solodov, and C. Stoeckl, "Saturation of the Two-Plasmon Decay Instability in Long-Scale-Length Plasmas Relevant to Direct-Drive Inertial Confinement Fusion," to be published in Physical Review Letters.

A. J. Harvey-Thompson, S. V. Lebedev, S. Patankar, S. N. Bland, G. Burdiak, J. P. Chittenden, A. Colaitis, P. De Grouchy, H. W. Doyle, G. N. Hall, E. Khoory, M. Hohenberger, L. Pickworth, F. Suzuki-Vidal, R. A. Smith, J. Skidmore, L. Suttle, and G. F. Swadling, "Optical Thomson Scattering Measurements of Plasma Parameters in the Ablation Stage of Wire Array *Z* Pinches," to be published in Physical Review Letters.

A. J. Harvey-Thompson, S. V. Lebedev, S. Patankar, S. N. Bland, G. Burdiak, J. P. Chittenden, A. Colaitis, P. De Grouchy, G. N. Hall, E. Khoory, M. Hohenberger, L. Pickworth, F. Suzuki-Vidal, R. A. Smith, J. Skidmore, L. Suttle, and G. F. Swadling, "Optical Thomson Scattering Measurements of Cylindrical Wire Array Parameters," to be published in Physics of Plasmas.

M. Hohenberger, P.-Y. Chang, G. Fiksel, J. P. Knauer, R. Betti, F. J. Marshall, D. D. Meyerhofer, F. H. Séguin, and R. D. Petrasso, "Inertial Confinement Fusion Implosions with Imposed Magnetic Field Compression Using the OMEGA Laser," to be published in Physics of Plasmas.

S. X. Hu, G. Fiksel, V. N. Goncharov, S. Skupsky, D. D. Meyerhofer, and V. A. Smalyuk, "Mitigating Laser Imprints in Direct-Drive ICF Implosions with High-*Z* Dopants," to be published in Physical Review Letters.

I. V. Igumenshchev, W. Seka, D. H. Edgell, D. H. Froula, V. N. Goncharov, R. S. Craxton, L. Divol, R. Follett, J. H. Kelly, T. Z. Kosc, D. T. Michel, P. Michel, R. L. McCrory, A. V. Maximov, D. D. Meyerhofer, J. F. Myatt, T. C. Sangster, A. Shvydky, S. Skupsky, and C. Stoeckl, "Crossed-Beam Energy Transfer in Direct-Drive Implosions," to be published in Physics of Plasmas.

I. Iñiquez-de-la-Torre, H. Rodilla, J. Mateos, T. González, H. Irie, and R. Sobolewski, "Monte Carlo Studies of the Intrinsic Time-Domain Response of Nanoscale Three-Branch Junctions," to be published in the Journal of Applied Physics.

A. V. Okishev, "Highly Efficient Room-Temperature Yb:YAG Ceramic Laser and Regenerative Amplifier," to be published in Optics Letters.

J. B. Oliver, P. Kupinski, A. L. Rigatti, A. W. Schmid, J. C. Lambropoulos, S. Papernov, A. Kozlov, S. Smith, and R. D. Hand "Stress Compensation in Hafnia/Silica Optical Coatings by Inclusion of Alumina Layers," to be published in Optics Express.

J. E. Schoenly, W. Seka, J. D. B. Featherstone, and P. Rechmann, "Near-UV Laser Treatment of Extrinsic Dental Enamel Stains," to be published in Lasers in Surgery and Medicine.

A. Visco, M. J. Grosskopf, S. H. Glenzer, D. H. Froula, G. Gregori, T. Döppner, F. W. Doss, and R. P. Drake, "Measurement of Radiative Shock Properties by X-Ray Thomson Scattering," to be published in Physical Review Letters.

S. K.-H. Wei, S. H. Chen, K. L. Marshall, C. Dorrer, and S. D. Jacobs, "Azimuthal Anchoring Energy and Pixel Resolution in a Photopatterned Liquid Crystal Cell Using Coumarin-Based Photoalignment Layers," to be published in the Japanese Journal of Applied Physics.

Conference Presentations

R. L. McCrory, "LLE's Perspective on FY13–FY18 Planning," ICF Executives Meeting, Albuquerque, NM, 18 January 2012.

A. V. Okishev, C. Dorrer, Y. Fisher, and M. Pavia, "A Multiwavelength, Variable-Pulse-Width, Diode-Pumped Laser System," Solid State Lasers XXI: Technology and Devices, San Francisco, CA, 21–26 January 2012.

The following presentations were made at the MAGLIF Workshop, Albuquerque, NM, 5–8 February 2012:

G. Fiksel, P.-Y. Chang, M. Hohenberger, J. P. Knauer, F. J. Marshall, D. D. Meyerhofer, R. Betti, F. H. Séguin, and R. D. Petrasso, "Effect of Magnetic Fields on Neutron Emission from ICF Implosions."

J. P. Knauer, P.-Y. Chang, M. Hohenberger, G. Fiksel, F. J. Marshall, D. D. Meyerhofer, R. Betti, F. H. Séguin, and R. D. Petrasso, "Compressing Magnetic Fields with High-Energy Lasers."

J. D. Hager, J. P. Knauer, V. A. Smalyuk, T. J. B. Collins, J. A. Delettrez, S. X. Hu, D. D. Meyerhofer, and T. C. Sangster, "Rayleigh–Taylor Measurements in Planar Targets with CH and SiO_2 Ablators on OMEGA," NIF User Group Meeting, Livermore, CA, 12–15 February 2012.

J. M. Soures, "High-Energy-Density-Physics Research at the Omega Laser Facility," 2012 Stewardship Science Academic Alliances Symposium, Washington, DC, 22–23 February 2012.


1850
MELIORA
UNIVERSITY of
ROCHESTER